Azimuthal Asymmetry and Transverse Momentum of Hadrons in Deep Inelastic Muon Scattering at 490 GeV.

by

Mark David Baker

Bachelor of Science, Honors Tutorial College, Ohio University

Submitted to the Department of Physics
in partial fulfillment of the requirements for the degree of

Doctor of Philosophy

at the

MASSACHUSETTS INSTITUTE OF TECHNOLOGY

February 1993

Azimuthal Asymmetry and Transverse Momentum of Hadrons in Deep Inelastic Muon Scattering at 490 GeV.

by
Mark David Baker

Submitted to the Department of Physics
on December 18, 1992, in partial fulfillment of the
requirements for the degree of
Doctor of Philosophy

Abstract

The forward charged hadrons produced in deep inelastic scattering of 490 GeV muons from deuterium were studied. The data were taken by the E665 collaboration during the 1987-1988 Fermilab fixed target run. 3×10^4 events (6×10^4 hadrons) were collected over a large range of kinematic variables: 100 GeV $< \nu <$ 500 GeV, 2 GeV^2 $< Q^2 <$ 100 GeV^2, $0.003 < x_{Bj} < 0.2$, and $0.2 < y_{Bj} < 0.9$.

Using the virtual photon axis as the z-axis, the distributions of the produced hadrons in azimuthal angle and in transverse momentum are examined. The primordial $k_\perp$ of the struck parton and $\mathcal{O}(\alpha_s)$ QCD effects are expected to contribute to an azimuthal asymmetry and to an increase in the average transverse momentum. Some theoretical work in the literature concerning these effects is described and some original results are derived concerning the effects of primordial $k_\perp$ on the azimuthal distribution. A Monte Carlo program is described which includes these theoretical effects and models fragmentation, the detector response, and the event reconstruction.

The data exhibit several surprising effects. First, the phi asymmetry in the data is independent of Q^2, while theoretically it should be more pronounced at low Q^2 and vanish at high Q^2. Second, the phi asymmetry is carried by the most energetic particle in each event, which we call the Rank 1 particle, and there is very little phi asymmetry of the other charged hadrons. Third, this phi asymmetry in the Rank 1 particle is independent of the hadron energy fraction z_h. The Monte Carlo predicts a strong z_h dependence and little rank dependence. Finally, the seagull plot shows an unexpected increase in transverse momentum p_T for high energy hadrons ($z_h > 0.4$) as a function of Q^2. It is clear from these results that more theoretical work is needed in order to understand primordial $k_\perp$ and the azimuthal asymmetry in deep inelastic scattering.

Thesis Supervisor: Louis S. Osborne
Title: Professor of Physics

Azimuthal Asymmetry and Transverse Momentum of Hadrons in Deep Inelastic Muon Scattering at 490 GeV.

by

Mark David Baker

Bachelor of Science, Honors Tutorial College, Ohio University

Submitted to the Department of Physics
in partial fulfillment of the requirements for the degree of

Doctor of Philosophy

at the

MASSACHUSETTS INSTITUTE OF TECHNOLOGY

February 1993

© Mark David Baker, MCMXCIII. All rights reserved.

The author hereby grants to MIT permission to reproduce and to distribute copies of this thesis document in whole or in part.

Author .....
Department of Physics
December 18, 1992

Certified by .....
Louis S. Osborne
Professor of Physics
Thesis Supervisor

Accepted by .....
George F. Koster
Chairman, Departmental Committee on Theses

Acknowledgments

I have had the pleasure during my years at MIT, both before and after the data-taking, of working in an environment which was challenging and empowering without being overly competitive or hostile. I would like to thank the senior members of the Counter Spark Chamber Group for providing such an environment: Wit Busza, Jerry Friedman, Henry Kendall, Vera Kistiakowsky, Louis Osborne, Larry Rosenson, Frank Taylor, and Robin Verdier.

Many people have contributed directly and indirectly to the work that I have done over the past 7 years. The E665 experiment at Fermilab was the product of several man-centuries of work, spread out over about a decade. I would therefore like to acknowledge the work of the entire E665 collaboration, which was essential to this thesis.

More specifically, I would like to thank my advisor, Louis Osborne, for his involvement in the physics analysis. He has been a wellspring of ideas, advice, and perspective over the years. I would also like to thank Wit Busza for his advice and especially for convincing me that there is little correlation between complicated mathematics and deep physics insight ... I have enjoyed working with my colleague and good friend John Ryan over the years. I've learned many things from him: to trust my sense of "iconoclasm in Science", how to build a detector, and countless technical details of data analysis. This thesis would have been much weaker without his help over the years and without his thesis results to build upon. I also enjoyed working with Perry Anthony, who was always very helpful during our years of working together. His involvement in maintaining the PTM/PTA system during the 1990 run went above and beyond the call of duty and made my life much easier.

I would like to thank Michael Schmitt for his friendship and for the many fruitful discussions of physics that we have had. His insight into physics and his passion for it were inspirational. I should also point out that he contributed significantly to the E665 software, and especially to the Calorimeter Analysis. I would like to thank my colleague Silhacène Aïd for his advice on System (and User) Management, for providing templates for the apparatus and Feynman diagram figures, and for his work on the E665 analysis and Monte Carlo software. I also enjoyed working with Don Geesaman, whose guidance was very welcome, and with Mathias Wilhelm, whose enthusiasm for computers was infectious.

I would like to thank Steve O'Day, probably the most practical of my fellow graduate students, for being a good friend. Through many lunchtime conversations he helped me keep my head on straight. I would like to thank both Steve O'Day and Shuichi Kunori for helping to make the Monte Carlo and the data analysis more robust. I would like to thank Wolfgang Wittek for his work on the analysis code and also for his insistence on rigor and completeness in both software and physics papers.

I would like to thank Rob Kennedy and Alex Salvarani for the work that they did on the PTM and PTA systems. Helmut Braun, Martin Erdmann, and Arnd Röser helped out immensely during the installation of the PTA chambers and electronics. Richard Nickerson was a pleasure to work with on the Pulse Injection upgrade to the PTM system. His high standards, deep knowledge of electronics, hard work, and gentle nature were all worthy of emulation. I would like to thank Frank Pipkin and Hugh Montgomery for their support during this period. I also learned many things from collaborating with Hans Kobrak, especially during the PTM upgrade. In addition to being a good friend over the years, Janet Conrad also offered lots of advice and help during the Run '90 upgrade as well as some useful suggestions during my data analysis.

I would like to thank Don Geesaman, Hugh Montgomery, Heidi Schellman, and Tom Kirk for their leadership and many suggestions during the various phases of the experiment. I also enjoyed collaborating and socializing with Clive Halliwell, Jorge Morfin, and Andreas Manz.

In addition to those already mentioned, I would like to thank my fellow students for their work on the equipment and analysis software: Anwar Bhatti, Uwe Ecker, Doug Jansen, Doug Michael, Eric Ramberg, and Alex Salvarani. Mark Adams, David Jaffe, and Tim Carroll have been invaluable to the experiment, both through building the SAT trigger and through their tireless desire to "do things right". Harry Melanson and Clive Halliwell were heavily involved in bringing the Pattern Recognition to fruition. I would also like to thank Harry for his unflagging interest in and enthusiasm for physics. I would like to thank Steve Wolbers for his overall contribution to E665. I would also like to thank Steve Wolbers and John Schell for the help that they has given me personally in performing my long distance analysis at Fermilab from MIT. I would like to thank Carlos Salgado, Detlev Hantke, and Harsh Venkataramania for their work on the E665 Monte Carlo program used in this thesis. Carlos was especially helpful to me in implementing my changes to the standard Monte Carlo.

While preparing this thesis, I used several products which made my life much easier and much more fun. These include: the typesetting programs LaTeX and TeX by Leslie Lamport and Donald Knuth, the algebraic manipulation program Mathematica by Steven Wolfram, the NeXT computer designed by Steve Jobs, and many useful software packages from CERN: CERNLIB, PAW, ZEBRA.

I would also like to thank my parents, David and Phyllis Baker, for their love and support during these long years of graduate school. I'm sure that they were beginning to despair of my ever really closing this chapter of my life. Finally, I would like to thank my fiancée, Brenda Lugo, for her love, support, advice, and patience during these last two, very draining, years.

If the problem is this absence of being and if what *is* is what is said then the more we talk, the more being there is.
The dream of science is that there be little being, that it be concentrated and sayable, $E = mc^2$. Wrong. To be saved at the very beginning, for all eternity, it is necessary for that being to be tangled. Like a serpent tied into knots by a drunken sailor: impossible to untie.

Umberto Eco in Foucault's Pendulum

It is the glory of God to conceal a matter,
But the glory of kings is to search out a matter.

Proverbs 25:2 (NASB Version)

The essential point in science is not a complicated mathematical formalism or a ritualized experimentation. Rather the heart of science is a kind of shrewd honesty that springs from really wanting to know what the hell is going on!

Saul-Paul Sirag as quoted by *Nick Herbert* in Quantum Reality

Contents

1 Introduction **19**

1.1 Thesis Overview 20

1.2 Conventions 21

2 Theory and Phenomenology **25**

2.1 The Standard Model of Particle Physics 26

2.1.1 The Cast of Characters 26

2.1.2 The Interactions 28

2.2 Inelastic Lepton Scattering 29

2.2.1 Experimental Kinematics 30

2.2.2 Cross Section 31

2.2.3 Radiative Corrections 33

2.3 The Quark Parton Model 34

2.3.1 DIS in the Naïve Quark Parton Model 34

2.3.2 DIS in the QCD-improved Parton Model 39

2.3.3 The Parton Model with Primordial $k_\perp$ 45

2.4 The E665 Monte Carlo Program 57

2.4.1 BEAMMC: Beam Simulation 57

2.4.2 LEPTO: Parton-level Leptoproduction Cross-section 57

2.4.3 JETSET: Hadronization 61

2.4.4 GEANT: Apparatus Simulation 61
2.4.5 MC2: Digitization and Chamber Efficiency Simulation 62
2.5 Summary 62

3 Experimental Apparatus **65**

3.1 Overview of the Apparatus 65
3.1.1 Detector 65
3.1.2 Muon Beam 66
3.1.3 E665 Coordinate System 67
3.2 Beam Spectrometer 68
3.3 Targets 69
3.4 Forward Spectrometer 70
3.4.1 PCV: Vertex Proportional Chambers 71
3.4.2 PCN: Proportional Chambers 71
3.4.3 PCF: Forward Proportional Chambers 72
3.4.4 DC: Drift Chambers 72
3.4.5 PSA: Small Angle Proportional Chambers 74
3.5 Muon Identification 74
3.5.1 SPM: Muon Scintillator Planes 75
3.5.2 SMS: Small Muon Scintillator Planes 75
3.5.3 PTM: Muon Proportional Tubes 76
3.6 Electromagnetic Calorimeter 79
3.7 Miscellaneous Detector Elements 80
3.7.1 Čerenkov Detectors 81
3.7.2 TOF: Time of Flight Chambers 81
3.7.3 PTA: Wide Angle Proportional Tubes 82
3.7.4 SC: Streamer Chamber 83

3.8 Triggers and Data Acquisition 83
3.8.1 LAT: Large Angle Trigger 84
3.8.2 SAT: Small Angle Trigger 85
3.8.3 Other Triggers 86
3.8.4 Data Acquisition 88
3.9 Detector Upgrades for the 1990–1991 Run 89
3.9.1 General Upgrades 89
3.9.2 Data Acquisition Upgrades 91
3.9.3 PTM Upgrades and Changes 91
3.9.4 Summary of Upgrades 94
3.10 Summary 95

4 Event Reconstruction **97**

4.1 Alignment and Calibration 98
4.2 Split and Filter 101
4.3 PTMV: Basic Event Reconstruction 103
4.3.1 Decoding and Translation 104
4.3.2 PR: Pattern Recognition 104
4.3.3 TF: Track Fitting 110
4.3.4 Duplicate Track Removal 112
4.3.5 MM: Muon Matching 112
4.3.6 VX: Vertex Finding 114
4.4 DR: Data Reduction 117
4.5 Calorimeter Analysis 119
4.6 Event Selection 121
4.7 Track Selection 124
4.8 Calorimeter Cluster Cuts 126

4.9 Correction Philosophy 130
4.10 Summary 132

5 Physics Results **135**

5.1 Some Definitions 135
5.2 History 138
5.2.1 Transverse Momentum History 138
5.2.2 Phi Asymmetry History 141
5.3 Phi Asymmetry 145
5.3.1 Phi Asymmetry versus z_h and Rank 147
5.3.2 Transverse Momentum Dependence of the Phi Asymmetry . . 159
5.3.3 Phi Asymmetry versus Event Kinematics 162
5.3.4 Further Phi Asymmetry Studies 168
5.4 Transverse Momentum Distributions 170
5.5 Cross-checks and Systematics 175
5.5.1 Detector Inefficiencies 175
5.5.2 LAT Trigger Inefficiency 175
5.5.3 Detector Alignment and Calibration Errors 179
5.5.4 Time-dependent Detector Effects 180
5.5.5 Radiative Corrections 180
5.6 Conclusions 183

6 Summary and Conclusions **185**

A Theoretical Calculations **187**

A.1 An exact calculation of $\xi(Q^2, \nu, k_\perp)$. 188
A.1.1 Explicit Derivation of the Exact Result 188
A.1.2 Some Interesting Limiting Cases 192

A.1.3 Summary . . . 193
A.2 Leading Order Phi Asymmetry due to $k_\perp$ . . . 193
A.2.1 The Calculation . . . 194
A.2.2 Some Interesting Limiting Cases . . . 198
A.2.3 Summary . . . 199
A.3 Phi Asymmetry to $\mathcal{O}(\alpha_s)$ with $k_\perp$ . . . 200
A.3.1 General Definitions and Results . . . 200
A.3.2 Explicit Results for Gluon Bremsstrahlung . . . 204
A.3.3 Explicit Results for Photon-Gluon Fusion . . . 206
A.3.4 Summary . . . 208

B Implementing the Phi Asymmetry in LEPTO **209**
B.1 Overview of the LEPTO Algorithm . . . 210
B.2 Code Organization . . . 212
B.3 Coordinate Systems . . . 217
B.3.1 LQGEV Coordinate System . . . 218
B.3.2 LQQBEV Coordinate System . . . 219
B.4 Explicit Expressions for the Distributions . . . 221
B.5 Methodology: Generating a Distribution . . . 224
B.5.1 Finding a One-to-One Map . . . 224
B.5.2 Brute Force Method . . . 225
B.5.3 Implementing the Phi Asymmetry Cross Section by Brute Force 225
B.6 Summary . . . 228

C Analysis Details **229**
C.1 Rank Mixing Acceptance Correction . . . 229
C.2 Propagation of Errors . . . 234

D The Fermilab E665 Collaboration **245**

E Glossary **247**

E.1 Glossary of Terms 247

E.2 Glossary of Symbols 253

List of Figures

2-1 Inelastic Muon-Nucleon Scattering. 30

2-2 Elastic Muon-Parton Scattering. 34

2-3 Helicity Conservation in the Breit Frame. 38

2-4 Gluon Bremsstrahlung. 39

2-5 Altarelli-Parisi Evolution. 42

2-6 Photon Gluon Fusion. 43

2-7 Altarelli-Parisi Splitting Functions. 44

2-8 The Definition of Phi. 49

2-9 A Simple Picture of $k_\perp$-induced Phi Asymmetry. 50

2-10 Theoretical Phi Asymmetry as a Function of $k_\perp/Q$. 52

2-11 Theoretical Phi Asymmetry as a Function of Q. 53

2-12 Theoretical Phi Asymmetry as a Function of y_{Bj}. 53

2-13 The Definition of Parton Phi in Gluon Bremsstrahlung. 54

2-14 Theoretical Phi Asymmetry including both QCD and $k_\perp$. 56

3-1 The E665 Beam Spectrometer. 68

3-2 The E665 Detector. 70

3-3 A Cross-section of a PTM Module. 77

3-4 The Calorimeter. 79

3-5 A PTA Diagonal Plane. 82

4-1 The Shift in the Alignment Constants from the Surveyed Values. . . . 100

4-2 An Illustration of a Space Point. 105

4-3 The Calorimeter Bremsstrahlung-removal Cut. 123

4-4 The Calorimeter Distance-to-nearest-track Cut. 129

5-1 EMC Seagull Plot. 140

5-2 EMC Transverse Momentum Balance Plot. 142

5-3 EMC φ_h versus Q^2. 143

5-4 EMC φ_h versus x_F. 144

5-5 Raw Hadronic Phi Distribution. 145

5-6 Raw Phi Distributions for Various z_{h1} Ranges (1). 148

5-7 Raw Phi Distributions for Various z_{h1} Ranges (2). 149

5-8 The z_h-dependence of the Phi Asymmetry for Rank 1 Hadrons. . . . 150

5-9 The z_h-dependence of the Phi Asymmetry by Hadron Rank. 151

5-10 The z_h-dependence of the Phi Asymmetry by Hadron Rank (MC). . . 151

5-11 The Effect of Rank Purity Cuts on the Raw z_h distributions. 154

5-12 Phi Asymmetry versus z_h — Unambiguous Rank 1. 155

5-13 The Measured z-distributions by Hadron Rank. 157

5-14 Corrected z_h-dependence of the Phi Asymmetry by Hadron Rank. . . 158

5-15 The p_T-dependence of the Phi Asymmetry by Hadron Rank. 160

5-16 The p_T-dependence of the Phi Asymmetry by Hadron Rank (MC). . . 161

5-17 The Q-dependence of the Phi Asymmetry. 163

5-18 The Q-dependence of the Phi Asymmetry (MC). 164

5-19 The y_{Bj}-dependence of the Phi Asymmetry. 166

5-20 The y_{Bj}-dependence of the Phi Asymmetry (MC). 167

5-21 The p_T-dependence of the Phi Asymmetry for Two Regions in Q. . . 168

5-22 The p_T-dependence of the Phi Asymmetry for Two Regions in Q (MC). 169

5-23 Seagull Distributions for Different Regions of Q. 171

5-24 Seagull Distributions for Different Regions of Q (MC). 172

5-25 Seagull Distributions by Hadron Rank. 173

5-26 Seagull Distributions by Hadron Rank (MC). 173

5-27 Seagull Distributions versus Q^2. Unambiguous Rank 1 Hadron. 174

5-28 LAT Triggering Inefficiency. 176

5-29 Hadronic Phi Asymmetry versus Lab Phi of the Scattered Muon. . . 177

5-30 Hadronic Phi Asymmetry versus Lab Phi of the Scattered Muon (MC). 178

5-31 p_T and p_T^2 Resolution. 181

5-32 φ and $\cos\varphi$ Resolution. 182

A-1 $\mathcal{O}(\alpha_s)$ Diagrams in DIS. 200

A-2 Gluon Bremsstrahlung. 204

A-3 Photon-Gluon Fusion. 206

B-1 Coordinate System for Lund Routine LQGEV. 218

B-2 Coordinate System for Lund Routine LQQBEV. 220

List of Tables

2.1 The Matter Particles of the Standard Model. 27

2.2 The Spin-1 Gauge Bosons of the Standard Model. 27

3.1 D_2 Target Characteristics — 1987 Run. 69

3.2 PTM Position Changes for the 1990–1991 Run. 94

4.1 The Shift in the Alignment Constants from the Surveyed Values. . . . 99

4.2 DR Statistics for the D_2 LAT Sample. 118

4.3 The Effect of my Private Event Cuts. 123

4.4 Event Statistics for the Final D_2 LAT Sample. 124

4.5 The Effect of my Private Hadron Cuts. 125

Chapter 1

Introduction

An ancient Chinese philosopher once said that "he who breaks a thing to find out what it is made of has left the path of wisdom". Nevertheless, physicists have been breaking nucleons, both protons and neutrons, for over twenty years in the attempt to understand the nature of the nucleon constituents, which are called partons, and the interactions which govern the behavior of these partons.

Deep inelastic lepton scattering (DIS) is a technique in which an incoming lepton, such as a muon, strikes a nucleon, resulting in the breakup of the nucleon. By studying the three-momentum distribution of the scattered leptons, we can extract information about the partons inside of the nucleons.

Ideally, by also studying the three-momentum distribution of the outgoing partons resulting from the nucleon breakup, we could extract even more information about the partons that were originally in the nucleon. This would allow us to make an unambiguous measurement of the structure of the nucleon and of the mutual interaction of the fundamental partons. The outgoing partons, however, cannot be detected directly. They *hadronize*, or turn into hadrons, by a process which is much faster than our detector, is approximately independent of the original interaction, and is not very well understood. This hadronization process obscures the exact kinematics and even the number of fundamental particles generated by the interaction. Nevertheless, the hadrons which result from the nucleonic breakup do contain useful information about the structure of the nucleon and the interactions and nature of the partons.

In this thesis, we will examine hadrons which have been generated in deep inelastic collisions of muons with deuterons. We will then attempt to interpret this data in the light of current theoretical expectations and previous experimental results. Given the incoming and outgoing muon momenta, we can define an axis for the momentum transfer direction. We will study the distribution of the produced hadrons in

azimuthal angle and in transverse momentum with respect to this axis. We will also discuss and expand upon the current theoretical expectations and previous experimental results regarding the azimuthal distribution. Our primary goal will be to determine whether the current theory adequately describes the observed azimuthal distribution and to quantify any disagreements.

1.1 Thesis Overview

Fermilab Experiment # 665 (E665) was a deep inelastic muon scattering experiment in which a muon beam with an average energy of 490 GeV collided with a variety of different targets. This experiment was originally proposed in 1980 [1]. I became involved in 1986 and joined officially in 1987, before the first data-producing run, which ran from October of 1987 through February of 1988. My main experimental responsibilities during this first run revolved around the muon-identification proportional tubes (PTMs) and the wide-angle proportional tubes (PTAs). These detector systems were the joint responsibility of the MIT[1] and UCSD[2] groups within E665. Additionally, I was responsible for the system management of the Data Acquisition computers during much of the first run and beyond. Before the second data taking run which began in 1990, I was involved in some improvements to the muon-identification proportional tubes (PTMs). During part of the 1990–1991 run, I was responsible for maintaining the PTM and PTA systems.

This thesis is based on data from the 1987–1988 run, but it includes some details of the improvements to the PTM system for the 1990–1991 run. The thesis is divided into chapters which contain the main points and appendices which contain detailed supporting material and documentation. Following is an overview of the contents of each chapter and appendix.

Chapter 1 (this chapter) provides an introduction to and overview of the thesis and describes the conventions that are used.

Chapter 2 describes the conventional theory and phenomenology used in deep inelastic scattering experiments. It then extends the theory to include an original treatment of the effect of primordial transverse momentum ($k_\perp$) of the partons. Finally the Monte Carlo program used in this thesis to simulate the physics of DIS and the detector response is described. The Monte Carlo simulation program has been augmented to include a theoretical effect, partonic

[1] Massachusetts Institute of Technology
[2] University of California at San Diego

phi asymmetry, which is usually neglected. This program will be used to correct the data for detector effects, to estimate the effects of hadronization on the phi asymmetry, and to make theoretical predictions of the hadron-level phi asymmetry.

Chapter 3 describes the Experimental Apparatus used by E665, with special emphasis on the PTM and PTA chambers for which I shared responsibility.

Chapter 4 describes the basic analysis of the data including the detector alignment, raw data handling, the E665 event reconstruction program (PTMV), general E665 analysis cuts, and the analysis of the Electromagnetic Calorimeter. This chapter also describes the cuts that were specific to my analysis and explains the rationale behind them.

Chapter 5 describes the physics analysis and results. It also outlines some of the previous experimental data that relates to this thesis.

Chapter 6 contains a summary of the thesis and my conclusions.

Appendix A contains the new theoretical calculations whose results are referred to in Chapter 2.

Appendix B contains details of the implementation of the phi asymmetry in the Lund Monte Carlo: LEPTO Versions 5.2 (Matrix Element) and 4.3.

Appendix C contains some analysis details. These include a description of the acceptance correction and an expression for the measurement error on some of the physics variables used in this thesis.

Appendix D contains a list of the members of the E665 who contributed to the 1987 Run data taking and/or analysis.

Appendix E contains a glossary of special acronyms, abbreviations, and terms, many of which are specific to high energy physics or the E665 experiment at Fermilab. This appendix also contains a listing of most of the symbols for physical quantities which are used in this thesis.

1.2 Conventions

Some basic conventions are described below which will be used throughout this thesis.

Notation

We will work in units where the speed of light (c) is unity. The energy unit GeV is defined as the amount of energy gained by an electron in traveling through a voltage increase of 1 billion (10^9) volts. Since we have set the speed of light to 1, the energy unit GeV will also serve as a unit of momentum (usually GeV/c) and of mass (usually GeV/c^2). Distances and times will be referred to in the metric system. Frequencies will be referred to in units of Hertz (Hz) which stands for events per second or clock cycles per second. Charge will be expressed in units of the positron charge e. Magnetic field strength will be expressed in terms of Tesla (T).

The metric system prefixes will be used normally in many cases: K=10^3, M=10^6, etc. This is also true when referring to numbers of events. For instance, 8.5 K events should be understood as 8500. The only exception to this rule is when we are referring to bytes or words of computer storage. In this case 1 Kb refers to 1 kilobyte which is 2^{10} (1024) bytes. Similarly 1 Mb refers to 1 megabyte which is 2^{20} bytes.

Latin indices $\{i, j, k, \ldots\}$ will typically be used to refer to components of a 3-vector. Components of 4-vectors will be represented in the usual way with greek indices ranging from 0–3 with 0 referring to the time component. We will use the conventional metric with

$$g^{\mu\nu} \equiv \begin{pmatrix} g^{00} & g^{01} & g^{02} & g^{03} \\ g^{10} & g^{11} & g^{12} & g^{13} \\ g^{20} & g^{21} & g^{22} & g^{23} \\ g^{30} & g^{31} & g^{32} & g^{33} \end{pmatrix} = \begin{pmatrix} 1 & 0 & 0 & 0 \\ 0 & -1 & 0 & 0 \\ 0 & 0 & -1 & 0 \\ 0 & 0 & 0 & -1 \end{pmatrix} \tag{1.1}$$

and $g^{\mu\nu} = g_{\mu\nu}$ for a given μ, ν. This means that for a four-momentum p, we have contravariant components:

$$p^{\mu} : \{E;\ p_x, p_y, p_z\}\,,$$

and covariant components:

$$p_{\mu} : \{E;\ -p_x, -p_y, -p_z\}\,.$$

In Figures which contain several plots, the individual plots will be labeled alphabetically from left to right and then top to bottom. For instance:

(a) (b)
(c) (d)

Abbreviations and acronyms will be defined where they are first used and will be included in the Glossary.

The Dirac Delta Function

The Dirac delta function will be used in several places. It has the following properties:

$$\delta(x) = \begin{cases} \infty, & \text{if } x = 0 \\ 0, & \text{if } x \neq 0 \end{cases} \tag{1.2}$$

$$\int_a^b f(x)\delta(x)dx = \begin{cases} f(0), & \text{if } a < 0 < b \\ -f(0), & \text{if } b < 0 < a \\ 0, & \text{otherwise} \end{cases} \tag{1.3}$$

and

$$\delta\left(f(x)\right) = \sum_j \frac{1}{|f'(x_0^{(j)})|}\delta\left(x - x_0^{(j)}\right), \tag{1.4}$$

where $x_0^{(j)}$ refers to the jth solution to the equation $f(x) = 0$, and $f'(x)$ refers to df/dx. A useful consequence of Equation 1.4 is:

$$\delta\left(af(x)\right) = \delta\left(f(x)\right)/|a|. \tag{1.5}$$

Errors, Fitting, and Error Propagation

The standard nomenclature for treatment of errors, fitting, and error propagation will be used. Details regarding the definitions and methods used in fitting and error handling can be found in Reference [2].

Chapter 2

Theory and Phenomenology

This chapter contains a sketch of the conventional theory of deep inelastic scattering, along with a discussion of some of the assumptions that limit its usefulness in describing the azimuthal asymmetry. It also contains a description of some generalizations of the standard theory which render some of these usual assumptions unnecessary. In particular, we consider the effect of non-negligible primordial transverse momentum of the struck partons. In addition to quoting results from other authors, this section contains original work. Finally, the Monte Carlo program is described. This program is used to model the physics of deep inelastic scattering, the hadronization process, and the detector response.

This chapter is organized into sections as follows:

Section 2.1 describes the Standard Model of Particle Physics.

Section 2.2 provides a very general description of inelastic lepton-nucleon scattering. This general description rests on well-founded aspects of the Standard Model and can be considered to be fairly model-independent.

Section 2.3 provides a description of lepton-nucleon inelastic scattering in the framework of the Quark-Parton-Model (QPM). The QPM is explained in its naïve form, its QCD-improved form, and in a form which includes the effect of primordial transverse momentum of the partons. My unique contribution to the theory is included in Section 2.3.3.

Section 2.4 provides a brief description of the E665 Monte Carlo program, including the implementation of the theoretical effects of primordial transverse momentum. This section also describes how the Lund parameters for the Monte Carlo used in this thesis differ from the default Lund settings.

Section 2.5 summarizes the chapter.

2.1 The Standard Model of Particle Physics

If we are going to describe the theoretical framework for deep inelastic scattering, the Standard Model is a natural place to start. This model incorporates our best understanding of the fundamental particles and their interactions.

2.1.1 The Cast of Characters

There are four types of particles which are currently considered fundamental and pointlike. The first type comprises the spin-$\frac{1}{2}$ fermions which are commonly known as *matter* particles. The second type comprises the spin-1 bosons which are known as *gauge* bosons. These bosons mediate all of the forces between fundamental particles, except for gravity. The third type of fundamental particle consists of a unique particle called the graviton, which mediates gravity. It is thought to be a spin-2 boson, but has not been explicitly detected. The gravitational force plays little role in particle physics experiments at the current energies. The fourth type of particle consists of a particle or group of particles called the Higgs boson(s). No such particle has been detected directly, but the Higgs boson is thought to generate the masses of the other particles through spontaneous symmetry breaking. In the simplest formulation of the Standard Model known as the Minimal Standard Model, the Higgs is a single spin-0 boson.

The spin-$\frac{1}{2}$ matter particles can be arranged in the manner shown in Table 2.1. The most striking feature of this arrangement is that the matter particles can be divided into three generations which are identical except for their masses and their *flavor* quantum numbers. The second and third generations appear to be higher mass copies of the first generation. The subscripts L and R denote helicity states of the fundamental particles. The parentheses demark weak-isospin multiplets. The column marked Q refers to the conventional electric charge while *color N-plet* column refers to the SU(3) multiplet associated with the strong force. The color-singlet matter particles, which are denoted in the table by color N-plet value of 1, have no color charge and are known collectively as leptons. The color-triplet particles, which are denoted in the table by color N-plet value of 3, interact strongly and are known as quarks. In addition to this extensive list of fundamental particles, each of the fermions in Table 2.1 is mirrored by a distinct anti-particle which is equally fundamental and which carries equal and opposite charges (electric, weak, and strong). It should be noted that the top quark (t) has not been seen and that the tau-neutrino (ν_τ) has

Gen. 1	Gen. 2	Gen. 3	Q	color N − plet
$\begin{pmatrix} \nu_e \\ e_L^- \end{pmatrix}$	$\begin{pmatrix} \nu_\mu \\ \mu_L^- \end{pmatrix}$	$\begin{pmatrix} \nu_\tau \\ \tau_L^- \end{pmatrix}$	$\begin{matrix} 0 \\ -1 \end{matrix}$	1
e_R^-	μ_R^-	τ_R^-	-1	1
$\begin{pmatrix} u_L \\ d_L \end{pmatrix}$	$\begin{pmatrix} c_L \\ s_L \end{pmatrix}$	$\begin{pmatrix} t_L \\ b_L \end{pmatrix}$	$\begin{matrix} +\frac{2}{3} \\ -\frac{1}{3} \end{matrix}$	3
u_R	c_R	t_R	$+\frac{2}{3}$	3
d_R	s_R	b_R	$-\frac{1}{3}$	3

Table 2.1: The Matter Particles of the Standard Model.
The fundamental spin-$\frac{1}{2}$ fermions of the Standard Model can be arranged as shown.

Particle	Q	weak N–plet	color N–plet
γ, Z^0	0	mixed $1 \oplus 3$	1
$W^\pm$	± 1	3	1
g	0	1	8

Table 2.2: The Spin-1 Gauge Bosons of the Standard Model.

only been seen indirectly.

The spin-1 gauge bosons can be arranged in the manner shown in Table 2.2. These gauge bosons mediate the interactions between particles. The variable Q again refers to electric charge. The remaining columns tell us the "charge" with regard to the weak and the strong interactions in the form of the weak-isospin multiplet and the color multiplet respectively. The photon (γ) and Z-zero (Z^0) particles are actually not pure weak isospin states, but are mixtures of weak-isospin singlet and triplet states. The electroweak force is mediated by the γ, Z^0, W^+, and W^- particles. The gluon (g) comes in eight colors corresponding to the octet representation of the SU(3) color symmetry group. The gluon mediates the strong force. The antiparticle structure of the spin-1 gauge bosons is more complicated than that of the matter particles. Every gauge boson is either its own antiparticle or else the antiparticle of another gauge boson. For instance, the W^+ is the antiparticle of the W^- while the γ is its own

antiparticle.

The properties of the spin-2 boson are shown below:

Particle	Q	Weak isospin	Color charge
graviton	0	0	0

The graviton, which is thought to mediate gravity, is its own antiparticle. It has no charge of any kind and only couples to mass (or energy). This particle has never been explicitly detected. As mentioned above, the graviton is usually ignored when considering the Standard Model.

The spin-0 particle, which is known as the Higgs, completes the Standard Model. Its properties are shown below:

Particle	Q	Weak isospin	Color charge
H	0	0	0

The Higgs particle has not been seen. It's existence is predicted by the Standard Model description of the electroweak interaction (the Weinberg-Salam model). The existence of this particle will not have any directly measurable effect on the results of this thesis.

2.1.2 The Interactions

In addition to classifying the fundamental particles, the Standard Model (SM) also describes their interactions.

The most familiar of these is the electromagnetic interaction which is governed by the theory of Quantum Electrodynamics (QED). QED is a unification of Quantum Field Theory and Classical Electrodynamics which takes the form of a field theory with a U(1) local gauge symmetry. While this theory presents many technical problems, and even a couple of problems of principle[1], it can be used to make accurate predictions which can be tested experimentally. Everywhere that it has been applicable, QED has thus far agreed with experimental results.

For neutrinos at any energy and for all other matter particles at high energy or high precision, the weak interaction becomes important. This interaction is best

[1]For instance, an elegant paper by Dyson [3] shows that Perturbative QED does not actually converge.

described by the Weinberg-Salam model which unifies the electromagnetic and weak interactions into the electroweak interaction. The electroweak interaction is also capable of making precise predictions and has been well tested. No deviations from the Standard Model have been seen. In fact, the theory correctly predicted a constraint between the neutral and charged current coupling strengths and the masses of the Z and W particles before they were measured. The electroweak theory is a field theory exhibiting a spontaneously broken SU(2) $\otimes$ U(1) local gauge symmetry.

The third type of interaction which is covered by the Standard Model is the strong interaction between quarks and gluons. The strong interaction is thought to be governed by a field theory which is SU(3) symmetric in a generalized charge known as *color*. The existence of a three-fold symmetric color quantum number of quarks is fairly well established. The cross-section for the process $e^+ e^- \rightarrow$ *hadrons* is three times larger than it would be if quarks came in only one color. Furthermore, the Δ^{++} particle consists of three up quarks (u) and has spin-$\frac{3}{2}$. The wavefunction for this particle is symmetric under spin interchange and the three quarks are in a relative s-state of angular momentum. It is hard to reconcile this Δ^{++} wave-function with the Dirac statistics of fermions unless the color degree of freedom exists, allowing the u quarks to be in an antisymmetric color state.

Despite these and many other qualitative successes, QCD has some major weaknesses as a theory. Since we can't solve the theory exactly, we must resort to perturbation expansions which are only well behaved in the region of hard scattering. The fact that QCD can't describe soft processes very well means that we are unable to use it to predict hadron masses, nuclear forces, hadron-hadron interaction cross-sections, or the detailed structure of hadrons in terms of quarks and gluons. We are also unable to understand the process of *hadronization* whereby the quarks and gluons of the theory are manifested asymptotically as hadrons. Furthermore, since the coupling constant is not small, it is difficult to calculate experimentally measurable quantities to high precision. Theoretical uncertainties in QCD calculations tend to be on the order of 10–20%. QCD is the best candidate for the strong interaction at this point, and work is proceeding on non-perturbative methods for solving the theory, but QCD is clearly not on as firm a footing as QED and the Weinberg-Salam model are.

The full Standard Model is described by a field theory with a complicated Lagrangian including the strong and electroweak interactions and all of the fundamental particles. This Lagrangian incorporates an SU(3) $\otimes$ SU(2) $\otimes$ U(1) local gauge symmetry.

2.2 Inelastic Lepton Scattering

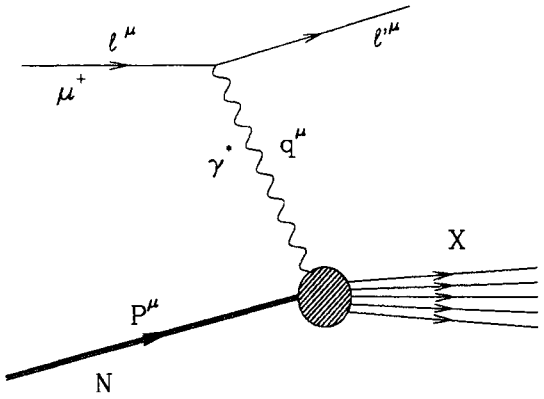

Figure 2-1: Inelastic Muon-Nucleon Scattering.
The blob at the vertex represents the complicated structure and dynamics involved in the interaction of a virtual photon with a nucleon. It is this structure and these dynamics that we hope to illuminate by studying this process.

Several features of Inelastic Lepton-Nucleon Scattering can be considered which are independent of the detailed structure of the nucleon. First of all, we note that the lepton will not interact strongly with the nucleon. Furthermore, at E665 energies, the effect of the Weak interaction is negligible. This means that the overall process can be described within the framework of the electromagnetic interaction (QED). Our knowledge of QED is sufficient for us to place constraints on the form of the cross-section. This section focuses on the scattering process from this fairly model-independent perspective. Section 2.3 will explore our current understanding of the internal dynamics of the nucleon and make further predictions.

2.2.1 Experimental Kinematics

Without loss of generality, we can describe the kinematics of Muon-Nucleon Scattering as if the scattering involved only a single virtual photon exchange between the muon and the nucleon. This leading order QED process is pictured in Figure 2-1. Even if higher order QED processes become important, we can still choose to describe the kinematics in these terms.

We can define the following quantities :

- l^μ is the incoming muon 4-momentum,
- l'^μ is the scattered muon 4-momentum,
- P^μ is the target nucleon 4-momentum,

- $q^\mu \equiv l^\mu - l'^\mu$ is the virtual photon 4-momentum,
- E is the incoming muon energy in the lab frame,
- E' is the scattered muon energy in the lab frame,
- θ is the muon scattering angle,
- m_l is the muon mass,
- M is the nucleon mass.

We can then express the kinematics of the events in terms of Lorentz scalars:

- $Q^2 \equiv -q^2$ which describes how far off mass-shell the virtual photon is;
- $\nu = \frac{P\cdot q}{\sqrt{P\cdot P}}$, which is the virtual photon energy in the nucleon rest frame;
- $y_{Bj} \equiv \frac{P\cdot q}{P\cdot l}$, which is the fraction of the incoming muon energy taken by the virtual photon in the nucleon rest frame;
- $x_{Bj} \equiv \frac{Q^2}{2P\cdot q}$ which is known as the Bjorken scaling variable;
- $W^2 \equiv (P+q)^2 = M^2 - Q^2 + 2M\nu$ which is the invariant mass of the photon-nucleon system, or equivalently, of the hadronic final state.

We generally assume that the nucleon is at rest in the lab frame, yielding:

- $P^\mu = \left\{M;\ \vec{0}\right\}$,
- $\nu = q_0^{lab}$,
- $y_{Bj} = \nu/E$.

2.2.2 Cross Section

Our knowledge of QED, the general principles of gauge invariance, and the parity-conserving nature of the electromagnetic interaction allow us to place strong constraints upon the form of the cross-section for inelastic muon-nucleon scattering [4].

Aside from phase space factors we have:

$$d\sigma \sim L_{\mu\nu}W^{\mu\nu}, \tag{2.1}$$

$$L_{\mu\nu} = 2\left[l_\mu l'_\nu + l'_\mu l_\nu - (l\cdot l' - m_l^2)g^{\mu\nu}\right], \tag{2.2}$$

$$W^{\mu\nu} = W_1(Q^2,\nu)\left(-g^{\mu\nu} - \frac{q^\mu q^\nu}{Q^2}\right) + W_2(Q^2,\nu)\frac{1}{M^2}A_N^\mu A_N^\nu, \tag{2.3}$$

where:

$$A_N^\mu \equiv P^\mu + \frac{P\cdot q}{Q^2}q^\mu. \tag{2.4}$$

Basically, our knowledge of the electromagnetic interaction with which we are probing the nucleon allows us to parameterize the nucleon's internal structure even before we measure it. In fact, all of the components of the nucleonic wavefunction that are probed by measuring the inclusive electromagnetic lepton-nucleon cross-section can be described by two scalar functions of two variables. For instance, the muon-nucleon cross-section can be written in the lab frame as:

$$\frac{d\sigma}{dE'd\Omega} = \frac{\alpha^2}{4E^2\sin^4\frac{\theta}{2}}\left\{W_2(\nu,Q^2)\cos^2\frac{\theta}{2} + 2W_1(\nu,Q^2)\sin^2\frac{\theta}{2}\right\}, \tag{2.5}$$

where the muon mass has now been neglected. This choice of parameterization of the nucleon structure in terms of $W_1(\nu,Q^2)$ and $W_2(\nu,Q^2)$ is somewhat arbitrary. This particular parameterization is popular because W_1 and W_2 are generalizations of the elastic form factors of the nucleon which can be easily related to the charge distribution and magnetic moment of the nucleon in the non-relativistic limit [4].

There is an alternative, and in some ways more intuitive, approach to the parameterization of the nucleon structure available to us. We can treat the muon beam as simply generating a flux of virtual photons with a particular distribution of 4-momentum and polarization. We can then parameterize the structure of the nucleon in terms of its cross-section for interacting with a virtual photon of a given 4-momentum and polarization. This parameterization must be performed in a fixed frame, generally taken as the lab frame. We define a longitudinal and a transverse cross-section, where the terms *longitudinal* and *transverse* are defined with respect to the momentum direction of the virtual photon. A transverse virtual photon has spin component $S_z = \pm 1$ along its momentum direction; a longitudinal virtual photon has spin component $S_z = 0$. The cross-section in this parameterization is [4]:

$$\frac{d\sigma}{dE'd\Omega} = \Gamma(\sigma_T + \varepsilon\sigma_L), \tag{2.6}$$

where the muon mass has again been neglected, and where:

$$\Gamma = \frac{\alpha K}{2\pi^2 Q^2}\frac{E'}{E}\frac{1}{1-\varepsilon} \tag{2.7}$$

$$\varepsilon = \left(1+2\frac{Q^2+\nu^2}{Q^2}\tan^2\frac{\theta}{2}\right)^{-1} = \frac{2(1-y)-Mx_{Bj}y_{Bj}/E}{1+(1-y)^2+Mx_{Bj}y_{Bj}/E} \tag{2.8}$$

$$K \equiv \nu(1-x_{Bj}). \tag{2.9}$$

It should be noted that the definition of the virtual photon flux factor K is somewhat arbitrary. For a given choice of the definition of K, we can relate our $\sigma_{T,L}$ parameterization to our $W_{1,2}$ parameterization:

$$\sigma_T = \frac{4\pi^2\alpha}{K}W_1 \tag{2.10}$$

$$\sigma_L = \frac{4\pi^2\alpha}{K}\left[\left(1+\frac{\nu^2}{Q^2}\right)W_2 - W_1\right].$$

In summary, either of these two alternative parameterizations — $W_{1,2}$ or $\sigma_{T,L}$ — is sufficient for describing the hadronic structure that we can discover by examining the cross-section for muon-nucleon scattering. Furthermore, these parameterizations form a general model-independent framework in which to discuss muon-nucleon scattering.

2.2.3 Radiative Corrections

In the rest of the chapter we will be assuming that the electroweak part of the interaction can be described strictly in terms of single photon exchange, neglecting the Weak interaction as well as higher order QED diagrams. At E665 energies, the effect of the Weak interaction — Z^0 or $W^{\pm}$ exchange — is negligible. Higher order QED diagrams, however, do contribute to the cross-section, mostly in the form of real photons being radiated by charged particles in the incident or final state. The dominant effect is that photons are emitted nearly collinearly from the incident or scattered muon. These processes have a small effect on the hadron distributions which are typically measured with reference to the apparent virtual photon momentum direction. Since the radiated photon carries away some of the original beam energy, the true virtual photon momentum direction and the true hadronic center-of-mass energy will be mismeasured.

Some of the dominant higher order electromagnetic processes have been calculated [5] and so it would be possible to correct for these effects theoretically. However, the basic approach that I will take in this thesis will be to attempt to identify and

cut the bulk of the hard radiative events by directly measuring the radiated photon. Some small systematic error will remain from these effects. See Section 5.5.5.

2.3 The Quark Parton Model

Deep inelastic scattering is generally thought of in terms of the Quark Parton Model (QPM). In this model, the nucleon is made up of a collection of point particles, called partons, which can undergo hard interactions with other particles. These partons are identified as the quarks, antiquarks, and gluons of the Standard Model. This model allows us to further constrain and interpret the functions $W_{1,2}$ and $\sigma_{T,L}$ defined in Section 2.2. Several different versions of the Quark Parton Model exist, with varying levels of sophistication. We will consider several of these approaches in this section.

2.3.1 DIS in the Naïve Quark Parton Model

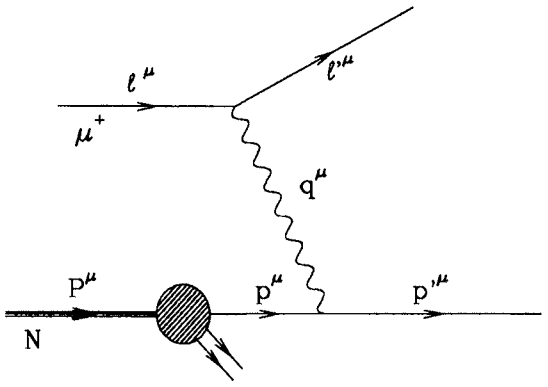

Figure 2-2: Elastic Muon-Parton Scattering.
The lowest order diagram for a muon scattering from a parton in the nucleon.

The Naïve Quark Parton Model (QPM) is a much more restrictive picture of the structure of the nucleon than the very general picture discussed in Section 2.2. The basic idea is that the nucleon is made up of point-like spin-$\frac{1}{2}$ Dirac particles: the quarks and anti-quarks of the Standard Model.

Figure 2-2 shows the Naïve QPM picture of deep inelastic scattering. The muon scatters elastically from a charged parton, a quark or an anti-quark, in the nucleon, thereby causing the nucleon to break up. Let us refer to the struck parton four-momentum as p^μ and the scattered parton four-momentum as p'^μ. We can't measure

these four-momenta directly since the scattered parton fragments into hadrons before we can detect it.

The Quark Parton Model is easiest to discuss in a Lorentz frame known as the Infinite Momentum Frame (S_∞). The Infinite Momentum Frame is reached from the Laboratory reference frame by boosting the target nucleon to an arbitrarily high momentum P in a direction opposite to the virtual photon three-momentum vector. In this frame, the kinematics can be simplified by assuming that the primordial transverse momentum ($k_\perp$) of the struck parton and the mass of the target nucleon are negligible. In S_∞, we can view the nucleon as an incoherent collection of non-interacting, quasi-free, massless partons. Deep inelastic scattering can be viewed as a hard scattering off of a single parton which is unaffected by the other (spectator) partons in the nucleon.

Given the above assumptions, we can write the four-momentum of the proton and the struck parton as:

$$\begin{array}{lllll} P^\mu & = \{ & P; & 0, \; 0, & -P\} \\ p^\mu & = \{ & \xi P; & 0, \; 0, & -\xi P\} \qquad (= \xi P^\mu). \end{array} \tag{2.11}$$

The constraint that we have elastic scattering off of the quark is given by:

$$(q+p)^2 = p'^2 \tag{2.12}$$

or

$$q^2 + 2p \cdot q = 0. \tag{2.13}$$

In the Naïve QPM, this yields:

$$-Q^2 + 2\xi P \cdot q = 0 \qquad \Longrightarrow \qquad \xi = Q^2/2P \cdot q \equiv x_{B_j} \tag{2.14}$$

Equation 2.14 shows that in the Naïve QPM, $\xi = x_{B_j}$. In other words, x_{B_j} represents the fraction of the nucleon's momentum that is taken up by the parton in the Infinite Momentum Frame. Equation 2.14 can be written in the useful form:

$$\xi = x_{B_j} = \frac{Q^2}{2M\nu}. \tag{2.15}$$

Within the framework of the Naïve QPM, we can also calculate the muon scattering cross-section. Evaluating the Feynman diagram in Figure 2-2 allows us to write the scattering cross-section in terms of the distribution, $q_i(x)$, of partons in the nucleon [4]. The cross-section for a muon scattering from a parton of type i with momentum fraction ξ can be written in the form of Equation 2.5 with the following

identifications:

$$\begin{aligned} W_1^{(\text{parton } i)}(\xi;\ Q^2,\nu) &= e_i^2 \frac{Q^2}{4M^2\xi^2}\delta(\nu - \frac{Q^2}{2M\xi}), \\ W_2^{(\text{parton } i)}(\xi;\ Q^2,\nu) &= e_i^2 \delta(\nu - \frac{Q^2}{2M\xi}), \end{aligned} \tag{2.16}$$

where e_i is the charge of quark flavor i in units of the positron charge. The values of this quantity for each quark flavor can be found in the Q column of Table 2.1.

Our original choice of $W_{1,2}$ for parameterizing the structure of the nucleon is not very useful for our current purposes because W_1 and W_2 are not dimensionless, but have dimension (energy)$^{-1}$. It is customary to define a new pair of dimensionless structure functions given by:

$$\begin{aligned} F_1 &= MW_1, \\ F_2 &= \nu W_2. \end{aligned} \tag{2.17}$$

We can then write:

$$\begin{aligned} F_1^{(\text{parton } i)}(\xi;\ x_{Bj}) &= e_i^2 \tfrac{Q^2}{4M\nu\xi^2}\delta(1 - \tfrac{Q^2}{2M\nu\xi}) = e_i^2 \tfrac{1}{2x_{Bj}}\delta(1 - \tfrac{x_{Bj}}{\xi}), \\ F_2^{(\text{parton } i)}(\xi;\ x_{Bj}) &= e_i^2 \delta(1 - \tfrac{Q^2}{2M\nu\xi}) = e_i^2 \delta(1 - \tfrac{x_{Bj}}{\xi}), \end{aligned} \tag{2.18}$$

where we have used the delta function identity given in Equation 1.5. The motivation for choosing to define the structure functions $F_{1,2}$ according to Equation 2.17 should now be clear. In addition to being dimensionless, the new structure functions are now functions only of x_{Bj} and not of Q^2 and ν independently.

Summing over the parton distributions $q_i(\xi)$ yields the structure functions for a nucleon. F_2 is given by:

$$F_2(x_{Bj}) = \sum_i \int d\xi q_i(\xi) F_2^{(\text{parton})}(\xi;\ x_{Bj}). \tag{2.19}$$

Using Equation 2.18 and the delta function identity given by Equation 1.4 yields:

$$F_2(x_{Bj}) = \sum_i \int d\xi e_i^2 q_i(\xi)\delta(1 - \frac{x_{Bj}}{\xi}) = \sum_i \int d\xi e_i^2 q_i(\xi)\delta(\xi - x_{Bj})/(x_{Bj}\xi^{-2}). \tag{2.20}$$

Integrating over the delta function yields a simple relationship between the structure function and the parton distribution.

$$F_2(x_{Bj}) = \sum_i e_i^2 x_{Bj} q_i(x_{Bj}). \tag{2.21}$$

Similarly, we can find F_1:

$$F_1(x_{B_j}) = \sum_i \int d\xi q_i(\xi) F_1^{(\text{parton})}(\xi;\ x_{B_j}) = \frac{1}{2x_{B_j}} \sum_i \int d\xi q_i(\xi) F_2^{(\text{parton})}(\xi;\ x_{B_j}). \quad (2.22)$$

This means that

$$F_1(x_{B_j}) = \frac{1}{2x} F_2(x). \quad (2.23)$$

Equation 2.23 is known as the Callan-Gross relation and it is a direct consequence of the spin-$\frac{1}{2}$ nature of the quarks in the QPM. Using our new parameterizations $F_{1,2}(x)$, we can now write the muon-nucleon scattering cross-section as a function of the variables x_{B_j} and y_{B_j}:

$$\frac{d\sigma}{dx_{B_j} dy_{B_j}} = \frac{2\pi\alpha^2}{MEx_{B_j}^2 y_{B_j}^2} \left\{ x_{B_j} y_{B_j}^2 F_1(x) + \left[1 - y_{B_j} - \frac{M x_{B_j} y_{B_j}}{2E} \right] F_2(x_{B_j}) \right\}. \quad (2.24)$$

It is also convenient to talk in terms of our $\sigma_{L,T}$ parameterization of nucleon structure. In particular, we can define:

$$R(\nu, Q^2) \equiv \frac{\sigma_L(\nu, Q^2)}{\sigma_T(\nu, Q^2)} = (1 + \frac{\nu^2}{Q^2}) \frac{W_2}{W_1} - 1 \quad (2.25)$$

or

$$R = (1 + \frac{\nu^2}{Q^2}) \frac{M}{\nu} \frac{F_2(x_{B_j})}{F_1(x_{B_j})} - 1. \quad (2.26)$$

For the Naïve QPM, we can use the Callan-Gross relation $F_2(x_{B_j}) = 2x_{B_j} F_1(x_{B_j})$ and the fact that $Q^2 \ll \nu^2$ to yield:

$$\begin{aligned} R &= (1 + \frac{\nu^2}{Q^2}) \frac{M}{\nu} 2x_{B_j} - 1 \\ &= \frac{2Mx_{B_j}}{\nu} + \frac{2Mx_{B_j}\nu}{Q^2} - 1 \\ &= \frac{2Mx_{B_j}}{\nu} = \frac{Q^2}{\nu^2} \\ R &\approx 0. \end{aligned} \quad (2.27)$$

The fact that the structure functions F_1 and F_2 have been measured to be approximately independent of Q^2 for fixed x_{B_j} and large Q^2 demonstrates that the partons are pointlike. The fact that $R(x_{B_j}) \approx 0$ experimentally for large Q^2, ν^2 demonstrates that the partons are spin-$\frac{1}{2}$.

The connection between the value of $R(x_{B_j})$ and the spin of the partons in the

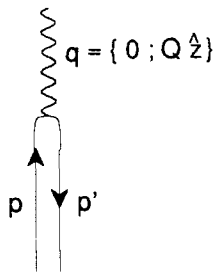

Figure 2-3: Helicity Conservation in the Breit Frame.
A quark scattering from a virtual photon in the Breit Frame. A spin-$\frac{1}{2}$ quark must flip spin in order to conserve helicity. A spin-0 quark cannot flip spin and conserve helicity.

Naïve QPM can be made clear by the following argument. Let us boost into the Breit frame where the virtual photon has zero energy. In this frame, shown in Figure 2-3, the struck parton rebounds with momentum $\vec{p}' = -\vec{p}$ where $|\vec{p}| = Q/2$. For large Q, this interaction conserves helicity. Helicity conservation for a spin-$\frac{1}{2}$ parton implies that it must flip its spin, which in turn means that it can only interact with a transverse photon (helicity $\lambda = \pm 1$). This implies that $\sigma_L = 0$ for a spin-$\frac{1}{2}$ parton, or $R(x_{Bj}) = 0$. In contrast, a spin-0 parton cannot undergo a spin flip, and therefore can only interact with a longitudinal photon ($\lambda = 0$). This implies that $\sigma_T = 0$ for a spin-0 parton, or $R(x_{Bj}) \to \infty$.

It turns out that the Naïve QPM contains some hidden assumptions. During our derivation of Equations 2.14 and 2.15, we assumed that we could always make the infinite-momentum frame momentum P big enough so that $k_\perp$ and M were negligible. A more careful treatment, such as that of Appendix Section A.1, shows that Equations 2.14 and 2.15 are actually only valid as long as $k_\perp^2 \ll Q^2 \ll \nu^2$.

Furthermore, if either the mass or primordial $k_\perp$ of the parton is non-negligible compared to Q, the simple helicity argument described above no longer holds, allowing a non-zero R. In the case of a non-negligible mass, the helicity is no longer exactly conserved[2], ruining the argument that $R = 0$. In the case of non-negligible $k_\perp$, the helicity axes of the partons are not lined up with that of the photon, also ruining the argument. Furthermore, if a higher order QCD process, such as gluon bremsstrahlung, comes into play, the drawing in Figure 2-3 is no longer valid, and R is no longer

[2]Chirality, which is the eigenvalue of the Dirac γ_5 operator, is exactly conserved in an electromagnetic interaction. Helicity, which is the eigenvalue of the $\vec{\sigma} \cdot \vec{p}$ operator, is only conserved in the limit of negligible mass [4].

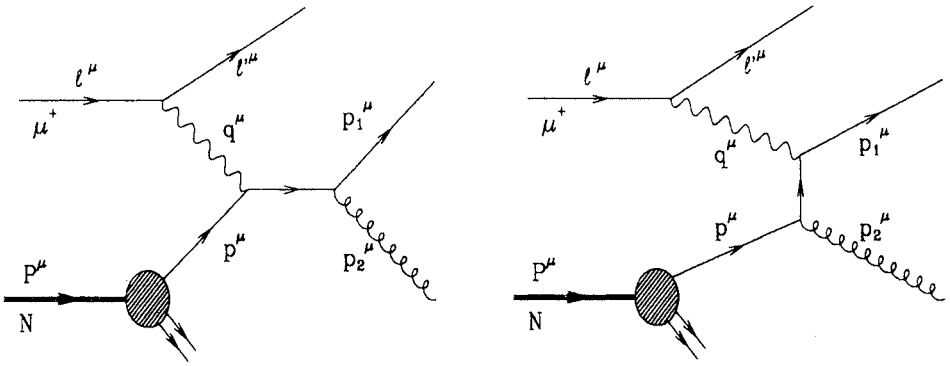

Figure 2-4: Gluon Bremsstrahlung.
Feynman diagrams corresponding to gluon bremsstrahlung: a) s-channel and b) t-channel.

predicted to be exactly zero.

For these and other reasons, the QPM is really only applicable when $Q^2, \nu^2 \to \infty$ with Q^2/ν held fixed. Experimentally, we try to consider the case where Q^2 and ν^2 are large compared to the mass and transverse momentum scales of the problem. This case is referred to as deep inelastic scattering, as opposed to merely inelastic scattering.

The formalism described in this section was very important historically for understanding the gross features of deep inelastic lepton scattering. In particular, the experimental fact that the structure functions are approximately independent of Q^2 at a fixed x_{Bj} was hailed as the final proof of the existence of quarks in the proton [6]. At higher precision, however, the formalism begins to break down as effects of primordial $k_\perp$ and of higher order QCD diagrams start to become important.

2.3.2 DIS in the QCD-improved Parton Model

As was mentioned above, the Naïve QPM is far from the whole story. The strong interaction is in fact *strong*, which means that the simple picture in Figure 2-2 is inadequate. There are higher order QCD diagrams which contribute. These are gluon bremsstrahlung, where the struck quark radiates a gluon, and photon-gluon fusion, where the virtual photon interacts with a gluon from the proton via t-channel quark exchange, generating a quark-antiquark pair.

Let us first consider the effect of gluon bremsstrahlung. The Feynman diagrams corresponding to this effect are shown in Figure 2-4. We have replaced the outgoing

quark 4-momentum p' of Figure 2-2 with the outgoing quark 4-momentum p_1 and the radiated gluon 4-momentum p_2. We also need the following definitions:

$$\begin{aligned} x &\equiv \frac{Q^2}{2P\cdot q} \qquad (= x_{Bj}) \\ \xi &\equiv \frac{p\cdot q}{P\cdot q} \\ \xi' &\equiv \frac{x_{Bj}}{\xi} = \frac{Q^2}{2p\cdot q} \end{aligned} \tag{2.28}$$

The first thing to note is that $\xi \neq x_{Bj}$. This is because Equation 2.12 is no longer valid. The variable $\hat{s} \equiv (p+q)^2$ can be allowed to vary independently from Q^2 and ν. We can find an expression for ξ from the definition of $\hat{s}$:

$$\hat{s} = q^2 + 2p\cdot q + p^2. \tag{2.29}$$

Solving for $p\cdot q$ yields:

$$\begin{aligned} p\cdot q &= \frac{1}{2}\left(Q^2 + \hat{s} + m_q^2\right), \\ \xi &= \frac{Q^2 + \hat{s} + m_q^2}{2M\nu}, \end{aligned} \tag{2.30}$$

where m_q is the mass of the quark ($\sqrt{p^2}$).

It is worth some effort to try and understand the meanings of these variables. The variable ξ represents the momentum fraction of the original parton in the nucleon before it was struck. The variable x refers to the apparent momentum fraction. In other words, if we chose to close our eyes to the details of the interaction, only paid attention to the muon kinematics, and assumed that the interaction occurred at lowest order, we would conclude that the parton had a momentum fraction x of the proton.

Armed with the definitions of these variables, we can write an expression for the cross-section. In general, it is believed that the nucleonic cross-section factorizes into the parton distribution in the nucleon and the partonic cross-section [7]:

$$\begin{aligned} \sigma_{\gamma^* N}(x,Q^2) &= \sum_i \int_0^1 d\xi' \int_0^1 d\xi q_i(\xi)\delta(x-\xi'\xi)\hat{\sigma}_{\gamma^* i}(\xi',Q^2) \\ &= \sum_i \int_x^1 \frac{d\xi}{\xi} q_i(\xi)\hat{\sigma}_{\gamma^* i}(x/\xi,Q^2). \end{aligned} \tag{2.31}$$

This formula was proved for perturbative QCD in the deep inelastic limit where $k_\perp \ll Q^2 \ll \nu^2$. We assume that it is approximately valid in general.

It is desirable to write the cross-section in terms of the F_1 and F_2 defined by Equations 2.5 and 2.17. Combining Equations 2.10 and 2.17, we can write:

$$\frac{F_2(x)}{x} = \frac{\sigma_T + \sigma_L}{\sigma_0}, \tag{2.32}$$

where

$$\sigma_0 \equiv \frac{4\pi^2\alpha}{2MK}. \tag{2.33}$$

The full $\mathcal{O}(\alpha_s)$ cross-sections σ_T and σ_L have been calculated for this process. It is often useful, however, to apply the Weizsäcker-Williams equivalent photon approximation from QED [8, 9] to QCD, generating what are known as the Altarelli-Parisi equations [10]. In this approximation, we treat the gluon bremsstrahlung process as consisting of two separate incoherent processes. For instance, the diagram shown in Figure 2-4b is viewed as two independent processes: a quark radiates a fairly soft collinear gluon and then is struck by a virtual photon. The probability of the quark radiating a gluon and retaining a fraction z of its original momentum is proportional to a splitting function which is denoted as $P_{q\to q}(z)$. Similarly, the probability of a quark radiating a gluon which carries away a fraction z of the quark's momentum is proportional to $P_{q\to g}(z)$. These functions are clearly related by momentum conservation: $P_{q\to q}(z) = P_{q\to g}(1-z)$. Taking into account the effects of the gluon bremsstrahlung process, the cross-section becomes:

$$\frac{F_2(x)}{x} = \sum_i e_i^2 \int_x^1 \frac{d\xi}{\xi} q_i(\xi) \left[\delta\left(1-\frac{x}{\xi}\right) + \frac{\alpha_s}{2\pi} P_{q\to q}\left(\frac{x}{\xi}\right) \ln\frac{Q^2}{\mu^2}\right]. \tag{2.34}$$

Technically, this cross-section is leading-log and not full $\mathcal{O}(\alpha_s)$. The immediate consequence of this QCD-improved parton model is that the Structure Function $F_2(x, Q^2)$ is now a (weak) function of Q^2 and no longer scales exactly. Furthermore, there is an arbitrary mass scale μ which had to be introduced.

Equation 2.34 describes the interaction in terms of a simple parton distribution which is independent of Q^2 and is solely a function of the nucleon structure. However, the dynamics are now very complicated, and the parton distribution is not directly measurable. It is conventional to reabsorb the Q^2 dependence of the cross-section into the parton distribution as follows:

$$\begin{aligned}\frac{F_2(x,Q^2)}{x} &= \sum_i e_i^2 \int_x^1 \frac{d\xi}{\xi} \left[q_i(\xi) + \Delta q_i(\xi, Q^2)\right] \delta\left(1-\frac{x}{\xi}\right) \\ &= \sum_i e_i^2 \left[q_i(x) + \Delta q_i(x, Q^2)\right]\end{aligned} \tag{2.35}$$

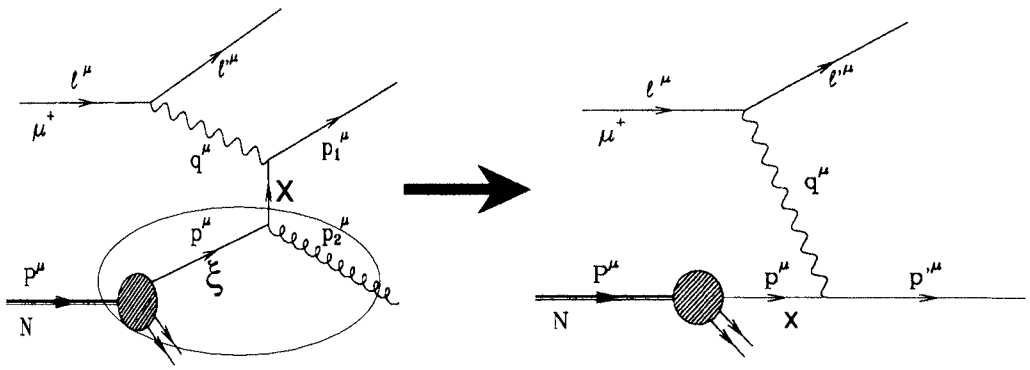

Figure 2-5: Altarelli-Parisi Evolution.
By integrating over the ξ degree of freedom, we collapse the large ellipse into the blob which represents the internal nucleon dynamics. Our parton distributions are now functions of x and Q^2 instead of ξ.

where

$$\Delta q_i(x,Q^2) \equiv \frac{\alpha_s}{2\pi} \ln \frac{Q^2}{\mu^2} \int_x^1 \frac{d\xi}{\xi} q_i(\xi) P_{q\to q}\left(\frac{x}{\xi}\right). \tag{2.36}$$

This can be rewritten in the form known as the Altarelli-Parisi evolution equation:

$$\frac{dq(x,Q^2)}{d\ln Q^2} = \frac{\alpha_s}{2\pi} \int_x^1 \frac{d\xi}{\xi} q(\xi) P_{q\to q}\left(\frac{x}{\xi}\right). \tag{2.37}$$

Essentially, we have redefined the meaning of "parton distribution" in the manner illustrated in Figure 2-5. We have collapsed the gluon bremsstrahlung process in the large ellipse so that it has become part of our "unknown internal nucleon dynamics" blob. Instead of having a distribution of partons with momentum fraction ξ, we now have a distribution of partons with momentum fraction x. We treat the gluon bremsstrahlung as part of the internal dynamics of the nucleon, rather than as part of the process of muon-nucleon scattering. This is somewhat strange, since the gluon radiation was caused by the fact that the original parton was accelerated by interacting electromagnetically with the muon. It turns out mathematically, however, that we are free to view the parton distribution in this perverse way. Furthermore, it is sometimes useful to do so, especially since x and Q^2 are directly measurable quantities and ξ is not. In this picture, we view the Q^2 dependence of the parton distribution as a reflection of the resolution afforded to us by a virtual photon with a given Q^2.

In general, we must also take into account the diagrams of photon-gluon fusion, shown in Figure 2-6. In the language of Altarelli-Parisi evolution, the gluons in the

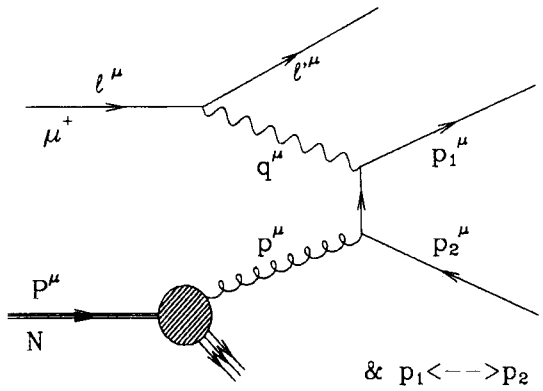

Figure 2-6: Photon Gluon Fusion.
The Feynman diagram corresponding to Photon-Gluon Fusion.

nucleon break up into $q\overline{q}$ pairs as we change the virtual photon resolution by changing the Q^2. This is described by the splitting function $P_{g\to q}(z)$.

The interactions which give rise to the Altarelli-Parisi evolution are shown in Figure 2-7, including the three-gluon vertex which gives rise to $P_{g\to g}(z)$. The result of all of this is the general set of Altarelli-Parisi equations:

$$\frac{dq_i(x,Q^2)}{d\ln Q^2} = \frac{\alpha_s(Q^2)}{2\pi}\int_x^1 \frac{d\xi}{\xi}\left[P_{q\to q}\left(\frac{x}{\xi}\right)q_i(\xi,Q^2) + P_{g\to q}\left(\frac{x}{\xi}\right)g(\xi,Q^2)\right] \quad (2.38)$$

$$\frac{dg(x,Q^2)}{d\ln Q^2} = \frac{\alpha_s(Q^2)}{2\pi}\int_x^1 \frac{d\xi}{\xi}\left[\sum_i P_{q\to g}\left(\frac{x}{\xi}\right)q_i(\xi,Q^2) + P_{g\to g}\left(\frac{x}{\xi}\right)g(\xi,Q^2)\right] \quad (2.39)$$

where the index i runs over all quark and antiquark flavors.

The formalism developed in this section works well for describing the muon-nucleon cross-section, but it neglects the effects of primordial transverse momentum ($k_\perp$).

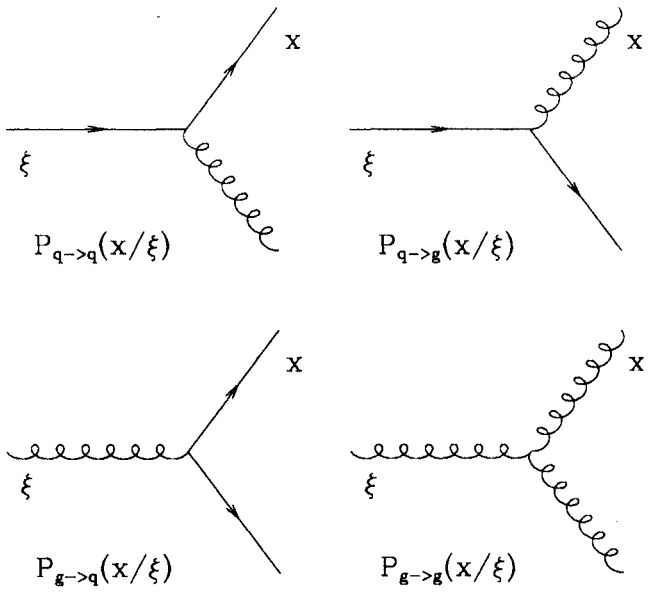

Figure 2-7: Altarelli-Parisi Splitting Functions.
The Altarelli-Parisi splitting functions correspond to these vertices: a) $P_{q\to q}\left(\frac{x}{\xi}\right)$ and b) $P_{q\to g}\left(\frac{x}{\xi}\right)$ are due to gluon bremsstrahlung; c) $P_{g\to q}\left(\frac{x}{\xi}\right)$ is due to the $q\overline{q}$ pair production from a gluon which occurs in photon-gluon fusion; d) $P_{g\to g}\left(\frac{x}{\xi}\right)$ is due to the three-gluon vertex.

2.3.3 The Parton Model with Primordial $k_\perp$

The existence of primordial transverse momentum of the quarks in the nucleon is usually ignored because it introduces several theoretical complications. Despite the difficulty, there are good reasons to consider the effects of non-negligible $k_\perp$. First, the transverse momentum distribution of quarks in the nucleon is interesting in its own right, providing information concerning the structure of the nucleon. Second, there are some phenomena that are predicted to be exactly zero in the Naïve QPM. Clearly the effects of $k_\perp$ are not guaranteed to be negligible when compared to zero. Third, a lot of well-behaved data exists at low Q^2. The data used in this thesis include events with Q^2 as low as 2 GeV^2, which can't really be classified as *deep* inelastic scattering. Some E665 hadron analyses have even used data down to $Q^2 = 0.1$ GeV^2. Since a typical scale for $k_\perp^2$ is 0.2 GeV^2, the assumption that $k_\perp^2 \ll Q^2$ breaks down.

In any case, many of the problems with the Naïve Quark Parton Model at low Q^2 are merely due to kinematic approximations, although some more fundamental problems do exist. It is useful, therefore, to recast many of the parton model results in kinematically exact terms which avoid the assumption of negligible $k_\perp$.

Let's consider some of the complications that primordial $k_\perp$ introduces. The problems that arise include the following:

- The definition of the scaling variable ξ must be made more precise.
- The parton distributions must now include $k_\perp$ and not just the longitudinal momentum.
- The cross-section is no longer azimuthally symmetric about the virtual photon axis.
- Our picture of the proton as an incoherent superposition of quasi-free non-mutually-interacting particles becomes harder to justify.

We will address the first three of these problems in order.

The definition of ξ

There are at least three different definitions of ξ in the literature. We can define:

$$\xi \equiv \frac{p_z^{(\infty)}}{P_z^{(\infty)}} \tag{2.40}$$

$$\xi_1 \equiv \frac{p_0^{(\infty)} - p_z^{(\infty)}}{P_0^{(\infty)} - P_z^{(\infty)}} \tag{2.41}$$

$$\xi_2 \equiv \frac{p \cdot q}{P \cdot q} \tag{2.42}$$

where $p_z^{(\infty)}$ denotes the longitudinal momentum component of p^μ in the Infinite Momentum Frame. Each of these definitions of ξ has advantages and disadvantages. In the Naïve QPM, they are all equivalent. If we allow $k_\perp^2/Q^2$ or Q^2/ν^2 to be non-negligible, then we must choose one definition of ξ and use it consistently. The main reason for the discrepancy between the three different definitions is that p^μ is no longer proportional to, or even collinear with, P^μ.

Following Feynman [11], I will use the definition of ξ given in Equation 2.40, which has the virtue of making the form of p^μ in the infinite momentum frame fairly simple. This in turn simplifies calculations of things such as cross-sections. The definition ξ_1 given in Equation 2.41 has the virtue that it is invariant under any Lorentz boosts along the virtual photon axis. On the other hand, it is somewhat more difficult to work with than our preferred definition of ξ, yielding a complicated expression for $\xi(Q^2, \nu, k_\perp)$ and for p^μ. The final definition, given in Equation 2.42, has many advantages. It is not only manifestly invariant under all Lorentz transformations, but for the leading order diagram (Figure 2-2), it also yields the same numerical value as the Naïve QPM: $\xi_2 = \frac{Q^2}{2M\nu} = x_{Bj}$. Unfortunately, this formulation, while elegant, buries all of the physics of the $k_\perp$ into a complicated form for p^μ, making explicit calculations complicated. We will use the definition found in Equation 2.40 for ease of calculation.

The next step, having defined ξ, is to relate it to our measurable variables Q^2 and ν. Unfortunately, even in leading order, ξ is a function of $k_\perp$ as well as of Q^2 and ν. An explicit expression is derived in Appendix Section A.1:

$$\xi^{LO}(Q^2, \nu, k_\perp) = \frac{\nu}{2M}\left(\sqrt{1 + \frac{Q^2}{\nu^2}} - 1\right)\left(1 + \sqrt{1 + \frac{4m_\perp^2}{Q^2}}\right), \tag{2.43}$$

where $m_\perp^2 \equiv k_\perp^2 + m_q^2$.

This expression includes the "target mass corrections" which take into account

the fact that $\frac{M}{\nu}$, or equivalently $\frac{Q^2}{\nu^2}$, may not be negligible. It also includes the effect of primordial $k_\perp$ and the parton mass m_q. It can be easily shown (see for instance Appendix Section A.1) that this result reduces to the Naïve QPM result, $\xi = x_{Bj}$, in the limit that $m_\perp^2 \ll Q^2 \ll \nu^2$. It is also shown in Appendix Section A.1 that when $Q^2 \ll \nu^2$ is valid, but no restriction is placed on $\frac{k_\perp^2}{Q^2}$, we have:

$$\xi \simeq \frac{Q^2}{2M\nu}\left(\frac{1}{2} + \frac{1}{2}\sqrt{1 + \frac{4m_\perp^2}{Q^2}}\right). \tag{2.44}$$

In this thesis, we are considering events with $\nu > 100$ GeV, so the approximation $Q^2 \ll \nu^2$ is quite good.

Parton distributions

The parton distributions must be modified in the presence of $k_\perp$. We must choose a scaling variable to use for the longitudinal momentum: x_{Bj}, ξ, ξ_1, or ξ_2, and we must choose a form for the $k_\perp$ distribution. The simplest prescription is to use a form such as:

$$\frac{d^3N_i}{dx_{Bj}dk_\perp^2 dQ^2} \propto q_i(x_{Bj}, Q^2)e^{-k_\perp^2/\sigma^2} \tag{2.45}$$

where the $k_\perp$ distribution is completely independent of x_{Bj} and Q^2. This is the approach taken by the LUND group in writing their Leptoproduction Monte Carlo [12], which is used in this thesis. Chay, Ellis, and Stirling [13] chose to parameterize the $k_\perp$ dependence as:

$$\frac{d^3N_i}{d\xi_2 dk_\perp^2 dQ^2} \propto q_i(\xi_2, Q^2)e^{-k_\perp^2/\sigma^2}, \tag{2.46}$$

where ξ_2 is defined in Equation 2.42. They argue that in this form, the moments of the parton distribution should factorize properly. For the leading order diagram (Fig. 2-2), these expressions are equivalent since $\xi_2 = x_{Bj}$. Since we are considering both QCD and $k_\perp$ simultaneously, the methods are no longer equivalent. In any case, the actual $k_\perp$ distribution has only been measured very roughly, so the difference between these methods is not yet relevant.

Another issue concerning the $k_\perp$ distribution is whether it depends upon kinematic variables such as Q^2 or x_{Bj}. The most natural assumption is that the primordial $k_\perp$ distribution is independent of the kinematics of the virtual photon since it is a feature of the nucleon dynamics. However, several different arguments have been presented for why such a dependence might occur in DIS or in Drell-Yan[3] interactions [14, 15, 16,

[3]The Drell-Yan process, $p\bar{p} \rightarrow \gamma^* X \rightarrow \mu^+\mu^- X$, is related to DIS by a crossing symmetry.

17]. The $k_\perp$ can be correlated with Q^2 or x_{B_j} through the fact that the cross-section depends upon $k_\perp$ or through the dynamics of the nucleon. The parton distribution need not be factorizable in the simple fashion given by Equation 2.45. In principle, $k_\perp$ could depend on Q^2, x_{B_j} or some other variable. Since this is an unsolved problem, we will take the expression in Equation 2.45 as a reasonable ansatz.

New Effects

The existence of non-negligible $k_\perp$ introduces some effects that should not occur according to the Naïve QPM. These are a non-zero value for $R(x)$ and an azimuthal asymmetry of the outgoing partons around the virtual photon axis. The first effect leads to a small change in the y_{B_j}-dependence of the cross-section for DIS while the second effect leads to an azimuthal asymmetry of the hadrons produced in DIS. We will consider these effects in more detail below.

Recall that in the Naïve QPM, we found that $R(x_{B_j}) = 0$. In the presence of primordial $k_\perp$, $R(x_{B_j}) \neq 0$. To leading order in $k_\perp/Q$, the result is:

$$R = \frac{4k_\perp^2}{Q^2} \tag{2.47}$$

when m_q is neglected. This result can be found in the literature [11] or in Equation A.51 of Appendix Section A.2.2.

The second effect mentioned above, the azimuthal asymmetry of the hadrons, is also missing in the Naïve QPM. Consider a deep inelastic scattering event in which a hadron is generated with momentum $\vec{p}_h$. Figure 2-8 shows the three-momentum vectors of the muons and the hadron in such an event. We can define a variable φ_h which describes the azimuthal angle of the hadron about the virtual photon axis with respect to the muon scattering plane. $\varphi_h = 0$ occurs when the hadron momentum is in the scattering plane and lies on the same side of the virtual photon axis as the scattered muon.

In the Naïve QPM, the hadrons should be produced isotropically in the variable φ_h, making them azimuthally symmetric about the virtual photon axis. This is because the struck parton is collinear with the virtual photon in this picture; any transverse momentum of the hadrons comes from hadronization, which should be random if hadronization is an incoherent phenomenon. In the presence of primordial $k_\perp$, however, the quark is not collinear with the virtual photon. Let us define the variable φ as the azimuthal angle of the incoming parton with respect to the virtual photon axis. This variable will be defined analogously to φ_h. The kinematics of the muon-parton scattering now depend upon the value of φ for the parton. Therefore

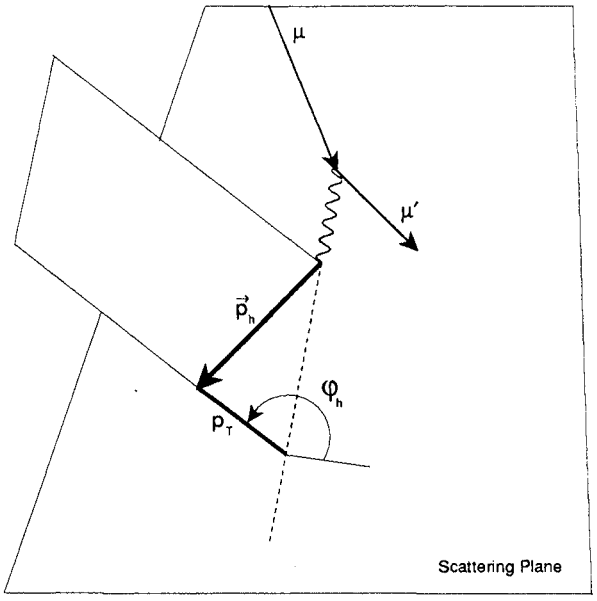

Figure 2-8: The Definition of Phi.
The variable φ_h is defined as the angle of a hadron's 3-momentum about the virtual photon 3-momentum axis with respect to the muon scattering plane; $\varphi_h = 0$ when the hadron momentum lies in the scattering plane on the same side as the scattered muon.

the scattering cross-section is now a function of φ as well. This will, in general, result in a phi asymmetry of the outgoing struck parton (φ') and therefore of the generated hadrons (φ_h).

The hadronic phi asymmetry in DIS was originally considered in the context of the QCD-improved parton model in the absence of $k_\perp$ by Georgi and Politzer [18]. They showed that QCD effects such as gluon bremsstrahlung and photon-gluon fusion are capable of generating a phi asymmetry in the outgoing partons. They claimed that this phi asymmetry in the partons should manifest itself in the hadrons and that the existence of this phi asymmetry in experiment would provide a clean test for QCD, since the Naïve QPM predicted no asymmetry. Shortly thereafter, however, Cahn [19] showed that at the finite values of Q^2 accessible to experiments, $k_\perp$ is not negligible. In particular, as described above, $k_\perp$ also leads to a phi asymmetry, even in the absence of QCD.

The phi asymmetry can be understood qualitatively from the fact that the leading order diagram shown in Figure 2-2 yields a cross-section of the following form:

$$\sigma \propto s^2 + u^2, \tag{2.48}$$

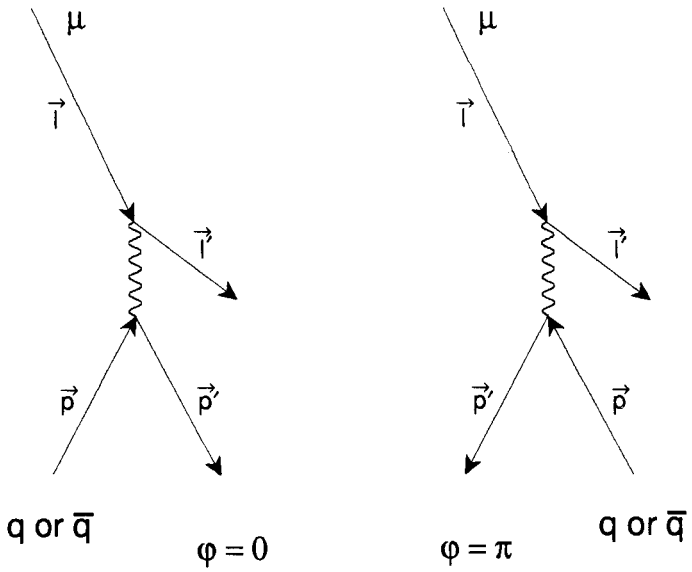

Figure 2-9: A Simple Picture of $k_\perp$-induced Phi Asymmetry.
The three-momentum vectors are shown for the muon-parton scattering for two cases: a) $\varphi = 0$, and b) $\varphi = \pi$. The $\varphi = \pi$ case is favored in the muon-parton scattering, yielding a phi asymmetry.

where

$$s \equiv (l + p)^2 \approx 4(l \cdot p)^2, \qquad u \equiv (l' - p)^2 \approx 4(l' \cdot p)^2 \tag{2.49}$$

Examining Figure 2-9, we see that the $\varphi = \pi$ case is generally favored over the $\varphi = 0$ case. This is because when $\varphi = \pi$, $\vec{p}$ is more nearly anti-collinear with $\vec{l}$ and $\vec{l'}$ than it is when $\varphi = 0$. This means that both s^2 and u^2 are larger and therefore the cross-section is larger for $\varphi = \pi$.

Cahn's quantitative result [19, 20] for the cross-section as a function of φ for fixed values of Q^2 and y_{Bj} is:

$$\frac{dN}{d\varphi} \sim A + B\cos\varphi + C\cos 2\varphi, \tag{2.50}$$

with

$$\begin{aligned} A &= \left[1 + (1 - y_{Bj})^2\right], \\ B &= -4\frac{k_\perp}{Q}(2 - y_{Bj})\sqrt{1 - y_{Bj}}, \\ C &= 4\frac{k_\perp^2}{Q^2}(1 - y_{Bj}). \end{aligned} \tag{2.51}$$

This can also be written as:

$$\begin{aligned} A &= \left[1+(1-y_{B_j})^2\right], \\ B &= -4\frac{k_\perp}{Q}Af_1(y_{B_j}), \\ C &= 4\frac{k_\perp^2}{Q^2}Af_2(y_{B_j}), \end{aligned} \tag{2.52}$$

where

$$\begin{aligned} f_1(y) &\equiv \frac{(2-y)\sqrt{1-y}}{1+(1-y)^2}, \\ f_2(y) &\equiv \frac{1-y}{1+(1-y)^2}. \end{aligned} \tag{2.53}$$

These results only include the leading term in $k_\perp/Q$ for each coefficient. When $k_\perp$ is comparable to Q, then the B term becomes very negative, yielding a cross-section that is negative in places. This result is not physical. A more complete calculation, such as that carried out in Appendix Section A.2 of this thesis, shows that the phi asymmetry is well behaved for any value of $k_\perp/Q$. The result is given by:

$$\begin{aligned} A &= \left[1+(1-y_{B_j})^2\right]\left(\tfrac{1}{\xi'^2}+\xi'^2\tfrac{k_\perp^4}{Q^4}\right)+8(1-y_{B_j})\tfrac{k_\perp^2}{Q^2}, \\ B &= -4\tfrac{k_\perp}{Q}\left(\tfrac{1}{\xi'}+\xi'\tfrac{k_\perp^2}{Q^2}\right)(2-y_{B_j})\sqrt{1-y_{B_j}}, \\ C &= 4\tfrac{k_\perp^2}{Q^2}(1-y_{B_j}). \end{aligned} \tag{2.54}$$

where $\xi' = \left(\frac{1}{2}+\frac{1}{2}\sqrt{1+\frac{4k_\perp^2}{Q^2}}\right)^{-1}$. These results are for massless quarks. Appendix A contains the result for massive quarks as well (see Equation A.47).

The difference between these two formulations can be seen most easily in Figure 2-10 which shows the behavior of B/A and C/A as a function of the dimensionless quantity $k_\perp/Q$ at a fixed value of $y_{B_j} = 0.5$. The Cahn formulation of B/A diverges linearly with increasing $k_\perp$ while the complete formulation reaches a limit of -1.305.[4] Similarly, the Cahn formulation of C/A diverges quadratically while the complete formulation reaches a limit of 0.308. In general, Cahn's formulation is accurate for $k_\perp/Q < 0.2$.

[4]It is a common misconception that $|B/A|$ must be less than unity and equivalently that $|\langle\cos\varphi\rangle| < 0.5$. See Equation A.53 on page 199 and the surrounding discussion for a refutation of this idea.

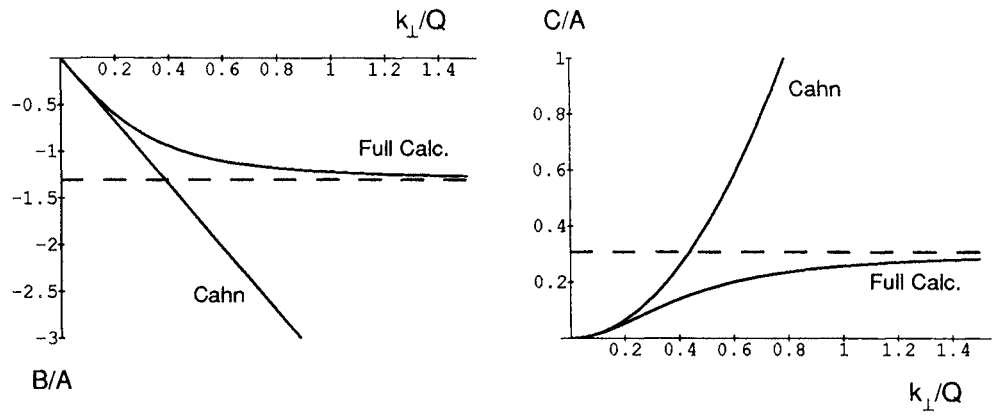

Figure 2-10: Theoretical Phi Asymmetry as a Function of $k_\perp/Q$.
This figure shows the difference between the approximate and exact treatment of the parton-level phi asymmetry as a function of the dimensionless parameter $k_\perp/Q$. This plot assumes a fixed value of $y_{Bj} = 0.5$. The full treatment is well-behaved for all values of $k_\perp/Q$.

The effect on the predicted parton-level phi asymmetry as a function of event kinematics is shown in Figures 2-11 and 2-12. In Cahn's formulation, the y_{Bj}-dependence of the moments $\langle \cos\varphi \rangle$ and $\langle \cos 2\varphi \rangle$ can are given by $f_1(y)$ and $f_2(y)$ respectively (as defined in Equation 2.53). In the full formulation, given in Equation 2.54, the y_{Bj}-dependence of the A term does not factorize in any simple way. Therefore, in general, there is no simple way to factorize the y_{Bj}-dependence of the parton phi asymmetry. On the other hand, Figure 2-12 shows that the Cahn formulation is still not a bad approximation when $Q \geq 2$ GeV and $k_\perp$ takes on reasonable values.

Our picture of what is happening in the interaction becomes even more complicated when we consider the simultaneous effect of QCD diagrams and primordial $k_\perp$. The struck quark in the gluon bremsstrahlung diagram (Figure 2-4) can have a non-negligible primordial $k_\perp$. Similarly, the struck gluon in the photon-gluon fusion diagram (Figure 2-6) can have a non-negligible $k_\perp$. Figure 2-13 shows the final state partons in a gluon-bremsstrahlung event, as well as the direction of the exchanged virtual photon. There are really two azimuthal angles of the partons. There is the angle of the outgoing quark around the $\hat{Z}^*$ axis and there is the angle of the $\hat{Z}^*$ axis around the virtual photon direction ($\hat{z}$). Of course, the hadron phi, which we actually measure, is still only defined with respect to the virtual photon axis, as is shown in Figure 2-8. The mixing of $k_\perp$ with the transverse momentum of the QCD radiation ($\hat{p}_{1T}$) means that there is no simple formula that describes the phi asymmetry in the presence of both QCD and $k_\perp$.

Joshipura and Kramer [21] showed that when both $k_\perp$ and QCD are important,

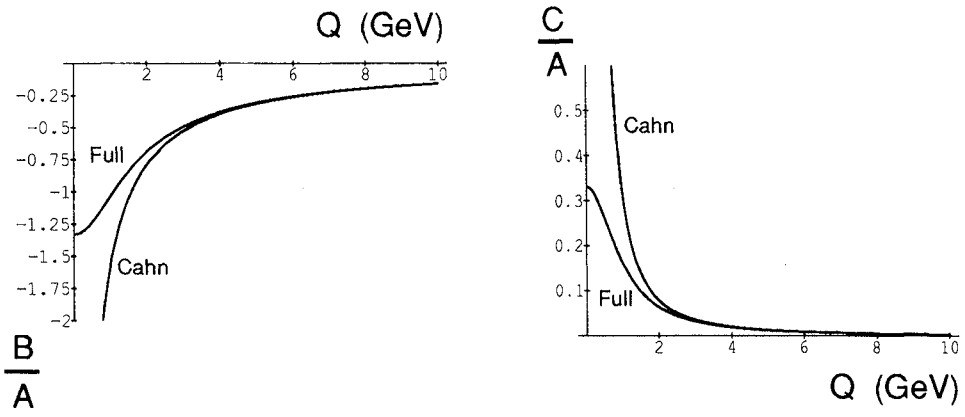

Figure 2-11: Theoretical Phi Asymmetry as a Function of Q.
This figure shows the difference between the approximate and exact theoretical predictions of the parton-level phi asymmetry as a function of Q for a fixed values of $k_\perp = 0.4$ GeV and $y_{B_j} = 0.2$.

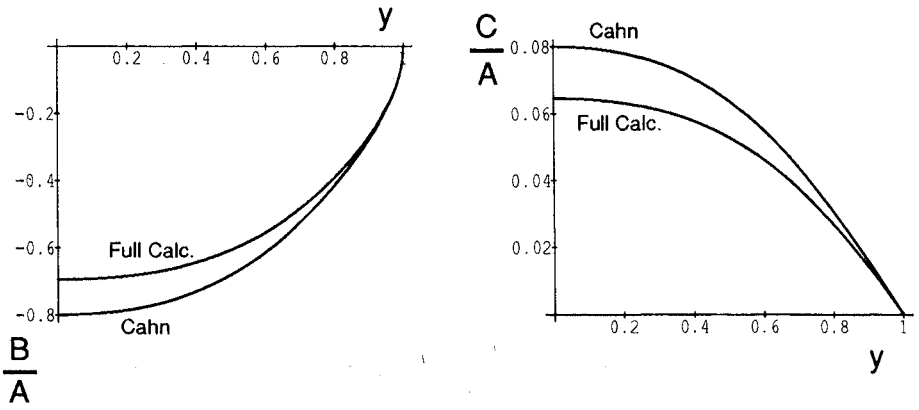

Figure 2-12: Theoretical Phi Asymmetry as a Function of y_{B_j}.
This figure shows the difference between the approximate and exact theoretical predictions of the parton-level phi asymmetry as a function of y_{B_j} for fixed values of $k_\perp = 0.4$ GeV and $Q = 2$ GeV.

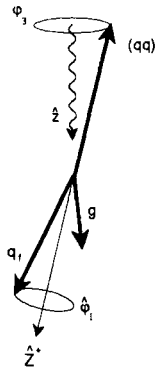

Figure 2-13: The Definition of Parton Phi in Gluon Bremsstrahlung.
The definition of the Phi Asymmetry at the parton level becomes complicated when both $k_\perp$ and QCD effects are important. There are two independent azimuthal angles that we must treat in the theory.

the cross-section takes on the fairly complicated form:

$$\frac{d\sigma}{dx_1 dx_2 d\varphi_3 d\hat{\varphi}_1 dp_T^2} = \frac{2\pi\Gamma\mathcal{F}(\mathbf{p})}{32(2\pi)^5\eta x_3(W^2+Q^2)} \times (T_U + f_1(y)T_I + 2f_2(y)(T_L+T_T)), \tag{2.55}$$

with

$$\begin{aligned}
T_U &= \tfrac{1}{2}T_1(\ \alpha_{1U} + \alpha_{2U}\cos 2\hat{\varphi}_1 + \alpha_{3U}\cos\hat{\varphi}_1) \\
T_L &= T_1(\ \alpha_{1L} + \alpha_{2L}\cos 2\hat{\varphi}_1 + \alpha_{3L}\cos\hat{\varphi}_1) \\
T_T &= \tfrac{1}{2}T_1[\ \cos 2\varphi_3(\alpha_{1T} + \alpha_{2T}\cos 2\hat{\varphi}_1 + \alpha_{3T}\cos\hat{\varphi}_1) \\
&\quad + \sin 2\varphi_3(\beta_{2T}\sin 2\hat{\varphi}_1 + \beta_{3T}\sin\hat{\varphi}_1)] \\
T_I &= -\tfrac{2}{Q}T_1[\ \cos\varphi_3(\alpha_{1I} + \alpha_{2I}\cos 2\hat{\varphi}_1 + \alpha_{3I}\cos\hat{\varphi}_1) \\
&\quad + \sin\varphi_3(\beta_{2I}\sin 2\hat{\varphi}_1 + \beta_{3I}\sin\hat{\varphi}_1)],
\end{aligned} \tag{2.56}$$

and

$$\Gamma = \frac{\alpha W^2}{4\pi^2 Q^2(W^2+Q^2)^2}[1+(1-y)^2]. \tag{2.57}$$

This formula is only valid when m_q is negligible. The variable p_T refers to $k_\perp$; x_1, x_2, and x_3 refer to the energy fractions of the two forward final state partons and the target remnant; $\hat{\varphi}_1$ refers to the azimuthal angle of forward parton 1 about the common axis $\hat{Z}^*$; φ_3 refers to the azimuthal angle of the remnant diquark about $\hat{z} \equiv -\hat{q}$; η refers to the longitudinal momentum fraction of the struck parton with respect to the nucleon in the hadronic cm frame. We also need to use the variable $\hat{p}_{1T}$, which refers to the transverse momentum of the forward partons with respect to their common axis $\hat{Z}^*$. These variables are defined more precisely in Appendix

Section A.3.

The coefficients α_{nX} and β_{nX} are complicated functions of the parton momenta. The expressions listed in Reference [21] contain errors. The correct results can be found in Appendix Section A.3 of this thesis. The main point is that, as shown in Figure 2-13, there are now two important azimuthal angles at the partonic level: $\hat{\varphi}_1$ and φ_3. In general, there is no simple description of our expectations for the φ_h of the hadrons.

However, in the limit that the $k_\perp$ is small with respect to the transverse momentum due to QCD, our results should reduce to the simple formula [22, 23] for the phi asymmetry in the absence of $k_\perp$:

$$d\sigma \propto A_{QCD} + B_{QCD} \cos\varphi + C_{QCD} \cos 2\varphi. \tag{2.58}$$

Similarly, in the limit that the QCD effect is very soft, we must recover the leading order results for the phi asymmetry due to the primordial $k_\perp$ of the struck parton. It should be noted that for very soft or collinear photon-gluon fusion, where the $k_\perp$ of the initial state *gluon* dominates over the transverse momentum of the $q\overline{q}$ pair, the phi asymmetry should be indistinguishable from that of a struck quark with the same $k_\perp$.

It is interesting to examine the phi distribution given in Equation 2.55 for different values of x_1, x_2, and $p_T = k_\perp$. Figure 2-14 shows the phi asymmetry in several different regimes. First, we see in Figure 2-14a that the cross-section for soft photon-gluon fusion (negligible $\hat{p}_{1T}$) is dominated by the effect of the primordial $k_\perp$ of the gluon. The cross-section is nearly independent of $\hat{\varphi}_1$ (the QCD angle), and is primarily a function of φ_3 (the $k_\perp$ angle). Similarly, soft gluon bremsstrahlung is dominated by the primordial $k_\perp$ of the struck quark (not shown). Figure 2-14b shows that in the limit of hard QCD, when the $k_\perp$ is negligible, the cross-section is primarily a function of $\varphi_3 + \hat{\varphi}_1$ and is almost independent of $\varphi_3 - \hat{\varphi}_1$. This makes sense, because the angle of the outgoing quark with respect to the virtual photon axis is given by $\varphi' \approx \varphi_3 + \hat{\varphi}_1$ in this limit. Figure 2-14c shows the complicated behavior of a photon-gluon fusion reaction when neither $k_\perp$ nor $\hat{p}_{1T}$ is negligible. Figure 2-14d shows the behavior of a gluon bremsstrahlung reaction where $k_\perp \approx \hat{p}_{1T}$. In both cases, the phi asymmetry with respect to the virtual photon direction is a complicated combination of the angles plotted.

The results of the full-fledged calculation involve two distinct azimuthal angles. This makes it difficult to come up with a simple prediction for the effect of QCD on the phi asymmetry of the hadrons in the presence of $k_\perp$. To a large extent the phi asymmetry will be washed out by the integration over the two different azimuthal angles.

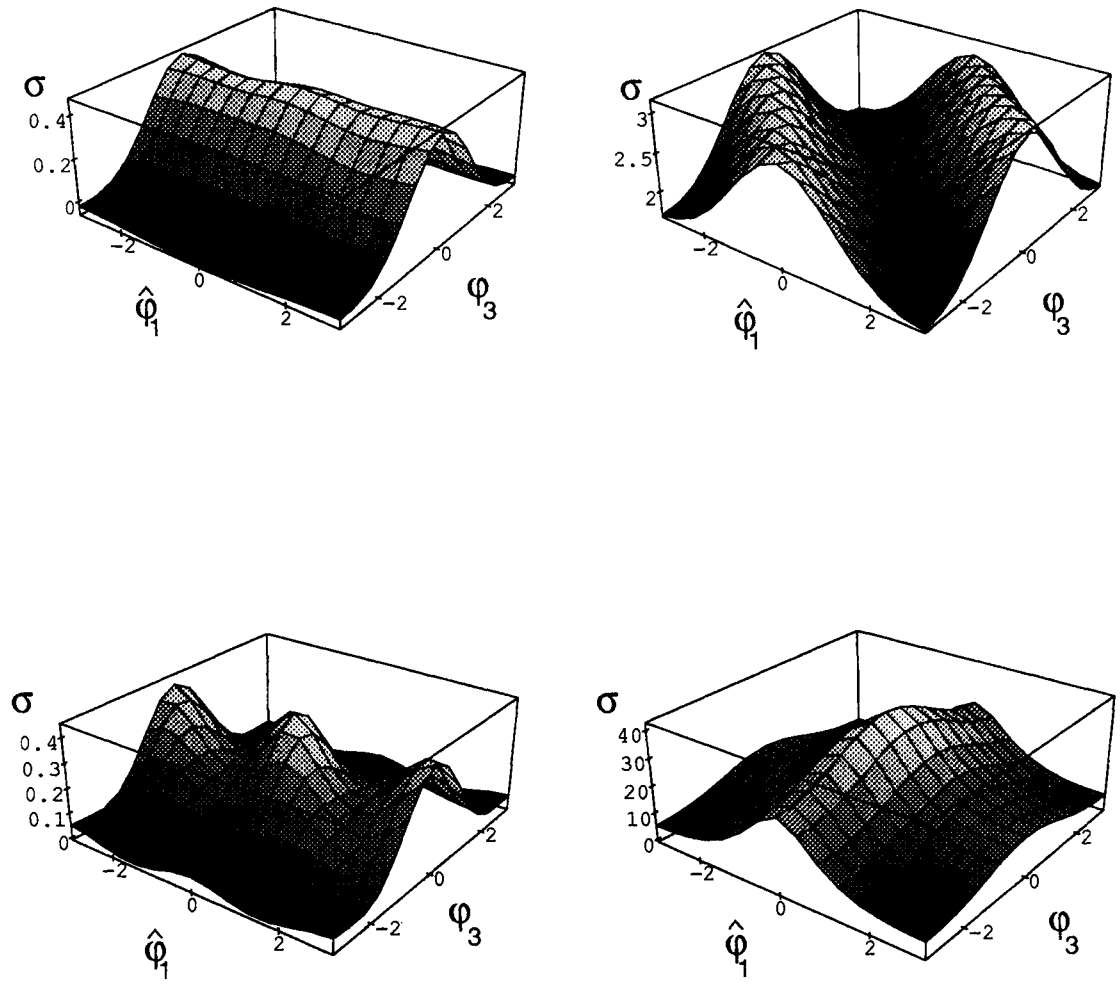

Figure 2-14: Theoretical Phi Asymmetry including both QCD and $k_\perp$.
Four different cases are plotted with arbitrary scales for σ. a) A photon-gluon fusion event that is particularly soft. b) A gluon bremsstrahlung event that is particularly hard. Note the suppressed zero for σ. c) A "typical" photon-gluon fusion event. d) A "typical" gluon bremsstrahlung event.

2.4 The E665 Monte Carlo Program

Having discussed the theory behind deep inelastic scattering, we now turn to the more mundane world of modeling DIS events in the E665 detector. The E665 Monte Carlo Program attempts to model the physics of the hard scattering, the physics of hadronization and particle decays, and the detector performance all in one program. The program itself consists of several distinct packages which are joined together. These packages are LEPTO, which models the hard scattering, JETSET, which models the hadronization, GEANT, which models the particle decays, secondary interactions and so forth, and local packages for digitization and efficiency modeling.

In this thesis, the Monte Carlo is used for two purposes:

1. To correct the data for the effects of acceptance and inefficiency in the detector and reconstruction code.
2. To generate a theoretical prediction given a certain set of theoretical assumptions and inputs. This allows us to compare various theories to the data.

Correcting for the effects that are specific to our experiment will allow the results from our experiment to be compared to future and past experiments. Comparing the results of this experiment to our best estimate of "known" physics effects allows us to pinpoint weaknesses in the current theories and models.

2.4.1 BEAMMC: Beam Simulation

The E665 Muon Beam was simulated by reconstructing actual events taken using the beam trigger (RBEAM) and storing the results in a file. The RBEAM trigger is described in Section 3.8. The actual phase space of the beams in the Monte Carlo simulation is therefore identical to that in the data.

2.4.2 LEPTO: Parton-level Leptoproduction Cross-section

LEPTO is the program module that models the hard scattering of partons. The purpose of the LEPTO subroutine is to generate a list of outgoing "partons" consisting of quarks, diquarks, gluons, and occasionally hadrons which come from the hard scattering process: $\gamma^* N \rightarrow$ partons. The hadrons generated in LEPTO come from complicated multi-quark target remnants which are sometimes broken up into

a hadron and a quark or diquark. Most of the hadrons in the event will be generated later when the quarks, diquarks, and gluons are hadronized by JETSET (see Section 2.4.3).

The version of LEPTO used in this thesis is Version 5.2 [12], which is capable of generating partons according to two different prescriptions: Matrix Element and Parton Shower. The Matrix Element Method involves an $\mathcal{O}(\alpha_s)$ calculation [22] of the hard scattering, given an input set of QCD-improved parton distributions. The Parton Shower method allows the initial and final state partons to undergo a sequence of Altarelli-Parisi-like (leading log) splittings. The Matrix Element method was used to generate the Monte Carlo events that were used in this thesis.

In addition to the regular version of Lepto 5.2 (ME), I generated a new version which also includes the effects of Phi Asymmetry as described in Section 2.3.3. This Phi Asymmetry option can be switched on and off at will. The theory used here includes some assumptions: that $M \ll \nu$ and that m_q is negligible. Since we use $\nu > 100$ GeV, the first assumption is safe. The assumption of negligible quark mass breaks down for charm quarks, but the Monte Carlo expectation is that only about 5% of our events will involve charm quarks in the hard scattering so this should not be a big problem.

Several topics need to be treated in more detail. These are: the usual implementation of primordial $k_\perp$ in LEPTO, my implementation of a phi asymmetry in LEPTO, and the parameter settings used. These topics are all discussed below.

Primordial $k_\perp$ in LEPTO

The language often used to describe the implementation of primordial transverse momentum in the LEPTO code (both 4.3 and 5.2 Matrix Element) is imprecise. The primordial $k_\perp$ distribution is often referred to as a Gaussian distribution in $k_\perp$ with σ given by the LEPTO parameter `PARL(3)`. Referring to this distribution as a Gaussian is vague and misleading. A one-dimensional Gaussian in $k_\perp$ should be given by: $\frac{dN}{dk_\perp} \sim \exp(-k_\perp^2/(2\sigma^2))$, which is not what is used by the LEPTO code. The LEPTO code actually uses a two dimensional Gaussian: $\frac{d^2N}{dk_x dk_y} \sim \exp(-k_\perp^2/\sigma^2)$, which is not the same thing.

The code in LEPTO which generates the primordial $k_\perp$ is a single line in subroutine `LPRIKT`:

```
PT=S*SQRT(-ALOG(RLU(0)))
```

with the variable `PT`$\equiv k_\perp$, the variable `S=PARL(3)`$\equiv \sigma$, and the function `RLU(0)`$\equiv r$,

where r is a random number between 0.0 and 1.0. This can be expressed mathematically as:

$$k_\perp = \sigma\sqrt{-\ln r}, \tag{2.59}$$

with the variable r being distributed according to:

$$\frac{dN}{dr} = 1. \tag{2.60}$$

Inverting Equation 2.59 yields:

$$r = \exp(-k_\perp^2/\sigma^2). \tag{2.61}$$

So the distribution in $k_\perp^2$ is:

$$\frac{dN}{d(k_\perp^2)} = \left|\frac{dN}{dr}\frac{dr}{d(k_\perp^2)}\right| = \frac{1}{\sigma^2}\exp(-k_\perp^2/\sigma^2). \tag{2.62}$$

This is equivalent to

$$\frac{dN}{dk_\perp} = \left|\frac{dN}{d(k_\perp^2)}\frac{d(k_\perp^2)}{dk_\perp}\right| = \frac{2k_\perp}{\sigma^2}\exp(-k_\perp^2/\sigma^2). \tag{2.63}$$

This distribution can be referred to as an exponential in $k_\perp^2$ or as a two-dimensional Gaussian in k_x, k_y, but NOT as a one-dimensional Gaussian in $k_\perp$. We can find the meaning of the quantity σ by examining the moments of the distributions.

$$\begin{aligned}
\langle k_\perp^2\rangle &\equiv \int_0^\infty k_\perp^2\frac{dN}{dk_\perp}dk_\perp && (2.64)\\
&= \frac{2}{\sigma^2}\int_0^\infty k_\perp^3\exp(-k_\perp^2/\sigma^2)dk_\perp = \frac{2}{\sigma^2}\frac{\sigma^4}{2} && (2.65)\\
&= \sigma^2 && (2.66)
\end{aligned}$$

$$\begin{aligned}
\langle k_\perp\rangle &\equiv \int_0^\infty k_\perp\frac{dN}{dk_\perp}dk_\perp && (2.67)\\
&= \frac{2}{\sigma^2}\int_0^\infty k_\perp^2\exp(-k_\perp^2/\sigma^2)dk_\perp = \frac{2}{\sigma^2}\frac{\sqrt{\pi}\sigma^3}{4} && (2.68)\\
&= \frac{\sqrt{\pi}}{2}\sigma && (2.69)
\end{aligned}$$

So, we know that the Lund σ parameter `PARL(3)` is really $\sqrt{\langle k_\perp^2\rangle}$.

Anywhere that the documentation of LEPTO discusses a Gaussian p_T distribution of any kind, it is referring to an exponential in p_T^2 as discussed above.

Phi Asymmetry in LEPTO

The Lund Leptoproduction Monte Carlo programs LEPTO 4.3 and LEPTO 5.2 (ME) do not incorporate any phi asymmetry due to primordial $k_\perp$. The code available allows one to turn on a partial phi asymmetry in the $\mathcal{O}(\alpha_s)$ terms, but this phi asymmetry was calculated under the assumption that $p_T^{jet} \gg k_\perp$ [22]. When one of the two forward jets is soft, the neglected $k_\perp$-dependence can become quite important (recall Figure 2-13 and the surrounding discussion).

König and Kroll developed a Monte Carlo [17] that took into account the effect of primordial $k_\perp$ and additionally the effect of non-zero parton masses. However, since this work was based on a complete rewrite of sections of a now obsolete version of the LUND code, it is difficult to use. Instead we will modify the latest version of the LUND code only slightly, being somewhat less rigorous mathematically, but allowing the code to be transportable.

Appendix A contains a complete calculation of the partonic cross-section to $\mathcal{O}(\alpha_s)$ in the presence of primordial $k_\perp$ for massless quarks. The E665 version of LEPTO has been modified to include this calculation as an option. Appendix B contains a detailed discussion of how this cross-section is implemented in the E665 version of LEPTO. The Monte Carlo used in this thesis includes this parton-level phi asymmetry.

Non-default Parameter Settings in LEPTO

The Lund contains several defaults, and these were changed very little. The only changes to Lepto parameters were that we used a different grid for the cross-section and that we used a different parton distribution.

The $\mathcal{O}(\alpha_s)$ cross-section calculation involves a two-dimensional kinematic grid. LEPTO contains a default grid, which is tuned for use by HERA experiments, and a non-default grid, nominally tuned for use by FNAL experiments such as E665. I used a hybrid grid, taking the FNAL W-range (5–45 GeV) and the HERA x_{Bj}-range (0.001–0.99).

We chose to use the Morfin-Tung SL-fit Leading Order parton distributions [24]. For the sake of consistency with these parton distributions, we also set $\Lambda_{QCD} = 0.144$

GeV in the cross-section calculation[5].

2.4.3 JETSET: Hadronization

We used JETSET Version 6.3 as our hadronization package. This package accepted as input a parton configuration from the LEPTO package and generated hadrons using a string fragmentation scheme which has been tuned extensively on data from $e^+ e^-$ collisions.

In using JETSET, we made two changes from the default running conditions. Both of these changes involved the handling of unstable particles generated during the hadronization. These unstable particles came in two types: resonances such as ρ^0's which can undergo decay effectively instantaneously in the lab frame, and unstable particles such as the K_s^0 which can travel in the lab for quite some distance before decaying. The resonances, by default, are generated with their exact masses, which is non-physical. We instead chose to generate the resonance masses according to a truncated Breit-Wigner shape[6]. Additionally, we turned off all non-instantaneous in-flight decays in JETSET. These decays were handled by the GEANT package instead.

2.4.4 GEANT: Apparatus Simulation

The particles generated by JETSET were tracked through the magnetic fields of the experiment by the GEANT package, version 3.12. This package includes user routines to define the aperture of the apparatus, the location of detector material, and so forth. Several physics background processes were modeled by GEANT: Gaussian Multiple Scattering, Particle Decay, Average Energy Loss, Compton Scattering, Pair Production, Bremsstrahlung[7], Delta-ray Production, $e^+ e^-$ Annihilation, and Hadronic Interaction.

[5]This was accomplished by modifying `PARL(10)`.

[6]This was accomplished by setting `MST(8)=1`.

[7]Electrons, and occasionally muons, can emit photons in the target or detector material. This process, handled by GEANT, should not be confused with QED bremsstrahlung associated with the hard DIS interaction.

2.4.5 MC2: Digitization and Chamber Efficiency Simulation

The MC2 package of E665 modeled the individual chamber efficiencies as measured for a particular part of the Deuterium running period [25, 26]. Possible detailed time-dependent effects were not included for this thesis.

In addition, the effects of the physics trigger (LAT) used in this thesis were approximated in the Monte Carlo by throwing away any events where the scattered muon entered the LAT veto counters (SMS1 or SMS4). The LAT is described in more detail in Section 3.8 while the SMS counters are described in Section 3.5. Inefficiencies in the LAT trigger components were not modeled in detail. The trigger components were assumed to behave ideally.

2.5 Summary

We have discussed the Minimal Standard Model of Particle Physics and the conventional understanding of the leptoproduction process. We have seen that the structure of the nucleon in this model can be understood in terms of partons — quarks and gluons. We have also seen that significant effects are expected to occur due to the existence of primordial transverse momentum ($k_\perp$) of the partons within the nucleon. The standard treatment of these $k_\perp$ effects has been extended so that the theory is better behaved at moderately low values of Q^2 (2–4 GeV^2).

Using the results derived by Cahn [19, 20], and assuming that the $k_\perp$ distribution is independent of Q^2, we found that the phi asymmetry due to $k_\perp$ should become more prominent at low values of Q^2. In particular, we found that to leading order in $\frac{k_\perp}{Q}$, the phi asymmetry should be proportional to $1/Q$. Since this theoretical treatment diverges as $Q^2 \to 0$, we calculated this effect using a more complete treatment of the parton kinematics. This treatment was better behaved as $Q^2 \to 0$, but the basic conclusion was unchanged. For values of Q^2 extending down to about 1 GeV^2, we expect the phi asymmetry due to $k_\perp$ to grow in magnitude as Q^2 decreases, assuming that $k_\perp$ is independent of Q^2. We also noted that $k_\perp$ may actually depend on Q^2 or ν.

When we considered the simultaneous effects of QCD and $k_\perp$, using the results of Joshipura and Kramer [21], we found that matters are more complicated then the usual treatments imply. Explicit results were derived for the parton-level angular distribution in this case.

When we included the $k_\perp$ effects in their full glory, we found that it was no longer

possible to factorize the y_{B_j}-dependence of the $\langle \cos\varphi \rangle$ moments. In other words, we discovered that the usual result that $\langle \cos\varphi \rangle \propto f_1(y_{B_j})$ is not exact.

All of these theoretical effects were incorporated into the standard leptoproduction Monte Carlo program along with the specifics of the E665 apparatus. It should be noted that the quark mass was treated as negligible. This program will be used to correct our data for apparatus and reconstruction effects and to make theoretical predictions to compare to our data.

Chapter 3

Experimental Apparatus

This chapter describes the E665 Detector as it existed during the 1987-1988 Fermilab fixed target run. Further details can be found in the general E665 apparatus paper [27] and the references therein. The upgrades to the apparatus for the 1990–1991 run are discussed briefly in Section 3.9. Special emphasis is given to the Data Acquisition and PTM systems since I was involved in those upgrades.

3.1 Overview of the Apparatus

3.1.1 Detector

The overall purpose of the E665 Collaboration, and therefore of the detector, was twofold. First, we wanted to study ratios of structure functions on different targets (e.g D_2/H_2 or Xe/D_2). This task only required the reconstruction of the muon kinematics. Second, we wanted to study the hadrons that were generated during the inelastic scattering. This required that we measure the outgoing hadrons, both charged and neutral, preferably with good acceptance, good reconstruction efficiency, and ideally including particle identification.

The E665 Detector was general-purpose in the sense that we tried to fulfill all of the goals alluded to in the previous paragraph. The basic layout of the experiment included two distinct spectrometers. The first was a single-dipole beam spectrometer which measured the beam momentum on an event by event basis. The second was an open air double-dipole forward spectrometer which measured the particles produced in the muon-nucleon collisions. The Detector also included a muon identification system, consisting of a steel absorber followed by a collection of wire chambers, scintillators,

and smaller concrete absorbers. Our apparatus also included a streamer chamber, an electromagnetic calorimeter, and a group of particle identification detectors. The streamer chamber presented almost a 4π-acceptance in the laboratory for charged particles, but was limited to only a fraction of the total luminosity since it had a long dead time. The electromagnetic calorimeter detected forward-going photons and helped to identify electrons. The particle identification chambers were capable of discriminating between pions, kaons, and protons over a broad range of energies. The general-purpose nature of the E665 Detector allowed a wide range of physics topics to be addressed. The streamer chamber and the particle identification chambers (except for muon identification) were not used in this thesis.

3.1.2 Muon Beam

The E665 Detector resided at the end of Fermilab's fixed target NM beamline. The beam consisted of positively charged muons with an average momentum of 490 GeV. As with all muon beams, the beam phase space was quite broad, both in terms of momentum spread ($\sigma_p \approx 60$ GeV) and in terms of the spatial distribution transverse to the beam direction (effective radius $\sim$ 3 cm). Additionally, there were muons, known as *halo* muons, which resided outside of the usable beam phase space. These halo muons amounted to about 20% of the usable beam.

The muons were generated as a tertiary beam. Protons at a momentum of 800 GeV were extracted from the Tevatron and struck a beryllium primary target, generating a secondary beam of pions and kaons. Any remaining protons were steered into a proton dump. The secondary beam of pions and kaons were momentum selected and transported for 1.1 km. During this transport, some of the pions and kaons decayed, producing a broad spectrum of muons. This mixture of pions, kaons, and muons was passed through a beryllium absorber, leaving a tertiary beam which was mostly composed of muons. This muon beam was then momentum selected, steered, and focussed to traverse the E665 Beam Spectrometer and impinge upon the E665 physics target. Due to the 53.1 MHz RF (Radio Frequency) structure of the Fermilab accelerator, muons were separated by integral multiples of 18.8 ns with a jitter of about 1 ns. Furthermore, the duty cycle of the accelerator was a 22 s active period known as a *spill* followed by a 35 s *interspill* period where no muons were available while the Tevatron proton beam was being refilled. The muon beam was (left-) circularly polarized. This was due to the fact that the muons were generated by parity-violating weak-interaction decays: $\pi^+ \rightarrow \mu^+ \, \nu_\mu^{(L)}$ and $K^+ \rightarrow \mu^+ \, \nu_\mu^{(L)}$. Since pions and kaons are spinless, the helicity (λ) for the μ^+ was $-\frac{1}{2}$ in the pion or kaon center-of-mass frame. In the lab frame, the helicity is correlated with the muon momentum. The average polarization of a muon with a momentum of 500 GeV was calculated to be -0.83 ± 0.13 [28], where the polarization is defined as $2 \cdot \lambda$, and

ranges from -1 to +1.

The Muon beam line at Fermilab can be tuned to various energies. During the 1987-88 fixed target run, we ran with an average beam energy of 490 GeV for most of the time. In a typical spill during good running conditions, the muon beamline delivered 2×10^7 muons. Some 100 GeV data were also taken, but weren't used in this thesis. Furthermore, electrons or protons were sometimes transported down the Muon beam line for special purpose studies such as the calorimeter calibration run which used an electron beam.

3.1.3 E665 Coordinate System

The E665 Coordinate System is a right-handed coordinate system with the X-axis along the nominal beam direction and the Z-axis pointing up (away from the center of the earth)[1]. The nominal beam direction (X) is roughly North and the Y-axis points roughly West. A given detector element is characterized by the coordinate that it measures. For instance, a wire chamber plane with horizontal wires (parallel to the Y-axis) measures the Z-coordinate and is referred to as a Z-plane. In general, the coordinate that a chamber measures is denoted by the symbol: Θ. For a chamber which is perpendicular to the X-axis, as most are, we define an angle α such that $\Theta = Y \sin\alpha - Z \cos\alpha$. We can also define a wire-orientation angle $\alpha^* \equiv \alpha - \frac{\pi}{2}$ which ranges from $-90°$ to $90°$ and describes the angle that the wires make with the vertical (measured about the X-axis). Given these definitions, we can divide the chambers into the following categories:

Y :	$\alpha \approx \frac{\pi}{2}$	$\alpha^* \approx 0°$,
Z :	$\alpha \approx \pi$	$\alpha^* \approx 90°$,
U :	$\frac{\pi}{2} < \alpha < \pi$	$\alpha^* > 0°$,
V :	$0 < \alpha < \frac{\pi}{2}$	$\alpha^* < 0°$,

Throughout this chapter, chamber dimensions will be referred to in the format $Y \times Z$. If a third dimension is used, it refers to the thickness of the counter or chamber. Wire orientations will be referred to from the vertical using α^*.

[1]Technically, there were two slightly different E665 coordinate systems. The system described here was the original E665 coordinate system used by the surveyors. The Software Coordinate System is discussed in more detail in Section 4.1.

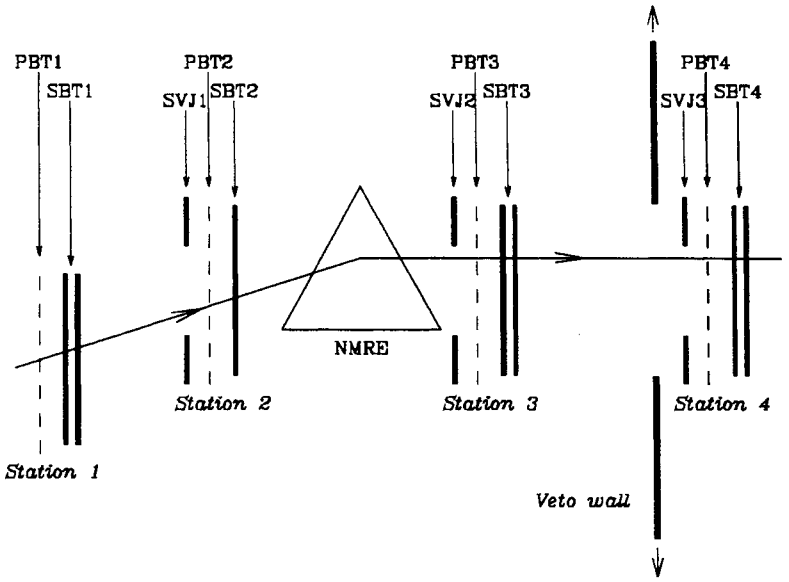

Figure 3-1: The E665 Beam Spectrometer. This diagram is not drawn to scale.

3.2 Beam Spectrometer

The E665 Beam Spectrometer, shown in Figure 3-1, consisted of four stations spread out over about 55 m, with a dipole analyzing magnet (NMRE) between stations 2 and 3. Each of these stations consisted of a collection of multi-wire proportional chambers (PBTs) and scintillation counters (SBTs). Three of the four stations also contained an extra set of scintillation counters (SVJs) to help remove halo muons close to the beam. Additionally, there was a wall of scintillators known as the Veto Wall (SVW). A 500 GeV muon traversing the beam spectrometer was bent by an angle of about 3 mr. The PBTs measured the bend angle, and thus the momentum, of the beam particle. The SBTs generated fast signals which were used as part of the trigger for the experiment and which were also latched for use in the offline analysis. The SVJ and SVW counters were used in the trigger to veto (reject) events which included halo muons. The fractional momentum resolution ($\delta p/p$) was about 0.5% for 500 GeV muons; the angular resolution of the measured beam direction was about 0.01 mr regardless of the beam momentum.

The PBTs were standard Fermilab "Fenker" chamber packets [29] with a 1 mm wire spacing and an active area of 12.8 cm$\times$ 12.8 cm. Each station contained 6 PBT planes, with wire orientations of $U(+30°)$, $Z(+90°)$, $Y(0°)$, $V(-30°)$, $Z'(+90°)$, and $Y'(0°)$. The Y' and Z' planes were offset by half a wire with respect to the Y and Z planes. This configuration, four stations with six planes each, provided a high degree

Length	1.15 m
Diameter	8.9 cm
Density	0.163 g/cm^3
Thickness	18.7 g/cm^2
Radiation Lengths	0.153
Interaction Lengths	0.342

Table 3.1: D_2 Target Characteristics — 1987 Run.

of redundancy and therefore the PBT system was very reliable.

The SBTs were scintillator paddles which were used to provide timing signals associated with each beam muon. The paddles were segmented to yield Y-view information in all of the stations and Z-view information in stations 1, 3, and 4. The active area of the SBTs was 0.14 m $\times$ 0.18 m. The timing information from the SBTs was used in triggering the experiment, allowing us to reject signals from out-of-time muons which arrived in a different bucket than the trigger muon. The SBT signals were also latched, allowing PBT hits from out-of-time muons to be rejected during the offline analysis when they couldn't be associated with an in-time SBT signal.

The SVW (Veto Wall Scintillator plane), along with the smaller adjustable SVJs (Veto Jaw Scintillators), served to limit the muon beam phase space by allowing the trigger to avoid events with halo muons in them. In particular, a halo muon far from the target was incapable of generating a DIS event in the target, but it could have caused fake triggers if it wasn't vetoed. The Veto Wall was a 7 m $\times$ 3 m wall of scintillator which was located just upstream of Beam Station 4. This wall was made up of individual 0.55 m $\times$ 1.5 m counters with 5 cm of steel shielding mounted on the upstream faces. Without this shielding, good beam muons would have tended to self-veto due to soft photon radiation. There was a 25 cm–square hole in the veto wall plane where the usable beam could pass without being vetoed. The Veto Jaws (SVJs) were located at beam stations 2–4 and covered a region that was 50 cm–square.

3.3 Targets

During the 1987–88 data run, three targets were used: liquid Deuterium, liquid Hydrogen, and pressurized gaseous Xenon. Only the Deuterium target is considered in this thesis since that was the target with the largest integrated luminosity. The Deuterium target was a cryogenic target constructed of 1 mm thick Kapton. It's characteristics are summarized in Table 3.1.

The thickness, number of radiation lengths, and number of interaction lengths were all calculated from the density and the length of the target. Clearly the thickness is just the product of the density and length. One radiation length in D_2 is 122.6 g/cm^2 while one nuclear interaction length is 54.7 g/cm^2 [30]. Since the target was only a fraction of a radiation length and a fraction of an interaction length, it qualified as a "thin" target. We used thin targets in E665 in order to minimize the effect of rescattering on the hadron distributions and in order to be able to use the Streamer Chamber described in Section 3.7. Our decision to use thin targets optimized our ability to study hadrons at the expense of luminosity.

3.4 Forward Spectrometer

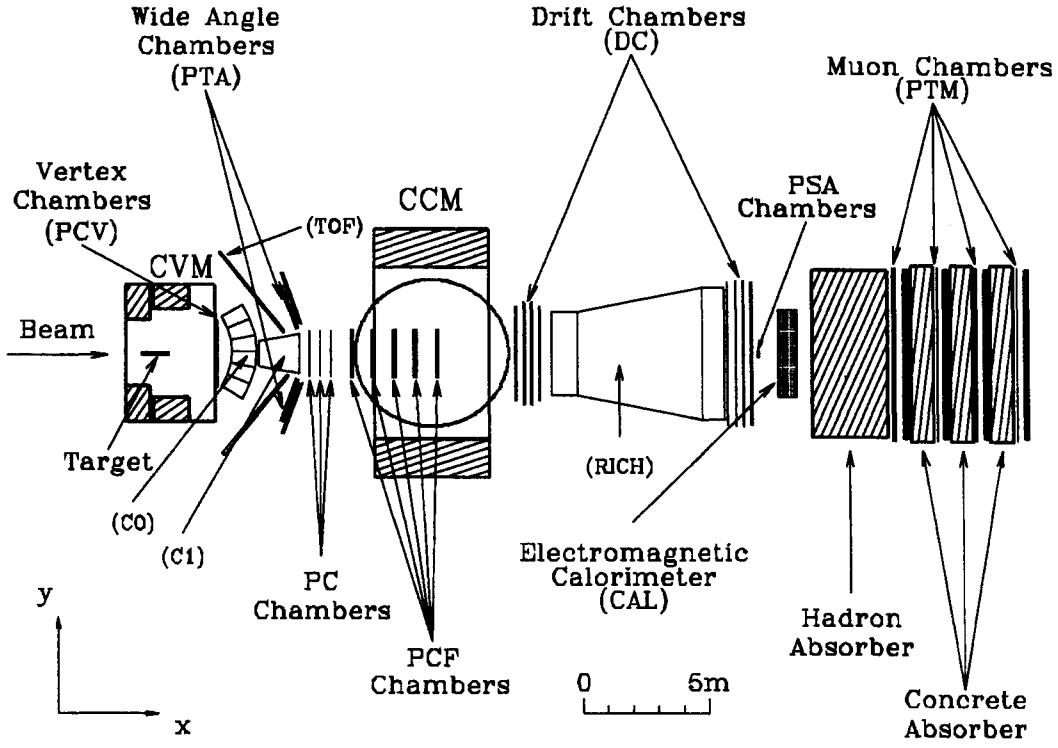

Figure 3-2: The E665 Detector.
This diagram, which includes the Forward Spectrometer and the Muon Identification system, is drawn to scale. This is a plan view, looking down on the detector from above.

The E665 Forward Spectrometer, shown in Figure 3-2, consisted of two superconducting dipole magnets of opposite polarity and several sets of tracking chambers. The experiment was designed so that a straight-through beam muon (μ^+) was bent first

in the $+Y$ direction (West) and then in the $-Y$ direction (East). Furthermore, the distances were arranged so that beam muons reached the first plane of Muon Proportional Tubes (see Section 3.5.3) at the same Y-position regardless of their energy. This focusing geometry greatly simplified scattered muon triggering and acceptance considerations.

The dipole magnet in which the target was located was called the CERN Vertex Magnet (CVM) and was previously used by the European Muon Collaboration (EMC). This magnet had a field integral ($\int \vec{B} dl$) of -4.3 Tm $\hat{z}$ for a straight line path along the x-axis. This was the total field integral seen by a very energetic particle traversing the magnet. The downstream magnet was called the Chicago Cyclotron Magnet (CCM) and was originally the main magnet in the University of Chicago 460 MeV cyclotron. It had a field integral of $+6.7$ Tm $\hat{z}$. It was the bending in the CCM that allowed the momenta and charges of the particles to be measured[2].

The Forward Spectrometer was designed to track particles with momenta above about 8 GeV. The momentum resolution depended upon how completely the track was reconstructed and upon the momentum of the particle itself. For a fully reconstructed track, we achieved a fractional momentum resolution ($\delta p/p$) of 2.5% $\times$ p/500 GeV and an angular resolution of 0.1 mr.

3.4.1 PCV: Vertex Proportional Chambers

The PCV chambers were the first set of tracking chambers downstream of the target. They were important to the momentum resolution and vertex finding because they had the best lever arm for determining the slope of a particle trajectory before it entered the CCM. The PCV package consisted of six planes with an active aperture of 2.8 m $\times$ 1.0 m. The wire spacing was 2 mm and the wire orientations were: $Y(0°)$, $U(+18.5°)$, $U'(+18.5°)$, $V(-18.5°)$, $V'(-18.5°)$, and $Y(0°)$. The central regions of the last two PCV planes failed and were dead during the 1987 data-taking run. This effect was simulated in the Monte Carlo program.

3.4.2 PCN: Proportional Chambers

Downstream of the PCVs, but still upstream of the CCM, were three packages of proportional chambers with four planes per package. These packages were known individually as PC1, PC2, and PC3, and collectively as the PCs or the PCNs. Each

[2]Technically, we only measured the sign of the charge and assumed unit magnitude.

package contained planes with the following views: $Y(0°)$, $Z(90°)$, $V(-28°)$, and $U(+28°)$. The wire spacing was 3 mm, and the active aperture was 2 m $\times$ 2 m.

Each PCN plane was divided into three regions: a 3 cm radius disk centered on the beam, an annulus with a 6 cm outer radius surrounding the central disk, and the rest of the plane. The planes were inefficient at the boundaries of these regions. Additionally, there were four support structures (zigzag Mylar strips known as *garlands*) in each of the PC Z-planes. These garlands ran perpendicular to the wires and caused stripes of inefficiency. These inefficient stripes were not in the beam region. All of these effects were included in the Monte Carlo used in this thesis, although some earlier versions of the Monte Carlo were missing the PC garland inefficiencies [26] due to a bug.

In addition to being used in the tracking, the PCN chambers were also used in some special purpose multiplicity-based triggers for the Streamer Chamber. These triggers are described in Section 3.8.3.

3.4.3 PCF: Forward Proportional Chambers

The PCF system consisted of five triplets of multiwire proportional chambers with a 2 mm wire spacing and an active aperture of 2 m $\times$ 1 m. Each triplet consisted of three views: $U(+15°)$, $V(-15°)$, and $Z(90°)$. Four of these triplets resided inside the magnetic field of the CCM, allowing us to follow the curved particle trajectories.

The PCF chambers contained support wires which ran perpendicular to the active anode wires. These support wires resulted in stripes of inefficiency. The Z planes each had two support wires, one on either side of the beam region. The U and V chambers each had only one support wire near the middle of the chambers. The support wires were at different locations in each plane so that the dead regions didn't overlap. These effects were included in the Monte Carlo.

3.4.4 DC: Drift Chambers

There were eight drift chamber packages which were referred to individually as DC1-8 and collectively as the DCs. All eight packages resided downstream of the CCM, but they were divided into two groups of four packages each, which were referred to as the DCAs (DC1-4) and the DCBs (DC5-8). The purpose of the DCs was to track high momentum particles ($p > 15$ GeV) after they left the CCM magnetic field. Splitting the DCs into DCAs and DCBs yielded a longer lever arm for determining the slope of the straight-line trajectory downstream of the CCM. This in turn improved the momentum resolution of tracks which had hits in all of the DCs.

Each group (the DCAs and the DCBs) included the following views: $Z(+90°)$, $U(+5.758°)$, $V(-5.758°)$, and $Z(+90°)$. The DCA chambers, which were just downstream of the CCM, had an active aperture of 4 m × 2 m. The DCB chambers, which were the last set of large aperture tracking chambers upstream of the Electromagnetic Calorimeter, had an active aperture of 6 m × 2 m.

Each package was deadened in the beam region. The dead regions were rectangular, with an average size of 10 cm × 5 cm. The spatial resolution of these chambers was about 400 μm, while the two-track resolution was about 4 mm. The chambers were composed of drift cells 50.8 mm (2") wide in the drift direction and 9.6 mm deep along the beam direction. Each Z-view wire was separated into two halves by a G10 septum located in the middle of the chamber, and each side (East and West) was read out separately. This improved the multi-hit capability of the system, but it also resulted in a vertical dead stripe in the middle of the DC Z-planes, in addition to the usual rectangular dead region.

Each individual package consisted of two layers. Both layers in a given package measured the same view, but were offset by half a drift cell. If there had been only one layer per package, this would have generated an ambiguity. We would have known the distance between the particle trajectory and the wire, but we wouldn't have known whether the particle passed on the + (west) side or the − (east) side of the wire. The double layering allowed us to resolve this ambiguity most of the time.

The DCs had some problems during most of the 1987 data-taking run. There was a short in one of the high voltage field shaping wires in plane DC2U1. This resulted in a segment of each drift cell in this plane being dead. About 20% of the total area of DC2U1 was dead. Furthermore, all of the DC planes had a different drift velocity in the outer region of the cell (0.6"–1" from the wire) than in the inner region.

The planned dead regions, the effect of the support wire, and the dead stripes in DC2U1 were all incorporated in the Monte Carlo. The Monte Carlo did not, however, incorporate any nonlinearities or discontinuities in the drift velocity. In principle, this should not matter much as long as the calibration curves in the data are correct and as long as the Monte Carlo is reconstructed with the same assumptions under which it was generated.

Some very high momentum particles (both muons and hadrons) remained in the beam profile at the DCs. These particles traveled through the dead region of the DC chambers and were not detected there. In particular, most of the scattered muons from the Small Angle Physics Trigger (SAT) passed through the dead region of the DCs.

3.4.5 PSA: Small Angle Proportional Chambers

The PSA chambers were designed to cover the central dead regions of the drift chambers. They consisted of two identical four-plane packages of proportional chambers based on the same standard Fermilab design [29] used in building the PBTs for the Beam Spectrometer. The PSA chambers were located just downstream of the DCBs and just upstream of the Calorimeter. The PSA planes had a 1 mm wire spacing and an active area of 12.8 cm × 12.8 cm.

The first four-plane package was mounted with orientations: $Z(+90°)$, $Y(0°)$, $Z'(+90°)$, and $Y'(0°)$. The primed planes were offset from the non-primed planes by 0.5 mm (half of the wirespacing). The second four-plane package was rotated by 45° with respect to its counterpart, resulting in the following chamber orientations: $U(+45°)$, $V(-45°)$, $U'(+45°)$, and $V'(-45°)$.

The main purpose of the PSA was to cover the DC dead region, allowing us to track particles which didn't leave the beam profile. They were especially important for tracking the scattered muons in events from the Small Angle Trigger (SAT).

3.5 Muon Identification

The muon identification system allowed us to distinguish muons from other charged particles. This served two purposes. It allowed us to pin down the kinematics of the event by identifying the scattered muon and it allowed us to trigger on events that were likely to be inelastic scatters.

Downstream of the Electromagnetic Calorimeter was a 3 m thick wall made primarily of steel which was called the Steel Absorber. Any hadrons, electrons, or photons which made it through the Calorimeter (or were produced in showers there) were absorbed in the Steel[3]. There were four groups of chambers downstream of the Steel Absorber, and these groups were separated by concrete absorbers 0.9 m (1 yard) thick. The spaces between absorbers in which the chambers resided were called *bays*. The concrete absorbers served to ensure that any electromagnetic showers generated by the muons were confined to a single bay. This helped to minimize the confusion in both tracking and triggering.

Each bay contained two proportional tube tracking chambers (PTMs) and a wall of scintillators (SPM/SMS). The active region of this system was roughly 7 m × 3 m. The PTM chambers contained a deadened region roughly 20 cm-square where the

[3]The pion punch-through probability was estimated to be about 10^{-8} (e^{-18}).

beam passed through the chamber. The upstream chamber in each bay was a PTM chamber oriented in the $Y(0°)$ direction. The next chamber downstream was a PTM chamber oriented in the $Z(90°)$ direction. Downstream of the PTM chambers in each bay was an SPM/SMS scintillator plane. Each SPM plane was a large wall of scintillation counters with a 20 cm-square hole in the middle for the beam. The hole in the SPMs and the dead regions in the PTMs were approximately lined up and were covered by the SMS counters. The SMS counters covered a region roughly 22 cm-square and were more finely segmented than the SPMs. The SPMs were used for triggering, while the PTMs were used for tracking muon segments behind the Steel. The SMSs were used for both tracking and triggering. During the 1990–1991 data-taking run, the PTMs were used for triggering as well as tracking (See Section 3.9).

The various components of the Muon Identification system are detailed below.

3.5.1 SPM: Muon Scintillator Planes

Each Muon Scintillator Plane (SPM) was segmented into an upper half and a lower half. Each half was further segmented into fifteen regions in Y across the plane. The individual scintillators measured 50 cm × 150 cm × 2.5 cm, except for the central counters directly above and below the beam. The central counters, which measured 28 cm × 140 cm × 2.5 cm, were offset in order to create a 20 cm-square hole. Wherever the scintillators met, they overlapped by at least 1.3 cm. These scintillators provided signals which were used to generate a scattered muon requirement in the LAT and Halo triggers. The signals from the SPMs were also latched and written to tape during an event.

3.5.2 SMS: Small Muon Scintillator Planes

The Small Muon Scintillator (SMS) planes covered the hole in the SPMs and the dead region in the PTMs. The SMS signals were used for several purposes. First, they were used in the Small Angle Floating-Veto Physics Trigger (SAT) to provide fine segmentation for detecting unscattered beam muons downstream of the Absorber. Second, the SMS signals were used as a veto in the Large Angle Physics Trigger (LAT) so that non-scatters or small-angle scatters were rejected. Finally, the SMS signals were latched and written to tape during an event in order to provide muon tracking in dead region of the PTMs. This was especially important for the small angle scattering events in the SAT data sample.

Each bay contained two planes of SMS counters, one segmented to provide information in the $Y(0°)$ view and one to provide information in the $Z(90°)$ view. The

SMS Y-planes consisted of sixteen vertical counters which were 21.6 cm long and 1.32 cm wide, except for the outer ones which were 1.96 cm wide. The effective overlap of adjacent counters was 0.03 cm. The SMS Z-planes were identical to the Y-planes, but the counters ran horizontally instead of vertically.

3.5.3 PTM: Muon Proportional Tubes

Muon tracking outside of the beam region was handled by the PTM chambers. These chambers were used to reconstruct straight line tracks downstream of the absorber, but outside of the beam region. Most of these tracks were due to muons which scattered from the target. There were also background tracks due to out-of-time halo muons, in-time halo muons, and cosmic rays. Occasionally an event would occur with more than one outgoing muon coming from the vertex. Such events were generally due to a higher order QED process known as a *trident* where a virtual photon was radiated and generated a $\mu^+\mu^-$ pair in addition to the scattered muon. Events with extra outgoing muons were fairly rare and were handled by ignoring the extra muons. It was also possible for a pion or kaon from the event to decay into a muon. During the 1990–1991 run, the PTMs were used as input to a target-pointing Level-II trigger as well as for tracking. The PTM system was the joint responsibility of the MIT and UCSD collaborators in E665.

As mentioned above, each muon system bay downstream of the Steel Absorber contained one PTM Y-plane and one PTM Z-plane. The active area of a PTM Y-plane was 7.2 m $\times$ 3.7 m. The active area of a PTM Z-plane was 7.3 m $\times$ 3.6 m. The PTMs were constructed of long aluminum tubes with a 25.4 mm square cross-section. Each tube contained one anode wire. The tubes in each plane were arranged in two layers and these two layers were displaced by 12.7 mm giving an effective wire spacing of 12.7 mm with no dead region between wires. In most cases, a muon caused a hit in both layers.

The actual units of construction consisted of *modules* which contained fifteen wires each, eight in one layer, and seven in another layer. Each wire was surrounded completely by a square tube which served as its cathode. The Y-view modules were 3.7 m long and there were 38 such modules per plane. The Z-view modules were 7.2 m long with only 19 modules per plane. Each module could in principle function as a complete detector by itself since it was a self-contained airtight independent gas volume. In practice, the modules were connected externally by tubes and pipes so that a complete gas volume consisted of a single plane. Similarly, the ground, high voltage, and low voltages were shared in common by groups of modules. Figure 3-3 is a cross-section view of a single module, showing the double layer construction.

The wires were 50 μm diameter gold-plated tungsten and were operated at 2.7 kV.

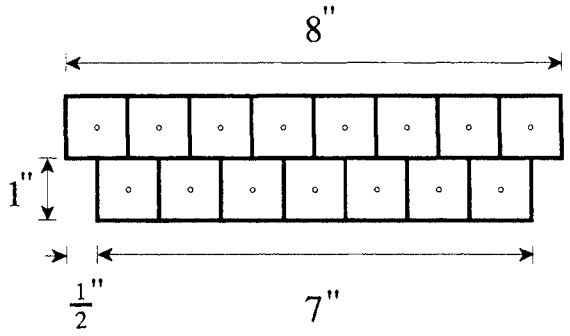

Figure 3-3: A Cross-section of a PTM Module.
The wall thicknesses and wire diameters are not drawn to scale.

The tubes were held at ground. It should be noted that the Z-view wires didn't require a support structure, even though they were 24' long. The gas mixture was 50%–50% Argon-Ethane bubbled through ethanol at $0°C$. The total gas volume was 380 cubic feet (10.8 kiloliters) and the leak rate was determined to be less than 1% of the volume per day. The tubes were run in proportional mode and on the plateau of the drift velocity curve. The drift velocity was roughly 50μm/ns over the whole region. Since the maximum drift distance for ionization electrons from a charged particle traversing a tube was 12.7 mm, this yielded an expected drift time range from 0–250 ns.

Hits in the PTMs were read out using Nanometrics N-272-E Readout Cards. Each card serviced one module (fifteen wires). The PTM signals were amplified and discriminated and a valid hit triggered a one-shot on the readout card, which was set to last for 200–300 ns. The outputs of these one-shots (one per wire) were latched into cyclic memories (32 bits per wire) on the readout cards. The clock frequency which we chose to use for the cyclic memories was 26.6 MHz which was half of the accelerator RF frequency.

When an E665 Data Acquisition trigger occurred, the latch memories were frozen and then read out using Nanometrics WCS-200 scanners. There was one scanner per plane and the planes were read out in parallel. It should be noted that the WCS-200 model scanner suffers from the limitation that it can only handle 63 clusters (of up to 7 wires each). Given the low muon multiplicity in our events, this limitation was not a problem.

Each PTM plane was positioned so that the bulk of the unscattered muon beam passed through a single module. Numbering the PTM Y-modules 1–38 from East to West and the PTM Z-modules 1–19 from Bottom to Top, the beam passed through Module 19 of a Y-plane and module 9 of a Z-plane. These modules were known as *beam-hole modules*. It should be noted that the aperture of the PTMs was not centered exactly on the beam. It was not centered in Y because there were an even

number of modules and we only wanted to deaden one module per plane. It was not centered in Z because of the placement of the Steel Absorber relative to the beam. The Steel Absorber actually rested on Concrete blocks and didn't extend all the way to the floor of the experimental hall. It was decided not to extend the PTMs below the Steel since the concrete alone provided inadequate protection against pion punch-through. The beam region, which was defined as the an 8" region along each wire in the beam hole modules was partially deadened during the 1987–1988 run. This deadening was accomplished by opening up the modules, removing some of the intercell webbing and coating the cathodes [25]. The PTM dead region was approximately a 20 cm square. For the 1990–1991 run, the PTM dead regions were deadened more fully by insulating both the wires and the cathodes in the beam region.

During the 1987–1988 run, the PTMs were aligned along the nominal beam axis as defined by the surveyors. The dead regions were lined up at the same Y and Z positions in each plane. The SMS chambers, in contrast, were centered on the actual beam profile (with all magnets on). This meant that the SMS chambers were not all at quite the same Y positions. SMS4 was positioned roughly 1 cm East of SMS1. During the 1990 run, the PTMs were moved to follow the actual beam rather than the nominal beamline. This yielded a better overlap between the SMSs and PTMs.

The effective efficiency of the PTM planes was somewhere in the range 90–95% per plane during the 1987–1988 data run. This number refers to the probability that the hit occurred in at least one cell of the plane. Several effects contributed to this inefficiency. Perhaps the most important was a subtle inefficiency in the readout electronics, which was not detected until after the run. Due an improperly terminated latching signal, each readout card would fail to latch any signals about 5% of the time. Even if a muon generated two hits, these hits were usually both on the same readout card and would simultaneously fail to latch. Since this problem occurred for an entire readout card simultaneously, rather than for a single channel, it decreased the overall per plane efficiency by about 5%. This effect was quantified and fixed before the 1990–1991 run with the help of the PTM Pulse Injection System which was designed in 1985 and redesigned, built, and implemented in 1989. This pulse injection system was capable of generating test signals on the PTM wires in a completely arbitrary pattern. This allowed the PTM readout system to be more fully debugged for the 1990–1991 data-taking run. Additionally, there was some evidence for a few percent inefficiency of the chambers themselves near the beam. This was consistent with the dead time associated with the high rates seen near the edge of the live region. This effect was partially alleviated for the 1990–1991 run by moving the PTMs so that the PTM dead regions were more fully centered on the beam.

PTM History

The PTM chambers were built by the MIT collaborators in E665 well before the 1987-88 run. The readout system was designed by the UCSD collaborators using Nanometrics brand readout cards and data scanners and some UCSD-designed custom logic boards. The power supplies were handled by MIT and UCSD in conjunction. The gas supplies and interface to the E665 Data Acquisition system were handled by MIT. The entire readout system was debugged and implemented in time for the 1987 data-taking run, with some design changes by MIT. My primary responsibilities regarding the PTMs during the 1987 run were to interface the PTMs to the E665 Data Acquisition system and to help in the installation of the electronics and maintenance of the overall PTM system. During the 1990 run, I was responsible for the entire PTM system. Details of the the 1990–1991 PTM upgrades can be found in Section 3.9.

3.6 Electromagnetic Calorimeter

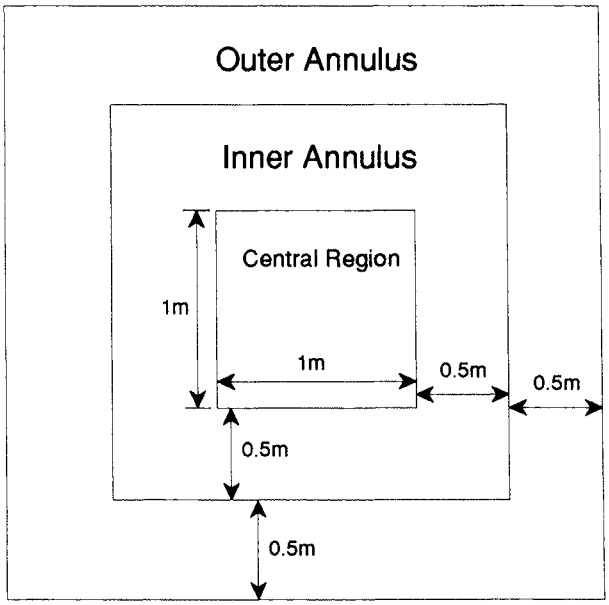

Figure 3-4: The Calorimeter.
This diagram, which is drawn to scale, shows a cross-section of the E665 Calorimeter. The beam direction is into the page and the Calorimeter is approximately centered on the beam. The three regions shown in the drawing contained different pad sizes, as described in the text.

The Electromagnetic Calorimeter (CAL) was designed to detect electromagnetically active particles, specifically electrons and photons, which were generated in the event.

The Calorimeter was located just upstream of the Steel Absorber, downstream of all of the Forward Spectrometer tracking chambers. The Calorimeter consisted of twenty planes of Lead interspersed with twenty wire chamber planes. Each plane of Lead was 5 mm thick. The material in one wire chamber plus one plane of Lead amounted to about one radiation length. The active area of the calorimeter was 3 m $\times$ 3 m. The wire chambers alternated between $Y(0°)$ views and $Z(+90°)$ views. The anode wires were read out in groups of sixteen adjacent wires, except for the four planes closest to the shower maximum where the wires were read out individually in the central 1 m of the detector and in pairs in the outer regions. The cathode planes were split into 1188 pads, and read out as towers summed over all planes.

A cross-section of the Calorimeter face is shown in Figure 3-4. Each Calorimeter plane was divided into three different regions: 1) a *central region* which was 1 m $\times$ 1 m, 2) an *inner annulus* which was outside the 1 m-square central region, but inside a 2 m square, and 3) an *outer annulus* which covered the rest of the Calorimeter. The pad size was different for each region: 4 cm $\times$ 4 cm in the central region, 8 cm $\times$ 8 cm in the inner annulus, and 16 cm $\times$ 16 cm in the outer annulus.

Using the pads in the central region, the position resolution for a given cluster was 1–2 cm, while the two cluster resolution was about 12 cm. Using the wires, the two cluster resolution was about 4 cm. The energy resolution of the calorimeter was given by: $\frac{\Delta E}{E} \sim 0.07 + 0.45/\sqrt{E}$ where E is the cluster energy in GeV.

The Electromagnetic Calorimeter was used in many analyses. The most common use was to remove events which were due to QED Bremsstrahlung from the muons or to elastic scattering from atomic electrons in the target. The Calorimeter was also useful in removing electrons from the hadron sample and in detecting neutral energy in the event due to photons or neutral pions.

It has been estimated that the Calorimeter intercepts roughly 95% of the photon energy in the event [31]. More details about the Electromagnetic Calorimeter can be found in References [31, 32].

3.7 Miscellaneous Detector Elements

There were several remaining detector elements which were **NOT** directly used in the analysis contained in this thesis. They are mentioned here for completeness. These elements fall into two classes. The first class consisted of four particle identification detectors: a Ring Imaging Čerenkov detector (RICH), two threshold Čerenkov detectors (C0, C1), and a Time of Flight detector (TQF). The second class consisted of two detectors (SC, PTA) which served to increase the acceptance for tracking parti-

cles. The Proportional Tube Arrays (PTAs) were wide angle tracking chambers which could track particles down to roughly 2 GeV. These chambers were also important for the TOF analysis. The Streamer Chamber (SC) covered a solid angle around the target of almost 4π steradians, handling any particle with an angle to the beamline under 150°. The SC, however, had a long dead time and was only able to take a fraction of the luminosity available to the rest of the detector. None of these six detector elements (RICH, C0, C1, TOF, PTA, SC) were used in the analysis contained in this thesis. All of these elements are discussed in more detail below.

3.7.1 Čerenkov Detectors

The C0 system was a threshold Čerenkov detector with with the pion, kaon, and proton momentum thresholds at 2.6, 9.3, and 17.6 GeV respectively. The average number of photoelectrons from a $\beta = 1$ particle was approximately fifteen.

The C1 system was a threshold Čerenkov detector with with the pion, kaon, and proton momentum thresholds at 4.3, 15.3, and 31.0 GeV respectively. The average number of photoelectrons from a $\beta = 1$ particle was approximately ten.

The RICH system was a Ring-Imaging Čerenkov detector with an active area of 3.7 m × 2.7 m. During the 1987-1988 data-taking period, the expected π/K resolution was 2.8σ at a momentum of 70 GeV, and the expected $(\pi, K)/p$ resolution was 3.7 σ at 110 GeV. Unfortunately, the RICH system did not really achieve stable successful running conditions and has not been used in any physics analyses.

3.7.2 TOF: Time of Flight Chambers

The Time of Flight system consisted of two hodoscope walls and a start counter. The hodoscope walls were situated so as to intercept low momentum ($p < 6$ GeV) particles which left the CVM at a wide angle to the original beam direction. Each wall consisted of thirty-eight counters and covered a sensitive area of 4.2 m × 1.6 m. Each counter was overlapped with its neighbors to ensure that there were no gaps. The counters varied in width from 10–15 cm and in thickness from 1.5–4 cm. These TOF walls were not oriented perpendicular to the beam, but were rotated by about $\frac{2}{3}$ radians (or ±38°) about the Z-axis. The start counter was installed in the beam just downstream of the first station of the beam spectrometer. It was segmented into 5 scintillators of unusual shape. The sensitive area was approximately an ellipse with a diameter of 0.155 m in the Y direction and 0.120 m in the Z direction. With this system it was possible to identify protons reliably in the momentum range from 0.3–2.5 GeV.

3.7.3 PTA: Wide Angle Proportional Tubes

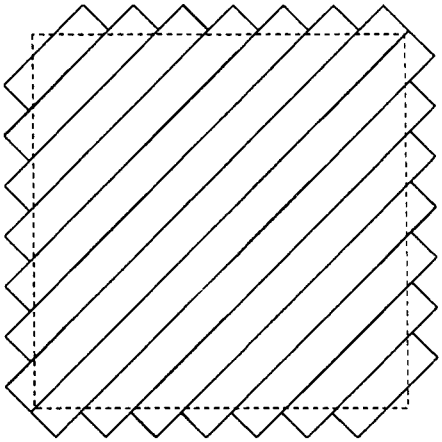

Figure 3-5: A PTA Diagonal Plane.
This diagram shows the arrangement of modules in a PTAU or PTAV plane. The diagonal rectangles represent the modules and correspond to the average position of the back and front layers of each double-layer module. The dotted-line square measures 2.0 m × 2.0 m and shows the approximate active area of the plane. This figure is drawn to scale.

There were two arrays of proportional tubes (four planes each) located behind the TOF system. These chambers detected low momentum particles (typically 2–8 GeV) which were swept out to wide angles. The PTAs were used to calibrate the TOF chamber and were also used in the analysis of the TOF. Their construction was similar to the PTM chambers described in section 3.5.3, but they were different in size and orientation. The PTA aperture was approximately 2 m × 2 m. Each array contained four planes, and each plane had two layers of wires. The PTA planes were oriented in the following views: $Z(+90°)$, $Y(0°)$, $U(+45°)$, and $V(-45°)$. It should be noted that these chambers were not parallel to the beam, so that U^*, V^*, and Y^* refer to the local coordinates of the PTA system and not the usual E665 coordinate system. The PTAs were rotated by ~ 0.34 radians ($19\frac{1}{2}°$) from being perpendicular with the beam axis. This rotation was about the Z-axis.

The PTA chambers were constructed in modules having the same cross-section as the PTM modules. The PTA modules, however, were significantly shorter in length than the PTM modules. The PTA Y- and Z-planes were made of modules which were 2.0 m long. The Y-planes measured 1.9 m × 2.0 m while the Z-planes measured 2.0 m × 1.9 m The PTA U and V-planes were approximately square, but were made up of modules oriented parallel to a diagonal of the square (see Figure 3-5). These modules varied in length from 0.6–2.9 m. The electronic readout system for the PTAs was very similar to that for the PTMs.

The PTAs suffered from noise problems that did not plague the PTMs. The PTA

threshold was set considerably higher than that of the PTMs (roughly 5 times as high), although the high voltage was the same (2.7 kV). Despite this fact, the PTAs would occasionally oscillate, causing all of the wires in a single plane to fire simultaneously. This happened in roughly 10% of the events. The PTAs were particularly useful in the physics analyses which also used the TOF.

PTA History

The PTAs were built and instrumented by the MIT collaborators on the experiment, including myself. The electronics were designed by UCSD collaborators and were redesigned and implemented by the MIT collaborators with help from the Wuppertal[4] and Freiburg[5] collaborators.

3.7.4 SC: Streamer Chamber

The Streamer Chamber (SC) was used previously by the EMC Collaboration [33] at CERN. It surrounded the target almost completely, allowing acceptance for particles scattering up to 150° from the beam direction. However, the Streamer Chamber had a dead time of almost 700 ms per event, whereas the data acquisition system had a dead time of only 2–3 ms. Because of this, information from the Streamer Chamber was only available for a fraction of the events which were written to tape. For this reason, a special set of triggers were used to trigger the Streamer Chamber. These triggers are described in Section 3.8.3.

3.8 Triggers and Data Acquisition

Physics, calibration, and monitoring triggers ran simultaneously during the data-taking. The motivation for and implementation of the physics triggers used during the 1987-88 data-taking run are described in this section.

The E665 muon beam energy was about twice that of previous muon beams, and there were two natural strategies that could have been employed to exploit this advantage. The first strategy would have been to examine events at high W^2 (up to around 900 GeV^2) and moderately high Q^2 (above 2 GeV^2). The second strategy would have been to examine events with very low x_{Bj} (down to around 2×10^{-5}),

[4]University of Wuppertal, Wuppertal, Germany
[5]University of Freiburg, Freiburg, Germany

but allowing fairly low Q^2 events (down to 0.01 GeV^2). In fact, E665 employed both strategies by having two complementary primary physics triggers during the 1987-1988 data taking run. The Large Angle Trigger (LAT) was optimized for the high W^2, moderately high Q^2 events. The Small Angle Trigger (SAT) was optimized to accept low Q^2 events, extending our reach to very low x_{Bj}. The SAT, however, was only able to accept a fraction of the luminosity, mostly due to the fact that the cross-section for DIS rises rapidly at low Q^2.

In addition to the LAT and SAT, several other triggers were used. A complete list of triggers that could occur during the spill is found below:

LAT Large Angle Physics Trigger,

SAT Small Angle Physics Trigger,

FCAL Calorimeter-based Physics Trigger,

PCLAT LAT with a PC hit multiplicity requirement,

PCSAT SAT with a PC hit multiplicity requirement,

PSLAT LAT randomly prescaled by a factor of 16,

PSSAT SAT randomly prescaled by a factor of 64,

RBEAM Random Sampling of the Beam available to the LAT,

RBSAT Random Sampling of the Beam available to the SAT,

HALO Halo Muon Trigger.

The following subsections describe these triggers in more detail. It should be noted that only the LAT data were used in this thesis.

3.8.1 LAT: Large Angle Trigger

The LAT trigger was conceptually quite simple. One attempted to trigger on an in-time beam muon which was scattered out of the beam. The hodoscope elements in the beam spectrometer provided fast signals detailing the muon's behavior before the target, while hodoscope elements in the muon spectrometer provided fast signals detailing the muon's behavior downstream of the target. For a beam muon which would have passed through the center of the PTM/SPM dead region, the LAT trigger demanded a minimum scattering angle of 3–4 mr.

The LAT requirements were:

- At least one in-time beam muon;
  - ⋆ 7/7 SBT coincidence
- No in-time halo muon;
  - ⋆ Event vetoed if SVW fired in the current, previous, or following bucket
  - ⋆ Event vetoed if any SVJ fired in the current bucket
- A scattered muon outside of the beam;
  - ⋆ 3/4 coincidence of SPM-top OR SPM-bottom
- No unscattered muon.
  - ⋆ Event vetoed if (SMS1Y AND SMS1Z) OR (SMS4Y AND SMS4Z)

The LAT was inefficient in some regions of the scattered muon phase space due to timing problems with the SPM signals [34]. The events should be isotropic in the azimuthal angle of the scattered muon in the E665 coordinate system, but they aren't. This feature was not modeled in the Monte Carlo. We should be alert to possible systematic effects from this asymmetry (see Section 5.5.2).

3.8.2 SAT: Small Angle Trigger

The SAT was considerably more sophisticated than the LAT. It incorporated a technique known as a *floating veto* in order to trigger on a whole class of interesting events at low x_{Bj} and low Q^2 that the LAT couldn't trigger on. Individual scattered muons at small angles ($\theta < 3$ mr) typically didn't leave the overall beam profile. The SAT trigger used the SBT signals to define a beam trajectory and consulted a fast electronic lookup table to predict the location of an unscattered muon in the SMSs. The appropriate SMS counters were then used to veto unscattered muons. The veto region in the SAT trigger was smaller than that in the LAT and the veto was moved (or floated) on an event-by-event basis according to the beam trajectory. The SAT veto region was a rectangle of dimension: 5 cm $\times$ 20 cm. The acceptance at $\theta = 1$ mr was roughly 50%. The SAT only used a limited portion of the beam phase space: 12% of that seen by the LAT.

The SAT requirements were:

- One and only one in-time beam muon in the limited phase space;

  - ⋆ 7/7 SBT coincidence, with only the central five counters used for SBT3Y, SBT3Z, SBT4Y, and SBT4Z.
  - ⋆ Veto on beams in the outermost counters of SBT3Y, SBT4Y, SBT4Z.

- No beam muon in neighboring (previous or following) accelerator buckets;
- No unscattered muon.
  - ⋆ event vetoed if there was a hit in the SMS1Y or SMS2Y that was too close to where an unscattered muon was predicted to go.

It should be noted that the SAT trigger had no positive scattered muon requirement.

During the 1987-88 data-taking run, only one target was in place at a given time, and this target was inside the CVM. This meant that the focusing geometry of the double-dipole spectrometer didn't really work perfectly. In particular, particles which originated from a vertex inside the CVM didn't really focus on the first PTM plane. The focal plane of the spectrometer depended upon particle momentum. The SAT trigger was significantly affected by this achromatic[6] focus. Furthermore, this effect varied with the vertex position, complicating both the triggering and the acceptance calculation. Scattered muons which originated from a vertex in the upstream end of the target were better focused than those that originated in the downstream end. The main effect caused by the target being inside the CVM was that the LAT and especially the SAT contained a higher proportion of junk triggers which were not due to muon scattering events. These junk triggers were removed during the analysis (see Section 4.2).

3.8.3 Other Triggers

Since the Streamer Chamber dead time limited its data-taking rate to about 1.5 Hz, we triggered it separately from the rest of the apparatus. Whenever the Streamer Chamber was triggered, the entire apparatus was also triggered, but the converse was not true. Two different triggering philosophies were employed for the Streamer Chamber. The primary philosophy was that we sought to increase the purity of the physics (DIS) sample seen by the SC at the expense of allowing some bias and inefficiency. This was accomplished by requiring a minimum hit multiplicity in the PCN chambers away from the beam region and out of the magnetic bend plane. The

[6] A momentum-dependent focus in charged particle optics is analogous to an energy-dependent, or achromatic, focus in conventional optics.

secondary philosophy, used primarily as a cross-check, aimed to minimize the bias. This was accomplished by simply prescaling the usual physics triggers. The regular LAT and SAT triggers were used as a basis for both philosophies.

Overall, there were four SC physics triggers:

PSLAT: LAT prescaled by a factor of 16.

PSSAT: SAT prescaled by a factor of 64.

PCLAT: LAT with a PCN hit multiplicity requirement.

PCSAT: SAT with a PCN hit multiplicity requirement.

All of these triggers were implemented as distinct Level-2 triggers based on the normal LAT or SAT as a Level-1 input. These special triggers were only used by the Streamer Chamber.

There was an additional physics trigger called the FCAL which was designed to check for inefficiencies in the other triggers and to be used in calibrating the Calorimeter. The FCAL trigger demanded that there be one in-time beam, no halo muon, and a total energy of at least 60 GeV in the Calorimeter outside of a 32 cm wide cross centered on the beam. It also required that there be energy in each of two opposite quadrants. Furthermore, the trigger vetoed if a muon arrived in any of the 15 buckets preceding the trigger-beam. This was necessary because of the memory time of the Calorimeter. The electronics of the FCAL trigger were not properly timed-in for the Deuterium and Xenon data. Therefore the FCAL trigger was only usable for the Hydrogen data and wasn't used in this thesis.

There were two triggers designed to select events where an in-time beam went through the Beam Spectrometer, whether the beam interacted in the target or not. These triggers were known as Random Beam (RBEAM) triggers. These beam triggers were used for various studies, including beam normalization and physics trigger efficiency studies. These triggers corresponded to the beam component of the LAT and the SAT triggers (see pages 84 and 85) and were known as RBEAM and RBSAT respectively. The RBEAM trigger required at least one in-time beam muon and no in-time halo muon and was prescaled by a factor of 2^{18} (for the Deuterium running). The RBSAT trigger required that there be one and only one in-time beam in the limited SAT beam phase space, demanded that there be no beam muon in neighboring accelerator buckets, and was prescaled by a factor of 2^{16}. The prescaling for the two triggers was deliberately correlated so that there was a significant overlap between the RBEAM and RBSAT samples.

There was also a HALO trigger which triggered on Halo muons outside of the usable beam phase space. This trigger was used to continuously monitor the chamber

alignment and efficiency and for diagnostic purposes. This trigger required a coincidence of the upstream veto wall or jaws and 3/4 of the SPM planes downstream of the absorber. Furthermore, this trigger was prescaled by a factor of roughly 20.

3.8.4 Data Acquisition

The E665 trigger logic was arranged in two levels, although for the 1987-88 data run, most of the Level-2 triggers were trivial copies of the Level-1 triggers. This two-tiered structure was used in order to allow for the possibility of more sophisticated Level-2 triggers which would take more time than the simple Level-1 triggers. The Streamer Chamber triggers fell into this category during the 1987 run and there were several Level-2 triggers during the 1990–1991 run. When a Level-1 trigger occurred without a subsequent Level-2 trigger, this resulted in a 2–3 μs/trigger dead time. When a Level-2 trigger occurred, this resulted in reading out the apparatus, which implied a dead time of 2–3 ms/event. We limited the Level-1 dead time to 10% by keeping the Level-1 trigger rate below 4×10^4 Hz. We limited the Level-2 dead time to 20% by keeping the Level-2 trigger rate below 80 Hz.

The Data Acquisition (DA) system [35] consisted of three front-end PDP-11/34s, six parallel CAMAC branches (two per PDP-11/34), a FASTBUS system, a serial CAMAC branch, and a μVAX II. The parallel CAMAC branches were used to read out the bulk of the data. The FASTBUS system was used to read out the Calorimeter. During a typical event the three PDPs and the FASTBUS system were read out in parallel, taking about 2–3 ms. This data was stored in bulk memory on the PDP UNIBUS and in the FASTBUS LRS1892 memory module. Asynchronously, the μVAX II read the buffered information over DR11W links, concatenated the data from all four sources into single events, and wrote the information onto 6250 bpi tapes. The system was capable of acquiring and logging data at an average rate of 250 kbyte/s. The event size was typically just under 10 Kbyte/event and the peak trigger rate was roughly 80 Hz. Therefore, the peak data-taking rate was about 750 kbyte/s. The asynchronous nature in which the events were logged to tape allowed us to store a backlog of events during the 22 s spill which were then written to tape during the 35 s interspill period.

In addition to normal events taken during the spill, specialized interspill monitoring/calibration events could be triggered and written to tape during the interspill period. These interspill events could be generated on the PDPs or on dedicated stand-alone microprocessor systems.

The various sub-detector systems were monitored and periodically calibrated. Monitoring and calibration took many forms. One form of monitoring was by a group of programs called Consumers which were specialized by detector subsystem

(e.g. the PTM Consumer). A Consumer ran on the VAX 11/780 and could copy events out of the data stream and analyze them. These could be normal events or specialized interspill events. The Consumer could also select events based on the triggers that they satisfied. Another form of monitoring involved immediate readback and standardized offline analysis of a subset of the raw data tapes shortly after they were written.

The PTM and PTA Consumers, for which I was responsible, were programs written in Fortran and used in the context of Fermilab's VAXONLINE and CONSUMER software. These consumers monitored the PTM and PTA pieces of the data stream and generated various sorts of wiremaps. Furthermore, they were capable of recognizing and dumping events that were strange in character, allowing us to find and fix hardware problems more quickly.

3.9 Detector Upgrades for the 1990–1991 Run

Several upgrades were implemented for the 1990–1991 Run and they will be outlined here. Particular emphasis will be placed on the DA and PTM Upgrades since I was involved in them. The 1990–1991 data sample was not directly used in this thesis.

The E665 upgrades for the 1990-1991 Run can be divided into six categories:

- Beam upgrades;
- Target system upgrades;
- New detector components;
- Trigger upgrades;
- Data Acquisition system upgrades;
- Maintenance and minor upgrades of existing detector components.

Most of these upgrades are described below. The maintenance and minor upgrades, however are not described, with the exception of the PTM system. The PTM detector system upgrades are described in some detail.

3.9.1 General Upgrades

The Muon beam intensity was increased for the 1990–1991 Run by a combination of improved tuning and increased primary proton beam luminosity. A side effect of the

new tune was that the beam trajectory through the apparatus changed slightly.

During the 1987–1988 run, only one target was in the beam at a given time and changing targets required shutting down the experiment for a day or two. This meant that targets were not changed very often. A given target was typically used for several weeks. This meant that time-dependent effects of chamber efficiencies and trigger efficiencies caused systematic errors in any comparison of different targets. In the 1990-1991 run, a sophisticated system was installed to allow the targets to be changed every spill, reducing the effect of any time-dependent systematic errors. In addition to having only one target available at a time during the 1987–1988 run, the target we did have was placed in the magnetic field. This was because it needed to be surrounded by the Streamer Chamber and this whole assembly needed to be in the magnetic field so that the Streamer Chamber could measure particle momenta. The fact that the target was in the magnetic field made triggering more difficult (especially for the Small Angle Trigger). In the 1990–1991 run, the target was placed upstream of the magnetic field both to simplify triggering and because it was easier and safer to operate the targets in a less confined region.

Several new chambers were added for the 1990–1991 run. The Streamer Chamber was replaced by a new set of chambers placed inside the CVM field called the VDCs (Vertex Drift Chambers). Like the Streamer Chamber, these chambers extended the acceptance of the Forward Spectrometer to include lower momentum tracks (less than 8 GeV). The VDC acceptance was not quite as complete as that of the Streamer Chamber, but unlike the Streamer Chamber, the VDCs were capable of being read out every event. In addition to the VDCs, there two packages of scintillator were added to the experiment. A small scintillator plane package, called the SVS (Small Veto Scintillator), was embedded in the downstream edge of the Steel Absorber in the beam region, just upstream of PTM1Y. This package was used in some of the large-angle triggers. A large double-layered wall of scintillator, called the SUM (Scintillator, Upstream Muon) Wall, was mounted upstream of the Steel Absorber and was also used for triggering purposes. An additional set of small wire chambers was added in the beam region, upstream of the DCAs to help track particles in the beam region. This package, called the PSC (Small Proportional chamber group C[7]) was similar to the PSA package described in Section 3.4.5. The PSC chambers were located just upstream of DC1.

In addition to new targets and new chambers, there were several new triggers which were used for the 1990–1991 run. The SAT trigger was upgraded to provide more rejection of junk triggers and to use a larger percentage of the beam phase space. Several new versions of the LAT trigger were generated to make use of the SUM wall and the SVS package and even the PTM chambers. One of these new LAT trigger

[7]An additional package known as the PSB was planned, but never implemented.

components was called the WAM2 (Wide Angle Muon Level 2) [36]. This trigger component used PTM signals as part of its input in order to search for a positive scattered muon signal (as opposed to vetoing on an unscattered muon). The WAM2 used target-pointing roads in the PTM chambers in order to determine whether there was a scattered muon. One of the immediate effects of the various trigger upgrades was that several non-trivial Level-2 triggers were used. This meant that chambers had to be prepared to take data if they saw a Level-1, but had to be able to quickly abort the readout if the Level-2 tests failed.

3.9.2 Data Acquisition Upgrades

The Data Acquisition system involved four major upgrades: the capability of writing Exabyte tapes was added, the main DA computer was upgraded, the DA computers were joined into a Local Area Vaxcluster, and the Fermilab VAXONLINE/DA software was upgraded. The first three of these upgrades are described below.

The Data Acquisition system was upgraded to include the capability of writing Exabyte tapes in addition to the conventional 6250 bpi tapes. The main advantage of this was increased storage density. We stored roughly 140 megabytes on a single 6250 bpi tape and roughly ten times that amount on an Exabyte tape. Furthermore, the Exabyte tapes were physically smaller and therefore easier to store and transport.

The main Data Acquisition Computer was upgraded from a μVax-II to a Vaxstation 3200, which is roughly three times as powerful in terms of raw computing power. This upgrade was performed because Don Geesaman concluded that the dead time was limited by the CPU (Central Processing Unit) power during the 1987 Run.

The various Vaxes and μVaxes in our Data Acquisition system were combined into a Local Area Vaxcluster. This allowed them to share resources more conveniently and also simplified the System Maintenance tasks.

3.9.3 PTM Upgrades and Changes

In addition to the various large upgrades mentioned above, there were small improvements to many of the existing chambers. For instance, several changes were made to the PTM system. These changes included:

- the redesign and implementation of the PTM Pulse Injection system,
- the modification of the system used to trigger the PTM readout,

- the correction of some inefficiencies in the PTM readout latching,
- a more complete deadening of the PTM dead regions,
- the implementation and debugging of fast-out signals needed by the WAM2 trigger component,
- a move of the PTM chambers so that the dead regions were centered more fully on the beam.

The implementation of the Pulse Injection System was the biggest change to the PTM system. A UCSD design for this Pulse Injection System already existed before the 1987 run, but was not implemented then due to time constraints. It was redesigned by a collection of people from Harvard (Prof. Richard Nickerson, Mr. Howard Hill), MIT (Mr. Mark Baker), and UCSD (Dr. Hans Kobrak, Mr. Allen White). It was built and implemented by me with help from UCSD, MIT, Harvard, and Fermilab. This system was designed to be able to apply a completely arbitrary hit pattern to the PTMs, firing any combination of the 3420 wires. The pulse height was adjustable on a plane-by-plane basis. The Pulse Injection system was run using software written in Fortran on a personal computer. This software communicated with the software on the Data Acquisition PDP-11/34 so that the Pulse Injection could not be fired during the spill when data-taking was in progress.

The logic used in triggering the PTMs (and the PTAs) had to be upgraded. There were two reasons for this. First, the new Pulse Injection system had to be able to trigger the PTM Readout for test purposes. Second, the Level-1 and Level-2 triggers were fully and distinctly implemented for the 1990 Run, whereas during the 1987 Run all of the Level-2 triggers seen by the main detector had just been delayed copies of the Level-1 triggers. During the 1987 Run, the readout process was initiated by any Level-1 trigger. During the 1990 Run, a Level-1 trigger merely froze the PTM and PTA readout systems, but did not initiate the readout process. After a Level-1 trigger, one of two things occurred: either a RESET signal or a Level-2 trigger. In the case of a RESET, the readout system was unfrozen and cleared and the wire outputs were again cycled into the memory chips. If, instead, a Level-2 trigger occurred, then the actual process of reading out the contents of the frozen wire memories was initiated. If neither signal occurred after a fixed amount of time, a RESET was assumed. The PTM system contained an additional complication relative to the PTAs. The PTM Level 1 trigger was an OR of the normal E665 Level 1 trigger and the Pulse Injection strobe signal. Similarly the Level 2 trigger was an OR of the normal E665 Level 2 and a delayed Pulse Injection strobe signal. This meant that the Pulse Injection system was capable of triggering the PTMs to read out.

Using the PTM Pulse Injection system, we discovered and fixed several small problems with the PTM readout system. There were some bad electronics channels

that needed to be fixed. These problems occurred at several different levels: single channels, four-channel groups (single chips), fifteen-channel groups (single readout cards), and even one seventy-five channel group (due to a bad motherboard). All of the problems that involved groups of adjacent channels were fixed along with many of the individual channels. A few percent of the individual channels remained bad. Since neighboring cells overlapped, an isolated bad channel did not really affect the efficiency of the plane very much. In addition to the bad channels, we discovered a more global problem: 5% of the time the entire card failed to latch any PTM signals into the memories, causing a 5% overall inefficiency in the PTM readout. This problem was initially traced to the Write Enable signal that latched all of the memories on a given plane. Widening this Write Enable pulse removed the inefficiency ($1 - \varepsilon < 0.1\%$) except for a few modules at the edge of the planes which remained inefficient at the 1–3% level. Later, during the 1990–1991 run, the problem was fixed more completely [37]. It was discovered that the Write Enable pulse was improperly terminated, and that widening the signal had been a kludge rather than a fix. When the signal was properly terminated, the global inefficiency vanished completely.

Some improvements and changes to the PTM chambers and electronics were necessitated by the requirements of the WAM2 trigger described in Section 3.9.1. The PTM dead region needed to be further deadened and the fast-out signals from the PTMs needed to be fully implemented and debugged.

The PTM dead region was not made completely dead during the 1987–1988 run. The efficiency was shown to be $< 5\%$ for the eleven wires in the center of the beam-hole modules and $\sim 20\%$ for the remaining four wires. A study showed that PTM signals from the beam region would have caused too many false WAM2 triggers [38]. Therefore, the beam regions were deadened completely for the 1990–1991 run by coating the wires in the dead region with Corona dope[8] and the walls of the chambers with Kapton tape and Corona dope.

In order to connect to the WAM2 trigger, the PTM readout cards contained an extra output for each wire, called a *fast-out*. These fast-outs were accessible on a 17-pair header which contained 16 differential-ECL signal pairs, one for each wire plus a fast-or of all 15 wires in the module. There was also an empty pair on each fast-out header. All of the signals for a given PTM plane were routed via twist-and-flat cable to a set of headers on a single patch panel for that plane. These signals were not used during the 1987–1988 run because the WAM2 trigger, although planned, was not implemented at that time. This meant that during the 1987–1988 run the readout cards were connected to unterminated twist-and-flat cables. When the signals were used and terminated during the 1990 run, three things were discovered: the readout

[8]This is an insulating material designed to prevent sparking and corona discharge in high voltage applications.

PTM bay	$\Delta Y = Y_{90} - Y_{88}$
PTM1	- 2 $\frac{2}{32}$ "
PTM2	- 2 $\frac{7}{32}$ "
PTM3	- 2 $\frac{15}{32}$ "
PTM4	- 2 $\frac{16}{32}$ "

Table 3.2: PTM Position Changes for the 1990–1991 Run.

cards were less noisy when these signals were terminated, several of the fast-out channels were defective, and there was a design mismatch between the PTM outputs and WAM2 inputs. Since the PTMs were already efficient enough, it was decided to run the PTMs at the same threshold voltage during the 1990–1991 run as during 1987–1988 run, not taking advantage of the quieter cards. The bad fast-out channels were fixed. The design mismatch was solved by a Harvard-MIT redesign of the PTM fast-out patch panels (Janet Conrad, Mark Baker, Richard Nickerson).

In addition to all of the above changes, the PTMs needed to be moved slightly for the 1990–1991 run. The main reason for this was that the PTM dead regions weren't quite centered on the muon beam during the 1987 run. This was more important in the 1990–1991 run because the beam intensity was increased. Another reason for the PTM move was that the beam position moved slightly when the intensity was increased. The PTM chambers were moved by the amounts shown in Table 3.2 in the Y-direction[9] in order to center the dead regions on the new beam position. It should be noted that the Y- and Z-planes in a given bay were moved by the same amount so that their dead regions continued to overlap. After the move, the rates on the most active PTM wires[10] reached 0.15 MHz for a beam intensity of 2×10^7 muons/spill. The PTM2Z chamber was also shifted in the X-direction by $-\frac{7}{8}''$ in order to accommodate some shielding that was added to SMS2.

3.9.4 Summary of Upgrades

Several changes were made to the overall apparatus for the 1990–1991 Run in order to improve the performance and increase the statistics. These upgrades were quite broad in extent, including the beam, the target, the trigger, the data acquisition system, and the implementation of new detector components, as well as maintenance and upgrades to the existing systems.

[9]The negative Y-direction corresponds to an eastward move.

[10]The most active PTM wires were the Y-wires adjacent to the dead region.

3.10 Summary

The Fermilab E665 Experiment was designed to study deep inelastic muon scattering at a high center-of-mass energy (W^2). The experiment ran during the 1987 fixed target run at a beam energy of 490 GeV. The data for this thesis were taken using the large-angle trigger (LAT) which emphasized high W^2 and high Q^2 events. The W^2 range used in this thesis was 200–1000 GeV^2 while the Q^2 range was 2–100 GeV^2.

Chapter 4

Event Reconstruction

The Raw Data stored on tape consists of very basic information about the detector response for each event. This information is in the form of simple digital quantities such as latched bits, pulse heights, wire addresses, and TDC values. This simple information is fairly far removed from interesting physical quantities such as event kinematics and particle momenta. Furthermore, the raw data contains a lot of events that aren't usable because they are due to false triggers, due to an uninteresting process, or they are in a kinematic range where our detector acceptance or kinematic resolution is poor. For these reasons it took a lot of work to reduce the raw data to a form where physics analyses could take place effectively. Since the problems and logistics of the basic data analysis were common to all physics analyses, several stages of the data analysis were performed by the E665 collaboration as a group. These included:

- overall alignment and calibration of detector elements,
- splitting off of the different trigger types,
- filtering out events that were due to junk triggers,
- decoding and translating the digital detector responses into *hits* corresponding to particle positions,
- pattern recognition to associate hits with particle trajectories or *tracks*,
- track fitting to extract momenta and charges of the particles from their tracks,
- removal of duplicate tracks,
- identification or *matching* of the muons in the event,

- finding of the primary event vertex,
- removal of unusable events,
- the analysis of the Calorimeter information.

These basic analysis steps are described in Sections 4.1–4.5 of this chapter.

After this common E665 analysis, we were left with a collection of tapes known as DR (Data Reduction) tapes. The analysis contained in this thesis is primarily unique in how the information on those tapes was further analyzed. This private analysis included tighter cuts to decide which events were kept in the sample and which tracks and clusters were used in a given event. Sections 4.6–4.8 of this chapter describe the event, track, and cluster cuts. Section 4.9 describes the use of the Monte Carlo Program. Finally, Section 4.10 summarizes the main points of this chapter, describing the basic data sample and the most important cuts. The actual physics analysis and results are contained in Chapter 5.

4.1 Alignment and Calibration

The original E665 coordinate system used by the surveyors was defined so that the X-axis was the nominal muon beam line. This line passed through the center of the CVM and 2" west of the center of the CCM. The X=0 point on the line was defined by the center of the CCM. This means that the center of the CCM was at $X = 0$, $Y = -0.0508$ cm, $Z = 0$ in the original coordinates. The spectrometer elements were optically surveyed with respect to this coordinate system. Figure 3-2 on page 70 shows the E665 Detector with the directions of the X and Y axes included.

The coordinate system actually used by the E665 software came from the results of the Alignment program. In this program, the survey information was treated as merely a first approximation to the actual position. Special alignment data-taking runs were made with the spectrometer magnets off. These provided straight-line muon tracks which were used by the Alignment program to generate a set of constants which described the various chamber positions. The rationale behind this approach was that, in principle, software alignment allowed better precision in measuring the Y and Z positions than the original survey did.

In order to perform this software fine-tuning of the alignment, however, some assumptions had to be made as to which information was the most reliable. The survey values were taken for the X-positions of all of the chambers. The β and γ angles, which measured how perpendicular the chambers were to the beam, were ignored in

Detector	X (in m)			ΔY (in mm)		
PBT3–4	-26.4	$\pm$	10.0	0.5	$\pm$	0.5
PCV	-8.6	$\pm$	0.1	0.5	$\pm$	0.5
PCF	-1.5	$\pm$	1.8	5.0	$\pm$	1.0
DC	8.0	$\pm$	4.7	8.5	$\pm$	0.5
PSA	13.0	$\pm$	0.04	7.0	$\pm$	1.0
PTM	20.9	$\pm$	2.5	10.0	$\pm$	3.0

Table 4.1: The Shift in the Alignment Constants from the Surveyed Values.
This table shows the X-position and the change in the Y-position from the survey values for each detector element. The error bars in X refer to the *extent* of the detector element in X. The error bars in ΔY refer to the *spread* of ΔY values. The Δy values were taken from Reference [39].

most cases and set to zero. It was assumed that the positions and the wire orientations (α) of the last two beam chamber stations (PBT3 and PBT4) were exactly correct as measured by the survey. Given the above assumptions, the constants that describe the positions of the other chambers were corrected so that the halo and beam muons traced straight lines in the detector when the magnets were off. This means that the coordinate system used in the E665 software may differ from the E665 survey coordinate system by a small translation and rotation. In fact, it is likely that these coordinate systems differ because the PTM survey numbers and the PTM software constants differed by 7–13 mm in Y. It is unlikely that the original survey was off by a full centimeter. It should be noted that the PTMs were the chambers which were farthest from the PBTs and were therefore the most sensitive to any rotation between the E665 survey coordinate system and the software coordinate system.

The difference between the original survey constants and the new (software) alignment constants is summarized in Reference [39] Table 3.2. We can extract the shifts in the Y-position of various chambers from this table and plot them as a function of the chamber position in X. Table 4.1 (of this thesis) summarizes this information. It should be noted that the "errors" in this table do not really represent normally distributed errors. In the case of the X-position, the error represents the extent in X of the detector element, which typically contains several planes at different well-known positions in X. In the case of the Y-shift values (ΔY), the error represents the approximate spread of values as reported in Reference [39].

The values from Table 4.1 are plotted in Figure 4-1 as ΔY versus X. The line on the plot is the best least-squares fit straight line through all of the points, treating the spread in ΔY as an actual error and ignoring the errors in X. It is difficult to draw any strong conclusions from this plot, but if we took the line fit seriously, we would

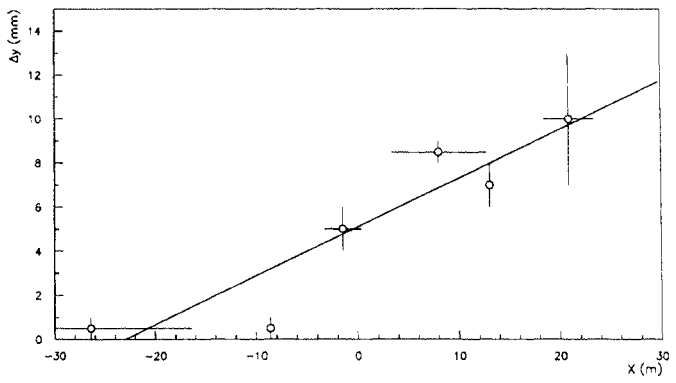

Figure 4-1: The Shift in the Alignment Constants from the Surveyed Values.
This figure shows the change in the Y-position of each detector element versus its X-position. The error bars in X refer to the *extent* of the detector element in X. The error bars in ΔY refer to the *spread* of ΔY values. The line in the plot is described in the text and is primarily intended to guide the eye. It corresponds to $\Delta Y = 5.1 \text{ mm} + 0.22 \cdot 10^{-3} X$.

conclude that the software X-axis was rotated by about 0.2 mr from the surveyors' X-axis. This rotation is quite large compared to the quoted resolution on the beam spectrometer angular resolution of 0.01 mr.

Another change that was made in software from the measured hardware values was that the wire spacing of the DCs was changed from of 50.8 mm (2") to 50.702 mm for the DCAs and 50.680 mm for the DCBs. The wire spacings of all other chambers were consistent with their known hardware values. The orientation angles (α) also changed slightly for the PBT, PCF and DC chambers as a result of the Alignment procedure.

Another change that was made in software was that the PCV and DCA chambers were believed to have moved in the Z-direction by $\frac{1}{2}$ mm when the magnets were turned on. This shift was applied to the constants used during the data taking.

In principle, these differences between the software coordinate system and the hardware coordinate system are not a problem. What matters is that the results are consistent and the detector position is correctly expressed in the software coordinate system. Reference [39] claims that there are no large problems in the alignment. Small alignment errors, however, are a possible source of systematic error in our physics measurements. This problem will be discussed in Section 5.5.3.

In addition to the overall detector alignment, several of the subsystems needed to be calibrated. This was accomplished using special runs with an electron beam and also by writing calibration information to tape during the interspill. The calibration

of the Electromagnetic Calorimeter, for instance, required both methods [32].

4.2 Split and Filter

The Split and Filter programs were the first two steps in the raw data analysis chain. They were designed to take a large number of raw data tapes and separate out the interesting physics events, leaving a more manageable set of physics tapes. The Split program also concentrated the calibration samples, making them more manageable as well.

Split

Events from all of the triggers described in Section 3.8 were written to tape sequentially in the order in which they physically occurred. Furthermore, interspill calibration events were written to tape during the off periods of the duty cycle (22 s on, 35 s off). This resulted in a complicated mix of triggers on each raw data tape. The Split program split the data from the raw tapes into tapes containing only one particular trigger or class of triggers. Unlike the Run '87 raw data tapes, the format of the split output tapes was machine-independent[1]. The trigger type for each event was determined by consulting the 128-bit trigger mask which was part of the raw data. This trigger mask consisted of bits which were latched copies of the various triggers as well as some information from the Bison Boxes on the front-ends. Several different output streams were used:

LAT	Large Angle Physics Trigger,
SAT	Small Angle Physics Trigger,
FCAL	Calorimeter-based Physics Trigger,
SC	All Streamer Chamber Triggers,
RBEAM	Random Sampling of the Beam available to the LAT,
RBSAT	Random Sampling of the Beam available to the SAT,
HALO	Halo Muon Trigger,
ISPL	All Interspill Triggers,
1%	A Random Selected 1% Sampling of all Input Events,
WASTE	Events where the Trigger information was not understood.

It should be noted that these streams were NOT mutually exclusive. Many events were output to more than one stream.

[1]The output tapes used the machine-independent ZEBRA format defined by CERN.

For the Deuterium (D_2) data, there were 12.9 M raw triggers of which 4.83 M were LAT triggers. Therefore the LAT Split program output sample amounted to 37% of the total number of raw triggers.

The "WASTE" stream consisted of events where the trigger word was garbled. These events could be due to a flaw in the Data Acquisition system or to an inefficiency in latching the trigger bits. For the Deuterium data, this output stream contained less than 0.01% of the total number of raw events.

Filter

Both the LAT and SAT split data samples contained many false triggers. Some of these false triggers were due to beam muons which interacted in some material in the detector other than the target (such as the calorimeter or absorber). Other false triggers were due to straight-through beam muons that were triggered on accidentally. A program was written in order to filter out good triggers from false triggers. At this stage, a good trigger was defined as any trigger which was due to an interaction in the target. These good triggers included purely electromagnetic target interactions (μe-scattering and γ bremsstrahlung) as well as the inelastic muon-nucleus interactions which the experiment was designed to study.

There were separate Filter programs for the LAT and SAT split samples. The philosophy behind both programs was to use tight cuts on the quality of the beam muon track and loose cuts on the quality of the rest of the event. Our loose event cuts were designed to reject events that were clearly junk rather than to select events that were clearly good. These programs were designed to minimize the loss of good events rather than to maximize the reduction factor. Tighter cuts were applied at a later stage in the analysis process.

The LAT filter program used a subset of the event reconstruction code (PTMV), described in Section 4.3. The filter required that there be one and only one reconstructed beam muon of good quality ($P_{\chi^2} > 0.01$) in the event. Furthermore, the single reconstructed beam muon was rejected unless it was determined to be in-time by having at least six out of the seven SBT hodoscopes associated with the track fire. It should be noted that the LAT hardware required all seven SBT hodoscopes to fire. Finally, the event was rejected unless the beam momentum was at least 300 GeV.

Any event that passed the incoming beam requirement was run through the primary filter. This primary filter attempted to eliminate events where the beam muon failed to scatter in the target. The program accomplished this by attempting to reconstruct tracks in the central region of the Forward Spectrometer (FS). Events with no reconstructed FS track or with more than one were kept. This was because we could

not prove whether they were good or bad at this early stage. Events with exactly one reconstructed FS track were tested further. The FS Track and the Beam Spectrometer (BS) track were then compared to see if they could be part of the same track. Since the two tracks were reported at different X-positions, this involved swimming the BS track downstream, through the CVM field, until we reached the X-position of the FS track. The event was eliminated if the incoming and outgoing muon track matched. In order to match, all of the following criteria had to be met for the tracks:

$$\begin{aligned} \Delta Y &< 1.0 \text{ mm} \\ \Delta Z &< 1.0 \text{ mm} \\ \Delta Y' &< 0.39 \text{ mr} \\ \Delta Z' &< 0.09 \text{ mr} \\ \Theta_\mu &< 0.29 \text{ mr} \\ \Delta p &< 50.0 \text{ GeV}. \end{aligned}$$

The variables ΔY and ΔZ are the differences in track locations, $\Delta Y'$ and $\Delta Z'$ are the differences in track slopes, Θ_μ is the angle between the tracks, and Δp is the measured momentum difference. These cut criteria correspond to roughly three times the rms values measured for beam particles using the RBEAM trigger.

In addition to the primary filter, described above, there was also a secondary filter which was meant to monitor the performance of the primary filter. It was designed to look for a positive muon signal in the PTM chambers. Only 50% of the events were run through the secondary filter. An event was kept if it passed either the primary or the secondary filter.

There were 4.83 M D_2 LAT events that were input to the LAT Filter program, and 1.48 M passed. Thus, the LAT Filter program kept 31% of the D_2 LAT events.

4.3 PTMV: Basic Event Reconstruction

Several of the basic analysis stages listed on page 97 were incorporated into a single program, known as the PTMV program. The acronym PTMV stands for "**P**attern recognition, **T**rack fitting, **M**uon matching, and **V**ertex processing program". The first task that this program performed was Decoding and Translation where the digital detector responses were converted into hits corresponding to particle positions. Next came the Pattern Recognition (PR) stage where hits were grouped into track candidates. Next came the Track Fitting (TF) stage where track candidates were fit with a quintic spline to yield a momentum measurement. During the Track Fitting

stage, some candidate tracks were augmented with PCV hits (PCV Hunt), had hits removed (Rescue and Superrescue), or were dropped altogether. The next stage was the Duplicate Track Removal pass. This procedure attempted to find cases where two or more nearly identical tracks were found and to keep only the best one. Next came the Muon Match (MM) stage where the forward spectrometer tracks were matched to the line segments in the PTM/SMS planes behind the steel absorber. This procedure allowed us to identify muons. The final stage in this process was the Vertex Processing stage (VX) where the tracks were fit to one or more vertices. The primary vertex included both the beam and scattered muon. Any other vertices were known as secondary vertices, and may have been due to a secondary interaction or particle decays. These PTMV stages are discussed in more detail below.

4.3.1 Decoding and Translation

Each detector subsystem (such as the PTMs or the PTAs) used a different method to encode the information that it obtained about the particles in an event. For this reason a separate decoder program was required for each subsystem. These decoders converted the information into a standardized format known in E665 as LDEC banks. In the case of wire chambers, the information was clustered so that if neighboring wires were hit they were reported as a single cluster. The LDEC bank then contained a wire number and a cluster size for each cluster and for each detector plane. In the case of the Drift chambers, the LDEC banks were not clustered. Each entry consisted of a wire number and a time slice number. For hodoscopes, each entry consisted of a counter hit, a pulse height value from an ADC, and a time slice value from a TDC. The RICH and the Calorimeter had their own special format for LDEC.

The translation of the data from decoded hits to coordinate values was where the Alignment and Calibration constants first entered into the data analysis. The translation subroutines converted the data from LDEC banks into another standardized E665 format known as LCOR banks. In the case of wire chambers, the LDEC clusters were converted to LCOR clusters using the alignment constants to associate wire positions with coordinates. In the case of the Drift Chambers, wire numbers and times were converted to positions based on a calibration curve. The Calorimeter and Time-of-Flight (TOF) chambers had their own special format for LCOR.

4.3.2 PR: Pattern Recognition

The basic task of the Pattern Recognition program was to collect hits into groups which corresponded to physically plausible candidate particle trajectories or *tracks*. The task of Pattern Recognition in E665 was broken up into several smaller tasks

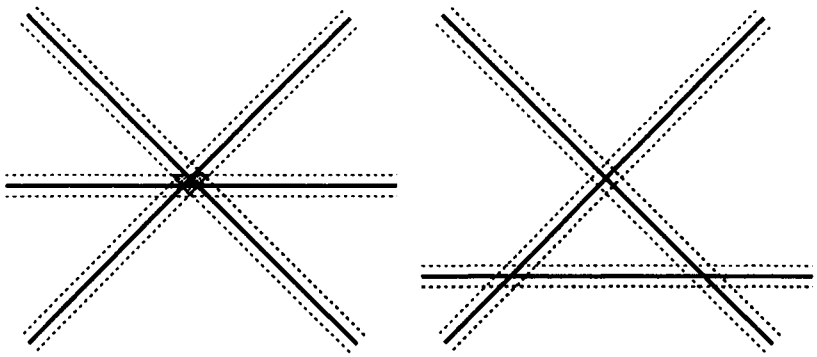

Figure 4-2: An Illustration of a Space Point.
Two different attempts to find a space point: a) successful, b) unsuccessful. The heavy lines represent the wires that were hit. The dotted lines delimit the range of possible values for the true hit coordinate. The shaded region in a) represents the reconstructed space point.

which were handled by software modules known as processors. Some of these processors performed local fits to space points, line segments, or curves and some of these processors matched local fits from other processors. The whole procedure was run in two global passes, allowing a tight set of cuts to pick up the high momentum tracks, especially the muon, and a looser set of cuts to pick up the remaining hadrons. Hits that were used during the first pass were dropped before the second pass was run.

General PR techniques

There were several general techniques used throughout the Pattern Recognition program. These included space point finding, projection finding, track segment matching, hit pickup, and fitting to curves.

Space point finding was a useful technique for chambers that included three or more planes at nearly the same X-coordinate. The basic idea was that a hit in a particular chamber constrained the particle that created it to lie in a given band. A combination of three hits from different views constrained a particle to lie on all three bands if it caused all three hits. If all three bands intersected at a single point (see Figure 4-2a), then this intersection point $\{X, Y, Z\}$ was called a *space point* and was assumed to have been caused by a single particle. It should be noted that space points had measurement errors associated with them due to nonzero resolution, so they weren't actually points. If the bands failed to intersect at a single point (see Figure 4-2b), then the hits must have been caused by different particles. At least three distinct planes were required to form a unique space point, but it was possible for space points to use more than three planes.

Projection finding was a technique that was used in regions where there was no

magnetic field. Given a group of planes which measured the same Θ coordinate at different X values, we fit groups of hits to a two-dimensional straight line in the X-Θ plane. We used a modified version of the CERNLIB subroutine `PTRACK` which we inherited from the EMC experiment at CERN.

Two more of the general techniques used in the PR program were track segment matching and hit pickup. These techniques both involved extrapolating track segments over a distance, in some cases through a magnetic field. The technique of matching involved extrapolating track segments in different regions of the detector towards each other to see whether they intersected or not. Hit pickup involved extrapolating one track segment towards another region of the detector to pick up isolated hits belonging to the track. Both of these procedures were complicated by the necessity of approximating the effect of the magnetic fields on these extrapolations.

In general, the task of fitting or projecting tracks of unknown momentum through a magnetic field was difficult. For a uniform magnetic field, the particle trajectory should be helical. Projecting a helical trajectory into the bend view (XY) yielded a circle and into the "non-bend" view (XZ) yielded a sinusoidal curve[2]. Because both of these projections are nonlinear, a full helical fit would have been time-consuming and would have required an iterative approach. For high momentum tracks, however, we could safely approximate the trajectory as a parabola in the bend view and a straight line in the non-bend view. Such a curve was easy to work with since a linear fit could be performed in both views and the two fits were independent. The subroutine `DHFIT3` was written for the purpose of performing such a fit. For tracks with momentum above about 50 GeV this fit worked quite well. Below this momentum the `DHFIT3` model began to break down [25]. The PR code continued to use `DHFIT3`, but applied corrections for tracks with a large curvature.

E665 PR Program Flow

The Pattern Recognition code was divided into four independent tasks:

1. Finding the beam track in the PBTs and associating the SBT hodoscope hits with the track;
2. Finding the muon projections in the PTM and SMS chambers;
3. Finding tracks in the Forward Spectrometer;
4. Finding Wide Angle tracks that never enter the CCM.

[2]Thus, the term non-bend is actually a misnomer.

If the program failed at the first task, finding the beam track, it aborted the event without attempting the other tasks. Similarly, if it failed to find a scattered muon, it aborted the event. If the beam and scattered muon were found successfully, then the program searched for tracks in the FS. This task was quite complicated because it involved linking hits from many different chambers residing in differing magnetic fields. The fourth task, finding Wide Angle tracks, resulted in tracks with hits in the PCVs, PCNs and PTAs. Since these tracks contained no hits in the CCM magnetic field, it was impossible to measure their momentum without the dangerous assumption that they came from the primary vertex. For this reason, Wide Angle tracks weren't used in this thesis. The Pattern Recognition tasks that were used in this thesis (BS, Muon, and FS) are described in more detail below.

The Beam Spectrometer stage of PR was performed by the PB processor. This processor found space points in each station and then grouped them together by fitting the projections. A valid beam track had to fit to a straight line through all four beam stations in the non-bend view (XZ). In the bend view (XY), the track had to fit to two line segments which intersected inside the NMRE magnet. After a beam track was found, the SB processor associated hodoscope hits with it.

The Muon Spectrometer stage of PR was designed to find XY and XZ projections in the PTM and SMS chambers. Since these chambers only consisted of Y and Z views, there was not enough information to associate the two-dimensional projections into three-dimensional tracks. Combining projections into tracks was done at a later stage (Muon Matching). The PM processor attempted to find projections in the PTMs and the SM processor in the SMSs. The OV processor then took all remaining PTM and SMS hits and tried to find more projections, allowing both PTM and SMS hits to coexist on the same projection. Some loose target pointing cuts were used in all three processors.

The Forward Spectrometer stage of PR was fairly complicated, and is described in the next few paragraphs. It started by finding some primitives from which to build tracks. In the DCs and PCs these primitives were projections. The DC processor found projections in the DCs and the PC processor found projections in the PCs. In the PSAs, which were all at roughly the same X-position, space points were used instead of projections. The PS processor found the space points in the PSAs. Similarly, the PV processor found space points in the PCV chambers.

These primitives, both line segments and space points, were then built into candidate tracks using three independent algorithms:

1. MA processor: Match PC and DC line segments through the PCFs, picking up hits.

2. PF processor: Project PC lines into the PCFs, picking up hits.

3. SF-SN chain: Find curved track primitives in the PCFs and project them out to the PCs, picking up hits.

The MA and PF processors were part of the original PR program design while the SF-SN chain was added later in order to improve the overall reconstruction efficiency.

The MA processor algorithm was designed to match line segments on opposite sides of the CCM magnetic field. This algorithm was based upon a principal components analysis of Monte Carlo tracks. This analysis yielded a set of parameters for the Y-projections (linear combinations of Y_{PC}, Y'_{PC}, Y_{DC}, and Y'_{DC}) and a range of acceptable values for these parameters. It yielded another set of parameters and a range of acceptable values for the Z-projections. The definitions of these parameters and the cut values were chosen before PTMV was run on the data. The MA processor used these parameters in order to find valid combinations of DC and PC projections with which to form a track. For each track candidate which passed the principal-components cuts, the MA processor formed roads along the track and attempted to pick up PCF hits along the roads. If it picked enough PCF hits, then the track match was considered a success. The track segments that were successfully matched were flagged and were not used in the PF processor or SF-SN chain.

The PF processor was designed primarily to pick up lower momentum (8–15 GeV) tracks that failed to make it all of the way through the CCM into the DCs. The PF processor took the track segments from the PC processor that were left unmatched by MA and performed a straight-line projection in the XZ view. In many cases this allowed the processor to pick up a Z-hit in the last PCF station (PCF5). If the processor did pick up such a Z-hit, it was used along with the PC track segment to determine a full helical trajectory for each hit in PCF5U and PCF5V. These helical trajectories were then used to pick up hits in the remainder of the PCF chambers. The best PC-PCF trajectory for the initial PC line was then fit using `DHFIT3`. If no Z-hit in PCF5 was picked up, the processor attempted to use PCF4 instead.

It was found that the MA and PF processors missed many PCF hits. This was primarily due to the fact that the algorithms relied on heavily on the PC chambers, requiring a complete PC line segment for each track. In retrospect, it is clear that the PCs should have been more efficient, or at least they should have been designed with more redundancy, given their importance to the reconstruction. In order to recover some of the unused PCF hits, the SF-SN chain was developed. The SF processor took PCF hits that were not used by the MA processor and found space points with them. It then collected them into curved track primitives through a convoluted algorithm which involved several approximations. This algorithm is discussed in Reference [25]. The SN processor took the PCF trajectories from SF, projected them into the PCs using `DHFIT3`, and picked up valid PC hits. This allowed us to reconstruct tracks that would otherwise have been lost.

The tracks found by the PF processor and the SF-SN chain contained some overlap, so some arbitration was required. If two such tracks shared too many hits, then the track with the least number of hits was dropped. If the tracks had an equal number of hits, then the track with the better P_{χ^2} (according to the DHFIT3 χ^2 model) was kept.

The final set of processors attempted to add DC, PSA and PCV hits onto the existing track segments. Any such hits (which were correctly assigned) improved the momentum resolution of the track. The MD processor projected PCN-PCF track segments from both the PF and SF-SN chains into the DCs using DHFIT3. First, the processor attempted to match the PCN-PCF segment to an unused DC track segment. Second, the processor attempted to add individual DC hits to the PC-PCF segment. Similarly, the MS processor projected PCN-PCF segments into the PSAs using DHFIT3 in order to pick up PSA space points. It should be noted that the approximations used in DHFIT3 were quite good for particles which were high enough momentum to make it into the PSAs. Finally, the MV processor projected all of the tracks into the PCV chambers in order to pick up PCV space points.

This entire procedure was repeated in two passes. The first pass contained the strictest cuts and was aimed at finding the highest momentum particles, especially the scattered muon. The second pass had looser cuts and was aimed at picking up any remaining hadrons, especially those with a lower momentum and higher curvature.

In summary, the processors were:

PB: Find beam tracks using space points and projections.
SB: Match beam tracks with SBT hodoscope hits.
PM: Find muon projections in the PTMs.
SM: Find muon projections in the SMSs.
OV: Find muon projections in the PTM/SMS system.
DC: Find straight line segments in the DCs.
PC: Find straight line segments in the PCs.
PS: Find PSA space points.
PV: Find PCV space points.
MA: Match PC and DC segments, picking up PCF hits.
PF: Project PC segments into PCF and pick up hits.
SF: Construct curved segments from PCF hits.
SN: Add PCN hits to curved segments from SF.
MD: Match PC-PCF segments with unused DC segments and hits.
MS: Match PC-PCF segments with PSA space points.
MV: Add PCV space points to tracks.

4.3.3 TF: Track Fitting

The Track Fitting program was designed to quantitatively fit the tracks that were found by the Pattern Recognition program. The results from the track fit are expressed in terms of the following parameters: X, Y, Z, Y', Z', and $1/p$. The parameters X, Y, and Z refer to the coordinate of a point on the track. The parameters Y' and Z' refer to the slope of the track tangent at that point:

$$Y' \equiv \left(\frac{dY}{dX}\right)_{\{X,Y,Z\}}, \qquad Z' \equiv \left(\frac{dZ}{dX}\right)_{\{X,Y,Z\}}.$$

The parameter $1/p$ refers to the inverse momentum of the track as measured from the track curvature in the CCM magnetic field. The Track Fitting code was responsible for fitting tracks from both the Beam Spectrometer and the Forward Spectrometer.

In the case of the Beam Spectrometer, the length of the magnet (NMRE) was negligible when compared to the the lever arm of the spectrometer. This meant that the effect of the magnet could be approximated as a constant impulse Δp_y imparted to the track at the center of the magnet. The impulse, or p_T-*kick*, of NMRE was proportional to $\int \vec{B} dl$ and was nearly independent of the path through the magnet. For a healthy track, PBT stations 1 and 2 yielded one straight line segment and stations 3 and 4 yielded another. In general, these line segments intersected at a point somewhere in the magnet. The track fitting in the Beam Spectrometer, therefore, amounted to two line fits and a matching of the line segments. The fractional momentum resolution was:

$$\frac{\delta p}{p} = 0.5\% \frac{p}{500 \text{ GeV}}. \tag{4.1}$$

The angular resolution of the beam direction upstream of the physics target was 15 μr in the X-Y plane and 5 μr in the X-Z plane.

In the case of the Forward Spectrometer, the task of Track Fitting was more complicated. There were several reasons for this. First, the CCM and CVM magnetic fields extended over a longer distance than the NMRE field. Second, the final state particles (scattered muon and hadrons) had a much larger spread in momentum and angle than the beam muons. Because of these effects, we couldn't use the impulse approximation in the FS as we did in the BS. Finally, the track multiplicity was higher in the Forward Spectrometer. This necessitated a more careful fit to ensure that misassigned hits were detected and removed. The TF program proceeded by performing a series of local fits (to line segments or to points) on subsections of each track. These local fits were then joined using a quintic spline fit [40] given the full field map of the CCM magnet. The fit was reported as $(Y, Z, Y', Z', 1/p)$ at a given value of X. Additionally the program reported a full 5×5 symmetric covariance matrix for the errors on $(Y, Z, Y', Z', 1/p)$ from the fit, given the known chamber

resolutions. This covariance matrix was then modified in order to take into account the momentum-dependent effects of multiple scattering on the track fit resolution.

It is important to note that until the track was fit and a momentum obtained, there was no quantitative measure of whether a particular hit belonged on a given track. This is because both the curvature of the valid particle trajectories and the errors due to multiple scattering were momentum-dependent. During the Pattern Recognition stage, we didn't know the momentum of the tracks, so generic road widths were used to determine what hits belonged on the track. The track fit and the full error matrix on that track fit, which became available after TF was run, allowed a quantitative measure (χ^2) of how well a particular hit fit to a particular track. This enabled us to test hits on a track after it was fit to see whether they were misassigned by PR.

It was discovered empirically that some of the tracks found by PR contained bad hits that didn't belong on the track. It was also found that the PR program often failed to assign PCV hits to a track on which they actually belonged. As explained above, the TF program was in a better position than PR to fix these bad tracks and to pick up the additional PCV hits since more information was available at the TF stage. The Rescue and Superrescue procedures were developed to throw away bad hits and the PCV Hunt procedure was developed to pick up additional PCV hits on tracks. The Rescue, Superrescue, and PCV Hunt procedures were run at the end of TF.

The Rescue procedure was performed for tracks with a low chi-squared probability ($P_{\chi^2}^{trk} < 5\%$). It was based on the assumption that the track was bad because PR included some incorrect hits on the track. The procedure dropped the hits, one by one, that contributed the most to the χ^2 of the track fit. It then refit the track after each hit was dropped. The Rescue procedure continued to drop hits and refit until one of the following conditions was met:

- If the P_{χ^2} improved sufficiently, the Rescue was declared a success: EXIT (SUCCESS).
- If there were no PCV hits on the original track and 10 hits had already been dropped, the Rescue was declared a failure: EXIT (FAILURE).
- If there were PCV hits on the original track and 3 hits had been dropped by Rescue, the Rescue was aborted and the Superrescue procedure was used instead: ABORT (Use SUPERRESCUE).
- If there were no longer enough degrees of freedom to refit the track after dropping hits, the Rescue was declared a failure: EXIT (FAILURE).

The Superrescue procedure was based on the assumption that the track was bad due to the fact that the PCV hits were misassigned to the track by Pattern Recognition. The original PR track was restored (reinstating any hits that Rescue dropped) and all PCV hits were dropped. This track was then refit and either kept or given a new Rescue attempt based on its new P_{χ^2}.

The PCV Hunt procedure was developed for cases where there was a valid track in the Forward Spectrometer with no PCV hits on it. Such tracks were usable as they were, but adding (valid) PCV hits to a track improved the momentum resolution significantly. For this reason, when tracks had no PCV hits, an attempt was made to pick some PCV hits up by projecting the track back to the PCV. This was similar in spirit to the MV processor in PR, but the PCV Hunt procedure made use of the measured track momentum which had been unavailable to the MV processor. If three or more PCV hits were consistent with the original track, then they were added to the track and the spline fit was repeated.

4.3.4 Duplicate Track Removal

After the Pattern Recognition and Track Fitting were run, there were a number of tracks which were found more than once. In other words, there were often groups of two or more tracks which shared too many hits to be due to different particles. The subroutine `TKSAME` was called after the Track Fitting in order to remove these extra tracks.

Two tracks were considered identical if they shared at least ten PC and PCF hits and had the same measured charge OR if they shared at least fifteen DC hits. The reason that tracks were not dropped if they shared PC and PCF hits but had opposite charges was that photon conversions in some of the material generated valid electron-positron pairs that were not well differentiated until after they reached the drift chambers. The decision of which track to drop in a group of "identical" tracks was based on P_{χ^2} and on the number of degrees of freedom.

4.3.5 MM: Muon Matching

The purpose of the Muon Matching program was to identify Forward Spectrometer tracks which were due to muons. This was done by matching projections in the PTMs and SMSs behind the Steel Absorber with tracks in the forward spectrometer. Tracks which matched were declared muons. The main usefulness of this procedure was that it enabled us to find the scattered muon which, along with the beam, determined the event kinematics. In some cases more than one muon was found in an event. The

muon match made no attempt to decide which muon was the scattered muon, but merely flagged tracks which were identified as muons.

As the program was implemented for the 1987-1988 data taking run, only tracks that had hits in the DCs or PSAs were eligible to be considered muons. This choice was made for simplicity. The muon track could be projected from the DCs or PSAs to the PTMs using a straight-line fit.

There were several sources of random error that had to be taken into account in the muon matching process. First there were errors in the two-dimensional line fit for the muon projections in the PTM/SMS system and in extrapolating these projections to the match point. There were also errors due to track measurement and extrapolation in the Forward Spectrometer, but these were negligible and were ignored. In addition to these errors, the fact that the muon could undergo Coulomb scattering in the Calorimeter or Absorber material complicated things. The changes in the track slope due to these processes could be estimated, but they were not distributed normally. The contribution was divided up into multiple small-angle scattering and single large-angle scattering. The muon match was divided into two stages. The first stage incorporated the effects of measurement error and multiple scattering while the second stage looked for muons that underwent a large-angle scatter in the detector material.

In the first stage, each Forward Spectrometer track was extrapolated to the downstream face of the absorber and compared with the Muon Spectrometer projections at that point. The χ^2 for each possible match was calculated in both the XY and XZ projections. This χ^2 included the errors from the Muon Spectrometer measurement and from multiple scattering added in quadrature. The error on the Forward Spectrometer track was neglected as it was much smaller than the other errors. While the error on the Muon Spectrometer measurement was independent of momentum, the error due to multiple scattering was inversely proportional to the track momentum. The Muon Match program used the measured momentum from the Track Fit in determining the χ^2. In order for a muon match to be successful in this first stage, both the Y and Z views had to match ($\chi^2 < 40$).

In the second stage, the Muon Match accounted for the possibility that a muon scattered at a large angle at a single point in the Calorimeter or the Absorber. If the FS track and the muon projections intersected at a point somewhere in the Calorimeter or the Absorber, then the match was accepted. In order to account for the error on finding the exact intersection point, intersections slightly upstream of the Calorimeter position or slightly downstream of the Absorber were also accepted. If more than one FS track matched a given projection during this second stage, then the track which required the smallest scattering angle in the material was used. It should be noted that most of the muons which were matched in the second stage were

due to beam muons which failed to interact with the physics target. These events were uninteresting, but they were not discriminated against by any of our triggers and had to be removed in software.

4.3.6 VX: Vertex Finding

The final step in the event reconstruction was finding the location of the interaction vertex. The kinematics of the event and the three-momenta of the produced particles were only properly defined at the correct vertex position. Furthermore, it was useful for many physics analyses to identify and remove particles which came from a secondary vertex. These secondary vertices were caused by particles which traveled some distance in the laboratory and then decayed or interacted with target or detector material. Of course, for some analyses, these secondary vertices were themselves interesting, but they have been ignored in this thesis.

The Vertex processor [41] operated in three stages. First, it identified the scattered muon and found the $\mu\mu$-vertex, using the beam and scattered muon and ignoring any hadrons. Second, it found the primary vertex by adding hadron tracks to the $\mu\mu$-vertex and refitting. Only hadron tracks which intersected the original vertex position, within errors, were used. Finally, several algorithms were used to search for secondary vertices.

The input to the Vertex Finding program was a collection of tracks from TF (with duplicate tracks removed). There were two classes of tracks that the Vertex processor was unable to use and which were therefore ignored. The first class comprised those tracks which were not reconstructed through the magnetic field of the CCM. These included wide-angle tracks that failed to make it into the magnet at all, as well as forward tracks whose PCF hits weren't found by PR. These tracks had no measured momentum and therefore couldn't be extrapolated into the CVM towards a possible vertex. The second class of unusable tracks were those that contained no hits upstream of the CCM. By construction, PR never generated such tracks, but the TF Rescue procedure occasionally dropped all of the hits upstream of the CCM. Such tracks were not used in the vertex fit.

In general, the Vertex processor found the point of closest approach of a collection of candidate tracks and removed tracks that failed to intersect within errors. The basic procedure involved in vertex fitting was an iterative one:

1. Take a nominal vertex position and a collection of tracks.
2. Extrapolate the (curved) tracks through the CCM field until you reach a point on each track closest to the nominal vertex position.

3. Assuming that the tracks can be approximated by straight lines (at least locally), find the point of closest approach between these straight lines. This is the new vertex position.

4. If the number of iterations taken exceeds 15, keep the fit with the best $P_{\chi^2}^{VTX}$ so far and exit.

5. If the vertex position remains outside the region -20.0 m $< X_{VTX} < 4.0$ m for two consecutive iterations, then the vertex fit is a failure. Abort the procedure.

6. If the vertex position moved by more than 0.5 mm, return to Step 2 for another iteration using the latest vertex position as input. If the vertex position moved by less than 0.5 mm then the procedure is successful. Keep the last vertex and exit.

After the procedure was complete, the fit quality was checked. If the chi-squared probability ($P_{\chi^2}^{VTX}$) was less than 0.001, then the track which made the largest χ^2 contribution was detached from the vertex. Tracks with a distance to the vertex exceeding 5 cm or distance/error values exceeding 100 were detached in any case[3]. The vertex was refit if any tracks were detached.

The procedure described above in Step 3 was the heart of the vertex fit, and deserves a bit more explanation. We started with a collection of tracks and a specific point on each track. We then made the approximation that the tracks were all straight lines given by the point and the tangent to the track at that point. Our goal was to find a vertex position that was "closest" to all of the lines in the sense of minimizing the distance/error from each track to the vertex (added in quadrature). This was equivalent to performing a weighted average of the track points with infinite error (and zero weight) along the track direction. Under the approximation that the tracks were straight lines, this procedure was linear and could be performed through matrix manipulation. If the tracks had really been straight lines in space at the vertex then we wouldn't have needed to iterate. However, since the target resided in the magnetic field of the CVM during the 1987 data taking run, it was necessary to iterate in order to reduce the effect of the nonlinearities. As the track points got closer to the vertex position, the validity of the straight-line approximation improved.

As mentioned above, this general procedure was repeated in three different stages. These stages were distinguished by their input tracks, by their input vertex position, and by additional requirements on track validity. Any tracks which were successfully included in a fit to a particular vertex were called *fitted* tracks with respect to that vertex.

[3]In practice, the distance-over-error cut at 100 was irrelevant. Tracks with distance-over-error values greater than about 4 were removed by the $P_{\chi^2}^{VTX}$ requirement anyway.

In the first phase of the VX processor, known as the muon-muon phase, a separate vertex was determined using each same-sign incoming-outgoing muon pair. For the 1987 data-taking run, the input vertex position for the first iteration was taken to be a particular point inside the target: $x = -11.5$ m, $y = z = 0$. If no same sign $\mu\mu$-vertex was found, then the program attempted to find opposite-sign muon vertices. If no $\mu\mu$-vertex was found at all then the vertex program aborted the event. In general, the $\mu\mu$-vertices are the least biased vertices, but the vertex position wasn't very well determined compared to the vertices which include at least one hadron.

In the second phase, known as the hadron phase, the $\mu\mu$-vertex was used as a seed vertex and a combined fit of the beam muon, the scattered muon, and all of the candidate hadrons was attempted. If the fit failed, the hadron track with the largest χ^2 contribution to the vertex fit was detached from the vertex and the vertex was refit. This procedure was repeated until a successful fit was made with $P_{\chi^2}^{VTX} > 0.001$. This vertex was called the *primary vertex.*

In the final phase, an attempt was made to form secondary vertices. The algorithm used to decide which hadrons combinations to test was fairly complicated and required arbitration when a track was able to fit to too many vertices. A track was only allowed to be fitted to one vertex, unless it was a connecting track. A *connecting track* was a track that began at one vertex, ended at another vertex and which was "fitted" to both. Connecting tracks were only allowed to be "fitted" to the two vertices which they connected. Furthermore, only one incoming connecting track was allowed per secondary vertex. The secondary vertices were classified into four types according to two criteria:

- Charged secondary vertex: One incoming connecting track.
  - ⋆ Charged decay vertex (kink): One charged track in and one charged track out of the same charge.
  - ⋆ Charged secondary interaction vertex: Any other charged secondary vertex.
- Neutral secondary vertex: No incoming connecting track.
  - ⋆ Neutral decay vertex (V^0): Two outgoing tracks of opposite charges whose combined invariant mass was consistent with one of the following decay modes: $K_S^0 \to \pi^+\pi^-$, $\Lambda^0 \to p\pi^-$, $\bar{\Lambda}^0 \to \bar{p}\pi^+$, $\gamma \to e^+e^-$.[4]
  - ⋆ Neutral secondary interaction vertex: Any other neutral secondary vertex.

[4]Strictly speaking the photon "decay" was really the electron pair production process: $\gamma \to e^+ e^-$. In practice, it looks like a decay since the $e^+ e^-$ invariant mass peaks at zero, the photon mass.

In some cases, a track that was successfully fit to the primary vertex was later found to fit even better to a secondary vertex. If such a track was not a connecting track, then it was detached from the primary vertex and the primary vertex was refit.

After all of the vertices were generated, each track was extrapolated to all vertices and the track parameters at the points of closest approach were stored. The tracks that were successfully fit to the particular vertex were flagged as *fitted* tracks while all other tracks were called *close* tracks for this particular vertex. This nomenclature has caused some confusion. A close track can be quite far away from the vertex. The term "close track" just means a valid track that is not fit to a particular vertex. Most tracks were fitted to either zero or one vertex. Connecting tracks were fitted to two vertices. It should be noted that the Vertex processor didn't refit the tracks, forcing them to pass exactly through the vertices that they were fitted to. Instead, the tracks were left as they were found by TF and the momentum of the hadron at the vertex was given by the track parameters at the point of closest approach between the track and the vertex. The covariance matrix for the errors on the track parameters was propagated to the point of closest approach and kept. Similarly, the covariance matrix corresponding to the error on the primary vertex position (including the hadrons) was kept. It should be noted that in order to calculate the error on the magnitude of a hadron momentum (p), one needs only the error on the track parameter $1/p$. However, in order to calculate the proper error on the momentum direction $\hat{p}$ at the true vertex, one must include both the error on the track parameters and the error on the vertex position. This is important for calculating the error on the hadron quantities: p_T and φ_h. This is described in more detail in Appendix C.

If more than one outgoing muon was fitted to the primary vertex, then the muon with the highest momentum was chosen as the scattered muon. The event kinematics and their associated errors were calculated and reported by the vertex processor based on the beam and scattered muon track parameters at the primary vertex. It should be noted that the hadrons in the event were used to constrain the vertex position. This dramatically improved the resolution on the kinematics for events which contained hadrons.

4.4 DR: Data Reduction

The Data Reduction (DR) program was designed to further purify and reduce the physics data sample to an even more manageable level. The PTMV output tapes still contained a lot of unusable events, including those where the PTMV program failed to reconstruct the primary vertex. In addition, there was a significant electromagnetic background that remained in the data sample. The requirements of the filter were designed to ensure that we kept events which were due to a target interaction, but no

selection was made at that time to ensure that the events were due to deep inelastic scattering.

The DR program threw away events which failed reconstruction, which were due to an interaction outside of the target, or which failed some very loose kinematic cuts. In the case of the LAT data sample, an additional kinematic cut, $x_{Bj} > 0.003$, was imposed in order to reduce the electromagnetic contamination.

The LAT cuts are tabulated below:

$$\begin{array}{rcccl} 0 \text{ GeV} & < & p_{Beam} & < & 10000 \text{ GeV} \\ 0 \text{ GeV}^2 & < & Q^2 & < & 10000 \text{ GeV}^2 \\ 10 \text{ GeV} & < & \nu & < & 10000 \text{ GeV} \\ 0.003 & < & x_{Bj} & < & 100.0 \\ -13.0 \text{ m} & < & X_{VTX} & < & -10.0 \text{ m} \end{array}$$

The DR program threw away most of the events that were input to it, retaining only 8%. More than half of the events were thrown out because they had no reconstructed vertex. Of the events with a vertex, roughly one quarter passed the kinematic cuts. Since the Filter program itself had a reduction factor of 31%, the final DR data sample is only $2\frac{1}{2}\%$ of the original D_2 LAT sample. Table 4.2 shows the sequential effect of the Split, Filter, and the DR programs on the size of the data sample.

Sample	Events	Red. Factor
Total D_2 Triggers:	12.9 M	
Split D_2 LAT:	4.83 M	37.4 %
Filtered D_2 LAT:	1.48 M	29.6 %
Data-Reduced D_2 LAT:	117 K	7.9 %

Table 4.2: DR Statistics for the D_2 LAT Sample.
This table shows the effect of the E665 analysis chain on the number of events in the data sample. It starts with the total number of raw triggers, shows the effect of the Split program (Section 4.2), the Filter program (Section 4.2), and finally the DR program (this section). Each line shows the number of events at a given step and the reduction factor **from the previous step.**

The numbers above refer to the entire D_2 LAT data sample from the 1987 run. Some E665 analyses have been restricted to the post-December-1 portion of the 1987 data sample which contains about one quarter of the total sample. In this thesis, I

use this entire data sample[5]. It should be noted that the pre-December 1 data and the post-December 1 data had the same DR reduction factor of 8%.

4.5 Calorimeter Analysis

The Calorimeter analysis was run separately from the rest of the event reconstruction (PTMV). In fact, it was run during the DR job. Each event which passed DR was analyzed for calorimeter information before it was output. The details are described in Reference [32] and will only be outlined here. The analysis proceeded in stages similar to those used in the analysis of a wire chamber. The stages were:

- Decoding - extraction of CAL data from raw event,
- Translation - conversion of data to energy/pad or energy/wire,
- Pattern Recognition - combining pad energies into clusters.

The decoding stage involved extracting the Calorimeter-specific information from the entire event record. The translation stage sought to come up with an energy value for each pad and wire of the calorimeter. This involved pedestal subtraction, application of the gain factor, and various corrections. The corrections compensated for the effects of power supply oscillations, dead channels, and gas gain variations with temperature and pressure. The pattern recognition involved using a clustering algorithm to combine neighboring pads into energy clusters, arbitrating between neighboring clusters. The output of the Calorimeter analysis was a set of LGLB banks which contained the clusters (or globs). The LGLB bank provided the following information:

E: Energy - The amount of energy deposited in GeV.

Y, Z: Position - The position coordinates of the center of the cluster on the face of the Calorimeter.

r: Breadth - The transverse breadth of the cluster. This was the energy-weighted mean radius of the cluster.

Λ: Center-of-Gravity - The longitudinal center of gravity of the cluster.

B/F: Back-over-Front ratio - The ratio of the energy deposited in the back half of the Calorimeter over the front half.

[5]See Section 4.6 for more details. I throw out about 25% of the data due to bad Calorimeter performance/calibration.

$N_{0.05}$: The First Plane - The point in the Calorimeter by which 5% of the shower energy has already been deposited.

In addition to the above quantities which could be read directly from the LGLB bank, the following additional quantities could be derived for each cluster:

η: Mean energy per pad.

d_{trk}: Distance $\left(\sqrt{(\Delta y)^2 + (\Delta z)^2}\right)$ to the nearest track - The distance between the cluster position and the nearest track position (at the Calorimeter face).

E_c/p_{trk}: Cluster Energy over Track Momentum - The energy of the cluster divided by the momentum of the nearest track.

The LGLB banks reported the cluster position as defined in the local coordinates (Y, Z). The center of the calorimeter face was at $Y = Z = 0$ in these local coordinates. Before the cluster positions were used a small alignment correction had to be applied. I used the correction found in Reference [42]:

$$Y_{E665} = Y_{LGLB} - 1.06 \text{ cm} \quad (4.2)$$

$$Z_{E665} = Z_{LGLB} - 0.52 \text{ cm} \quad (4.3)$$

If we assume that the cluster was generated by a photon from the primary vertex, then we can reconstruct its four-momentum from the energy and the position of the cluster. Consider the three-vector $(\vec{r})$ in the E665 Coordinate system defined by:

$$\vec{r} \equiv \vec{r}_{GLOB} - \vec{r}_{VTX},$$

where $\vec{r}_{GLOB}$ is the position vector of the cluster, with the X-position of the cluster defined as 13.838 m. The photon three-momentum is then: $\vec{p} = E\hat{r}$, where $\hat{r} \equiv \vec{r}/|\vec{r}|$. Reconstructing the momentum vector of a photon in this fashion is subject to a much larger bias than simply measuring its energy. In particular, if the photon doesn't really belong to the primary vertex, then our momentum measurement will be wrong. For this reason, the photons from the Calorimeter aren't placed on equal footing with the charged hadrons in this thesis. The use of the clusters is described in Section 4.8.

The Calorimeter analysis used in this thesis was the one that was performed during the original Data Reduction program. This Calorimeter analysis had some known bugs. Occasionally, the clustering algorithm would fail and generate a cluster with a negative energy or with a position outside the calorimeter. Furthermore, whenever such a bad cluster was generated, the shower shape information for all of the clusters in that event was lost. This problem occurred in about 7% of the events

(after my kinematic cuts). I was able to salvage most of these clusters, as described in Section 4.8. Another problem was that roughly 2% of all events contained no LGLB bank at all. These were events where the entire Calorimeter failed and they were removed from the data sample in my analysis.

The clusters in the LGLB bank weren't all due to photons. Some were due to hadrons or muons or electrons. The cuts used to select valid clusters are described in Section 4.8.

4.6 Event Selection

In addition to the cuts performed in most E665 data analyses, the analysis in this thesis included the following additional cuts on the events:

- $N_{beams} = 1$,
- $P_{\chi^2}^{VTX} > 0.001$,
- $W^2 > 0$ GeV^2,
- $Q^2 > 2.0$ GeV^2,
- $y_{Bj} < 0.9$,
- $\nu > 100$ GeV,
- -11.8 m $\leq X_{VTX} \leq -10.5$ m.

Most of these requirements helped to clean up the sample significantly with only a small cost to the statistics. The ν cut, on the other hand, removed quite a few events, and therefore requires some justification. The main motivation behind this cut was that the ν resolution was quite poor at low values of ν. This was because both the scattered and beam muon were at high momentum in low ν events. In order to calculate ν, we had to take the difference of two large quantities (E and E'). In such cases, even small fractional errors on the momentum measurements were magnified. A poor measurement of ν immediately translated into a poor measurement of longitudinal hadronic kinematic variables such as z_h or x_F. We chose events with $\nu > 100$ GeV because they typically had $\delta\nu/\nu < 10\%$.

Even after the $x_{Bj} > 0.003$ cut in the DR program, some unwanted photon bremsstrahlung remained in the sample. The $Q^2 > 2$ GeV^2 cut removed some bremsstrahlung and the $y_{Bj} < 0.9$ cut was designed explicitly to reduce the effects of bremsstrahlung. In order to reduce any remaining contamination from photon bremsstrahlung

events, some event cuts were used which included calorimeter information. All of the clusters in the calorimeter with $E > 5$ GeV were examined. Both the number of such clusters and the total energy in the clusters were kept. The event was cut if the calorimeter showed one cluster with $\Sigma E_{clus} > 0.40\nu$, two clusters with $\Sigma E_{clus} > 0.50\nu$, or three or four clusters with $\Sigma E_{clus} > 0.75\nu$. Furthermore, any event was cut if $\Sigma E_{clus} > 0.95\nu$ regardless of the number of clusters. It should be noted that the Calorimeter saturates so that clusters above about 200–250 GeV were difficult to measure accurately. Furthermore, these clusters had their energy systematically underestimated. This is the reason that single clusters with E/ν as low as 0.4 needed to be removed.

Figure 4-3 shows a two-dimensional distribution of the number of clusters (with energy over 5 GeV) versus the quantity ρ_E which is defined as:

$$\rho_E \equiv \sum E_{clus}/\nu.$$

Figure 4-3a is a surface plot of this two-dimensional distribution. The bremsstrahlung peak is the rightmost peak and is characterized by a large value of ρ_E with few clusters. Generally such events are dominated by one large bremsstrahlung photon which takes most of the energy of the event. The broader peak on the left is primarily due to the DIS sample. Figure 4-3b shows the same distribution as a "BOX" plot, with the bremsstrahlung cut indicated. In this plot, the size of each box is proportional to the number of entries in that bin. We removed all events which fall to the right of the cut line. In both plots (a and b), the y_{B_j} cut described above was loosened to include the region $0.9 < y_{B_j} < 1.0$. The purpose of this was to enhance the bremsstrahlung peak in the plot. The other cuts described above were still active. All clusters with energy above 5 GeV that were reported by the Calorimeter analysis code were included. No additional cluster quality cuts were imposed when measuring the energy sums for this cut.

As was noted in Section 4.5, events where the LGLB banks were missing were removed from the event sample. This condition was due to a hardware failure in the Calorimeter.

Table 4.3 shows the effect of my private cuts on the D_2 LAT data sample, starting from the E665 DR tapes. All D_2 LAT DR tapes were used, but a cut was made to ensure that the Run number was greater than 1940. This cut removed all of the D_2 LAT data taken prior to 23-October-1987. This was necessary because the Calorimeter was not properly calibrated before that time. Additionally, the run blocks from 2641–2670 (inclusive) were removed. This was because they had an excess of neutral energy in the events, possibly because the target was not completely full. The table also includes results divided into four time periods of roughly equal input statistics. Some previous analyses have only used time period IV, the post-

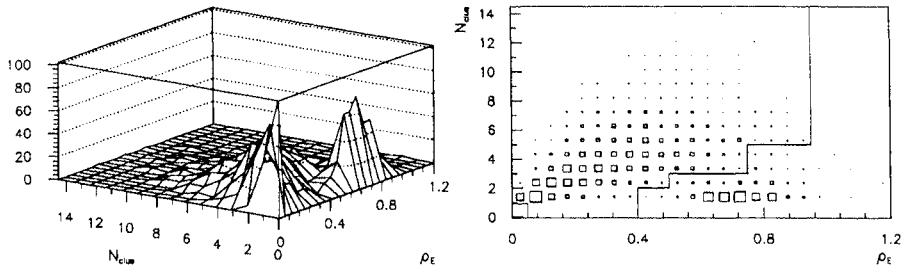

Figure 4-3: The Calorimeter Bremsstrahlung-removal Cut.
The number of clusters is plotted versus ρ_E (the total calorimeter energy scaled by ν). Only clusters with $E > 5$ GeV were used. The plots show the same two-dimensional distribution as a) a surface plot, and b) a "BOX" plot. The line on plot b defines the bremsstrahlung cut value. The plots in this figure are not corrected for acceptance. The y_{B_j} cut has been loosened to $y_{B_j} < 1.0$.

Description	D_2 LAT DR sample		I	II	III	IV
Input Sample:	117,113		35,032	31,447	19,088	31,546
Bad Runs:	27,848		25,919	0	1,851	78
Good Runs:	89,265	100.0 %	9,113	31,447	17,237	31,468
multi-beam	3,605	4.0 %	4.4 %	3.7 %	3.8 %	4.5 %
$W^2 < 0$	18	0.02%	0.01%	0.02%	0.02%	0.02%
$P_{\chi^2}^{VTX} < 0.001$	913	1.0 %	1.2 %	1.0 %	1.0 %	1.0 %
Bad X_{VTX}	3,690	4.1 %	3.7 %	4.3 %	4.0 %	4.2 %
$Q^2 < 2.0$ GeV^2	6,631	7.4 %	7.1 %	7.3 %	8.0 %	7.3 %
$\nu < 100$ GeV	32,380	36.3 %	37.1 %	36.6 %	36.1 %	35.8 %
$y_{B_j} > 0.9$	4,935	5.5 %	5.3 %	5.5 %	5.5 %	5.6 %
Cal. Missing	800	0.9 %	0.1 %	0.5 %	1.4 %	1.2 %
Bremsstrahlung	5,560	6.2 %	6.5 %	6.2 %	6.0 %	6.4 %
Output sample:	30,733	34.4 %	34.6 %	34.8 %	34.4 %	34.0 %

Table 4.3: The Effect of my Private Event Cuts on the D_2 LAT DR Data Sample.
The "D_2 LAT DR sample" column refers to the entire data sample, and the percentages in this column are defined with respect to the good runs from the total input sample. The individual time period columns I–IV are subsets of the total sample and the percentages are defined in terms of the events from good runs for that column only.

Step	Events	Red. Factor
Total D_2 Triggers:	12.9 M	—
D_2 LAT:	4.83 M	37.4 %
Filtered D_2 LAT:	1.48 M	29.6 %
Data-Reduced D_2 LAT:	117 K	7.9 %
DR Good Runs D_2 LAT:	89.3 K	76.2 %
Selected events D_2 LAT:	30.7 K	34.4 %

Table 4.4: Event Statistics for the Final D_2 LAT Sample.
This table shows the effect of the E665 analysis chain and my private cuts on the number of events in the data sample. It starts with the total number of raw triggers, shows the effect of the Split program (Section 4.2), the Filter program (Section 4.2), the DR program (Section 4.4), and my private cuts. Each line shows the number of events at a given step and the reduction factor **from the previous step.**

December 1 data sample. It should be noted that the tape XGAB50 includes some pre-December 1 data (78 events). However, after we cut the events from run block 2641–2670, only post-Dec. 1 data remained in time period IV. The time periods used in this thesis are defined as follows:

Time Period	Description	E665 DR tapes	Dates (good runs)
I:	Very early D_2 LAT	XGAB56–60	Oct. 23–24, 1987
II:	Early D_2 LAT	XGAB61–65	Oct. 25 – Nov. 8, 1987
III:	Early D_2 LAT	XGAB66–69	Nov. 8–13, 1987
IV:	post-Dec. 1 D_2 LAT	XGAB50–55	Dec. 1–8, 1987

Table 4.3 shows that the effect of the cuts did not vary strongly from time period to time period. Before the bad runs were eliminated, the Bremsstrahlung cut removed twice as many events in Time Period I than it did in the other time periods. The cuts were imposed sequentially in the order shown in the table. The most significant cut was the cut on ν.

The effect on the event statistics of the entire analysis chain from raw data through my event cuts is summarized in Table 4.4. The number of original raw data triggers that make it through all of these cuts is $\frac{1}{4}\%$.

4.7 Track Selection

My analysis imposed the following quality cuts on the reconstructed hadrons:

Description	D_2 LAT DR sample		I	II	III	IV
Input events:	30,733		3,152	10,941	5,927	10,713
Input hadrons:	107,359	100.0 %	11,234	37,947	20,294	37,884
Muon tracks:	2,593	2.4 %	2.6 %	2.4 %	2.2 %	2.5 %
Unfitted tracks:	37,668	35.1 %	33.6 %	34.9 %	34.9 %	35.9 %
Dist. to vertex:	272	0.3 %	0.2 %	0.2 %	0.3 %	0.3 %
RESCUE Failure:	50	0.05%	0.03%	0.07%	0.03%	0.03%
Bad $P_{\chi^2}^{trk}$:	1,575	1.5 %	1.3 %	1.4 %	1.5 %	1.5 %
Hadron kinematics:	1,892	1.8 %	2.0 %	1.7 %	1.6 %	1.8 %
$\delta p/p > 10\%$:	397	0.4 %	0.3 %	0.4 %	0.3 %	0.4 %
Output hadrons:	62,912	58.6 %	60.0 %	59.0 %	59.1 %	57.6 %
Hadrons / event:	2.05		2.14	2.05	2.02	2.04
$h^+ / (h^+ + h^-)$	51.6%		50.4%	51.8%	52.1%	51.7%

Table 4.5: The effect of my private hadron cuts on my final D_2 LAT Sample.

- The track must not have been a muon.
- The track must have been fitted to the primary vertex.
- The track must not have failed the RESCUE.
- If the RESCUE procedure was used, the tracks had to satisfy $P_{\chi^2}^{trk} > 0.0005$, otherwise the tracks had to satisfy $P_{\chi^2}^{trk} > 0.005$.
- The track had to have $\delta p/p < 10\%$.
- The track had to pass within 1 cm of the primary vertex.

My analysis also imposed the following kinematic cuts on the hadrons:

- $z_h < 1.1$,
- 6 GeV $< E_h <$ 500 GeV,
- $x_F > 0.0$.

The most substantial cut on the hadrons was the requirement that the hadrons be fitted to the primary vertex. Monte Carlo studies have shown that most of the non-fitted tracks don't belong to the primary vertex. They are primarily due to tracks which belong to a secondary vertex, to halo muon tracks, and to ghosts. The other cuts clean up problem tracks without much cost to the statistics.

4.8 Calorimeter Cluster Cuts

In this thesis, the Calorimeter was used to eliminate unwanted events. First, we removed all events which appeared to be due to photon bremsstrahlung. This cut is described in Section 4.6. This cut was active in all physics plots in this thesis. Second, we defined an event subsample where the most energetic charged particle, known as Rank 1, was unambiguously the most energetic particle in the event, both charged and uncharged. The Calorimeter was also used to define this subsample. This second cut is described in more detail in Section 5.3.1.

The information that we needed from the Calorimeter for the Bremsstrahlung cut was the raw number of clusters with $E > 5$ GeV and their total energy. The information that we needed for the second cut was the total energy in the Calorimeter due to photons, the energy of the most energetic photon, and the energy of the most energetic π^0 candidate.

In order to find the total photon energy and the highest energy photon in the event, we had to select clusters which were likely to be photons. Typically, a photon or an electron passing through 20 radiation lengths of material, such as we had in the Calorimeter, will deposit all of its energy, allowing us to measure the total photon energy. A hadron, however, will also deposit some energy; we want to avoid counting the hadron energy as a photon. In order to use the individual clusters as photons, it was necessary to choose cuts which removed clusters which were due to hadrons or noise. These cuts were made in three passes. The first pass was an energy and fiducial cut. Any clusters with an energy of less than 5 GeV were cut. Furthermore, any cluster whose position was within 10 cm of the edge of the Calorimeter was cut. The clusters were concentrated in the middle of the Calorimeter so this fiducial cut was not very severe. It's main purpose was to ensure that we captured all of the energy associated with a cluster. The second pass eliminated clusters which had tracks pointing to them and whose energy was significantly less than the track momentum. These clusters were generally due to hadrons. Finally, a group of cuts was made in order to constrain the shape of the shower. Photon (and electron) showers should start early and should deposit most of their energy in the front half of the calorimeter.

The possibility of distinguishing hadrons from photons by shower shapes was discussed in Reference [32]. The main conclusion was that it is possible, but difficult, to distinguish the showers by shape alone. In fact, if we consider clusters with energies below 20 GeV, the separation between hadrons and photons becomes even more difficult. The breadth parameter r was not useful in distinguishing electrons and hadrons as the shower breadths were not very different. It was, however, useful in removing noise clusters; those with very large or very small values of r were probably due to noise and could be discarded. We used a lower cutoff for breadth of 1 cm and

a position-dependent upper cutoff: 6 cm in the inner region of the Calorimeter, 8 cm in the inner annulus, and 10 cm in the outer annulus. The varying cutoffs were due to the varying pad sizes in the different regions. There was another shower shape parameter, known as η, which measured the mean energy per pad. This parameter wasn't very useful because it was a strong function of total shower energy and of cluster position (due to the varying pad sizes).

A more promising approach for discriminating between hadron clusters and photon clusters was to examine the longitudinal information. A photon tended to deposit most of its energy in the front half of the Calorimeter while a hadron deposited energy throughout the Calorimeter. The longitudinal center-of-gravity parameter Λ, therefore, provided some hadron/photon discrimination. Photon clusters had center-of-gravities in the forward half of the spectrometer while hadron clusters were distributed throughout the Calorimeter. We used a lower cutoff of 0.2 for Λ and an upper cutoff of 0.5. The lower cutoff reflected the fact that any cluster which was too far forward was probably due to noise. Similarly we expected the B/F parameter to be less than 1 for most photons. We eliminated clusters with B/F > 1.5. The *first plane parameter* $N_{0.05}$ is yet another measure of longitudinal shower shape. We expect the first 5% of the shower energy to appear somewhere in the front half of the detector; we demand that $N_{0.05} \leq 7$.

Clusters with nearby tracks were much easier to diagnose. When the cluster energy was significantly less than the track energy, we could assume that the cluster and the track were both due to a hadron (or muon). In such cases, we removed the cluster even if its shape was electromagnetic in appearance. If the cluster and track energies were nearly identical, we could assume that the cluster and track were both due to an electron. If the cluster energy was significantly larger then the track energy, we could assume that their proximity was coincidental. The cluster was probably due to a photon and the track was probably an unrelated hadron. In practice, we ignored the possibility that the track was an electron because there was no evidence of a peak near unity in the E_{clus}/p_{trk} distribution. If a cluster was near a track and $E_{clus}/p_{trk} < 1.5$ then we assumed that the cluster was due to a hadron and removed it. If, on the other hand, $E_{clus}/p_{trk} > 1.5$ the cluster was kept or rejected based on its shower shape as if the track were not there[6].

Since we treated clusters differently depending on how close they were to the nearest track, we need to define this cut first. Figure 4-4 shows the distance to the nearest track for the entire calorimeter and for each of the three calorimeter regions (central region, inner annulus, outer annulus) separately. Since the pad sizes get larger as you move farther from the center, and the track densities get smaller, it is natural for our cut value to be different in the different regions. The cut values for

[6]This case is fairly rare. Usually clusters associated with tracks are less energetic than the tracks.

deciding whether a cluster is "near" a track are also shown on Figures 4-4b-d. The cuts are at 4 cm, 8 cm, and 12 cm for the central, inner, and outer regions respectively.

To summarize the procedure, we divided the cluster sample into charged and neutral clusters according to the following algorithm. Clusters which were near tracks and which had $E_c/p_{trk} < 1.5$ were declared charged clusters and were eliminated. Clusters which were isolated or which had $E_c/p_{trk} > 1.5$ were declared neutral. Neutral clusters were further examined to ensure that they had an appropriate electromagnetic shower shape.

The following cuts must all be satisfied in order for a cluster to be considered to be due to a photon:

- $E > 5$ GeV
- $|Y_{local}| < 1.4$ m
- $|Z_{local}| < 1.4$ m
- Reasonable breadth:
  - $\star$ 1 cm $< r <$ 6 cm for the central region
  - $\star$ 1 cm $< r <$ 8 cm for the inner annulus
  - $\star$ 1 cm $< r <$ 10 cm for the outer annulus
- The cluster must be neutral:
  - $\star$ $d_{trk} > 4$ cm .OR. $E_c/p_{trk} > 1.5$ for the central region
  - $\star$ $d_{trk} > 8$ cm .OR. $E_c/p_{trk} > 1.5$ for the inner annulus
  - $\star$ $d_{trk} > 12$ cm .OR. $E_c/p_{trk} > 1.5$ for the outer annulus
- $0.2 < \Lambda < 0.5$
- $B/F < 1.5$
- $N_{0.05} \leq 7$

There was a small class of events in which there was an error in one cluster of the calorimeter. Due to a logical flaw, such an error caused the shape information to be lost for all clusters in that event. For this reason, a modified set of cuts was applied to such events. The energy cut was raised to 10 GeV and the shape cuts were no longer applied. About 7% of the events had this problem. The cuts for these events are summarized below:

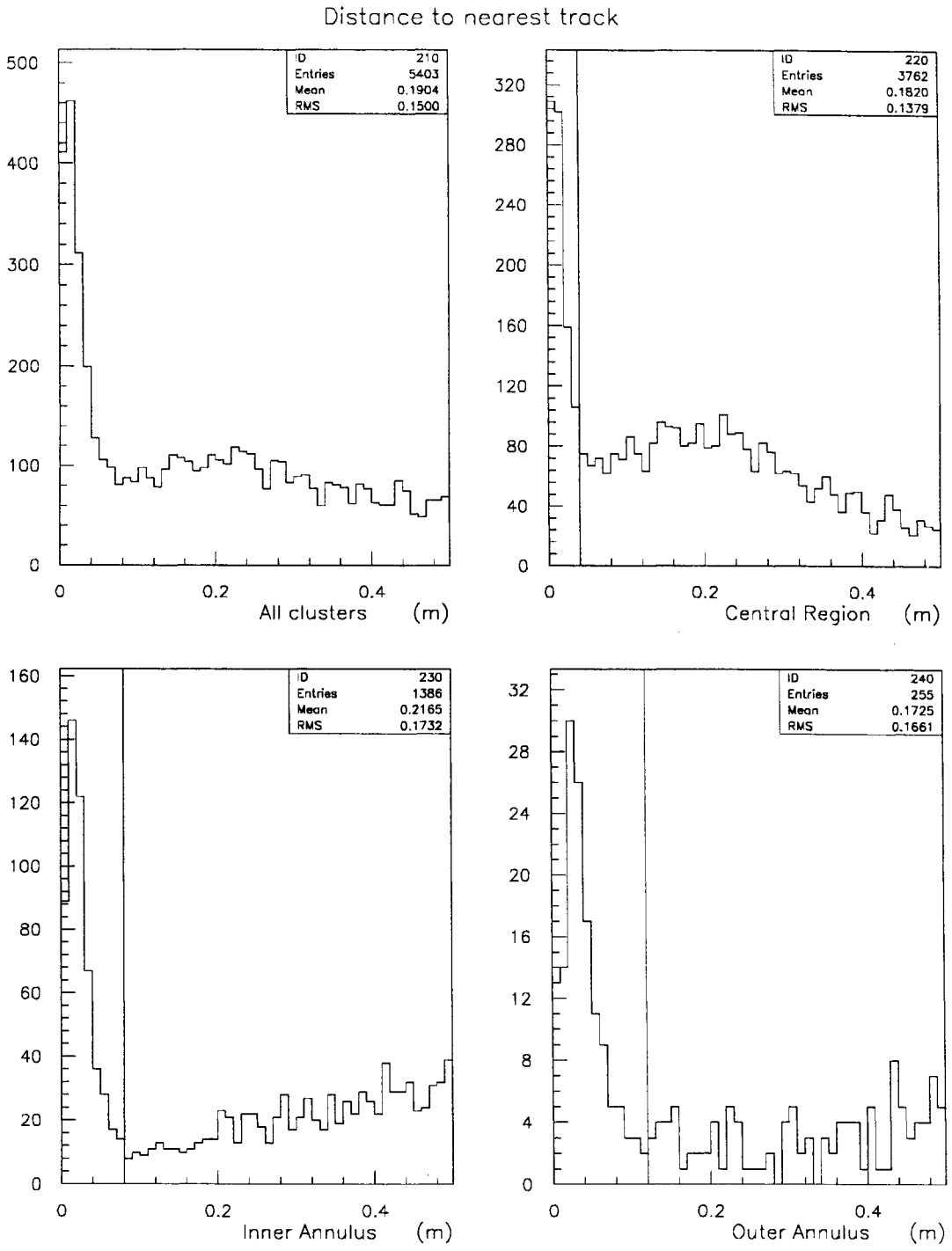

Figure 4-4: The Calorimeter Distance-to-nearest-track Cut.
The distance from the center of each cluster to the closest track is plotted in meters for clusters a) throughout the Calorimeter, b) in the central region only, c) in the inner annulus, and d) in the outer annulus. Only clusters with energy of at least 5 GeV are included. Plots b–d show the cut value that defines whether a cluster is "near" a track or not. The data in this plot are uncorrected. No cluster quality cuts have been made on the clusters in these plots.

- $E > 10$ GeV
- $|Y_{local}| < 1.4$ m
- $|Z_{local}| < 1.4$ m
- Neutral cluster:
  - ⋆ $d_{trk} > 4$ cm .OR. $E_c/p_{trk} > 1.5$ for the central region
  - ⋆ $d_{trk} > 8$ cm .OR. $E_c/p_{trk} > 1.5$ for the inner annulus
  - ⋆ $d_{trk} > 12$ cm .OR. $E_c/p_{trk} > 1.5$ for the outer annulus

4.9 Correction Philosophy

Given the data and a set of cuts on events and tracks, we can generate a collection of raw data plots. In some cases, however, these raw data plots contain effects from the E665 apparatus as well as the physics in which we are interested. Thus, it would be difficult to compare our raw data directly to other experiments. By comparing the raw data to results from a Monte Carlo which includes many of the apparatus effects, we can draw some useful conclusions. It would, however, be difficult to compare our data to theories other than the one built into our Monte Carlo. It would be preferable if the data stood by itself so that other theories and experiments can be tested against it in the future. Therefore, in order for the analysis results to be broadly applicable, we must attempt to eliminate any apparatus-specific effects.

There are two approaches to this goal, and both will be employed in this thesis. The first approach involves choosing a restrictive set of cuts so that we consider a region of event and hadron kinematics where the apparatus effects are known to be small. The second approach involves correcting for the known apparatus effects and presenting results as they would appear in an "ideal detector".

In order to define an ideal detector, we must define the "truth" quantities that we would expect to be able to measure with such a detector. The processes that are thought to occur during an event are:

1. A relatively hard interaction occurs, involving fundamental particles, such as muons, quarks, and gluons.
2. A collection of soft processes occur, including fragmentation and possible final state interactions.
3. Strong resonance decays occur for particles such as neutral rhos.

4. Other fast decays occur, such as that of the neutral pion ($c\tau = 25$ nm).

5. Semi-stable particles may decay with $c\tau$ values ranging from a few microns to kilometers.

6. Produced particles may undergo a secondary interaction in the target or the apparatus material.

7. The detector records particles, but with an imperfect acceptance and efficiency.

8. The software reconstructs particle momenta, but with some inefficiency.

There is no obvious place to draw the line between the interaction and the apparatus effects. Clearly processes 1 and 2 are part of the physics while processes 6–8 are detector-specific and have no place in an ideal detector. There are two main ambiguities involved in defining our ideal detector. The first question is what particles should be considered "detectable". For instance, a neutrino is detectable in principle, but not by our apparatus. We could take the point of view that this is an apparatus inefficiency. However, in this thesis, I will handle such cases by defining the "truth" physics distributions so as to exclude neutrinos. The second question involves whether our ideal detector should detect the primary particles before they decay. This question is actually quite difficult since unstable particles have a broad range of decay times. Clearly a muon with a $c\tau$ of nearly a kilometer should be treated as a stable particle. Any rare decay that does occur would be considered an apparatus inefficiency. On the other extreme are resonances such as the rho-zero. One could take the point of view that a rho-zero is reconstructible from its decay mode into charged pions and that an ideal detector would be able to reconstruct them with 100% efficiency. In this thesis, however, we will treat such resonance decays as part of the physics of the event, like fragmentation. Thus, a rho-zero is not considered a detectable particle, but the pions from its decay are considered detectable.

To summarize, "truth" charged particles consist of stable charged hadrons which were produced directly by the "interaction", where the interaction is understood to include the nearly instantaneous decays of unstable particles. A stable particle is any particle with a $c\tau > 1$ cm, whereas an unstable particle is any particle that has $c\tau < 1$ cm. The stable particles thus include $\pi^{\pm}$, $\mu^{\pm}$, $e^{\pm}$, $K^{\pm}$, p, and $\Sigma^{\pm}$ as well as the neutral particles: γ, $K^0_{S,L}$, Λ^0, and n. The unstable particles are resonances and short-lived particles such as: Σ^0, $D^{\pm}$, $D_s^{\pm}(F^{\pm})$. These definitions of stable versus unstable particles are the standard ones used in the E665 Monte Carlo. The π^0 is a special case. It is short-lived ($c\tau \sim 25$ nm), but we will treat it as a "truth" particle since it is so common and corresponds directly with the very common $\pi^{\pm}$ particle. Primary muons are not counted as truth particles since they are not used.

Truth charged hadrons must also satisfy the following additional cuts:

$$x_F^{true} > 0.0,$$

$$6 \text{ GeV} < E_h^{true} < 500 \text{ GeV}.$$

The motivation behind these cuts is that the reconstructed hadrons in the data had to satisfy similar cuts. We are limiting the "truth" distributions to those particles which are most easily measured in our detector. This will allow other experiments to be compared to ours within those ranges.

4.10 Summary

The data sample used in this thesis came from the 1987 Fixed Target run of Fermilab Experiment #665. The beam energy ranged from 300–700 GeV and averaged 490 GeV. The events used were taken with the Large Angle Trigger (LAT) and were from the Deuterium (D_2) target. The main cuts that were employed in this data sample were:

- One and only one beam,
- Vertex position in target,
- Calorimeter operational
  - ⋆ (1940 < Run # < 2640) .OR. (Run # > 2670)
  - ⋆ LGLB bank exists
- $x_{Bj} > 0.003$,
- $Q^2 > 2$ GeV^2,
- $\nu > 100$ GeV,
- $y_{Bj} < 0.9$,
- Bremsstrahlung-like events removed using the Calorimeter.

Additional quality cuts were imposed on the events as well as the requirement that the event be successfully reconstructed. 30.7×10^3 events survived the cuts.

The main cuts that were used for selecting charged hadrons were:

- $z_h < 1.1$,
- 6 GeV $< E_h <$ 500 GeV,
- $x_F > 0.0$.

Various additional quality cuts were also imposed on the tracks. The average number of charged hadrons per event was 2.05.

The clusters in the Electromagnetic Calorimeter were used to eliminate photon bremsstrahlung events. The energies of the highest energy neutral cluster and the highest energy π^0 candidate were saved for use in the "unambiguous Rank 1 cut" defined in Section 5.3.1.

Chapter 5

Physics Results

This chapter contains the main results of my physics analysis. Section 5.1 establishes some definitions of physics quantities. Section 5.2 contains a brief discussion of some of the previous results which are relevant to this analysis. Section 5.3 contains the results on the hadronic phi asymmetry in DIS. Section 5.4 contains the results on the hadronic transverse momentum in DIS. Section 5.5 describes some of the systematic errors that might be expected. Section 5.6 summarizes the results of this chapter. Chapter 6 summarizes the entire thesis.

5.1 Some Definitions

We will define the event kinematics in ways that are experimentally measurable. In Chapter 2 many of these quantities were defined as Lorentz invariant expressions. The experimental and theoretical definitions will coincide as long as the nucleon is at rest in the lab frame.

The beam and scattered muon energies are denoted E and E'. The energy transferred from muon to the nucleon during the scatter is known as ν: $\nu \equiv E - E'$. The fractional energy transfer is known as y_{Bj}: $y_{Bj} \equiv \nu/E$. The four momenta of the beam muon, scattered muon, and the "virtual photon" are known as l^μ, l'^μ, and $q^\mu = l^\mu - l'^\mu$. As was mentioned in Chapter 2, we choose to think of the four-momentum transfer as being carried by a virtual photon. This is really only true in leading order QED, but we will call the four-momentum-transfer q^μ in any case. The virtuality of the exchanged photon is given by $Q^2 \equiv -q^2$. After having absorbed the virtual photon, the hadronic final state has an invariant mass-squared given by $W^2 = 2M\nu - Q^2 + M^2$. Finally, the Bjorken scaling variable is given by $x_{Bj} = \frac{Q^2}{2M\nu}$. In the Naïve QPM this scaling variable is equivalent to ξ, the struck parton's longitudinal momentum frac-

tion (with respect to the nucleon) in the infinite momentum frame.

One of the unique features of muon scattering is that we know the direction taken by the virtual photon. Since the initial nucleon was at rest, the virtual photon direction should determine the direction that the outgoing hadrons will take in the lab. Any deviations from this direction will be due to the internal dynamics of the nucleon, the interactions of the partons, or the hadronization process. We will use $\hat{q}$ to denote the virtual photon three-momentum direction unit vector; this will also be known as the virtual photon axis.

In addition to measuring the basic event kinematics, we are also concerned with measuring the behavior of the hadrons produced in deep inelastic scattering events. E_h is the hadron energy in the lab frame. $z_h \equiv E_h/\nu$ is the fraction of the virtual photon energy that the hadron takes in the lab frame. $p_T^{(h)}$ is the transverse momentum of the hadron in the lab frame with respect to the virtual photon axis. φ_h is the azimuthal angle that the hadron makes about the virtual photon axis defined with respect to the scattered muon direction. $\varphi_h = 0$ when the hadron lies in the scattering plane on the side of the scattered muon (see Figure 2-8 on page 49).

By boosting along the virtual photon axis, we can transform the event into the center-of-mass frame of the hadronic final state. This transformation will not change $p_T^{(h)}$ or φ_h since they are transverse variables. In contrast, the longitudinal momentum and energy of the hadron will change. We can define a new variable in this cm frame: $x_F \equiv p_{||}/p_{||}^{(max)}$ or $x_F = 2p_{||}/W$. The values taken on by the variable x_F range from -1 to 1. The $x_F < 0$ particles lie in the *backward hemisphere* and generally are considered to belong to the target remnant or spectator jet. The $x_F > 0$ particles, known as *forward hadrons*, are the only ones considered in this thesis. For high values of z ($z \gtrsim 0.2$), $z \approx x_F$.

Another quantity that can be defined for each particle is its *rank*. In this thesis, rank will be defined according to the z_h of each particle. The most energetic particle will be called the *Rank 1* or *leading* particle, the particle with the next largest z_h will be called the *Rank 2* particle, and so forth. The z_h and φ_h of the Rank 1 particle will be denoted z_{h1} and φ_{h1} respectively.

This experimentally defined quantity of rank (in z_h) should not be confused with the theoretical concept of the rank of a particle in a hadronization chain such as that used in the Lund program. Insofar as the Lund string fragmentation model is valid there will be a correlation between the hadronization rank and the z_h rank, but they will not be identical.

The term rank will be used in two slightly different senses in this thesis. The uses will be distinguished by the "universe" of particles which we are ordering:

1. All stable charged particles from the DIS interaction.

2. All measurable particles from the interaction: stable charged particles plus π^0s, K^0s and so forth.

In general, we will be using the first definition of Rank 1: the leading charged particle. The reason for this is that the neutral particles (mostly π^0s) have a very different character in our detector than the charged particles (mostly $\pi^{\pm}$s). The neutral pions decay almost instantaneously into photons, each of which is reconstructed with an energy resolution of 10–20%. It is difficult to reconstruct these neutral pions on an event-by-event basis. Furthermore, there is no way to tell whether a photon came from the primary vertex or from some other downstream process such as a bremsstrahlung in the detector material, a decay, or a secondary interaction. In contrast, the charged pions are measured more precisely, with a momentum resolution of less than 10%. Furthermore, since charged particles leave tracks in the detector, we can tell which ones came from the primary vertex and which ones did not.

Physically, however, the second definition of rank makes the most sense and is the most interesting. For this reason, many of the plots will have cuts that allow us to use this definition. We will look at the leading particle only in events where we have detected it unambiguously. Other plots will be corrected to represent a measurement according to the second definition under the assumption that neutral and charged pions behave identically.

Some of the plots in this chapter will be corrected for acceptance. There are really two types of correction possible. The main effect of imperfect acceptance is that some particles are lost. A simple acceptance correction would take into account the fact that we are not 100% efficient at detecting particles. This type of correction would involve measuring the efficiency of particle detection and weighting the particles accordingly to account for the inefficiency. Another effect of imperfect acceptance is that we tend to mismeasure the rank. If we miss the Rank 1 particle then we will mislabel the Rank 2 particle as Rank 1. We will call this *rank mixing*. It is only important for low values of z_h. A rank mixing correction would modify Rank 1 distributions based on the distributions for Rank 2 and Rank 3 particles, given the efficiency. It is the rank mixing correction that will be applied in this thesis, while the simple acceptance effects will be treated as a small systematic error.

5.2 History

5.2.1 Transverse Momentum History

In 1980, the transverse momentum of the hadrons produced in DIS was believed to arise from three sources:

1. Intrinsic or primordial transverse momentum of the partons,
2. Perturbative QCD effects,
3. Non-perturbative hadronization.

All three of these sources are manifestations of the strong interactions. If we understood the strong interactions completely, the transverse momentum distribution could be predicted unambiguously. Despite their common origin in the strong interaction, these sources can be considered as physically distinct because they arise from different dynamics and have different experimental signatures. The primordial $k_\perp$ of the struck parton arises because it was originally bound in the struck nucleon. The perturbative QCD effects are part of the hard interaction between the muon and quasi-free quarks and gluons. The hadronization involves the recombination of quarks and gluons into hadrons. The differences between these processes should show up in the way that the transverse momenta of the hadrons in the event are correlated.

The intrinsic transverse momentum ($k_\perp$) is due to the motion of the partons inside the nucleon. Instead of being free, as assumed in the Naïve QPM, the struck parton had been interacting with other partons, normally thought of as spectators in the interaction, giving it a $k_\perp$. When the quark is struck, it retains this $k_\perp$ with respect to the virtual photon axis. In order to conserve momentum, the target remnant will have to have an equal and opposite $k_\perp$. If we view this process in the center-of-mass frame, the struck quark and the target remnant will still be traveling back-to-back, but the overall axis will be rotated away from the virtual photon axis. Experimentally, then, the intrinsic transverse momentum should show up as an increase in the hadrons' p_T at large $|x_F|$ in both hemispheres ($p_T^2 \sim x_F^2 k_\perp^2$). Furthermore, the additional p_T contributed to the hadrons in the forward hemisphere ($x_F > 0$) should be compensated by a nearly equal and opposite p_T contribution in the backward hemisphere ($x_F < 0$).

Perturbative QCD also contributes to the hadron p_T. For example, a quark that initially has no p_T with respect to the virtual photon direction can acquire p_T by radiating a gluon. Both the quark and the gluon will acquire p_T in this fashion. They will then share this p_T among the hadrons in the forward hemisphere. Alternatively, a gluon from the nucleon can fuse with the virtual photon to generate a $q\bar{q}$-pair

each of which will have p_T. The main distinguishing feature of the perturbative QCD contribution is that the generated transverse momentum will primarily occur in the forward hemisphere. In the case of gluon bremsstrahlung, for instance, the gluon radiation is due to the fact that the struck quark has been accelerated by its interaction with the muon. The target remnant object (a diquark or perhaps a more complicated object) is a spectator and should not be accelerated. A similar argument for the case of photon-gluon fusion shows that the p_T should be generated in the forward hemisphere for that process as well. In general, QCD will cause any transverse momentum in the very forward direction to be compensated in the forward hemisphere.

The hadronization process itself will generate p_T in the produced hadrons. Even if the partons in the event all had $p_T = 0$, the hadrons would have some p_T. This p_T induced by hadronization is expected to be independent of the event kinematics. The argument is that the hadronization process is basically independent of underlying partonic process. If we assume that some sort of string-like fragmentation scheme is valid, then when a string breaks at a given point the q and $\overline{q}$ will acquire equal and opposite p_T with respect to the string. This will tend to cause neighboring particles in z_h or x_F to have compensating p_T.

In 1980, EMC examined the transverse momentum of forward charged hadrons in DIS [43]. The amount of p_T due to hadronization was set by comparison with $e^+ e^-$ experiments and the p_T due to QCD was calculated numerically in the Monte Carlo. They found that they need to set $\langle k_\perp^2 \rangle \sim (0.8 \text{ GeV})^2$ in their Monte Carlo in order to explain the large amount of p_T for the very forward particles ($z_h > 0.3$).

Due to the high value of $k_\perp$ indicated by the EMC data, a fourth source of transverse momentum was considered [44]. The basic idea behind this new source was that it is possible for the struck quark to undergo multiple "soft" gluon radiation in addition to the perturbative "hard" gluon radiation that we can calculate. This "soft gluon radiation" would take place in the forward hemisphere only. This idea was attractive because the value of $\langle k_\perp^2 \rangle$ implied by the EMC data was considered to be too high. If we consider a quark to be confined within a nucleon with a radius of about 1 fm, then the uncertainty principle implies a value for $\langle k_\perp^2 \rangle$ of roughly $(0.1\text{–}0.2 \text{ GeV})^2$. The soft gluons allowed one to fit the forward hemisphere data without such large values of $k_\perp$. The disadvantage of this main source is that it adds yet another parameter to the models, decreasing their predictive power. Indeed, this new parameter was implemented in the Lund Monte Carlo in a rather ad hoc fashion. It basically just added some random p_T to each hadron in the forward hemisphere. With so many sources of transverse momentum and so many different parameters it is difficult to understand the experiments unambiguously.

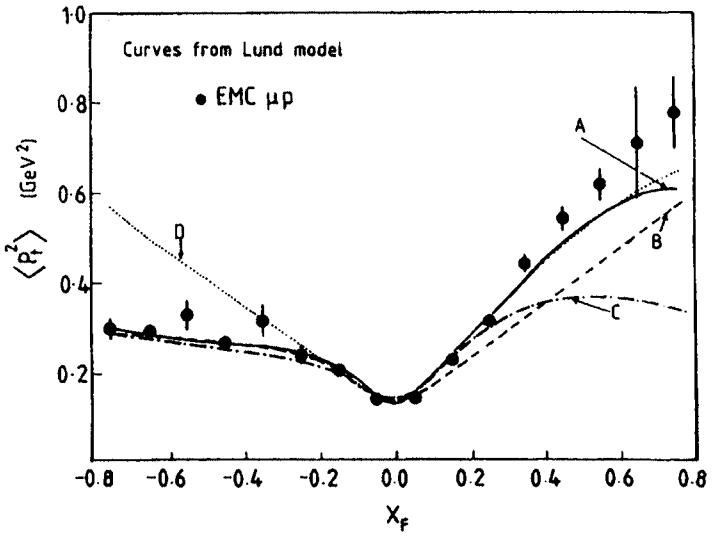

Figure 5-1: EMC Seagull Plot.
This plot, taken from Reference [46], shows the $\langle p_T^2 \rangle$ as a function of x_F. It is compared with predictions of the Lund (Lepto 4.3) model. The data favors curve A: Hard QCD on, Soft Gluons on, $\langle k_\perp^2 \rangle = (0.44 \text{ GeV})^2$, and $\sigma_q = 0.44$ GeV. The other curves are described in the text.

In 1984 and 1987, EMC examined the hadrons in the backward hemisphere [45, 46] as well as those in the forward hemisphere. Figure 5-1, taken from Reference [46], shows the result. The data are compared to the predictions of the Lund Monte Carlo (Lepto 4.3) with four different settings for the parameters. These settings are:

A Hard QCD active, Soft gluons active, $\langle k_\perp^2 \rangle = (0.44 \text{ GeV})^2$

B Hard QCD OFF, Soft gluons active, $\langle k_\perp^2 \rangle = (0.44 \text{ GeV})^2$

C Hard QCD active, Soft gluons OFF, $\langle k_\perp^2 \rangle = (0.44 \text{ GeV})^2$

D Hard QCD active, Soft gluons OFF, $\langle k_\perp^2 \rangle = (0.88 \text{ GeV})^2$

In all four cases the fragmentation p_T parameter was given by $\sigma_q = 0.44$ GeV.

Curves A and D both fit the data in the forward hemisphere. It was this fact which led to a debate as to whether the forward seagull plot should be attributed to a large amount of primordial $k_\perp$ or to the effect of soft gluons. The new data showed that the seagull plot was asymmetric. There is more transverse momentum in the far forward direction than in the far backward direction. This result favors the

soft gluon interpretation (curve A) since increased primordial $k_\perp$ (curve D) leads to a symmetric seagull plot. Of the sources that we have discussed, only QCD (soft or hard) contributes asymmetrically to the forward and backward hemisphere. Hence, only soft or hard QCD can explain this effect. One important caveat should be included. The forward-backward asymmetry in the data is primarily due to comparing backward protons with forward π^+s. If one examines only the negative particles, which are primarily π^-s, then no conclusion can be drawn [45]. Despite this caveat, it seems clear that we need an explanation for this forward-backward asymmetry. Soft QCD serves this purpose, at the cost of an additional arbitrary parameter.

An additional piece of evidence in favor of the soft-gluon model is the fact that it does a much better job of describing the transverse momentum balance plots. In this case, only events which contained a very energetic hadron ($z_h > 0.5$) were examined. Define the direction vector of the leading hadron p_T as $\hat{p}_T^{(1)}$. We are interested in the quantity $p_T^{bal} \equiv \left\langle \vec{p}_T \cdot \hat{p}_T^{(1)} \right\rangle$ for the remaining particles in the event. This tells us where the leading particle's $\vec{p}_T$ is balanced. If the dominant source of p_T is the primordial $k_\perp$, then the p_T should be balanced primarily in the backward hemisphere. On the other hand, QCD effects (soft or hard) should show up in the forward hemisphere. Figure 5-2 (also from Reference [46]) shows the result of p_T^{bal} plotted versus rapidity:

$$y^* \equiv \frac{1}{2} \ln \left(\frac{E + p_{||}}{E - p_{||}} \right).$$

The data strongly disagree with the large $k_\perp$ model (curve D) and again favor the soft gluon model (curve A).

5.2.2 Phi Asymmetry History

A phi asymmetry in the hadrons was expected [18, 19] due to the effects of QCD and primordial $k_\perp$. An early muon result from Fermilab [47] found very little phi asymmetry ($\langle \cos\varphi \rangle \sim -0.03$). The statistical precision of the data was not very good, however, and they drew no firm conclusion. They used a beam energy of 219 GeV. Their result ranged from 2–30 GeV^2 in Q^2 and showed no significant dependence on Q^2.

In 1983, the EMC Collaboration measured the phi asymmetry with better statistical precision [48]. They chose to plot it in terms of $\langle \cos\varphi \rangle / f_1(y)$,[1] where $f_1(y)$ is defined as $(2-y)\sqrt{1-y}/[1+(1-y)^2]$ (See Equation 2.53 on page 51 of this thesis).

[1] Actually, it is unclear from the EMC paper whether they are plotting $\langle \cos\varphi / f_1(y) \rangle$, $\langle \cos\varphi \rangle / \langle f_1(y) \rangle$, or $\langle \cos\varphi \rangle / f_1(\langle y \rangle)$.

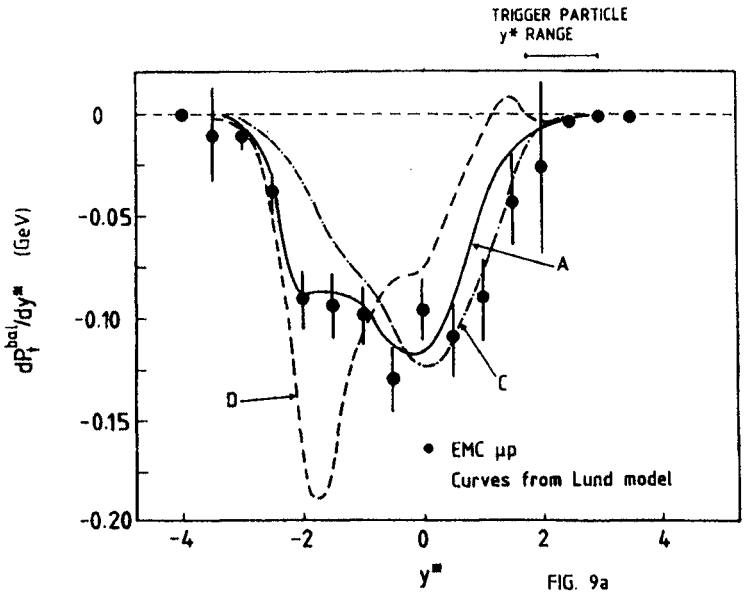

Figure 5-2: EMC Transverse Momentum Balance Plot.
This plot, taken from Reference [46], shows the p_T^{bal} as a function of the rapidity y^*. It is compared with predictions of the Lund (Lepto 4.3) model. The data favors curve A: Hard QCD on, Soft Gluons on, $\langle k_\perp^2 \rangle = (0.44 \text{ GeV})^2$, and $\sigma_q = 0.44$ GeV. The other curves are described in the text.

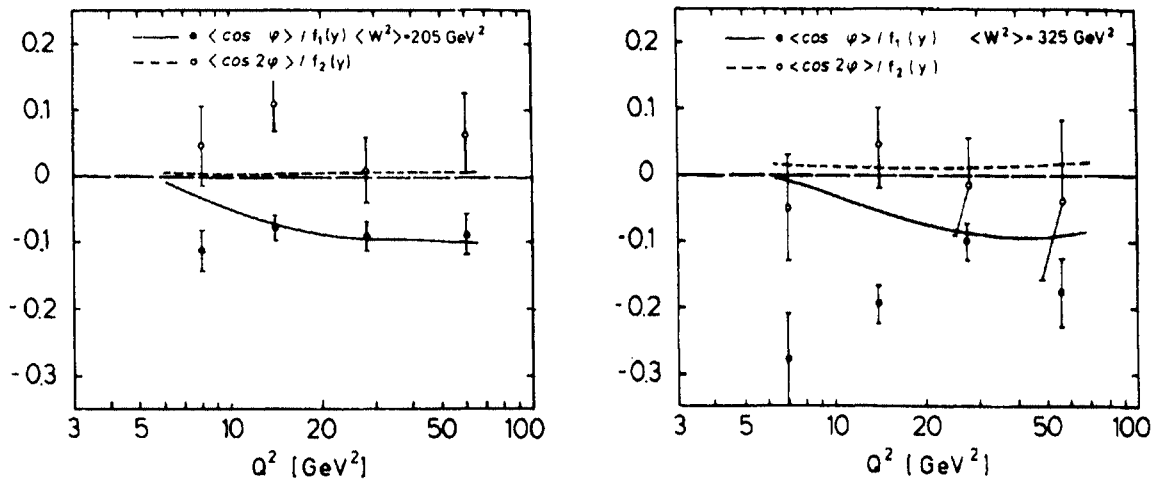

Figure 5-3: EMC φ_h versus Q^2.
This plot, taken from Reference [48], shows $\langle \cos\varphi \rangle / f_1(y)$ as a function of Q^2 for a beam energy of 280 GeV. The data are shown in two different ranges of W^2: a) $160 < W^2 < 260$ GeV^2 and b) $260 < W^2 < 460$ GeV^2.

This choice was due to the fact that the calculated value for $\langle \cos\varphi \rangle_{parton}$ is proportional to $f_1(y)$. They found a phi asymmetry in the data which was nonzero and they showed that it was nearly independent of Q^2. They compared their results to the model by König and Kroll [17] with a large value of the primordial transverse momentum parameter $\left\langle k_T^F \right\rangle = 0.7$ GeV. This parameter is meant to be equivalent to average $k_\perp$, but must be understood in the context of König and Kroll's theory. In their theory, the $k_\perp$ distribution is cut off at high values of $k_\perp$. Furthermore, this $k_\perp$ cutoff depends on the kinematics of the interaction. The cutoff becomes more severe at low values of Q^2, going to 0 as $Q^2 \to 0$. In their theory, therefore, **the effective value of $\langle k_\perp \rangle$ depends on Q^2 and x_{Bj}**. Based on this, they predict that the phi asymmetry will vanish at low values of Q^2, reach a maximum at moderately high values of $Q^2 \approx 50$ GeV^2 and then decrease to zero for large values of Q^2. In contrast, Cahn's model predicts a large asymmetry for low values of Q^2 and a vanishing asymmetry at large values of Q^2. The EMC data, shown in Figure 5-3, do not favor the phi asymmetry vanishing at low or high Q^2, causing problems for both models. The EMC data show little dependence of the phi asymmetry on Q^2. The statistical precision of the high energy data, however, make it difficult to tell whether the phi asymmetry is getting more pronounced at low Q^2, as predicted by Cahn.

In 1987, EMC compared the behavior of the phi asymmetry of the hadrons in the backward hemisphere and the forward hemisphere [49]. Theoretical results [17, 19] indicated that the the phi asymmetry of the forward hadrons should be dominated

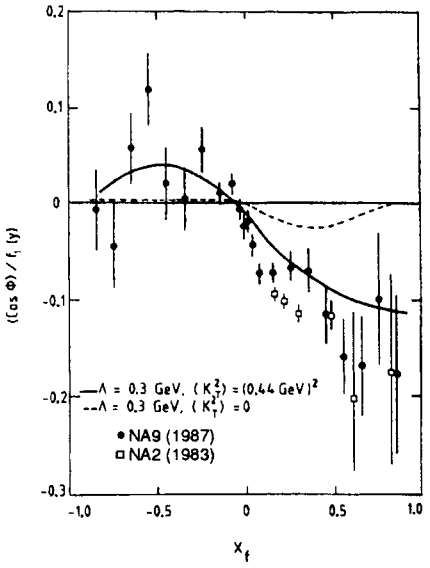

Figure 5-4: EMC φ_h versus x_F.
This plot, taken from Reference [49], shows $\langle\cos\varphi\rangle / f_1(y)$ as a function of x_F for charged hadrons with $p_T > 0.2$ GeV. The curves show the predictions from Reference [17].

by the effects of primordial $k_\perp$ at the values of Q^2 probed by EMC. This implied that the phi asymmetry in the backward hemisphere should be nearly equal and opposite to that in the forward hemisphere. The EMC data are shown in Figure 5-4. The prediction is from König and Kroll [17]. This model didn't include any kind of soft gluon effect. The forward hemisphere data showed a more pronounced phi asymmetry than predicted. This suggested that there should be more $k_\perp$ or a stronger effect from the QCD. The EMC Collaboration pointed out that even a value of $\langle k_\perp^2\rangle = (0.88\ \text{GeV})^2$ wasn't quite enough to match the data. The data in the backward hemisphere suffered from a lack of statistical precision. Nevertheless, it seems clear that the backward hemisphere phi asymmetry is not equal and opposite to the forward hemisphere phi asymmetry.

We will now turn to the analysis of the data from Experiment #665 at Fermilab. Using the post-December 1 data from the 1987 run, Ryan [25] examined the phi asymmetry and raised some intriguing points. First he showed that the phi asymmetry appears to depend upon the rank of the hadron independently of the z_h of the hadron. Second, he conjectured that the z_h-dependence of the phi asymmetry may actually just be an artifact of the dependence on rank. Unfortunately, no firm conclusions could be drawn regarding this conjecture, due to the lack of statistical precision. Using all of the data from the 1987 run, Jansen [50] also examined the phi asymmetry as a function of several variables.

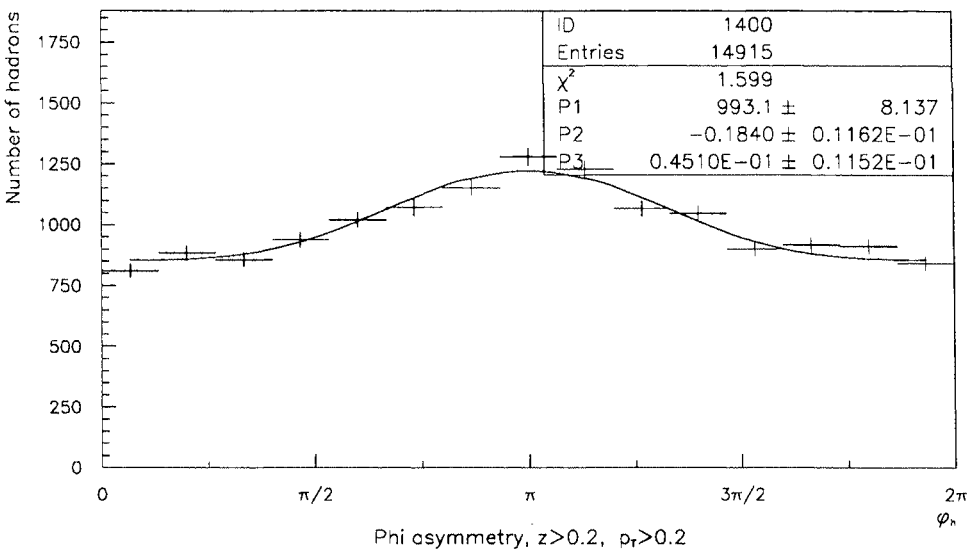

Figure 5-5: Raw Hadronic Phi Distribution.
Uncorrected phi distribution with arbitrary normalization. This plot shows all reconstructed hadrons with $z_h > 0.2$ and $p_T > 0.2$ GeV. The fit is of the form $P1(1 + P2\cos\varphi_h + P3\cos 2\varphi_h)$.

It would be nice if we could present a consistent picture of the phi asymmetry and the transverse momentum distributions and correlations. Unfortunately, the results seem inconclusive. It doesn't really seem possible to fit the p_T and φ_h distributions simultaneously. The phi asymmetry and p_T seem to be large in the forward hemisphere, suggesting that $\langle k_\perp^2 \rangle$ is larger than $(0.44\ \text{GeV})^2$. The phi asymmetry, the overall p_T, and the p_T-balance in the backward hemisphere seem to be too small to allow for more $k_\perp$.

5.3 Phi Asymmetry

Since the existence of a phi asymmetry in the hadrons produced in deep inelastic scattering is well established, the major objective of this analysis is to examine the phi asymmetry in detail in order to see whether it can be explained in terms of known effects. We will pay particular attention to the rank and z_h dependence of the phi asymmetry as well as the Q^2 dependence.

The hadronic phi asymmetry is easily seen in our raw data. Figure 5-5 shows the uncorrected phi distribution for hadrons with $z_h > 0.2$ and $p_T > 0.2$ GeV. The cut

values for z_h and p_T were chosen in order to compare with previous results. The cut on z_h also enhances the effect. The curve is a fit to the functional form:

$$\frac{dN}{d\varphi_h} = A + B\cos\varphi_h + C\cos 2\varphi_h. \tag{5.1}$$

More explicitly, the fit parameters P1–P3 are given by:

$$\frac{dN}{d\varphi_h} = P1(1 + P2\cos\varphi_h + P3\cos 2\varphi_h). \tag{5.2}$$

The parameters have the following meanings:

$P1$: This parameter is proportional to the multiplicity: $P1 = N_{\mu'}N_h/2\pi$,

$P2$: This parameter characterizes the strength of the $\cos\varphi_h$ term: $P2 \equiv B/A = 2\langle\cos\varphi_h\rangle$,

$P3$: This parameter characterizes the strength of the $\cos 2\varphi_h$ term: $P3 \equiv C/A = 2\langle\cos 2\varphi_h\rangle$.

Since we aren't interested in multiplicity in this analysis, we can ignore $P1$. We are only interested in the parameters which characterize the phi asymmetry: $P2 \equiv B/A$ and $P3 \equiv C/A$. We can see from Figure 5-5 that the B/A term is quite significant. This is the quantity that we want to study in more detail. If the parent distribution is of the form given in Equation 5.1, then the fit parameters will be equivalent to the moments:

$$\begin{aligned} B/A &= 2\langle\cos\varphi_h\rangle, \\ C/A &= 2\langle\cos 2\varphi_h\rangle \end{aligned} \tag{5.3}$$

where

$$\langle f(\varphi_h)\rangle \equiv \int_0^{2\pi} f(\varphi_h)\frac{dN}{d\varphi_h}d\varphi_h \Big/ \int_0^{2\pi} \frac{dN}{d\varphi_h}d\varphi_h. \tag{5.4}$$

In fact, since the functions 1, $\cos\varphi_h$, and $\cos 2\varphi_h$ are orthogonal, the fit parameters and moments will be nearly equivalent even if the parent distribution is different from Equation 5.1. To be more specific, Equation 5.1 doesn't contain a term proportional to $\sin\varphi$. This is because previous results have shown this quantity to be negligible. We have neglected it so as to simplify the presentation of the data. Since $\cos\varphi$ and $\sin\varphi$ are orthogonal functions ($\int_0^{2\pi}\sin\varphi\cos\varphi = 0$), any small $\sin\varphi$ term in the true distribution won't affect our measurement of the coefficient of $\cos\varphi$.

Broadly speaking, there are two main thrusts to this analysis. The first is to investigate the behavior of the phi asymmetry with respect to other hadron variables

such as z_h and p_T. The second is to investigate the behavior of the phi asymmetry with respect to event kinematics. This is interesting because the theory (see Chapter 2) makes very specific predictions for the behavior of the parton-level phi asymmetry as a function of Q^2 and y_{B_J}.

Some previous analyses have assumed that the parton-level theory for the y_{B_J}-dependence was correct and also valid for hadrons. For this reason, they plotted quantities such as $\langle \cos\varphi \rangle / \left\langle f_1(y_{B_J}) \right\rangle$. Even if the theory is correct regarding the underlying parton dynamics, we expect that the process of fragmentation will tend to wash out the phi asymmetry that is seen in the hadrons. This means that the phi asymmetry in the hadrons need not be proportional to $f_1(y)$ even if the underlying partonic theory is correct. Furthermore, even if we expected $\langle \cos\varphi_h \rangle$ to be proportional to $f_1(y)$, we would want to compare our data to our theoretical expectations rather than assume that the the theory is true.

5.3.1 Phi Asymmetry versus z_h and Rank

In order to investigate the rank dependence of the phi asymmetry meaningfully we must simultaneously examine the z_h dependence of the phi asymmetry. This is because the rank and z_h are directly correlated; the rank is defined as the order in z_h. We want to compare the behavior of particles of different rank at the same value of z_h (from different events) in order to separate out the effects.

For instance, we would like to investigate the z_h-dependence of the phi asymmetry of the leading charged particle. In order to do this we break the data up into several subsamples according to the value of z_{h1} (the z_h of the leading hadron). We then plot and fit the $dN/d\varphi_{h1}$ distribution for each subsample. Figures 5-6 and 5-7 show the results of this operation. In order to emphasize the z_h-dependence, the next step is to extract the fit quantities: $P2 \equiv B/A$ and $P3 \equiv C/A$ for each individual range of z_{h1}. We can then make a plot of B/A and Z/A versus z_{h1}. Figure 5-8 shows the result. As we noticed before, there is a strong $\cos\varphi_h$ moment and only marginal evidence for the existence of a $\cos 2\varphi_h$ moment.

In a similar fashion we can plot the z_h-dependence of the non-leading particles. Figure 5-9 shows the z_h-dependence plots for Rank 1, Rank 2, and Rank > 2 overlaid. It is clear that there is a strong Rank dependence of the phi asymmetry, in particular the B/A term, in the data. The leading particle (Rank 1) behaves differently than the other particles. This result has not been predicted by any of the models in the literature. There is no significant difference seen here between particles of Rank 2 and those of Rank> 2. At high z_h, the phi asymmetry seems to be nearly independent of z_h. At low z_h, however, the phi asymmetry of the leading particle seems to depend on z_h. It is possible that this apparent z_h-dependence is actually an artifact of the

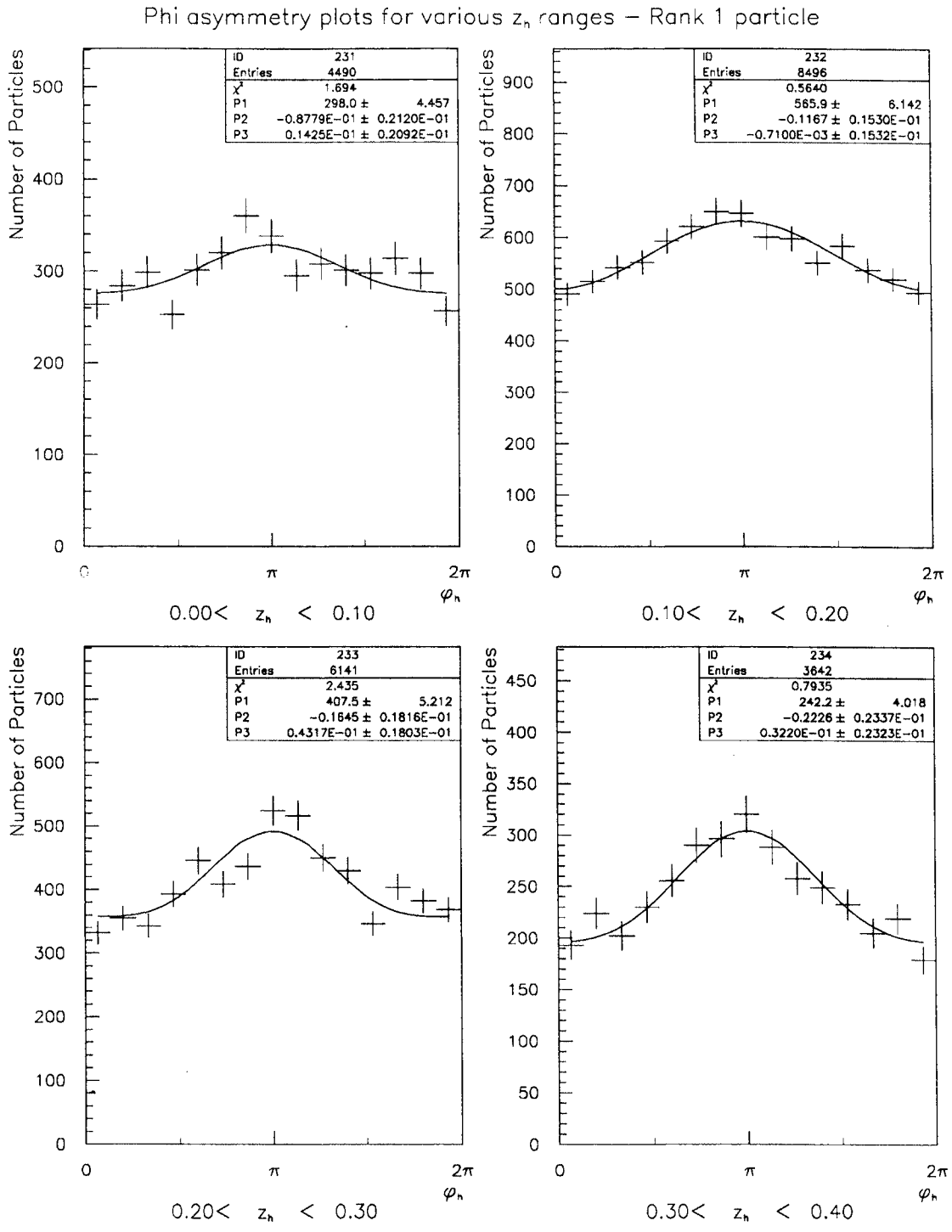

Figure 5-6: Raw Phi Distributions for Various z_{h1} Ranges (1).
Uncorrected phi distributions with arbitrary normalizations. These plots include all leading charged hadrons. The different plots correspond to different ranges of the variable z_{h1}. The fits are of the form: $P1(1 + P2\cos\varphi_h + P3\cos 2\varphi_h)$.

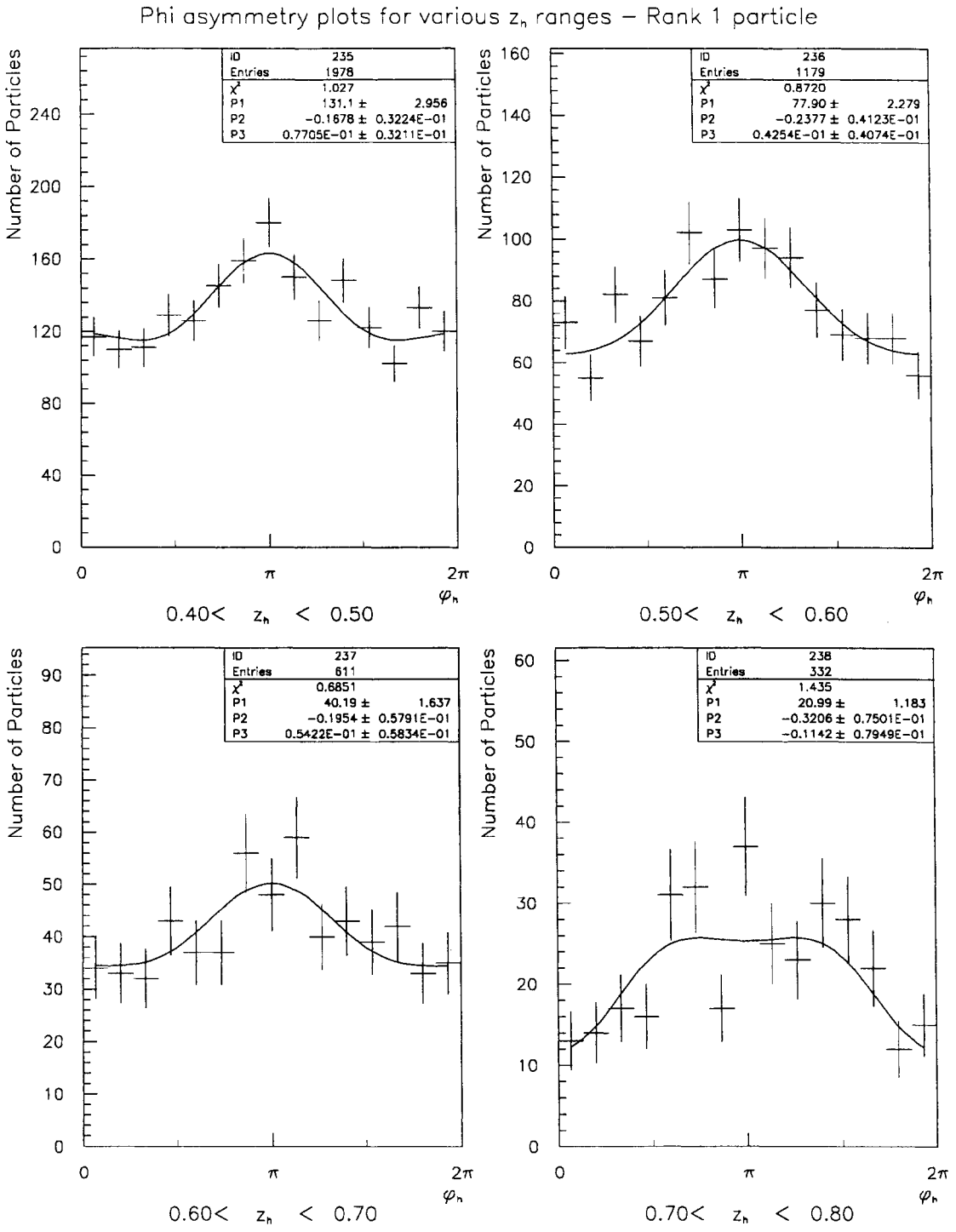

Figure 5-7: Raw Phi Distributions for Various z_{h1} Ranges (2).
Uncorrected phi distributions with arbitrary normalizations. These plots include all leading charged hadrons. The different plots correspond to different ranges of the variable z_{h1}. The fits are of the form: $P1(1 + P2\cos\varphi_h + P3\cos 2\varphi_h)$.

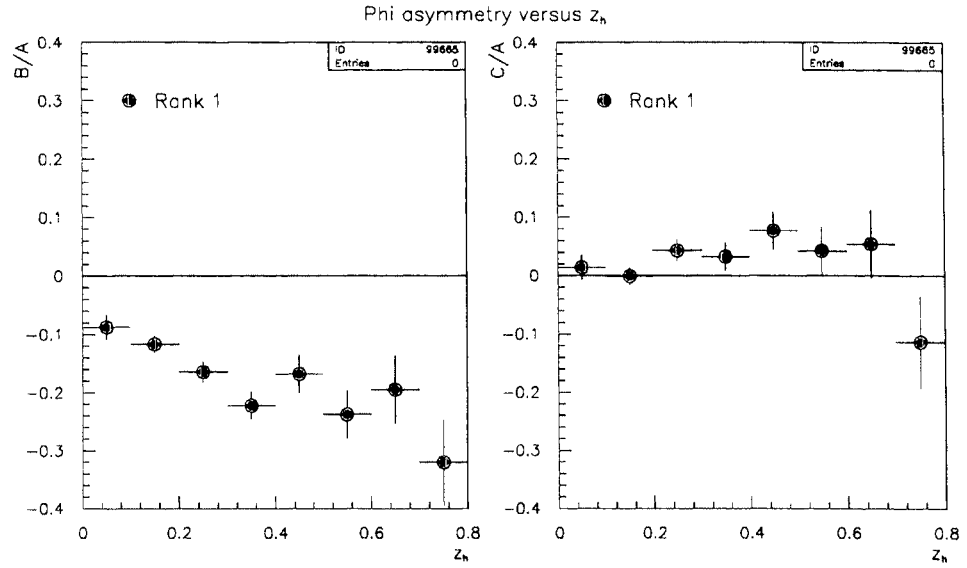

Figure 5-8: The z_h-dependence of the Phi Asymmetry for Rank 1 Hadrons.
Fit parameters $B/A \approx 2\langle\cos\varphi\rangle$ and $C/A \approx 2\langle\cos 2\varphi\rangle$ versus z_{h1} for the leading charged particle. These data are not corrected for acceptance.

rank mixing (see Section 5.1). At low z_h, some of the particles which we measure as Rank 1 could actually be Rank 2 particles. At high z_h, the Rank 1 sample is fairly pure.

Two questions immediately arise. First, is the rank-dependence already "understood" and present in our Monte Carlo? Second, what are the effects of acceptance on the z_h- and rank-dependence of the phi asymmetry?

In order to address the first question, we note that there are several complicated effects modeled in the Monte Carlo which could contribute to the difference between particles of differing ranks. These include the physics of fragmentation, the fact that the leading hadron is more likely to come from the leading parton in QCD events, and the detector acceptance. The Monte Carlo contains a simple fragmentation model and contains all of the understood detector effects, so we should be able to address this question. Figure 5-10 shows that the Monte Carlo predicts little dependence on rank, but it does predict a dependence on z_h.

The conclusion that we should draw from these plots is that there is a significant difference in the phi asymmetry in the data between leading and non-leading charged particles in an event, even at the same value of z_h. Furthermore, this rank dependence is larger than expected, based on the Monte Carlo.

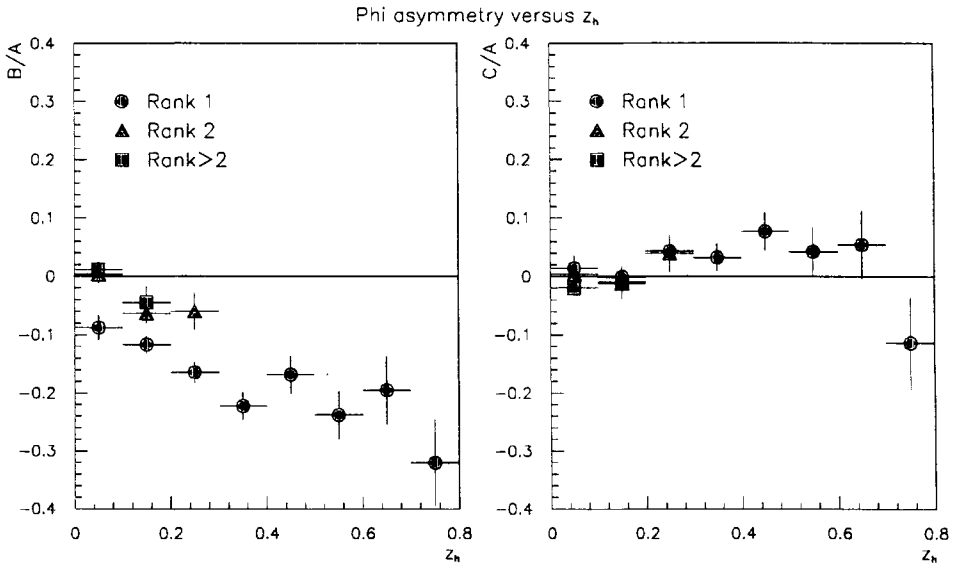

Figure 5-9: The z_h-dependence of the Phi Asymmetry by Hadron Rank.
Fit parameters $B/A \approx 2\langle\cos\varphi\rangle$ and $C/A \approx 2\langle\cos 2\varphi\rangle$ versus z_h for different particle ranks. These data are not corrected for acceptance.

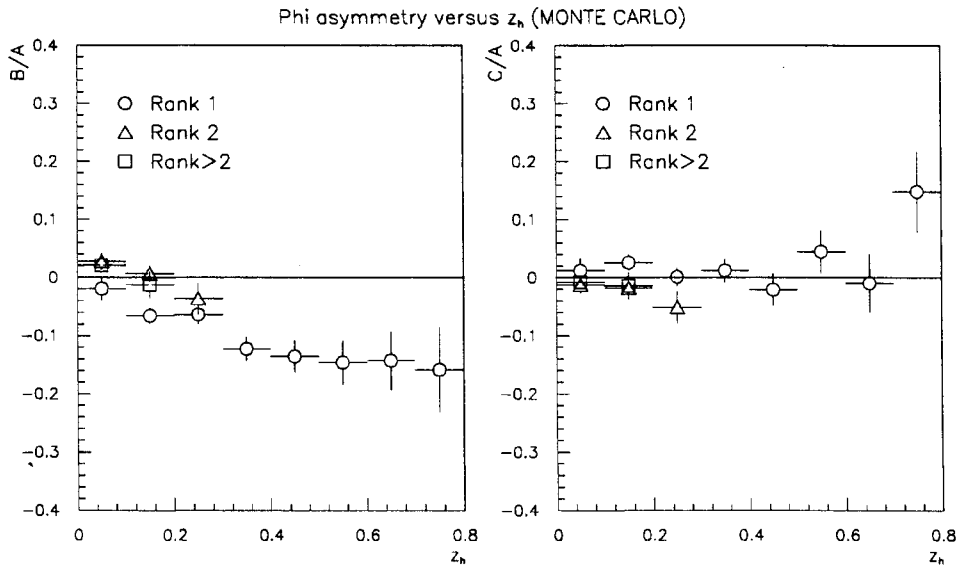

Figure 5-10: The z_h-dependence of the Phi Asymmetry by Hadron Rank (MC).
Fit parameters $B/A \approx 2\langle\cos\varphi\rangle$ and $C/A \approx 2\langle\cos 2\varphi\rangle$ versus z_h for different particle ranks in Monte Carlo. These Monte Carlo results include the full apparatus and reconstruction code simulation and should be compared to uncorrected data.

The second question from above, concerning the effect of acceptance, is a much trickier one to address. First, we should note that the effect of a simple acceptance correction to Figure 5-9 will be small, except in the first bin ($0.0 < z_h < 0.1$). A larger effect will come from the rank mixing. In general, the effect of the rank mixing should be to contaminate the Rank 1 sample with Rank 2 particles. This will tend to make the ranks less distinctive, weakening the measured rank dependence. For this reason the corrected data should show a bigger difference between leading and non-leading particles.

There are two approaches that we can take in order to try and get at the more fundamental distribution. We can attempt to find a cut on the data that will explicitly minimize the effect of the rank mixing, hopefully without losing all of the statistical precision. Alternatively, we can attempt to correct for the rank mixing (defined on page 137) by using Monte Carlo estimates of the hadron reconstruction efficiency. Both of these approaches will be employed.

Selecting Events with Good Reconstruction Efficiency

In this section, we will try to find a fairly pure sample of Rank 1 hadrons. Let's define a quantity $\Sigma_{ch}z$. $\Sigma_{ch}z$ is the sum of measured z values for all charged particles. If the z of the leading particle (z_{h1}) is large enough, $z_{h1} > 1 - \Sigma_{ch}z$, then we know that the leading charged particle is really the leading particle (charged or otherwise). This is because any missing particle must have $z_h < 1 - \Sigma_{ch}z < z_{h1}$. Unfortunately, this cut is quite extreme. It has the effect of throwing away almost all of the leading particles except those with $z > 0.3$. Since there are very few Rank 2 particles with $z > 0.3$, there is no longer any overlap for us to be able to compare the different ranks. Furthermore, we already know that there is no z-dependence of the phi asymmetry for $z_{h1} > 0.3$ anyway and we won't learn anything new.

A more practical cut can be chosen if we define the quantity $\Sigma_{all}z$:

$$\begin{aligned} \Sigma_{all}z &\equiv [(\sum E_h^{chgd.}) + (\sum E_{CAL})]/\nu \\ &= \sum_{ch} z_h + [(\sum E_{CAL})/\nu], \end{aligned} \tag{5.5}$$

where $\sum E_{CAL}$ is the sum of the electromagnetic energy in the Calorimeter. See Section 4.8 for a description of the cuts that go into defining this sum. Now, if $z_{h1} > 1 - \Sigma_{all}z$, then we know that there is no missing charged particle with $z_h > z_{h1}$. This cut picks out the most energetic of the charged particle. It leaves open the possibility that there was a π^0 or other neutral particle with even more energy than our leading charged particle. In order to get at the sample of charged particles which are the leading particles in the entire event, we must also remove any events which

appear to have a leading π^0. A π^0 decays almost instantaneously into a pair of photons, which can show up in the Calorimeter in several different forms:

- Two isolated clusters with a combined invariant mass near m_{π^0}. In this case, $E_{\pi^0} = E_{\gamma 1} + E_{\gamma 2}$.
- A single cluster due to two merged photons. In this case, $E_{\pi^0} = E_{cluster}$.
- A single cluster due to the loss of one (usually low energy) photon. In this case, $E_{\pi^0} \gtrsim E_{cluster}$.

In order for the Rank 1 charged particle to be unambiguously Rank 1, it must be more energetic than every Calorimeter cluster. Furthermore, the Rank 1 charged particle must be more energetic than any π^0 candidates[2]. This set of cuts defines a relatively pure sample of charged hadrons that are Rank 1 in the most restrictive sense.

Figure 5-11 illustrates the effects of the various cuts on the raw data sample. The effect of the cuts on the Rank 1 particle can be seen in the three curves in Figure 5-11a. The highest curve shows the uncut distribution, while the second highest curve shows the distribution of particles satisfying $z_{h1} \ni z_{h1} > \max\{(1 - \Sigma_{all} z), z_\gamma, z_{\pi^0}\}$, and the lowest curve shows the distribution of particles satisfying $z_{h1} \ni z_{h1} > 1 - \Sigma_{ch} z$. Figure 5-11b shows the Rank 2 particle distributions for events in which the Rank 1 particle satisfies the cuts described above. The main point of this plot is to show that the $z_{h1} \ni z_{h1} > 1 - \Sigma_{ch} z$ cut is too severe. After such a cut is made, the Rank 1 particles which remain have $z_h > 0.3$. This is not very useful for comparison with Rank 2. The cut using the Calorimeter also hurts the statistical precision, but some overlap between Rank 1 and Rank 2 remains. Furthermore, we can now investigate the behavior of the Rank 1 particle when it is in the range $0.2 < z_h < 0.3$.

The Rank 1 particles that survive the cut:

$$z_{h1} \ni z_{h1} > \max\{(1 - \Sigma_{all} z), z_\gamma, z_{\pi^0}\}$$

will be known as *unambiguous Rank 1 particles*. These are particles that we believe are the leading particle in the entire event, including neutrals.

Figure 5-12 shows the result of keeping only the events where we know the Rank 1 charged hadron is actually *the* leading particle. From these plots we can conclude that the leading charged particle behaves differently than the non-leading charged particles even if they have the same value of z_h (for $z_h > 0.2$). We can also conclude that the z-dependence for a particle of a given rank is very weak. The dominant effect is the

[2] A π^0 candidate is any photon-pair with a combined invariant mass in the range 100–180 MeV.

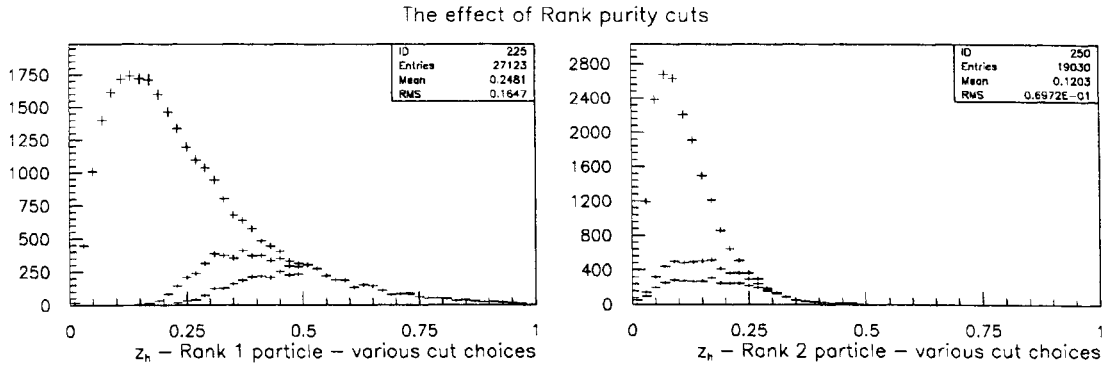

Figure 5-11: The Effect of Rank Purity Cuts on the Raw z_h distributions.
The raw z_h distribution is shown for a) The Rank 1 particle and b) the Rank 2 particle. The curve with the most data in each plot is the distribution before purity cuts. The next most populated distribution includes the cut $z_{h1} > \max\{(1 - \Sigma_{all} z), z_\gamma, z_{\pi^0}\}$. The least populated distribution contains the cut $z_{h1} > 1 - \Sigma_{ch} z$. These data are not corrected for acceptance.

rank dependence. Thus the data are in direct opposition to the assumptions that are usually built into our theories.

Correcting for the Rank Mixing

Another approach to the problem of rank mixing is to understand the effect and correct for it. Let's define the *Overall Efficiency* as the total probability of detecting and reconstructing a hadron which was generated in a DIS interaction somewhere in the physics target. The measured distribution of hadrons in z_h and φ_h is then a function of the *Overall Efficiency* and the true distribution. In order to correct the data, we must model the effect of the inefficiency on the measured distribution and then try to extract the true distribution.

These corrections are quite important when we are trying to measure a distribution which is absolutely normalized such as $\frac{1}{N_{\mu'}}\frac{dN}{dz}$ or $\frac{1}{N_{\mu'}}\frac{dN}{d\varphi}$. The normalization constant $N_{\mu'}$ denotes the number of scattered muons. These distributions are differential probabilities normalized as number of hadrons per scattered muon. Similarly when we fit to a form such as:

$$\frac{dN}{d\varphi} = A + B\cos\varphi + C\cos 2\varphi,$$

the fit parameters A, B, and C are sensitive to this absolute acceptance. Fortunately,

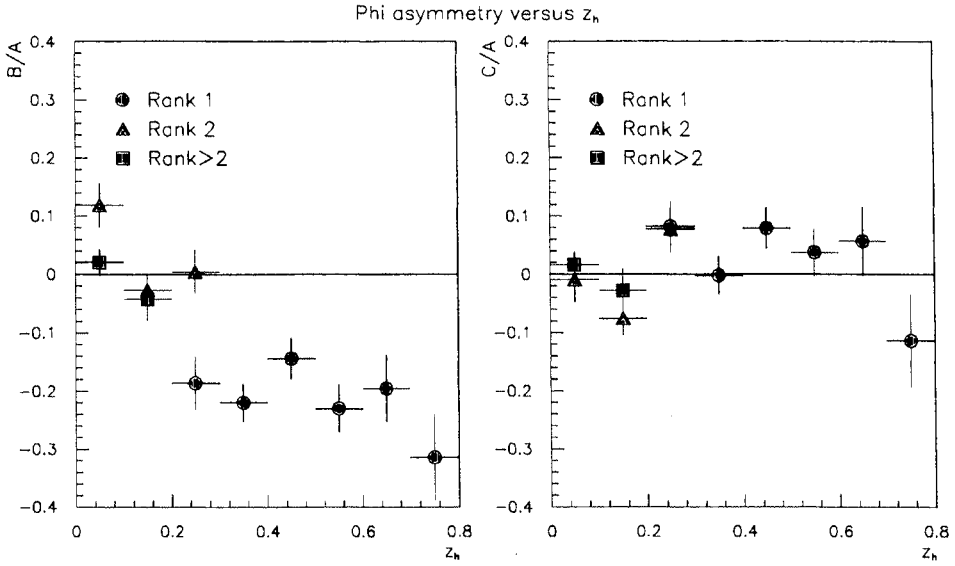

Figure 5-12: Phi Asymmetry versus z_h — Unambiguous Rank 1.
Fit parameters B/A and C/A versus z_h for different particle ranks in Data for events with an unambiguous Rank 1 charged particle. These data are not corrected for acceptance.

however, the parameters that we are interested in, B/A and C/A, are not strongly affected by the acceptance. The most significant effect due to acceptance will be the rank mixing. What we measure as a Rank 1 particle may actually be a Rank 2 particle if we have missed the true Rank 1 particle. It is this effect that we must consider.

Appendix C contains a description of a method to correct for the rank mixing effect. The assumptions behind this correction are:

- the neutral particles behave as the charged particles do, and constitute 1/3 of the generated forward particles;
- the overall efficiency can be treated as a weakly varying function of z_h for $z_h > 0.1$;
- the efficiency is not dependent on the variable φ_h.

These assumptions are discussed further in Appendix C. In addition to the above assumptions, we will need three things:

1. The efficiency for finding a charged particle.

2. The ratio of observed z-distributions for charged particles of ranks 1–3.

3. The measured distributions of B/A for each rank: 1–3.

The first item is discussed in Appendix C. The second item we will get directly from the data. Figure 5-13a–b shows the uncorrected measured z-distributions for Rank 1, Rank 2, Rank 3, and Rank > 3 (denoted $D^m_{4+}(z)$) charged particles. Figures 5-13c–f show the ratios $\frac{D^m_2(z)}{D^m_1(z)}$, $\frac{D^m_3(z)}{D^m_1(z)}$, and $\frac{D^m_3(z)}{D^m_2(z)}$, which are needed to perform the correction, as well as $\frac{D^m_{4+}(z)}{D^m_1(z)}$, which justifies our ignoring particles with Rank>3. The third item in the above list, the measured dependence of B/A on z_h and rank can be found in Figure 5-9 on page 151.

Figure 5-14 shows the result of performing the correction. This result shows that there is no discernible z-dependence to the phi asymmetry of the leading particle for $z > 0.1$. In previous experiments which showed a z_h dependence to the $\langle \cos\varphi \rangle$ moment for all hadrons, the z_h dependence was actually due to the rank dependence (above $z_h > 0.1$). In fact, the rank dependence of the phi asymmetry may help explain the EMC result (see Figure 5-4 on page 144 of this thesis). The EMC data show that the phi asymmetry falls off very rapidly as one approaches $x_F = 0$ from above. Existing models can't really explain this effect in the EMC data. The effect may be due to the fact that the percentage of particles that are Rank 1 falls off rapidly as one approaches $x_F = 0$. Since the phi asymmetry is predominantly carried by the Rank 1 particles, the effect vanishes rapidly as well.

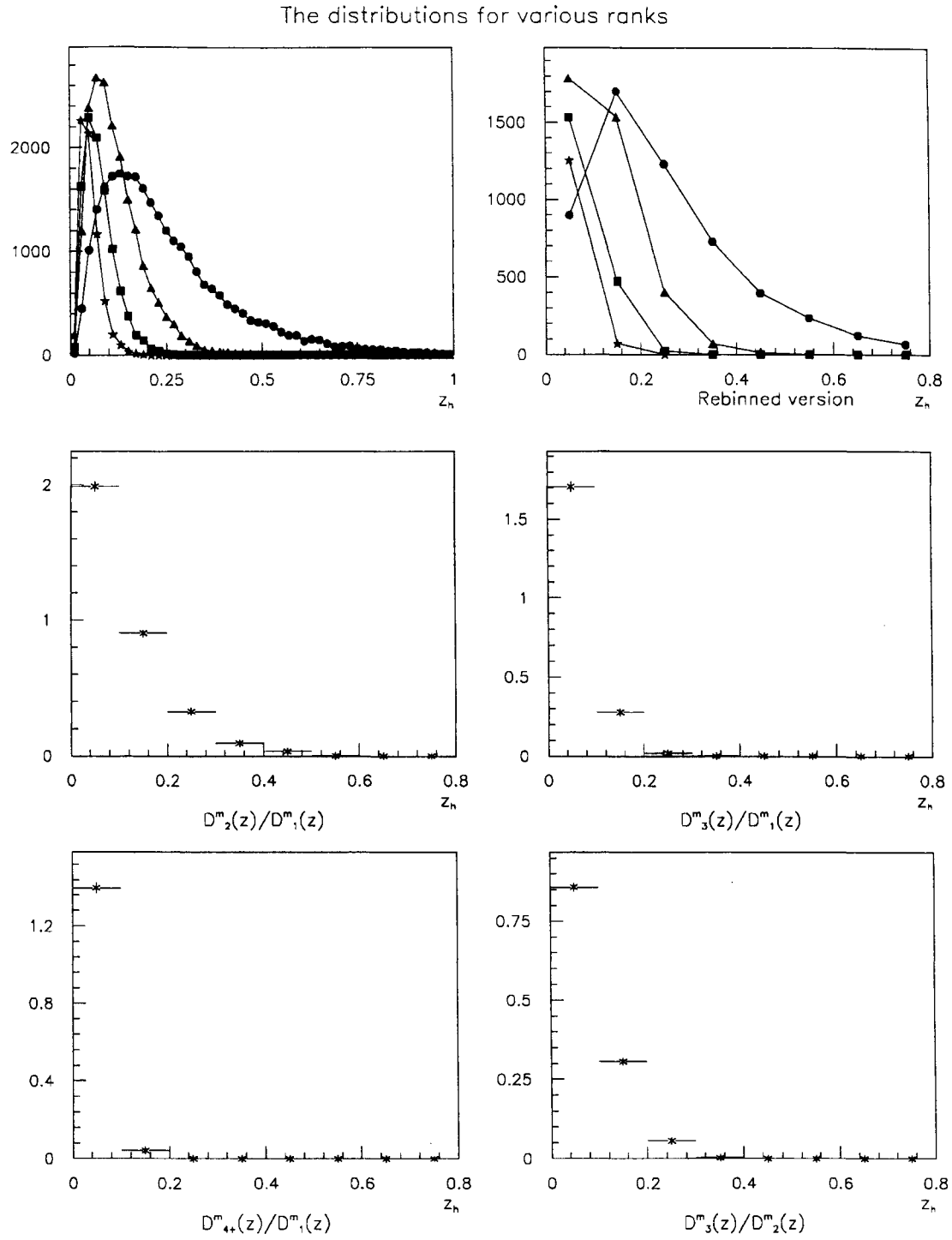

Figure 5-13: The Measured z-distributions by Hadron Rank.
The plots show a) $D_1^m(z)$ (circle), $D_2^m(z)$ (triangle), $D_3^m(z)$ (square), and $D_{4+}^m(z)$ (asterisk) overlaid, b) the same plot with different binning, c) $\frac{D_2^m(z)}{D_1^m(z)}$, d) $\frac{D_3^m(z)}{D_1^m(z)}$, e) $\frac{D_{4+}^m(z)}{D_1^m(z)}$, and f) $\frac{D_3^m(z)}{D_2^m(z)}$. These data are not corrected for acceptance.

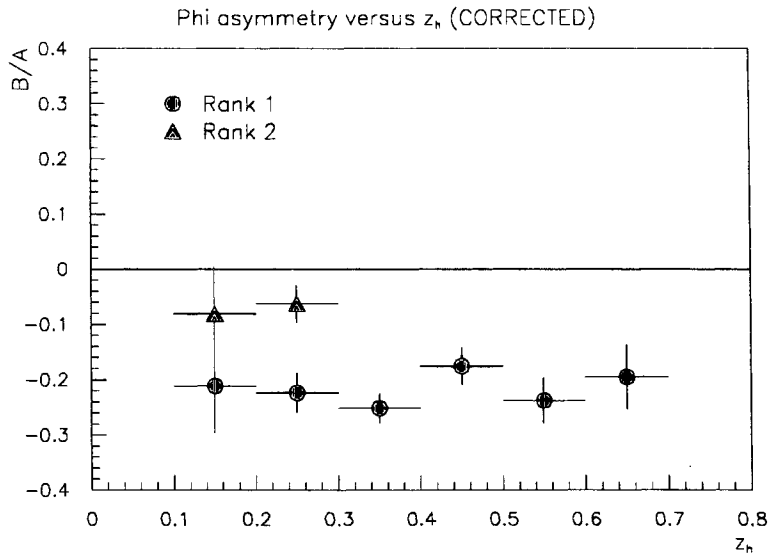

Figure 5-14: Corrected z_h-dependence of the Phi Asymmetry by Hadron Rank. Fit parameter $B/A \approx 2\langle\cos\varphi\rangle$ versus z_h for the leading particle. This should correspond to the leading particle in the event, whether charged or neutral, assuming that there is no difference. These data are corrected for acceptance, including Rank Mixing.

5.3.2 Transverse Momentum Dependence of the Phi Asymmetry

We can find the p_T-dependence of the phi asymmetry in the same way that we found the z_h-dependence. We can fit the $dN/d\varphi_h$ distributions for various ranges of p_T. Figure 5-15a–b shows the results for all events. There is a strong p_T-dependence of the phi asymmetry for the leading particle; the phi asymmetry becomes more pronounced for increasing p_T. Figure 5-15c–d shows the same results when we restrict ourselves to events where the Rank 1 charged particle was the unambiguous Rank 1 particle.

Figure 5-16 shows the distribution for reconstructed Monte Carlo. The Monte Carlo results have a small rank dependence. From Figure 5-10, we know that this rank dependence is actually due to the different z_h values of the various ranks. The Monte Carlo shows a very weak dependence of B/A on the hadron p_T, while the data show a strong dependence on p_T for the Rank 1 charged particles and also for the Rank$>$ 2 sample. The unambiguous leading particles also show a p_T dependence.

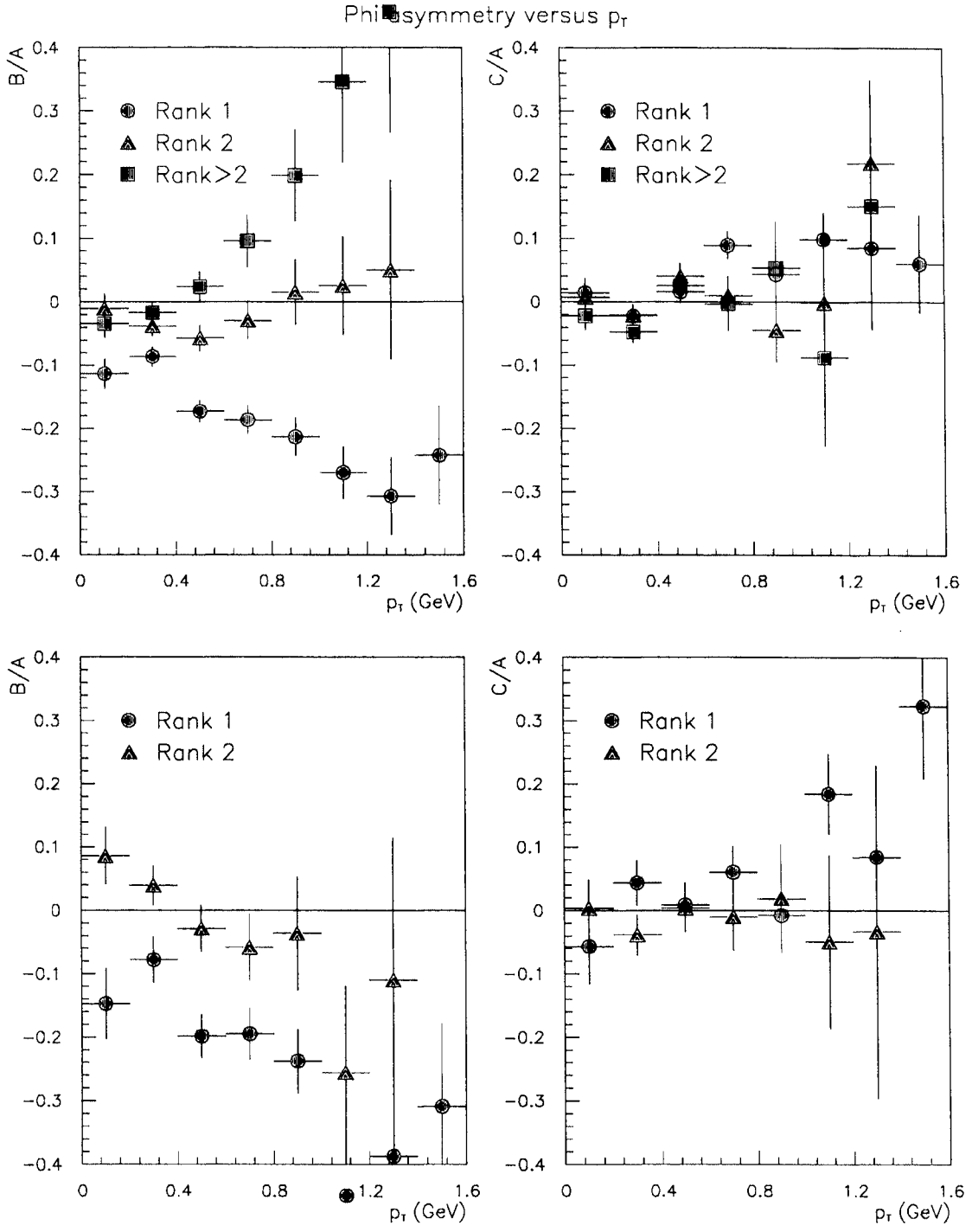

Figure 5-15: The p_T-dependence of the Phi Asymmetry by Hadron Rank.
a) B/A raw distribution, b) C/A raw distribution, c) B/A for events with unambiguous Rank 1, d) C/A for events with unambiguous Rank 1. These data are not corrected for acceptance.

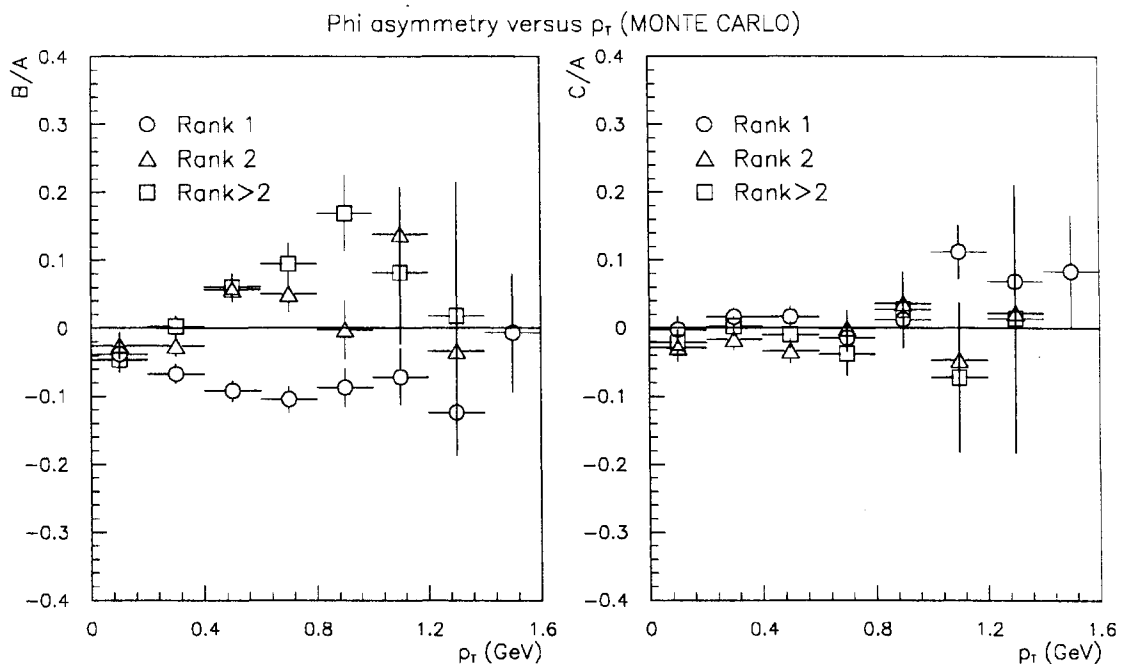

Figure 5-16: The p_T-dependence of the Phi Asymmetry by Hadron Rank (MC). a) B/A distribution, b) C/A distribution. These Monte Carlo results were run through the entire reconstruction chain and should correspond to uncorrected data.

5.3.3 Phi Asymmetry versus Event Kinematics

In this section, we examine the dependence of the phi asymmetry on event kinematics. Theoretical models such as the one explored in Section 2.3.3 make explicit predictions for the behavior of the parton-level phi asymmetry as a function of Q^2 and y_{B_j}. If the phi asymmetry is dominated by the leading order diagram, then we should find the following dependence:

$$\langle \cos\varphi \rangle_{partons} \propto -\frac{k_\perp}{Q} f_1(y_{B_j}) \tag{5.6}$$

Since the phi asymmetry for charged hadrons is primarily carried by the leading charged hadron, it makes sense to examine just these leading charged hadrons. If there is an underlying partonic phi asymmetry, these leading particles apparently reflect it in the least diluted fashion. For this reason, we will examine the Q $(= \sqrt{Q^2})$ and y_{B_j} dependences of B/A and C/A for these particles. In practice, of course, this is very similar to the cut on $z_h > 0.2$ which has been used in previous experiments and analyses. Since we now know, however, that the z_h dependence is incidental, it makes more sense to use the leading particle, whatever its value of z_h.

Figure 5-17 shows the Q dependence of the B/A and C/A fit coefficients for the leading charged particle and for the unambiguously leading charged particle in data. The effect seems to be nearly independent of Q over a broad range. The data correspond to a Q^2 range from roughly 2 GeV^2 to 90 GeV^2. Restricting the sample to include only the unambiguous Rank 1 hadrons increases the overall magnitude of the phi asymmetry while leaving it nearly independent of Q.

Figure 5-18 shows the corresponding results for reconstructed Monte Carlo events. The theory predicts that the B/A effect will disappear at high values of Q. Qualitatively, this is easy to understand. The phi asymmetry is dominated at our energies by the effects of primordial $k_\perp$ [13]. Since we have assumed that the $k_\perp$ is independent of Q, the phi asymmetry in the partons should be roughly proportional to $1/Q$, causing the hadronic phi asymmetry to vanish at high Q. Clearly, the phi asymmetry in the data persists to higher values of Q^2 than was expected. There are several possibilities for why this might occur. They include:

- The hadron phi asymmetry may not reflect the behavior of the partons very well.
- The partons may not behave in the way that we expect them to from our theoretical bias.
- The primordial $k_\perp$ distribution of the partons may be dependent on Q. We might speculate that the effective $\langle k_\perp \rangle$ is roughly proportional to Q.

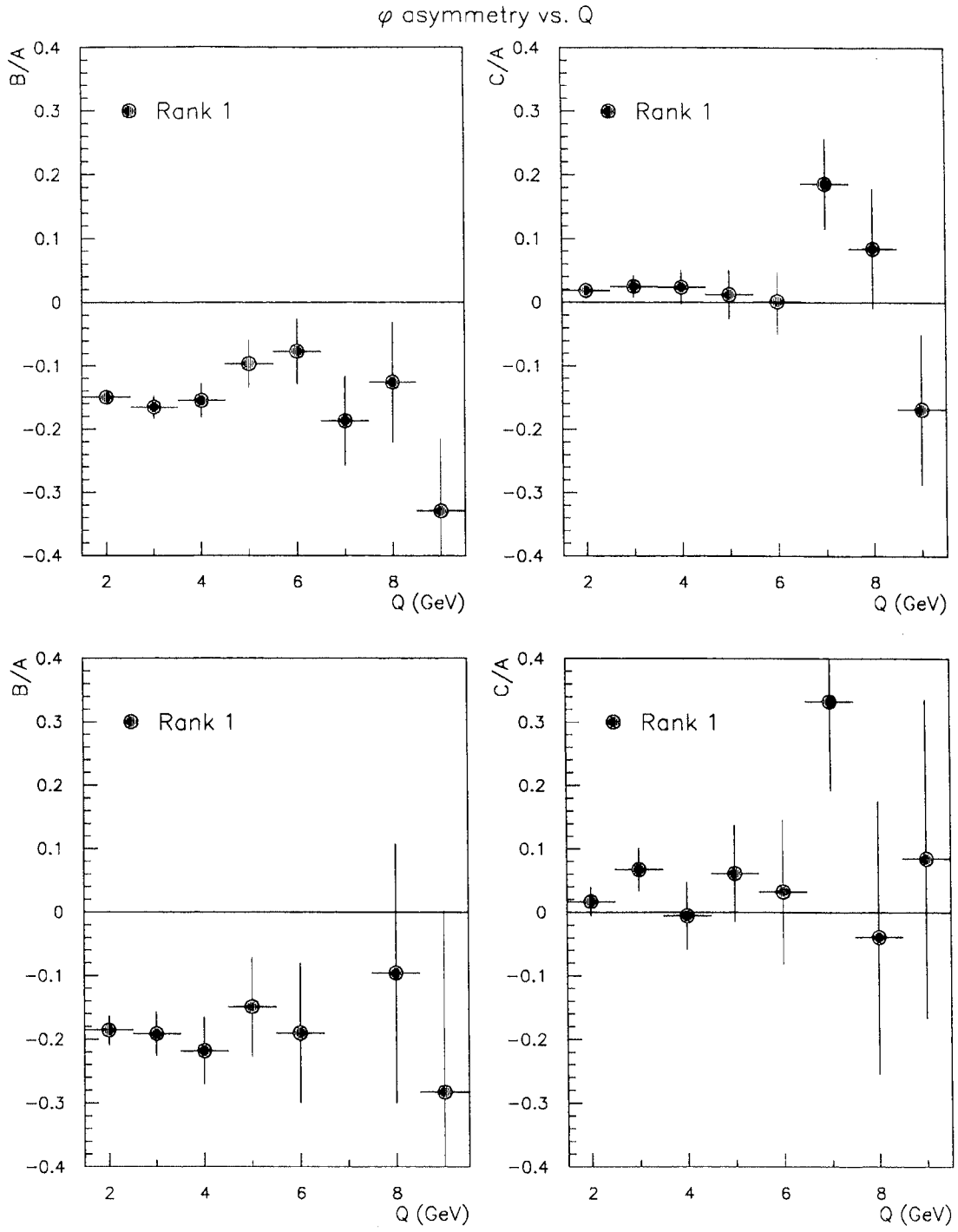

Figure 5-17: The Q-dependence of the Phi Asymmetry.
The coefficients B/A and C/A are plotted versus Q for the sample of all leading charged particles and for the sample of unambiguously leading charged particles. The plots are organized as follows: a) B/A for Rank 1, b) C/A for Rank 1, c) B/A for unambiguous Rank 1, d) C/A for unambiguous Rank 1. These data are not corrected for acceptance.

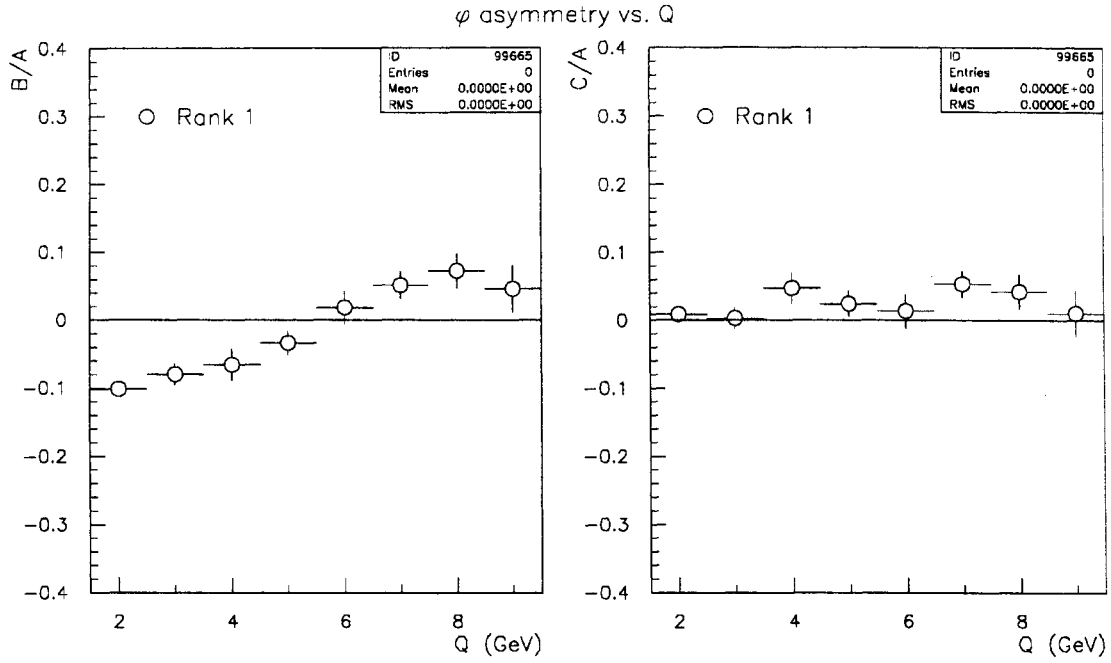

Figure 5-18: The Q-dependence of the Phi Asymmetry (Monte Carlo).
The coefficients B/A and C/A are plotted versus Q for the sample of all leading charged particles and for the sample of unambiguously leading charged particles. The plots are organized as follows: a) B/A for Measured Rank 1, b) C/A for Measured Rank 1. These Monte Carlo results were run through the entire reconstruction chain and should correspond to uncorrected data.

The measured y_{B_j}-dependence of the phi asymmetry for the leading charged particle is shown in Figure 5-19. This distribution is inconsistent with the form $f_1(y)$, shown in Figure 2-12 on page 53. The same distributions for Monte Carlo are shown in Figure 5-20. It should be noted that the Monte Carlo is also inconsistent with the form $f_1(y)$ even though that dependence is built in at the parton level. A possible explanation for this discrepancy is that hadronization may tend to wash out the phi asymmetry in the hadrons. The effects of hadronization should be more important for low values of y_{B_j} where W^2 is smaller and the p_T due to hadronization is thought to be constant. This means that a "jet" of hadrons coming from a quark should be better collimated for higher values of y_{B_j}, enhancing the phi asymmetry.

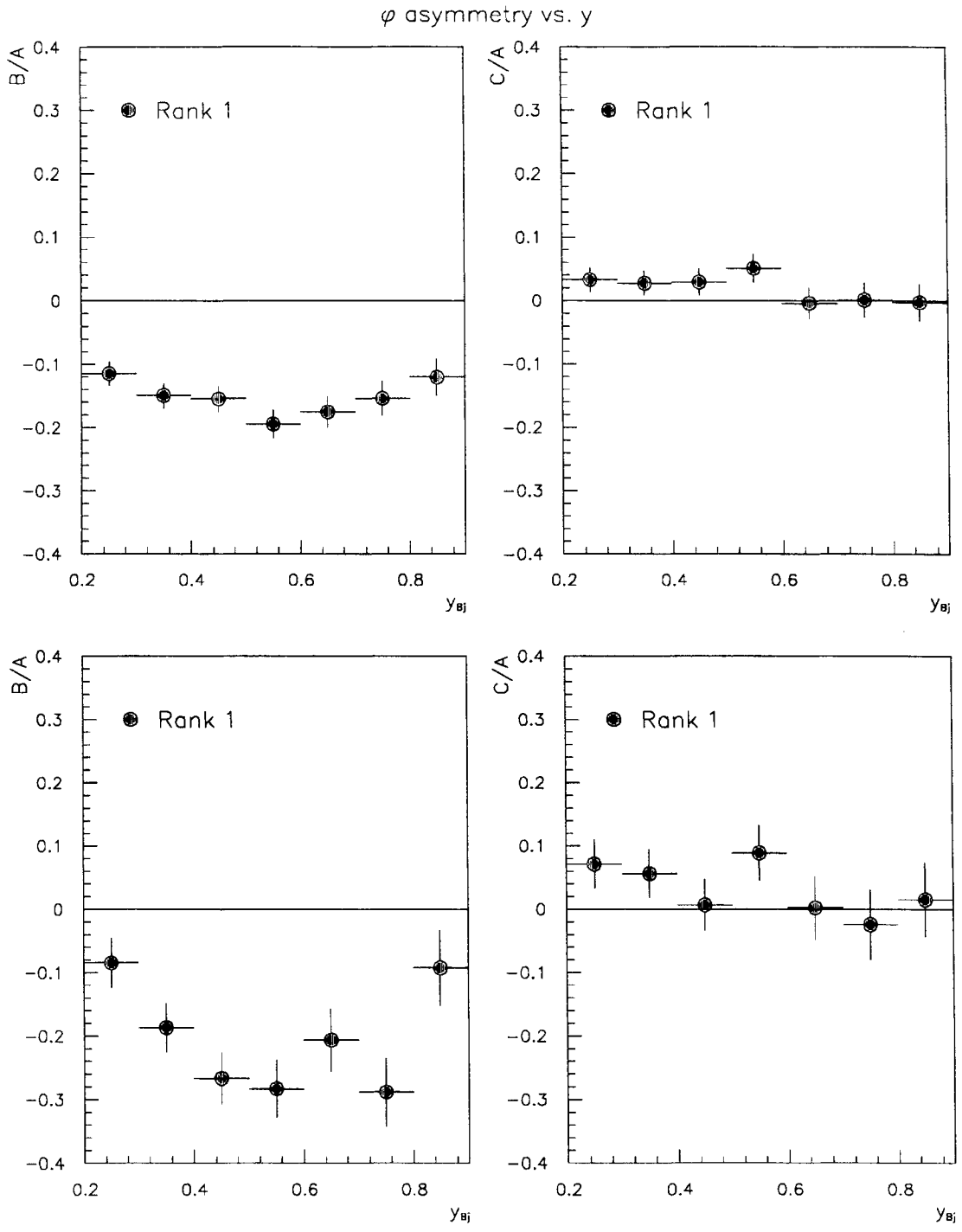

Figure 5-19: The y_{B_j}-dependence of the Phi Asymmetry.
The coefficients B/A and C/A are plotted versus y_{B_j} for the sample of all leading charged particles and for the sample of unambiguously leading charged particles. The plots are organized as follows: a) B/A for Rank 1, b) C/A for Rank 1, c) B/A for unambiguous Rank 1, d) C/A for unambiguous Rank 1. These data are not corrected for acceptance.

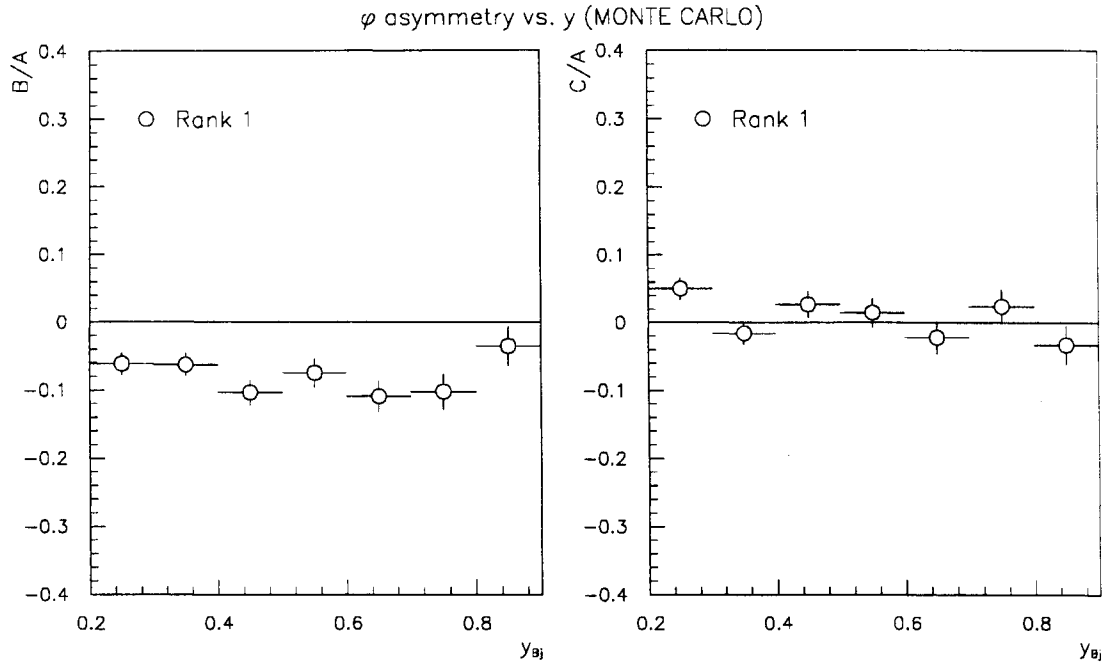

Figure 5-20: The y_{B_j}-dependence of the Phi Asymmetry (Monte Carlo).
The coefficients B/A and C/A are plotted versus y_{B_j} for the sample of all leading charged particles and for the sample of unambiguously leading charged particles. The plots are organized as follows: a) B/A for Measured Rank 1, b) C/A for Measured Rank 1. These Monte Carlo results were run through the entire reconstruction chain and should correspond to uncorrected data.

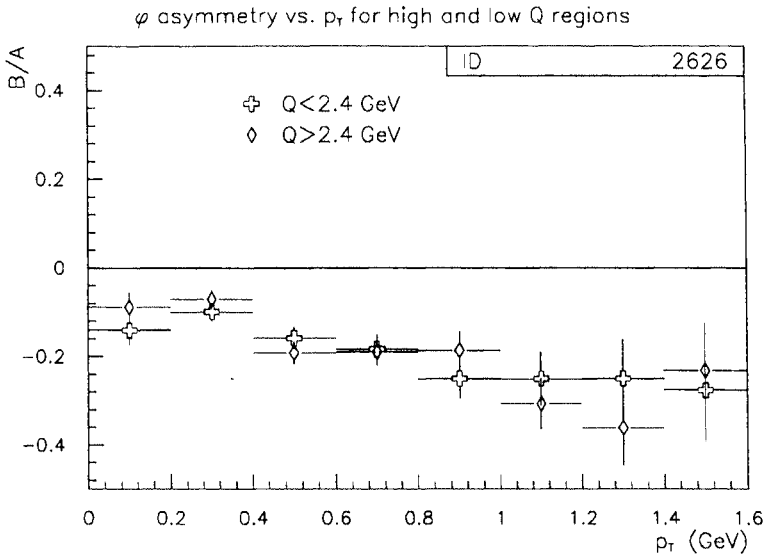

Figure 5-21: The p_T-dependence of the Phi Asymmetry for Two Regions in Q. The coefficient B/A is plotted versus p_T for the leading charged particle in each event. The event sample has been broken into two regions of nearly equal size: 1.414 GeV $< Q <$ 2.4 GeV and $Q >$ 2.4 GeV. These data have not been corrected for acceptance.

5.3.4 Further Phi Asymmetry Studies

Two of the results that we have considered surprising are the lack of Q dependence in the phi asymmetry and the existence of a p_T dependence. It is interesting to attempt to find a connection by plotting the p_T dependence of the phi asymmetry in two different regions of Q^2: high and low. If, for instance, the p_T of the hadron were highly correlated with the $k_\perp$ of the parton, then we would expect that the p_T dependence would be different for different regions of Q. This is because the theory predicts that the phi asymmetry goes like $k_\perp/Q$.

Figure 5-21 shows the quantity B/A plotted versus the hadron p_T for two different regions of Q: $Q <$ 2.4 GeV and $Q >$ 2.4 GeV. The average values of Q for the two samples are 1.9 GeVand 3.8 GeV. The high and low Q samples are indistinguishable in the data. There is no evidence for any Q^2 dependence of the phi asymmetry, even for fixed values of hadron p_T.

Figure 5-22 shows the same plot for the reconstructed Monte Carlo. The average values of Q for the two samples are 1.8 GeVand 3.8 GeV. There are two qualitative features in the Monte Carlo that are different from the data. First, the p_T dependence

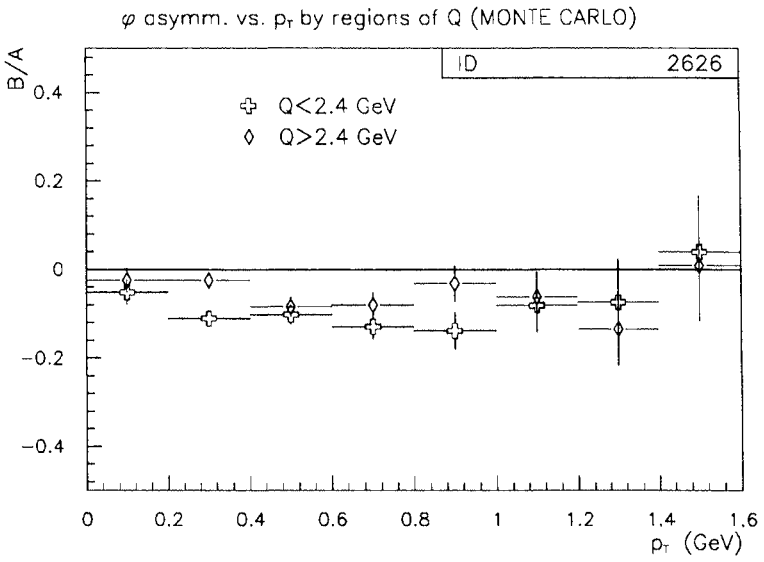

Figure 5-22: The p_T-dependence of the Phi Asymmetry for Two Regions in Q (MC).] The coefficient B/A is plotted versus p_T for the leading charged particle in each event. The event sample has been broken into two regions of nearly equal size: 1.414 GeV $< Q <$ 2.4 GeV and $Q >$ 2.4 GeV. These Monte Carlo results were run through the entire reconstruction chain and should correspond to uncorrected data.

is not very strong, as was noted before. Second, the high Q sample is systematically lower than the low Q sample, as expected from the theory built into the Monte-Carlo.

We must conclude from this that our naïve picture sketched above is inadequate. Either the hadronic p_T is not well correlated with the partonic $k_\perp$ or something other than the leading order partonic process is behind the phi asymmetry.

5.4 Transverse Momentum Distributions

In order to further characterize the physics, it is useful to consider the actual transverse momentum distributions of the particles. These distributions are even trickier to interpret than the phi asymmetry distributions because the transverse momentum of the hadrons is believed to come from several different sources: 1) the primordial $k_\perp$ of the parton within the nucleus; 2) hard QCD processes — hard gluon radiation from the struck quark or the process of photon-gluon fusion; 3) soft gluon radiation from the struck quark; and 4) hadronization.

It is common to consider the hadron p_T^2 as arising from a sum in quadrature of these four independent sources:

$$p^2_{T(hadron)} = z_h^2 k^2_{\perp(parton)} + p^2_{T(hard\ QCD)} + p^2_{T(soft\ QCD)} + p^2_{T(hadronization)} \qquad (5.7)$$

Equations similar to Equation 5.7 have inspired a class of plots, loosely called seagull plots, in which one plots the average p_T^2 in bins of a longitudinal variable such as x_F. Usually these seagull plots are averaged over all available hadrons and are not broken down in terms of particle rank.

Figure 5-23 contains seagull plots for various ranks in the two different regions of Q for data. The most striking effect is that the high Q data has a larger $\langle p_T^2 \rangle$ than the low Q data, especially in the high z region. Figure 5-24 contains similar plots for reconstructed Monte Carlo. The difference between the high and low Q plots in the Monte Carlo is much smaller than the difference in the data.

Figure 5-25 contains the same information as Figure 5-23, but the information is organized somewhat differently. The rank dependence is emphasized here rather than the Q dependence. Figure 5-26 is the Monte Carlo version of the same plot. The data show a larger amount of p_T than exists in the Monte Carlo at high Q and high z_h. Furthermore, the data show a bit more rank dependence than the Monte Carlo results do.

Figure 5-27 shows the effect of restricting our sample to events with an unambiguous Rank 1 hadron. The results are not very different from Figure 5-23 without the cut. This means that the corrections for rank mixing aren't very important above z_h of 0.2.

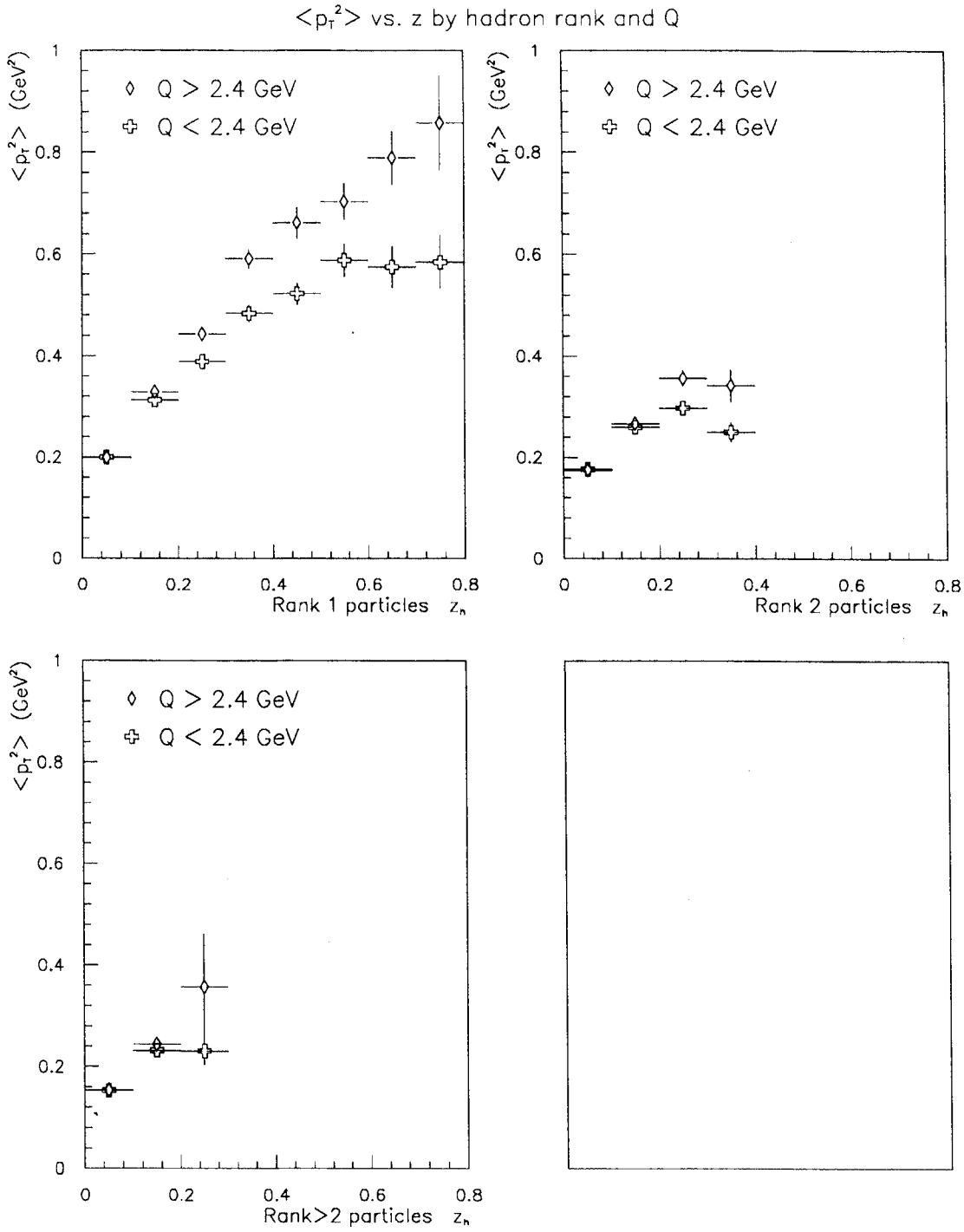

Figure 5-23: Seagull Distributions for Different Regions of Q.
The seagull distributions ($\left\langle p_T^2 \right\rangle$ versus z_h) are compared for the low and high Q regions. This comparison is made for a) Rank 1 charged particles, b) Rank 2 charged particles, and c) Rank> 2 charged particles. The distributions have not been corrected for acceptance.

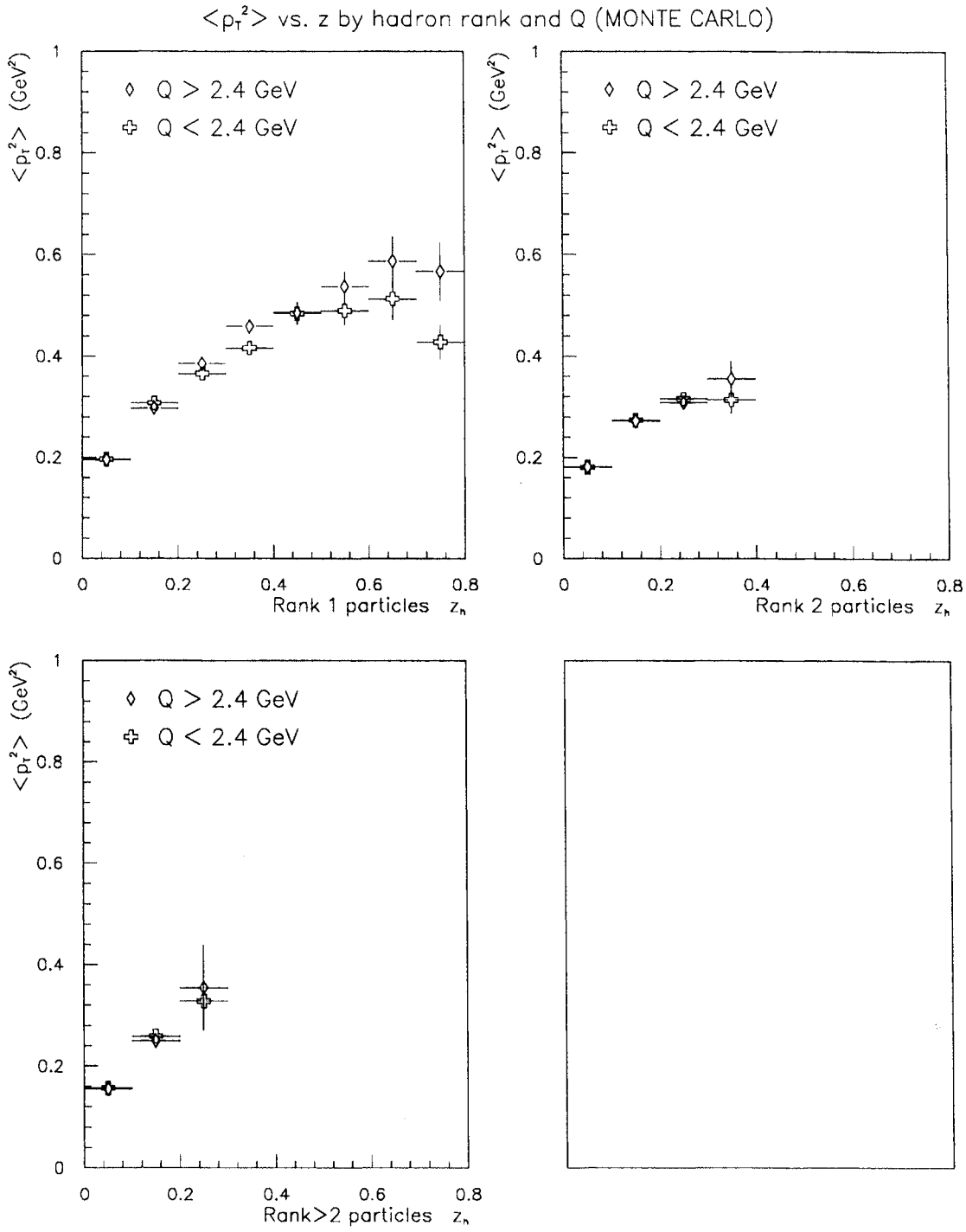

Figure 5-24: Seagull Distributions for Different Regions of Q (Monte Carlo).
The seagull distributions ($\left\langle p_T^2 \right\rangle$ versus z_h) are compared for the low and high Q regions in the Monte Carlo. This comparison is made for a) Rank 1 charged particles, b) Rank 2 charged particles, and c) Rank> 2 charged particles. These Monte Carlo results include the full apparatus and reconstruction code simulation and should be compared to uncorrected data.

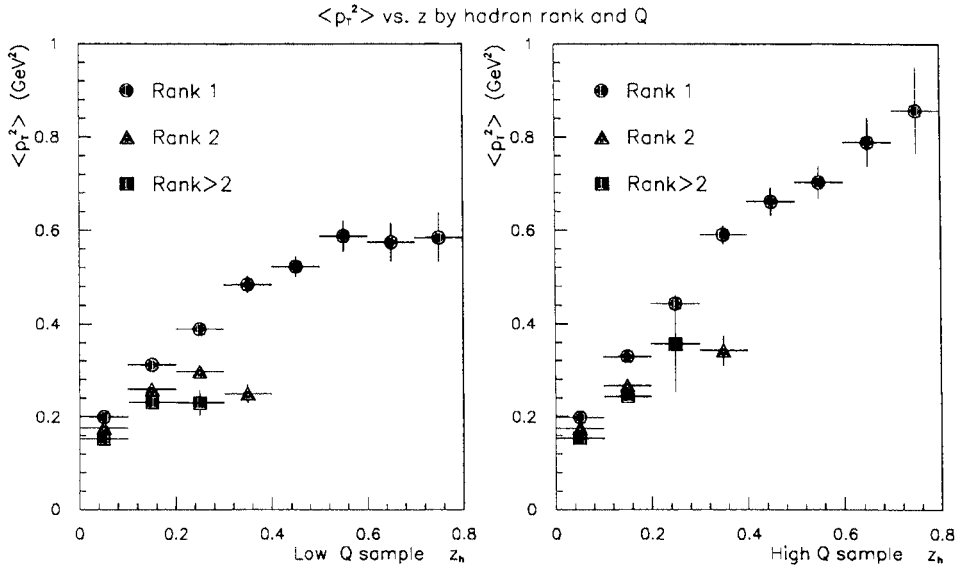

Figure 5-25: Seagull Distributions by Hadron Rank.
This figure compares the seagull distributions for hadrons of different ranks. This comparison is made for a) low and b) high Q^2 regions. These data are not corrected for acceptance.

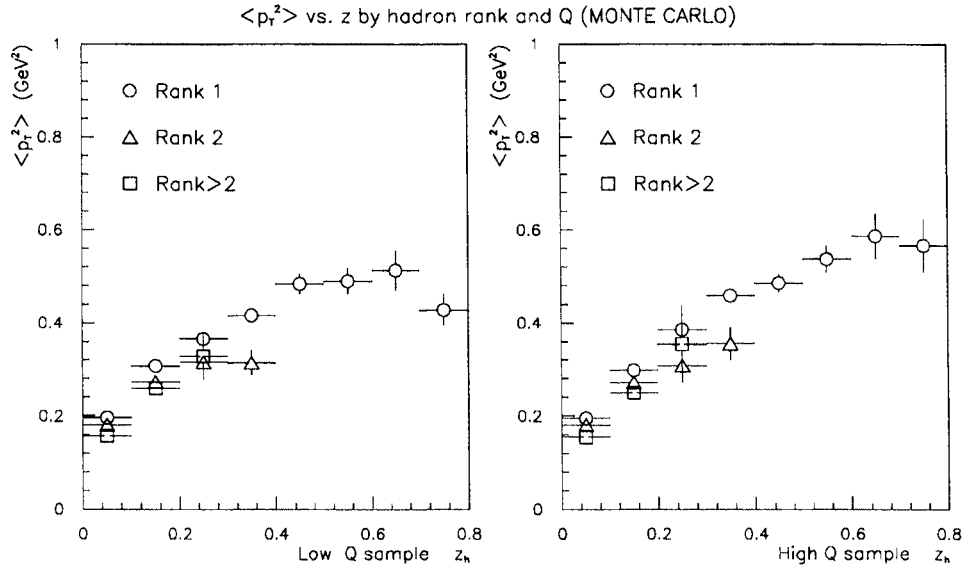

Figure 5-26: Seagull Distributions by Hadron Rank (Monte Carlo).
This figure compares the seagull distributions for hadrons of different ranks for the Monte Carlo. This comparison is made for a) low and b) high Q^2 regions. These Monte Carlo results include the full apparatus and reconstruction code simulation and should be compared to uncorrected data.

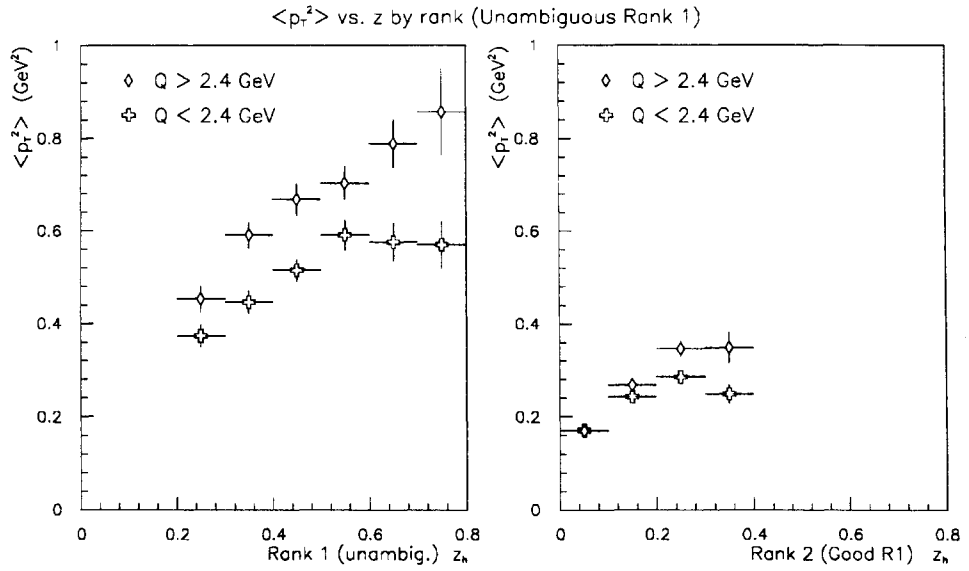

Figure 5-27: Seagull Distributions versus Q^2. Unambiguous Rank 1 Hadron.
This figure compares the seagull distributions for the low and high Q regions for events with an unambiguous Rank 1 particle. This comparison is made for a) Rank 1 charged particles, b) Rank 2 charged particles, and c) Rank> 2 charged particles. The distributions have not been corrected for acceptance.

5.5 Cross-checks and Systematics

There are several potential sources of systematic error that need to be considered. We will consider the following in this section:

1. Detector inefficiencies,
2. LAT trigger inefficiency,
3. Detector alignment errors,
4. Time-dependent detector effects,
5. Radiative corrections (internal and external bremsstrahlung).

5.5.1 Detector Inefficiencies

As was discussed in Section 2.4.5, we made detailed maps of the efficiencies of the various detector components. These efficiency maps have been included in the Monte Carlo. Any plot which is labeled "reconstructed Monte Carlo" will include these effects. Furthermore any plot which is labeled "corrected" will have been corrected for these known inefficiencies.

Using a Monte Carlo with no phi asymmetry, Jansen [50] showed that any fake phi asymmetry generated by the E665 apparatus was small (± 0.03). The only exception to this was that he saw some evidence for a fake positive phi asymmetry at high Q^2 values ($\delta \cos\varphi = +0.05$ for $Q^2 \gtrsim 20$ GeV^2).

5.5.2 LAT Trigger Inefficiency

The LAT Trigger had some timing problems during the 1987 run which resulted in an inefficiency in triggering on scattered muons [34]. The dominant effect was an up-down asymmetry in the scattered muons. Figure 5-28 shows the azimuthal angle of the scattered muon about the beam muon in the laboratory frame in both data and Monte Carlo. $\phi_\mu^{(lab)} = 0$ is along the E665 Y-axis and $\phi_\mu^{(lab)} = \frac{\pi}{2}$ is along the E665 Z-axis.

There is no physics reason for there to be any phi asymmetry in this plot. All of the asymmetry should be attributed to the LAT inefficiency. By itself, this problem should not make a big difference to our results. This is because the physics of the event

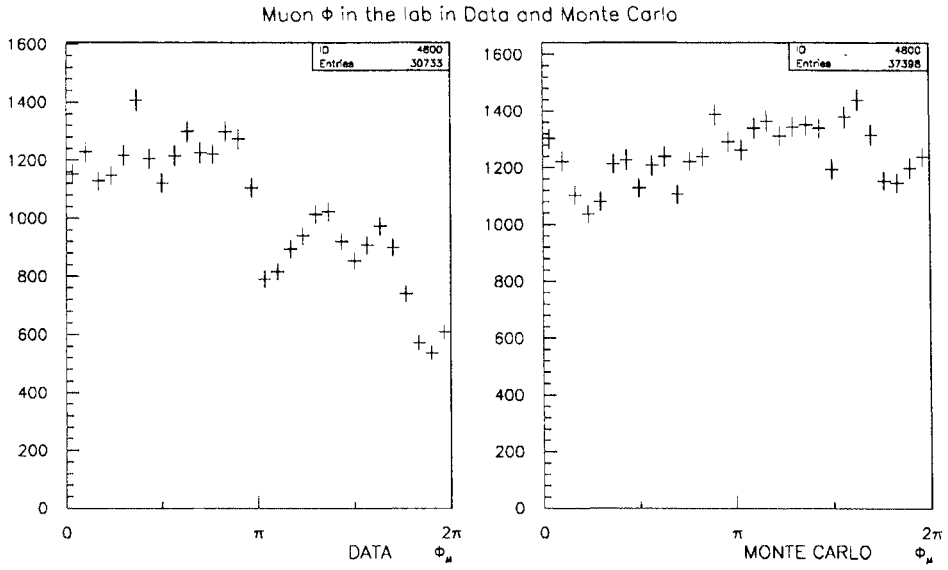

Figure 5-28: LAT Triggering Inefficiency.
This figure shows the phi distribution of the scattered muon in the lab frame in a) data and b) Monte Carlo. A clear up-down asymmetry is evident in the data. These data are not corrected for acceptance.

should not care about the orientation of the E665 Y-axis. In practice, this triggering asymmetry will couple with any asymmetries in our detector efficiency/acceptance to generate small effects. Figure 5-29 shows the dependence of B/A and C/A on the muon phi. Any variation is due to statistics or to an apparatus effect since the physics should be independent of the orientation of the E665 Y-axis. Figure 5-29a compares the B/A for Rank 1 and Rank 2 particles in the "low z" range: $0.1 < z_h < 0.3$. It is clear from this plot that the phi asymmetry isn't manufactured by a simple hole in one part of the apparatus since there is a significant phi asymmetry independent of $\phi_\mu^{(lab)}$. Furthermore, the Rank 1 sample lies below the Rank 2 sample at every point, making it unlikely that a hole in the apparatus manufactures the rank dependence. Figure 5-29b shows that the C/A term is not significantly affected by $\phi_\mu^{(lab)}$. Figure 5-29c-d show the result for the "high z" range: $z_h > 0.3$. Figure 5-30 shows the same plots for Monte Carlo, which has no LAT triggering inefficiency.

Fortunately, most of our asymmetries in the detector are due to the magnetic field and are East-West (notice the small East-West variations in Figure 5-29a,c) while the LAT asymmetry is an Up-Down asymmetry. For this reason, any acceptance effects tend to cancel out; after integrating over $\phi_\mu^{(lab)}$, the overall effect should be negligible.

An additional problem caused by the trigger inefficiencies is that the kinematic distributions will be slightly distorted. This effect should not be very important for

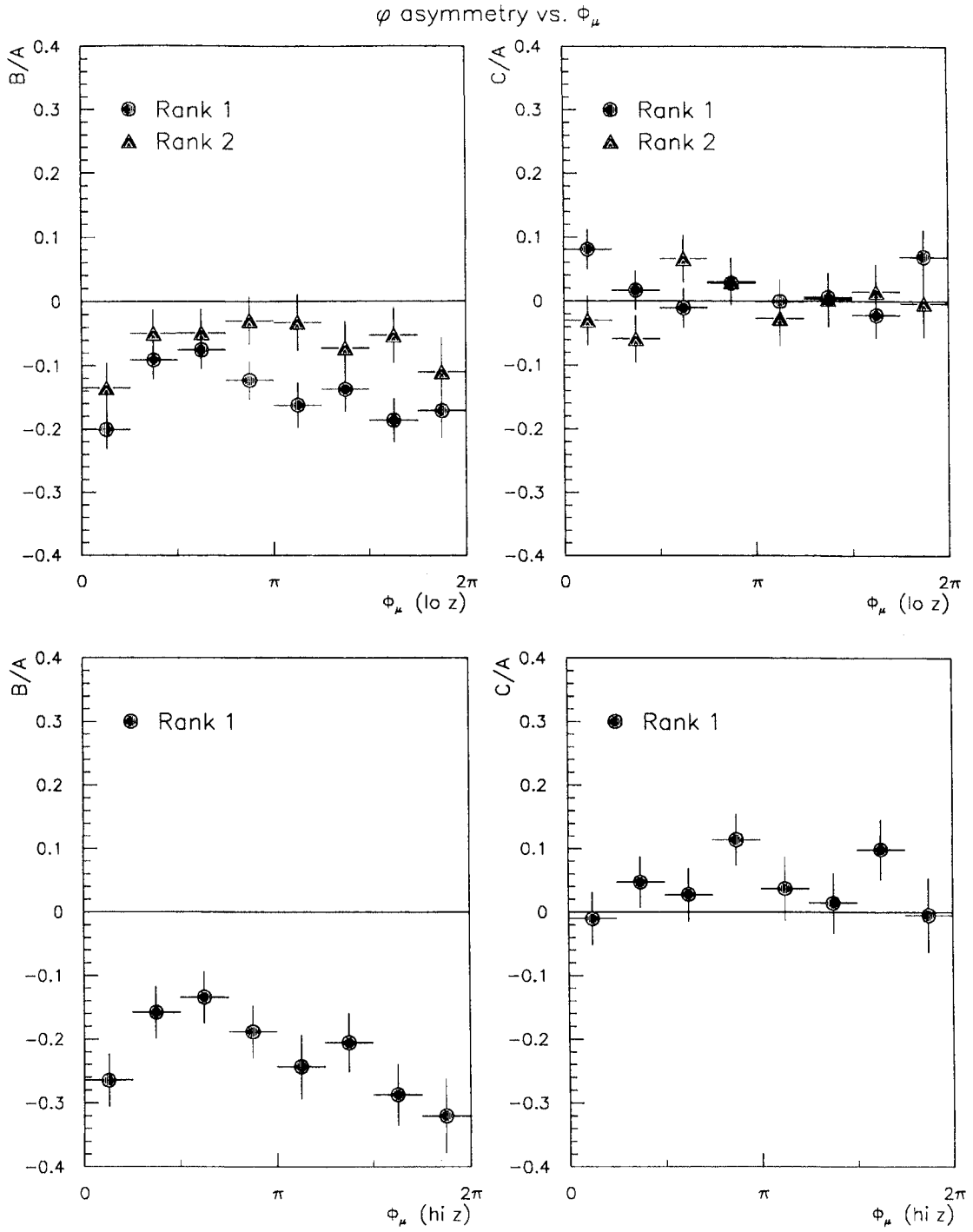

Figure 5-29: Hadronic Phi Asymmetry versus Lab Phi of the Scattered Muon. This figure shows the dependence of B/A and C/A on the laboratory phi of the scattered muon: a) B/A for Rank 1 and 2 particles with $0.1 < z < 0.3$, b) C/A for Rank 1 and 2 particles with $0.1 < z < 0.3$, c) B/A for Rank 1 particles with $z > 0.3$, and d) C/A for Rank 1 particles with $z > 0.3$. These data are not corrected for acceptance.

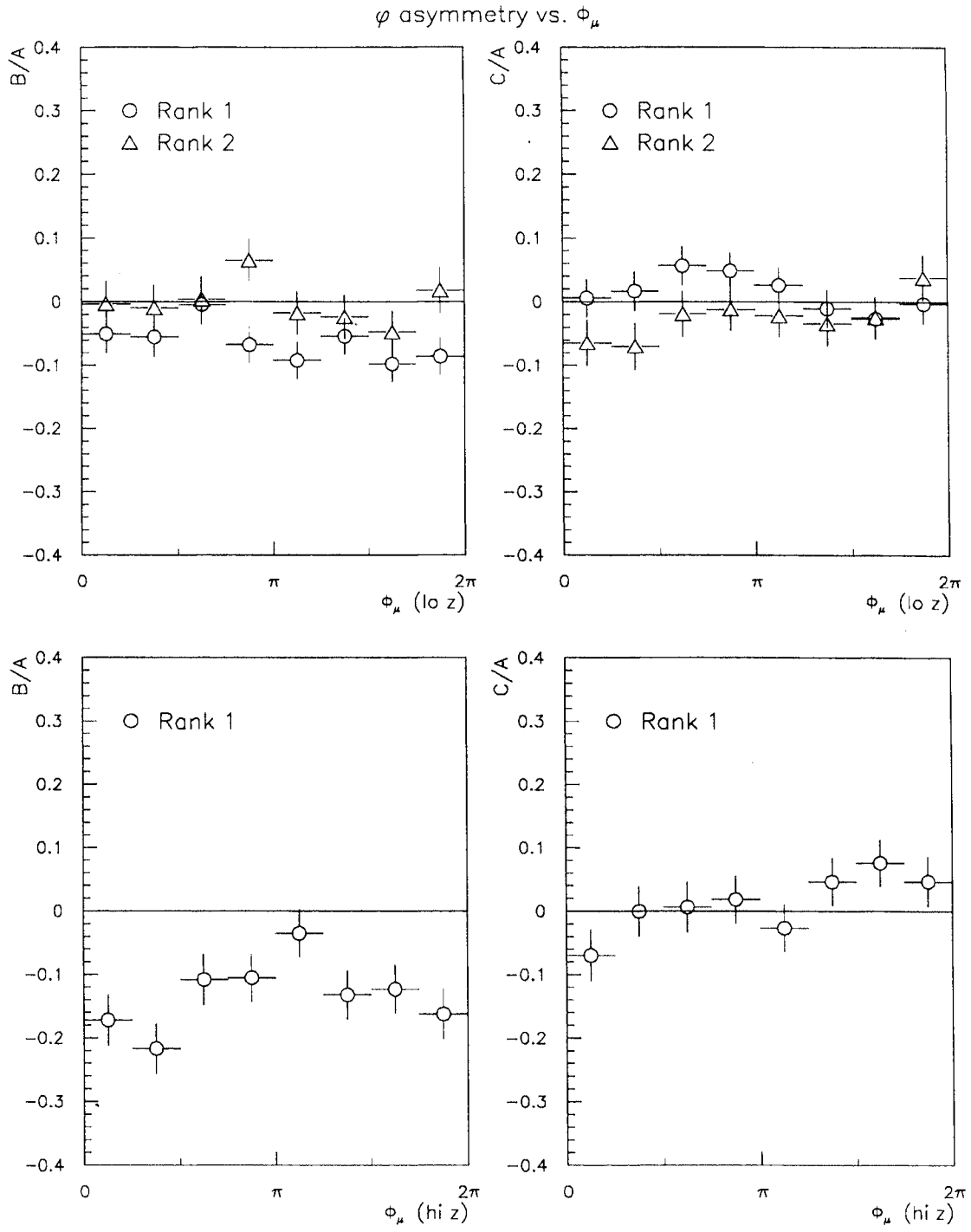

Figure 5-30: Hadronic Phi Asymmetry versus Lab Phi of the Scattered Muon (MC). This figure shows the dependence of B/A and C/A on the laboratory phi of the scattered muon in the Monte Carlo: a) B/A for Rank 1 and 2 particles with $0.1 < z < 0.3$, b) C/A for Rank 1 and 2 particles with $0.1 < z < 0.3$, c) B/A for Rank 1 particles with $z > 0.3$, and d) C/A for Rank 1 particles with $z > 0.3$. These Monte Carlo results include the full apparatus and reconstruction code simulation and should be compared to uncorrected data.

this thesis.

5.5.3 Detector Alignment and Calibration Errors

Small errors in the alignment can cause systematic shifts in the data. There is evidence that the Reconstruction Code used in analyzing the E665 data from the 1987 Run had errors in the alignment and calibration at the level of $\frac{1}{2}\sigma$. The clearest signal for this problem is in the sample of events from the RBEAM trigger. This trigger selects events which are mostly straight-through beams which don't interact anywhere in the detector. If we measure the ν of these beams, the result should be centered on zero with some spread due to resolution. In fact, the mean value of ν is about 7 GeV which corresponds to a shift of about $\frac{1}{2}\sigma$. This problem is known as the "Nu offset". The evidence to date indicates that this error arose from 3 sources:

1. A small error in the measurement of the p_T-kick of the NMRE magnet in the beam spectrometer,

2. A small misalignment of the beam spectrometer due to the assumption that the wire orientation (α) values of the PBT chambers were known from the survey,

3. A small misalignment of the forward spectrometer due to the misalignment of the beam spectrometer. The beam spectrometer position was used as input to the forward spectrometer alignment.

Rather than trying to make some assumptions about the error and correcting for it, we will instead treat the effect as a systematic error on the results for p_T and φ_h. We will assume that there is an error of $\frac{1}{2}\sigma$ on the vertex position, all of the beam track parameters, all of the scattered muon track parameters, and all of the hadron track parameters. We will then propagate these errors as if they were normally distributed and use this as an estimate of the systematic shift in the value of the physics variables. The σs for the vertex position and the track parameters will come from the Vertex Processor. This error propagation will also tell us the magnitude of our resolution on p_T and φ_h. The details are described in Appendix C.

Figure 5-31 shows the measurement errors on p_T and p_T^2 calculated for the data. Figure 5-31a shows the error on p_T as a function of p_T by Rank; the error is a weak function of p_T. Figure 5-31b shows the error on p_T^2, the physics variable that we used in the seagull plots, as a function of p_T for all particles. Figure 5-31c shows the error on p_T^2 as a function of z_h by Rank. This plot shows that most of the rank dependence in the error is due to the z_h dependence. Figures 5-31d-f show the error on p_T^2 as a function of φ_h, Q, and y_{Bj}. Note that the error is not a very strong

function of Q. These plots yield a quantitative measure of the resolution that we have on p_T^2. This resolution is best at low z_h, high y_{B_j}, and low p_T. We can estimate the systematic error on p_T^2 and on the seagull plot due to misalignment by taking $\frac{1}{2}\sigma$. These systematic errors are smaller than the statistical errors and are independent of Q. Clearly these errors don't cause the Q dependence of the seagull plot.

Figure 5-32 shows the measurement errors on φ_h and $\cos\varphi_h$ calculated for the data. Figure 5-32a shows the error on φ_h as a function of φ_h; Figure 5-32b shows the error on the more relevant quantity $\cos\varphi_h$ as a function of φ_h. The error σ_φ varies weakly with φ_h; the error $\sigma_{\cos\varphi}$ therefore is proportional to $\sin\varphi$, as is readily seen. The average error on φ is about 0.06, while the average error on $\cos\varphi$ is 0.04. Figure 5-32c shows the error on $\cos\varphi$ as a function of z_h by Rank. This plot shows that the error is independent of rank and increases with increasing z_h. Figures 5-32d-f show the error on $\cos\varphi$ as a function of p_T, Q, and y_{B_j}. Note that the error is nearly independent of Q. The resolution is best at low z_h, high y_{B_j}, and high p_T. We can estimate the systematic error on $\cos\varphi$ due to misalignment by taking $\frac{1}{2}\sigma$.

5.5.4 Time-dependent Detector Effects

The time dependence of the chamber efficiencies was measured for two different periods in the post-December 1 data sample. The difference between these two periods amounted to a 2% shift in the full acceptance for finding a charged particle [25]. The details of the pre-December 1 time dependence have not been examined. Certain run blocks were removed due to bad Calorimeter performance, but no serious differences were found with the data.

In this thesis, I have treated all of the data using the values for the early post-December 1 period and assume that the error due to time dependence is small. Since I am not trying to measure absolute normalization (number of hadrons per scattered muons) any small time-dependence should have a negligible effect.

5.5.5 Radiative Corrections

The Calorimeter cut described in Section 4.6 should remove most of the effects of hard QED bremsstrahlung. Nevertheless, we may be affected slightly by soft bremsstrahlung. We can estimate the overall effects of radiative corrections on the hadron variables and show that they are fairly small [51]. Since we have removed some of the bremsstrahlung our effect will be smaller still.

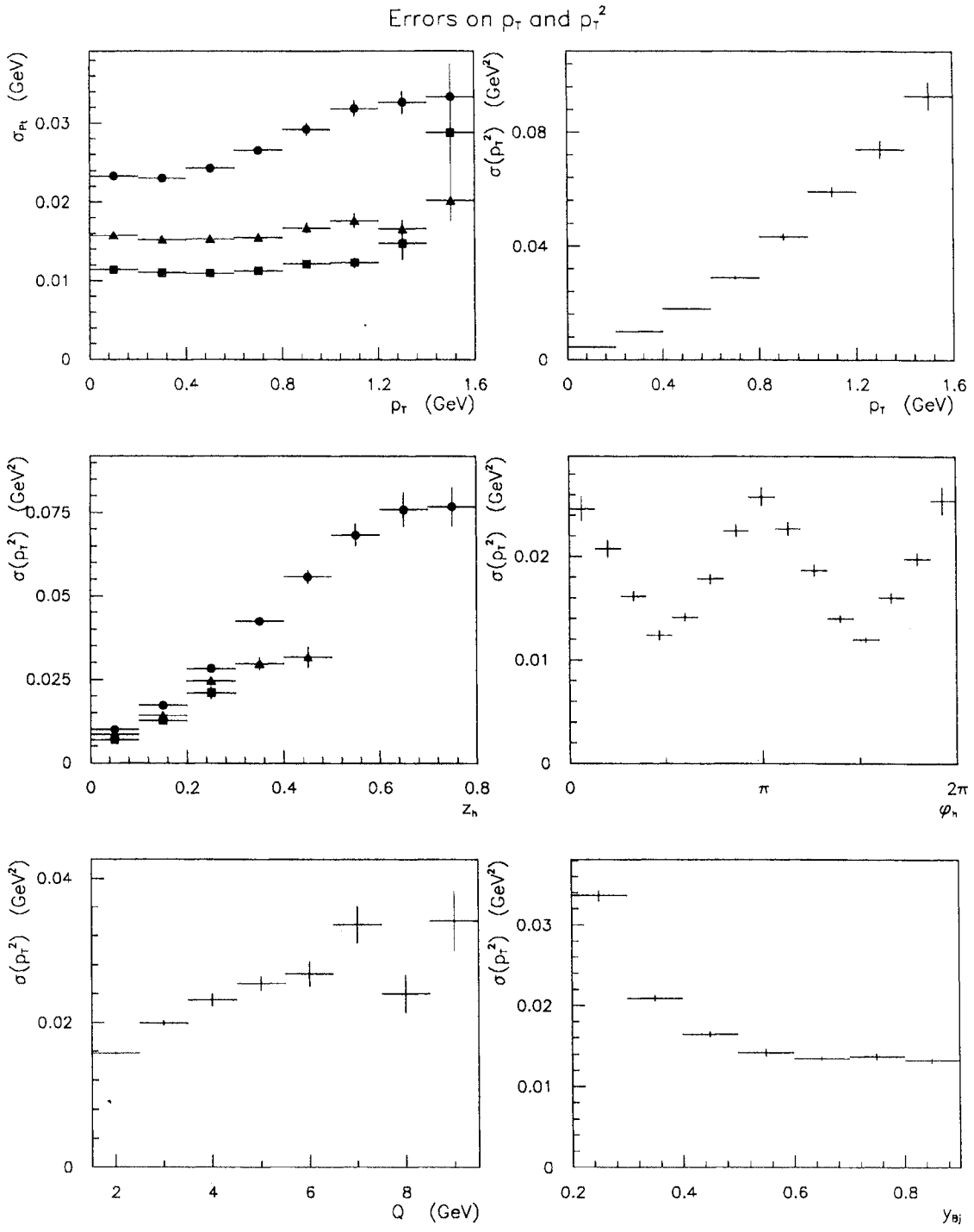

Figure 5-31: p_T and p_T^2 Resolution.
Calculated measurement errors for p_T and p_T^2 from data. Circles stand for Rank 1 (measured), triangles for Rank 2 (measured), and squares for Rank 3 (measured). a) σ_{p_T} vs. p_T by Rank, b) $\sigma_{p_T^2}$ vs. p_T^2, c) $\sigma_{p_T^2}$ vs. z_h by Rank, d) $\sigma_{p_T^2}$ vs. φ_h, e) $\sigma_{p_T^2}$ vs. Q, and f) $\sigma_{p_T^2}$ vs. y_{Bj}.

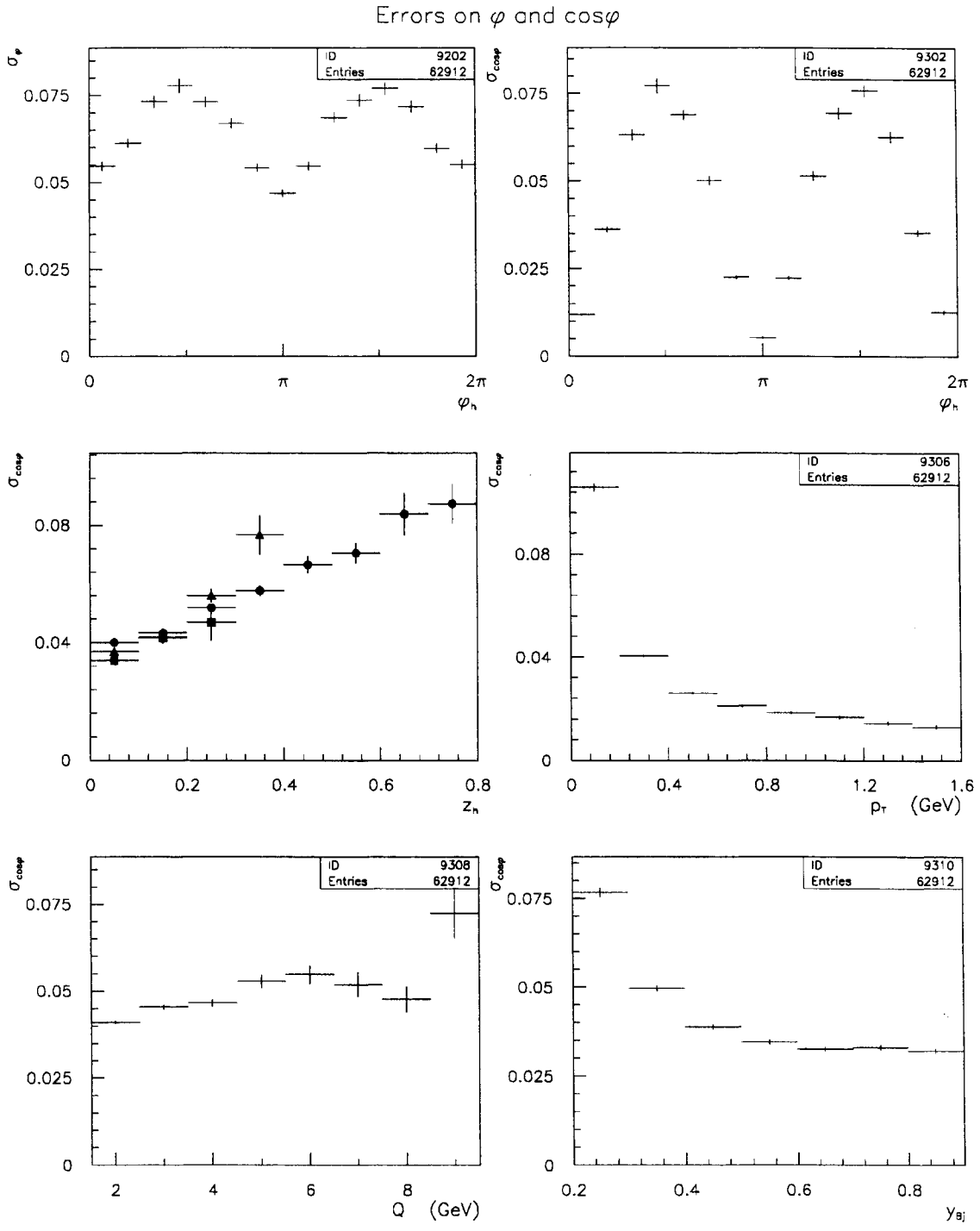

Figure 5-32: φ and $\cos\varphi$ Resolution.
Calculated measurement errors for φ and $\cos\varphi$ from data. Circles stand for Rank 1 (measured), triangles for Rank 2 (measured), and squares for Rank 3 (measured). a) σ_φ vs. φ_h by Rank, b) $\sigma_{\cos\varphi}$ vs. φ_h, c) $\sigma_{\cos\varphi}$ vs. z_h by Rank, d) $\sigma_{\cos\varphi}$ vs. p_T, e) $\sigma_{\cos\varphi}$ vs. Q, and f) $\sigma_{\cos\varphi}$ vs. y_{Bj}.

As described in Reference [50]:

$$\left\langle \delta p_T^2 \right\rangle \propto (1 - z_h^2) z_h^2 Q^2.$$

Taking a fairly extreme case, $z_h = 0.5$ and $Q^2 = 15$ GeV^2, we find that $\left\langle p_T^2 \right\rangle = 0.01$ GeV^2, which is negligible. Since this error is so small compared to our typical value of p_T^2 of 0.5 GeV^2, the error on $\cos\varphi_h$ is also small.

5.6 Conclusions

To summarize, the data on the phi asymmetry are somewhat surprising. They are consistent with previous data and previous analyses, but are inconsistent with naïve theoretical expectations and with more detailed Monte Carlo simulations which include the fragmentation process and known detector effects.

The first big effect is that the phi asymmetry of the hadrons is almost exclusively carried by the most energetic hadron in each event. Furthermore, this leading hadron phi asymmetry seems to be independent of z_h for $z_h > 0.1$. In contrast, most theoretical treatments which assume a conventional fragmentation scheme predict that the phi asymmetry should increase with increasing z and be nearly independent of the hadron rank. It would appear that the leading particle in the event retains more of the original parton direction than the other particles regardless of the values of z. The z_h dependence (for $z_h > 0.1$) measured in previous experiments is seen to be a consequence of the rank dependence and not fundamental in its own right. Furthermore, there is a marked p_T dependence of the $\langle \cos\varphi \rangle$ moment in the data for the leading charged particle that is not found in the Monte Carlo. Finally, the overall magnitude of the phi asymmetry is somewhat larger everywhere in the data than in the Monte Carlo.

The difficulty in describing the dependence of the phi asymmetry on the hadron variables suggests that there may be a problem with the conventional fragmentation scheme. Alternatively, the partonic level theory of the phi asymmetry may be wrong; the phi asymmetry may be due to some other mechanism than $k_\perp$ and hard QCD. In any case, it seems clear that our current theoretical description of how a phi asymmetry arises in the hadrons is incomplete. It also seems clear that the particle rank should be considered as an important variable in discussing the phi asymmetry in the hadrons in future measurements and models.

The second big effect was that the phi asymmetry was independent of $Q = \sqrt{Q^2}$. If we assume that the $k_\perp$ is truly independent of the kinematics, then we expect the phi asymmetry due to $k_\perp$ to vanish at large values of Q. If, however, the effective

$k_\perp$ in a given event were proportional to Q, then the data could be explained. The question of whether the $k_\perp$ is dependent on Q^2 or x_{B_j} is unresolved in the literature. It has generally been assumed to be independent for convenience and simplicity. Again, if the $k_\perp$ is the main cause of the phi asymmetry, then the hypothesis of $k_\perp$ being independent of event kinematics must be abandoned. Another small problem is that the y_{B_j}-dependence of the partonic phi asymmetry does not carry through to the hadronic level. This may be due to the effects of fragmentation being more pronounced at low W^2 and low y_{B_j}.

Additional support for the idea of the higher values of $k_\perp$ at higher values of Q is found in the seagull plots. We see that the high z_h particles have more p_T for the high Q events than for the low Q events. Unfortunately, this conclusion is somewhat ambiguous since we only observe forward hadrons; there are several sources of forward hadron p_T. The increase in p_T being predominantly at high z suggests $k_\perp$ as the source. However, EMC showed that it is possible to mimic $k_\perp$ in the forward hemisphere with "soft gluons".

Finally, we also note that, in general, the data prefer more phi asymmetry and more p_T overall than are provided by the Lepto 5.2(ME) Monte Carlo. This could be due to an increase in overall effective $k_\perp$, to the effect of soft gluons, or to some unknown process.

An interesting measurement that would add quite a bit of information to this whole discussion would be to examine the target remnant jet in the backward hemisphere. In particular, we could reconstruct the backward jet direction separately from the forward jet(s). This would allow us to measure the transverse momenta of the leading forward hadron and the non-leading forward hadrons with respect to the backward jet direction. This might help clarify why the leading hadron behaves differently from the other hadrons in the event. Furthermore, if the phi asymmetry is primarily due to the effect of $k_\perp$, then it should be equal and opposite in the backward hemisphere. There is already some evidence from the EMC results (see Figure 5-4 on page 144) that the phi asymmetry in the backward hemisphere is not strong enough to compensate the phi asymmetry in the forward hemisphere. Unfortunately their lack of statistical precision make it difficult to tell what is going on. Finally, by comparing the forward and backward hemisphere, it might be possible to determine whether the Q dependence of the seagull plot really arises from $k_\perp$ or from some other source.

Another interesting measurement that could be performed in the future would be to examine the behavior of the φ asymmetry at even higher values of Q^2, such as those accessible at HERA, to see whether any Q^2 dependence of the φ asymmetry shows up.

Chapter 6

Summary and Conclusions

In summary, we have examined the hadronic final state of Deep Inelastic Scattering events in order to improve our understanding of the structure of the proton and of the dynamics of the partons within the nucleon. In particular, we were concerned with the manifestations of the primordial $k_\perp$ of partons within the nucleon.

First we examined the theory of Deep Inelastic Scattering in some detail, starting with a Model Independent Framework based on well-established physics, moving through the quark-parton model which contains some further assumptions, and even discussed the implementation of the primordial $k_\perp$ of the partons within the framework of the QPM. The theoretical treatment of $k_\perp$ started from the assumption that we could use the Quark Parton Model and treat the $k_\perp$ as primarily a kinematic effect. Existing theoretical results in the literature for this type of approach were improved upon and then incorporated into a Monte Carlo which modeled the effects of the fragmentation process and the detector.

One of the clearest handles on the primordial $k_\perp$ was found to be the azimuthal asymmetry of partons about the virtual photon direction. The main effect of $k_\perp$ is that the partons prefer to end up at $\varphi = \pi$. This is in the scattering plane, but opposite the scattered muon. The phi asymmetry in the hadrons was expected to be primarily due to this effect with some QCD effects mixed in as well.

Several effects were found in the data which could not be accounted for in the theory. The firmest conclusion that can be drawn from the data is that the phi asymmetry has not really been understood. We found more phi asymmetry in the hadrons than expected. We found that this hadronic phi asymmetry depends on the rank of the hadrons and not directly on z_h, contrary to our expectations. We also found that the phi asymmetry is nearly independent of Q^2. This contradicts expectations if we assume that the $k_\perp$ is independent of the event kinematics. Finally,

we found that the high z_h particles have a larger value of $\left\langle p_T^2 \right\rangle$ for the higher Q^2 events.

On a more speculative note, the data suggest that the conventional fragmentation model is inadequate and that the leading particle carries more of the underlying parton's direction than expected. The data also suggest that the effective primordial $k_\perp$ of the parton in the nucleon may be dependent on event kinematics (Q^2 or ν).

Alternatively, it is possible that soft QCD, fragmentation effects, or some other unknown effect causes the phi asymmetry and our $k_\perp$ model is just wrong.

The current picture could be somewhat clarified in the future by a careful multivariate examination of the phi asymmetry in DIS. Examining the backward hemisphere, reconstructing jets, having higher statistics, and having a larger range in Q^2 would all be helpful. Both E665 at Fermilab and the detectors at HERA should be able to examine these questions in the future.

Appendix A

Theoretical Calculations

Although it is not always made explicit, most discussions of the parton model involve the assumption that the primordial transverse momentum of the parton inside the quark is small when compared to the Q^2 scale of the virtual photon. In E665, the assumption of large Q^2 is not valid for some of our data. A typical scale for $k_\perp^2$ is 0.2 GeV^2 while data down to $Q^2 = 2$ GeV^2 are used in this thesis. Some E665 hadron analyses have even used data down to $Q^2 = 0.1$ GeV^2.

It can be argued that many aspects of the parton model break down at such low values of Q^2, so that there is no point in considering the effect of $k_\perp$ beyond the leading order terms in $k_\perp/Q$. However, the data in the low Q^2 region are quite well-behaved and smoothly varying, with no evidence of singularities other than the Q^{-4} behavior of the cross-section. Furthermore, many of the problems with the naïve parton model at low Q^2 are simply due to kinematic approximations. It is useful, therefore, to recast the parton model in kinematically exact terms, cavalierly bypassing some of the more subtle theoretical problems that such a treatment entails.

To this end, this appendix contains some new calculations which don't appear in the literature. They are referenced in the body of the thesis, but details which might have been distracting are relegated here.

Section A.1 contains a general calculation of ξ, the longitudinal momentum fraction of the parton in the nucleon. This calculation is valid even when $k_\perp^2/Q^2$ and Q^2/ν^2 aren't negligible. Many of the usual results, such as $\xi = x_{B_J}$, are shown to be special cases.

Section A.2 contains a calculation of the leading order parton phi asymmetry that is valid even when $k_\perp^2$ and m_q^2 aren't negligible with respect to Q^2. We do still demand that $Q^2 \ll \nu^2$. The results by Cahn [19] are shown to be a special

case.

Section A.3 contains a calculation of the $\mathcal{O}(\alpha_S)$ parton phi asymmetry when both the QCD and $k_\perp$ effects are in place. This result is also available in Reference [21], but that paper contains some errors.

A.1 An exact calculation of $\xi(Q^2, \nu, k_\perp)$.

We seek an expression for the longitudinal momentum fraction, ξ, of the struck parton in the infinite momentum frame. The only approximation that we need is that the scattering cross-section is dominated by elastic single-photon scattering off of quasi-free quarks. Essentially we adopt the framework of the parton model, but without neglecting $k_\perp$. We do, however, neglect QCD effects.

The usual Naïve QPM result is that

$$\xi \equiv \frac{p_z^{(\infty)}}{P_z^{(\infty)}} \approx \frac{Q^2}{2M\nu} \equiv x_{Bj}. \tag{A.1}$$

This formula has the nice feature that it expresses ξ strictly in terms the virtual photon 4-momentum which is directly measurable: $q_\mu = l_\mu - l'_\mu$. Unfortunately, the usual derivation of this result relies, either implicitly or explicitly, on two additional assumptions. These are that the parton has a negligible transverse momentum with respect to the virtual photon axis, and that Q^2 is negligible when compared to ν^2. More explicitly, we must assume that $k_T^2 \ll Q^2 \ll \nu^2$. It is possible to calculate ξ without using these assumptions, but then, as we shall soon see, ξ is also a function of $k_\perp$, spoiling its status as an easily measured variable.

This calculation is performed below, and a general expression for ξ is found. Some standard expressions for ξ are shown to be special cases.

A.1.1 Explicit Derivation of the Exact Result

In the lab frame, with $\hat{z}$ defined along the direction of the virtual photon 3-momentum, the 4-momenta of the proton (P^μ) and of the virtual photon (q^μ) are given by:

$$\begin{aligned} P^\mu_{Lab} &= \{M;\ 0,\ 0,\ 0\}, \\ q^\mu_{Lab} &= \left\{\nu;\ 0,\ 0,\ \sqrt{Q^2+\nu^2}\right\}. \end{aligned} \tag{A.2}$$

We can perform a Lorentz boost along $-\hat{z}$ into a frame where the proton has very large momentum $\vec{P} = -P\hat{z}$. We can then relate ξ to our other quantities in this frame. In order for our formalism to make sense, the explicit value of P must drop out of our final answer when $P \to \infty$. In this frame, which we call the infinite-momentum frame (S_∞), the proton 4-momentum is:

$$P^\mu = \left\{\sqrt{P^2 + M^2};\ \ 0,\ 0,\ -P\right\}; \tag{A.3}$$

the boost parameters are given by:

$$\gamma = \frac{P}{M}\sqrt{1 + \frac{M^2}{P^2}}\ , \qquad \beta = \left(1 + \frac{M^2}{P^2}\right)^{-\frac{1}{2}}\ , \qquad \gamma\beta = \frac{P}{M}\ ; \tag{A.4}$$

and the virtual photon 4-momentum is:

$$q^\mu = \left\{\gamma\nu\left(1 - \beta\sqrt{1 + Q^2/\nu^2}\right);\ \ 0,\ 0,\ \gamma\nu\left(\sqrt{1 + Q^2/\nu^2} - \beta\right)\right\}. \tag{A.5}$$

We define the kinematics of the parton in the infinite momentum frame as follows: ξ is the fraction of the proton's longitudinal momentum carried by the interacting parton ($\xi \equiv \frac{p_z^\infty}{P_z^\infty}$); $k_\perp$ is the primordial transverse momentum of the parton with respect to the virtual photon axis; and m_q is the parton mass. The parton's 4-momentum in S_∞ is then, by definition:

$$p^\mu \equiv \left\{\sqrt{\xi^2 P^2 + m_\perp^2};\ \ k_\perp\cos\varphi,\ k_\perp\sin\varphi,\ -\xi P\right\}, \tag{A.6}$$

where $m_\perp^2 \equiv k_\perp^2 + m_q^2$.

Now, for elastic scattering off of a single quark, we have one important constraint on the 4-vectors p^μ and q^μ:

$$(p+q)^2 = m_q^2 \quad \Rightarrow \quad q^2 + 2p\cdot q = 0 \quad \Rightarrow \quad Q^2 = 2p\cdot q. \tag{A.7}$$

Combining Equations A.5, A.6, and A.7 yields the following equation:

$$Q^2 = 2\nu P\gamma\xi\left\{\sqrt{1 + \frac{m_\perp^2}{\xi^2 P^2}}\left(1 - \beta\sqrt{1 + \frac{Q^2}{\nu^2}}\right) + \left(\sqrt{1 + \frac{Q^2}{\nu^2}} - \beta\right)\right\}, \tag{A.8}$$

which we can rewrite as:

$$\frac{Q^2}{2\nu P\gamma\xi} + \beta - \sqrt{1 + \frac{Q^2}{\nu^2}} = \left(1 - \beta\sqrt{1 + \frac{Q^2}{\nu^2}}\right)\sqrt{1 + \frac{m_\perp^2}{\xi^2 P^2}}. \tag{A.9}$$

We have implicitly assumed here that

$$\xi > 0. \tag{A.10}$$

This assumption is justified for the following reasons. If $\xi = 0$, then Equation A.7 has no solution unless $Q^2 = m_q^2 = p_\perp^2 = 0$. If $\xi < 0$, then energy cannot be conserved since the parton energy, when boosted back to the lab frame, diverges.

Proceeding with the calculation, we square both sides of Equation A.9, yielding:

$$\frac{Q^4}{4\nu^2 P^2\gamma^2\xi^2} + 2\left(\beta - \sqrt{1+\frac{Q^2}{\nu^2}}\right)\frac{Q^2}{2\nu P\gamma\xi} + \left(\beta - \sqrt{1+\frac{Q^2}{\nu^2}}\right)^2 = \left(1 - \beta\sqrt{1+\frac{Q^2}{\nu^2}}\right)^2\left(1 + \frac{m_\perp^2}{P^2\xi^2}\right). \tag{A.11}$$

Collecting terms, we find that:

$$0 = \frac{1}{\xi^2}\left[\frac{Q^4}{4\nu^2P^2\gamma^2} - \left(1 - \beta\sqrt{1+\frac{Q^2}{\nu^2}}\right)^2\frac{m_\perp^2}{P^2}\right] + \frac{1}{\xi}\left[\left(\beta - \sqrt{1+\frac{Q^2}{\nu^2}}\right)\frac{Q^2}{\nu P\gamma}\right] + \left[\left(\beta - \sqrt{1+\frac{Q^2}{\nu^2}}\right)^2 - \left(1 - \beta\sqrt{1+\frac{Q^2}{\nu^2}}\right)^2\right]. \tag{A.12}$$

We can simplify slightly, noting that:

$$\begin{aligned}&\left[\left(\beta - \sqrt{1+\frac{Q^2}{\nu^2}}\right)^2 - \left(1 - \beta\sqrt{1+\frac{Q^2}{\nu^2}}\right)^2\right] \\ &= \beta^2 - 2\beta\sqrt{1+\frac{Q^2}{\nu^2}} + \left(1+\frac{Q^2}{\nu^2}\right) - 1 + 2\beta\sqrt{1+\frac{Q^2}{\nu^2}} - \beta^2\left(1+\frac{Q^2}{\nu^2}\right) \\ &= (1-\beta^2)\left(\frac{Q^2}{\nu^2}\right) = \frac{1}{\gamma^2}\frac{Q^2}{\nu^2}.\end{aligned} \tag{A.13}$$

Multiplying Equation A.12 by ξ^2 and using Equations A.10 and A.13 we find a qua-

dratic equation in ξ:

$$\begin{aligned} 0 &= a\xi^2 + b\xi + c, \\ a &= \frac{1}{\gamma^2}\frac{Q^2}{\nu^2}, \\ b &= \frac{Q^2}{\nu P \gamma}\left(\beta - \sqrt{1+\frac{Q^2}{\nu^2}}\right), \\ c &= \frac{Q^4}{4\nu^2 P^2 \gamma^2} - \left(1 - \beta\sqrt{1+\frac{Q^2}{\nu^2}}\right)^2 \frac{m_\perp^2}{P^2}. \end{aligned} \tag{A.14}$$

We can solve the quadratic equation as follows, noting that $a > 0$:

$$\xi = \frac{-b \pm \sqrt{b^2 - 4ac}}{2a} = -\frac{b}{2a} \pm \sqrt{\frac{b^2}{4a^2} - \frac{c}{a}} \ ; \tag{A.15}$$

$$\begin{aligned} \xi &= \frac{\nu\gamma}{2P}\left(\sqrt{1+\frac{Q^2}{\nu^2}} - \beta\right) \pm \\ &\left\{\frac{\nu^2\gamma^2}{4P^2}\left(\beta - \sqrt{1+\frac{Q^2}{\nu^2}}\right)^2 - \left[\frac{Q^2}{4P^2} - \left(1 - \beta\sqrt{1+\frac{Q^2}{\nu^2}}\right)^2 \frac{m_\perp^2\gamma^2\nu^2}{P^2Q^2}\right]\right\}^{\frac{1}{2}}. \end{aligned} \tag{A.16}$$

Substituting $\gamma = \frac{P}{M\beta}$ and simplifying yields:

$$\begin{aligned} \xi &= \frac{\nu}{2M}\left(\beta^{-1}\sqrt{1+\frac{Q^2}{\nu^2}} - 1\right) \pm \\ &\left\{\frac{\nu^2}{4M^2\beta^2}\left(\beta - \sqrt{1+\frac{Q^2}{\nu^2}}\right)^2 - \left[\frac{Q^2}{4P^2} - \left(1 - \beta\sqrt{1+\frac{Q^2}{\nu^2}}\right)^2 \frac{m_\perp^2\nu^2}{M^2Q^2\beta^2}\right]\right\}^{\frac{1}{2}}. \end{aligned} \tag{A.17}$$

Now, taking $P \to \infty$ (and therefore $\beta \to 1$) yields:

$$\begin{aligned} \xi &= \frac{\nu}{2M}\left(\sqrt{1+\frac{Q^2}{\nu^2}} - 1\right) \pm \\ &\left\{\frac{\nu^2}{4M^2}\left(1 - \sqrt{1+\frac{Q^2}{\nu^2}}\right)^2 + \left(1 - \sqrt{1+\frac{Q^2}{\nu^2}}\right)^2 \frac{m_\perp^2\nu^2}{M^2Q^2}\right\}^{\frac{1}{2}}. \end{aligned} \tag{A.18}$$

Equation A.10 requires that we use the positive root. Collecting terms, we arrive at our final answer:

$$\boxed{\xi = \frac{\nu}{2M}\left(\sqrt{1+\frac{Q^2}{\nu^2}}-1\right)\left(1+\sqrt{1+\frac{4m_\perp^2}{Q^2}}\right)}. \tag{A.19}$$

A.1.2 Some Interesting Limiting Cases

Now that we have the exact result, we can consider various limits. If $Q^2 \ll \nu^2$ (or equivalently $\nu \gg M$), we can perform the binomial expansion:

$$\sqrt{1+\frac{Q^2}{\nu^2}} \approx 1 + \frac{Q^2}{2\nu^2} - \frac{Q^4}{8\nu^4}. \tag{A.20}$$

This yields:

$$\xi \cong \frac{Q^2}{2M\nu}\left(1-\frac{Q^2}{4\nu^2}\right)\left(\frac{1}{2}+\frac{1}{2}\sqrt{1+\frac{4m_\perp^2}{Q^2}}\right). \tag{A.21}$$

If we additionally assume that $m_\perp^2 \ll Q^2$, then:

$$\begin{aligned}\xi &\simeq \frac{Q^2}{2M\nu}\left(1-\frac{Q^2}{4\nu^2}\right)\left[\frac{1}{2}+\frac{1}{2}\left(1+\frac{2m_\perp^2}{Q^2}\right)\right] \\ \xi &\simeq \frac{Q^2}{2M\nu}\left(1-\frac{M^2x^2}{Q^2}\right)\left(1+\frac{m_\perp^2}{Q^2}\right),\end{aligned} \tag{A.22}$$

where $x \equiv x_{Bj} \equiv \frac{Q^2}{2M\nu}$. Dropping the term of order $\mathcal{O}\left(\frac{M^2m_\perp^2}{Q^4}\right)$ yields:

$$\xi \simeq x\left(1+\frac{m_\perp^2 - x^2M^2}{Q^2}\right). \tag{A.23}$$

This result also appears in Reference [52] (Equation 14.2.16). It is a special case of the exact formula given above in Equation A.19. It assumes that the approximation $k_\perp^2 \ll Q^2 \ll \nu^2$ is valid.

For E665 kinematics, we know that $\nu \gg M$ is a very safe approximation and we can drop the "target mass correction" term which is of order $\mathcal{O}\left(\frac{x^3M^2}{Q^2}\right)$, yielding:

$$\xi \simeq \frac{Q^2+m_\perp^2}{2M\nu} \simeq \frac{Q^2+m_\perp^2}{W^2}. \tag{A.24}$$

If we assume that $m_\perp^2 = 0$, along with $Q^2 \ll \nu^2$, then we recover the Naïve Parton Model result:

$$\xi \approx \frac{Q^2}{2M\nu} \equiv x_{B_j}. \tag{A.25}$$

Again, the Naïve Parton Model result is seen to be a special case of the exact formula given in Equation A.19.

Given the kinematic range used in this thesis, it is useful to derive a form which includes the assumption that $Q^2 \ll \nu^2$, but which makes no assumption at all about $k_\perp$. Starting with Equation A.19 and expanding $\sqrt{1+\frac{Q^2}{\nu^2}} \simeq 1 + \frac{Q^2}{2\nu^2}$ yields:

$$\boxed{\xi \simeq \frac{Q^2}{2M\nu}\left(\frac{1}{2} + \frac{1}{2}\sqrt{1+\frac{4m_\perp^2}{Q^2}}\right)}. \tag{A.26}$$

A.1.3 Summary

In conclusion, we note that Equation A.19 is an exact kinematic result and that many of the usual results are approximations which are useful in certain circumstances. Equation A.23, which can also be found in Reference [52], is useful when $\frac{Q}{\nu}$ and $\frac{k_T}{Q}$ are small, but not completely negligible. When we take the extreme limit of $k_T^2 \ll Q^2 \ll \nu^2$, we recover the usual Naïve Parton Model result given by Equation A.25. For the kinematic range of this experiment, the most useful theoretical form is that contained in Equation A.26 above. This is the form that will be used in Appendix Section A.2 and which is therefore incorporated into my version of the Lund Monte Carlo for the leading order process.

A.2 Leading Order Phi Asymmetry due to $k_\perp$

Cahn [19, 20] calculated the leading order parton-level phi asymmetry under the assumption that $k_\perp^2 \ll Q^2$ and $m_q = 0$. In this section, we extend this calculation by removing the assumption that $k_\perp$ is small: $k_\perp^2 \ll Q^2$. We also consider the case $m_q \neq 0$. We continue to assume that the leading DIS naïve parton model diagram (Figure 2-2) dominates and that $Q^2 \ll \nu^2$.

A.2.1 The Calculation

We define x, ξ, and ξ' as follows:

$$\begin{aligned} x &\equiv -\frac{q^2}{2P\cdot q} = \frac{Q^2}{2M\nu} \equiv x_{Bj}, \\ \xi &\equiv \frac{p_z^\infty}{P_z^\infty}, \\ \xi' &\equiv \frac{x}{\xi}. \end{aligned} \tag{A.27}$$

We will perform this calculation in the same S_∞ frame defined in Section A.1. From Equation A.26 we know that ξ' can be written:

$$\xi' = \left(\frac{1}{2} + \frac{1}{2}\sqrt{1 + \frac{4m_\perp^2}{Q^2}}\right)^{-1}. \tag{A.28}$$

The incoming parton's 4-momentum in S_∞ is given by equation A.6, while the incoming and outgoing muon momenta are:

$$\begin{aligned} l^\mu &= \{E\gamma(1-\beta\cos\alpha); \quad E\sin\alpha, \quad 0, \quad E\gamma(\cos\alpha-\beta)\} \\ l'^\mu &= \{E'\gamma(1-\beta\cos\alpha'); \quad E'\sin\alpha', \quad 0, \quad E'\gamma(\cos\alpha'-\beta)\}. \end{aligned} \tag{A.29}$$

The variable α refers to the angle that the beam momentum vector makes with the virtual photon direction in the lab frame. Similarly, α' refers to the angle that the scattered muon momentum vector makes with the virtual photon direction in the lab frame. These angles are given by the following expressions:

$$\begin{aligned} \cos\alpha &\cong 1 - \tfrac{Q^2}{2\nu^2}\tfrac{E'}{E} \simeq 1, & \sin\alpha &\cong \tfrac{Q}{\nu}\sqrt{\tfrac{E'}{E}}, \\ \cos\alpha' &\cong 1 - \tfrac{Q^2}{2\nu^2}\tfrac{E}{E'} \simeq 1, & \sin\alpha' &\cong \tfrac{Q}{\nu}\sqrt{\tfrac{E}{E'}}, \\ \gamma &\cong \tfrac{P}{M}, & \beta &\cong 1 - \tfrac{1}{2\gamma^2}, \end{aligned} \tag{A.30}$$

where we have assumed that the mass of the muon is negligible.

Now, leading order QED yields the following result [19]:

$$\sigma \propto s^2 + u^2, \tag{A.31}$$

where $s \equiv (l+p)^2$ and $u \equiv (l'-p)^2$. From Equations A.6 and A.29, we have:

$$2l \cdot p = 2E\gamma P\xi \left[(1-\beta\cos\alpha)\sqrt{1+\frac{m_\perp^2}{\xi^2 P^2}} + \cos\alpha - \beta \right] - 2k_\perp E \sin\alpha\cos\varphi. \qquad \text{(A.32)}$$

Expanding the square root binomially and regrouping terms yields:

$$2l \cdot p \cong 2E\gamma P\xi \left[(1-\beta)(1+\cos\alpha) + \frac{m_\perp^2}{2\xi^2 P^2}(1-\beta\cos\alpha) \right] - 2k_\perp E \sin\alpha\cos\varphi. \qquad \text{(A.33)}$$

Using Equation A.30 yields:

$$\begin{aligned} 2l \cdot p \;\cong\; & 2E\gamma P\xi \left[\frac{1}{2\gamma^2}\left(2 - \frac{Q^2}{2\nu^2}\frac{E'}{E}\right) + \frac{m_\perp^2}{2\xi^2 P^2}\left(\frac{Q^2}{2\nu^2}\frac{E'}{E} + \mathcal{O}\left(\frac{1}{\gamma^2}\right)\right)\right] \\ & -2k_\perp \frac{Q}{\nu}\sqrt{EE'}\cos\varphi. \end{aligned} \qquad \text{(A.34)}$$

Taking $\gamma \to \frac{P}{M}$ and keeping only the leading order terms in M/P yields:

$$2l \cdot p \cong 2ME\xi \left[1 - \frac{Q^2}{4\nu^2}\frac{E'}{E} + \frac{m_\perp^2}{\xi^2 M^2}\frac{Q^2}{4\nu^2}\frac{E'}{E} \right] - 2k_\perp \frac{Q}{\nu}\sqrt{EE'}\cos\varphi. \qquad \text{(A.35)}$$

Recalling that $Q^2 \ll \nu^2$, we can drop the $\mathcal{O}(Q^2/\nu^2)$ term:

$$2l \cdot p \cong 2ME\xi \left[1 + \frac{m_\perp^2}{\xi^2 M^2}\frac{Q^2}{4\nu^2}\frac{E'}{E} \right] - 2k_\perp \frac{Q}{\nu}\sqrt{EE'}\cos\varphi. \qquad \text{(A.36)}$$

A similar calculation yields:

$$2l' \cdot p \cong 2ME'\xi \left[1 + \frac{m_\perp^2}{\xi^2 M^2}\frac{Q^2}{4\nu^2}\frac{E}{E'} \right] - 2k_\perp \frac{Q}{\nu}\sqrt{EE'}\cos\varphi. \qquad \text{(A.37)}$$

Equation A.37 is the same as Equation A.36 with the interchange $\{E \leftrightarrow E'\}$.

We are now in a position to calculate the quantity s by using Equation A.36,

substituting $\xi = x/\xi'$, and simplifying:

$$\begin{aligned} s &= 2l\cdot p + m_q^2 \\ &\cong 2MEx\left[\frac{1}{\xi'} + \xi' m_\perp^2 \frac{Q^2}{4M^2\nu^2x^2}\frac{E'}{E}\right] - 2MEx\frac{2k_\perp}{Q}\sqrt{\frac{E'}{E}}\cos\varphi + m_q^2 \\ &\simeq 2MEx\left[\frac{1}{\xi'} + \xi'\frac{m_\perp^2}{Q^2}(1-y) - \frac{2k_\perp}{Q}\sqrt{1-y}\cos\varphi\right] + m_q^2, \end{aligned} \tag{A.38}$$

where $y \equiv \frac{P\cdot q}{l\cdot q} = \frac{E-E'}{E}$. Similarly, we can construct:

$$\begin{aligned} -u &= 2l'\cdot p - m_q^2 \\ &\cong 2ME'x\left[\frac{1}{\xi'} + \xi' m_\perp^2 \frac{Q^2}{4M^2\nu^2x^2}\frac{E}{E'}\right] - 2ME'x\frac{2k_\perp}{Q}\sqrt{\frac{E}{E'}}\cos\varphi - m_q^2 \\ &\simeq 2MEx(1-y)\left[\frac{1}{\xi'} + \frac{\xi'}{1-y}\frac{m_\perp^2}{Q^2} - \frac{2k_\perp}{Q}\frac{1}{\sqrt{1-y}}\cos\varphi\right] - m_q^2. \end{aligned} \tag{A.39}$$

Neglecting m_q^2 and assembling, we have:

$$\sigma \propto s^2 + u^2 \propto 4M^2E^2x^2\left[(a - b\cos\varphi)^2 + (a' - b\cos\varphi)^2\right], \tag{A.40}$$

where:

$$\begin{aligned} a &= \frac{1}{\xi'} + \xi'\frac{k_\perp^2}{Q^2}(1-y) \\ a' &= \frac{1}{\xi'}(1-y) + \xi'\frac{k_\perp^2}{Q^2} \\ b &= 2\frac{k_\perp}{Q}\sqrt{1-y}. \end{aligned} \tag{A.41}$$

Using Equation A.40 and the identity $\cos^2\varphi = \frac{1}{2}(1+\cos 2\varphi)$, we see that:

$$\sigma \propto (a^2 + a'^2 + b^2) - 2(a+a')b\cos\varphi + b^2\cos 2\varphi. \tag{A.42}$$

Assembling the results, we have:

$$\sigma \propto A + B\cos\varphi + C\cos 2\varphi, \tag{A.43}$$

with

$$\boxed{\begin{aligned} A &= [1+(1-y)^2]\left(\tfrac{1}{\xi'^2}+\xi'^2\tfrac{k_\perp^4}{Q^4}\right)+8(1-y)\tfrac{k_\perp^2}{Q^2} \\ B &= -4\tfrac{k_\perp}{Q}\left(\tfrac{1}{\xi'}+\xi'\tfrac{k_\perp^2}{Q^2}\right)(2-y)\sqrt{1-y} \\ C &= 4\tfrac{k_\perp^2}{Q^2}(1-y) \end{aligned}} \tag{A.44}$$

and where $\xi' = \left(\frac{1}{2}+\frac{1}{2}\sqrt{1+\frac{4k_\perp^2}{Q^2}}\right)^{-1}$.

Equation A.44 is the result for the partonic cross-section at leading order in α_s assuming massless quarks and assuming that $Q^2 \ll \nu^2$. We can easily generalize to arbitrary quark mass m_q at the expense of making the result for A somewhat messier.

Equations A.38 and A.39 still hold, since they were derived for arbitrary quark mass. Therefore, Equations A.40 and A.42 still hold as long as we modify Equation A.41 as follows:

$$\begin{aligned} a &= \frac{1}{\xi'}+\xi'\frac{m_\perp^2}{Q^2}(1-y)+\frac{m_q^2y^2}{Q^2} \\ a' &= \frac{1}{\xi'}(1-y)+\xi'\frac{m_\perp^2}{Q^2}-\frac{m_q^2y^2}{Q^2} \\ b &= 2\frac{k_\perp}{Q}\sqrt{1-y}. \end{aligned} \tag{A.45}$$

The fully general case, for arbitrary $k_\perp$ and arbitrary m_q is therefore:

$$\sigma \propto A + B\cos\varphi + C\cos 2\varphi, \tag{A.46}$$

with

$$\begin{aligned} A &= \left[1+(1-y)^2\right]\left(\frac{1}{\xi'^2}+\xi'^2\frac{m_\perp^4}{Q^4}\right)+8(1-y)\frac{k_\perp^2+\frac{1}{2}m_q^2}{Q^2} \\ &\quad +2\frac{m_q^2y^2}{Q^2}\left(\frac{1}{\xi'}-\xi'\frac{m_\perp^2}{Q^2}+\frac{m_q^2}{Q^2}\right) \\ B &= -4\frac{k_\perp}{Q}\left(\frac{1}{\xi'}+\xi'\frac{m_\perp^2}{Q^2}\right)(2-y)\sqrt{1-y} \\ C &= 4\frac{k_\perp^2}{Q^2}(1-y) \end{aligned} \tag{A.47}$$

and $\xi' = \left(\frac{1}{2} + \frac{1}{2}\sqrt{1 + \frac{4m_\perp^2}{Q^2}}\right)^{-1}$.

A.2.2 Some Interesting Limiting Cases

Several interesting facts can be pointed out regarding the results in Equation A.44, where we are again neglecting m_q. If we keep only the leading terms in $\frac{k_\perp}{Q}$, we recover Cahn's results [19, 20]:

$$\begin{aligned} A &\approx \left[1 + (1-y)^2\right] \\ B &\approx -4\frac{k_\perp}{Q}(2-y)\sqrt{1-y} \\ C &= 4\frac{k_\perp^2}{Q^2}(1-y). \end{aligned} \tag{A.48}$$

Furthermore, if we integrate over phi, we find that:

$$\sigma \propto A = \left[1 + (1-y)^2\right]\left(\frac{1}{\xi'^2} + \xi'^2\frac{k_\perp^4}{Q^4}\right) + 8(1-y)\frac{k_\perp^2}{Q^2}. \tag{A.49}$$

Since $\sigma \propto [1 + (1-y)^2]\,\sigma_T + 2(1-y)\sigma_L$, we can extract a prediction for $R \equiv \frac{\sigma_L}{\sigma_T}$ due to the effect of primordial $k_\perp$:

$$R = 4\frac{k_\perp^2}{Q^2}\left(\frac{1}{\xi'^2} + \xi'^2\frac{k_\perp^4}{Q^4}\right)^{-1}. \tag{A.50}$$

If we again keep only the leading terms in $\frac{k_\perp}{Q}$, we are left with the result:

$$R = 4\frac{k_\perp^2}{Q^2} \tag{A.51}$$

which is a standard result in the literature [11].

When Q^2 is small or $k_\perp^2$ large, the approximation given by Equation A.48 is very poorly behaved. The cross-section even becomes negative in places. In contrast, the exact result given in Equation A.44 is quite well-behaved, even in the limit that

$\frac{k_\perp}{Q} \to \infty$ where we have:

$$\begin{aligned}
\xi' &\to \frac{Q}{k_\perp} \quad (\to 0), \\
A &\to \frac{k_\perp^2}{Q^2}\left\{2\left[1+(1-y^2)\right]+8(1-y)\right\}, \\
B &\to -8\frac{k_\perp^2}{Q^2}(2-y)\sqrt{1-y}, \\
C &= 4\frac{k_\perp^2}{Q^2}(1-y), \\
\sigma &\to \left\{2\left[1+(1-y^2)\right]+8(1-y)\right\} - 8(2-y)\sqrt{1-y}\cos\varphi + 4(1-y)\cos 2\varphi.
\end{aligned} \tag{A.52}$$

The maximal violation of phi symmetry occurs for this limit of $Q \to 0$ with $y = 0$. In this case, we have:

$$\begin{aligned}
\sigma &\propto 1 - \frac{4}{3}\cos\varphi + \frac{1}{3}\cos 2\varphi \\
&= \frac{2}{3} - \frac{4}{3}\cos\varphi + \frac{2}{3}\cos\varphi^2 \\
&= \frac{2}{3}(1-\cos\varphi)^2
\end{aligned} \tag{A.53}$$

which is still a positive definite cross-section. It is sometimes claimed (see, for instance, Reference [48]) that the magnitude of the moment $\langle\cos\varphi\rangle = \frac{B}{2A}$ must not exceed $\frac{1}{2}$ for a physical cross-section or hadron distribution of the general form: $A + B\cos\varphi + C\cos 2\varphi + D\sin\varphi$. Equation A.53 consists of a refutation of this claim. The only true constraint is that the cross-section or hadron distribution must remain positive definite.

A.2.3 Summary

A calculation was presented of the phi asymmetry caused at leading order by the presence of primordial transverse momentum. The cases of negligible and non-negligible quark mass (m_q) were both considered. This calculation made no assumptions about the size of $k_\perp$, but only assumed that $Q^2 \ll \nu^2$. The main result, Equation A.44, reduces to Cahn's results [19] in the limit of small $k_\perp$, but is better behaved when $k_\perp$ is large.

A.3 Phi Asymmetry to $\mathcal{O}(\alpha_s)$ with $k_\perp$

This section contains a calculation of the parton-level phi asymmetry to $\mathcal{O}(\alpha_s)$ in QCD in the presence of primordial $k_\perp$. Many calculations exist which describe the $\mathcal{O}(\alpha_s)$ parton-level cross-section under the assumption that the primordial transverse momentum is exactly zero [18, 22, 23]. When the primordial $k_\perp$ is non-negligible with respect to either Q^2 or the $p_\perp$ of the two forward jets, then matters become considerably more complicated. The complete calculation is described in detail in Reference [21], which unfortunately, contains several errors. Their basic method is sound and is outlined below with the correct results included. The importance of primordial $k_\perp$ in the context of phi asymmetry was also noted by König and Kroll [17], but the details of their work are not available in the refereed literature.

A.3.1 General Definitions and Results

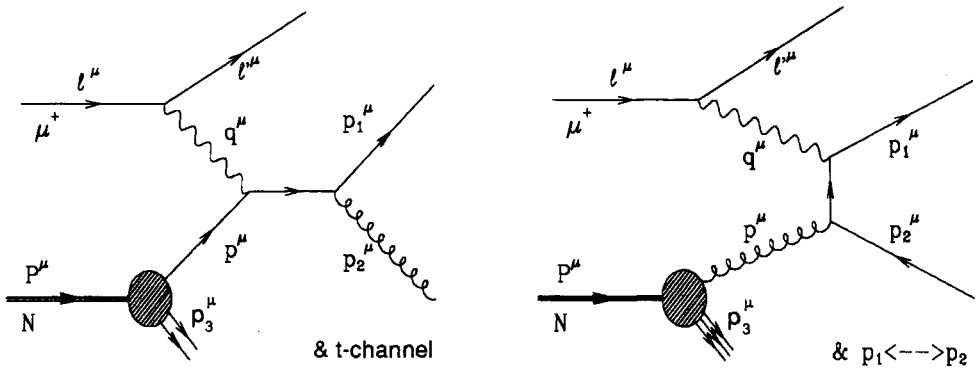

Figure A-1: $\mathcal{O}(\alpha_s)$ Diagrams in DIS.
Feynman diagrams corresponding to a) s-channel gluon bremsstrahlung and b) photon-gluon fusion. Note: t-channel gluon bremsstrahlung and the photon-gluon fusion $q\bar{q}$-exchanged diagrams are not shown.

We will consider two first order processes: gluon bremsstrahlung and photon-gluon fusion (See Figure A-1). Each process can be viewed at the purely partonic level, or at the level of the photon-nucleon interaction. The various possibilities are tabulated below.

Process	Partonic description	Nucleonic description
Gluon Bremsstrahlung	$\gamma(q) + q(p) \rightarrow q(p_1) + g(p_2)$	$\gamma(q) + N(P) \rightarrow q(p_1) + g(p_2) + T(p_3)$
Photon-Gluon Fusion	$\gamma(q) + g(p) \rightarrow q(p_1) + \bar{q}(p_2)$	$\gamma(q) + N(P) \rightarrow q(p_1) + \bar{q}(p_2) + T(p_3)$

The quantity in parentheses by a given particle is the particle's four-momentum. The symbol T refers to the target remnant which consists of the target minus the struck quark or gluon. One can relate the partonic description to the nucleonic description by noting that $p^\mu = P^\mu - p_3^\mu$.

In order to calculate explicit results, it is necessary to define some explicit coordinate systems. In this appendix section we will use the coordinate systems defined by Joshipura and Kramer [21]. It should be noted that these frames differ slightly from those used in the Lund Monte Carlo and in the bulk of this thesis. The details of how to relate these theoretical quantities to the variables in the LUND program are contained in Appendix B.

The $S(x,y,z)$ coordinate system is defined as the photon-nucleon-cm frame with the z-axis in the direction of $\vec{P}$, and the x-axis such that the muon scattering plane is the x-z plane with a positive x-component for the muon momenta. The variables φ, φ_1, φ_3 refer to the azimuthal angles of p, p_1, and p_3 in this frame. The variables p_T (p_{1T}), p_L (p_{1L}), p_0 (p_{10}), are the transverse momentum, longitudinal momentum, and energy corresponding to p (p_1). The virtual photon 4-momentum is given by: $q^\mu \equiv (q_0; 0, 0, -|\mathbf{q}|)$. It should be noted that the variables φ_3 and φ obey the following relation: $\varphi_3 = \varphi + \pi$. This coordinate system S is related quite simply to the normal hadronic-cm frame that is used throughout the bulk of this thesis. The relationship is given by $x \to x$, $y \to -y$, and $z \to -z$, which corresponds to a rotation of π about the x-axis. Furthermore, the variable p_T corresponds to the primordial transverse momentum of the struck parton, referred to in this thesis as $k_\perp$.

Continuing to follow Joshipura and Kramer, we define an additional coordinate system $\hat{S}(X,Y,Z)$ with the Z-axis along the target remnant direction. We denote the S-frame momenta $\mathbf{p_i}$ in this new frame $\hat{S}$ as $\hat{\mathbf{p}}_\mathbf{i}$. By definition, we have $\hat{\mathbf{p}}_\mathbf{3} = |\mathbf{p_3}|(0,0,1)$, and more generally we can write: $\hat{\mathbf{p}}_\mathbf{i} = R_{\hat{y}}(\theta_3)R_z(\varphi_3)\mathbf{p_i}$, where θ_3 and φ_3 are just the polar and azimuthal angles of $\mathbf{p_3}$ in the original S system.

Armed with these definitions, we can proceed with our calculation. Let's consider a DIS collision of a virtual photon of fixed kinematics (ν, Q^2) with a parton inside a proton (or nucleus). We can assemble the cross section given in the Joshipura and Kramer paper [21] from their Equations 2.3 and 2.25. The result is

$$\frac{d\sigma}{dx_1 dx_2 d\varphi_3 d\hat{\varphi}_1 dp_T^2} = \frac{2\pi\Gamma\mathcal{F}(\mathbf{p})}{32(2\pi)^5\eta x_3(W^2+Q^2)} \times \left(T_U + \frac{2(1-y)}{1+(1-y)^2}(T_L+T_T) + \frac{(2-y)\sqrt{1-y}}{1+(1-y)^2}T_I\right), \tag{A.54}$$

where Γ, the equivalent virtual photon flux, is given in their notation[1] as:

$$\Gamma = \frac{\alpha W^2}{4\pi^2 Q^2 (W^2+Q^2)^2}[1+(1-y)^2], \tag{A.55}$$

η is given by $\eta \equiv p_L/P$, $x_i \equiv 2p_{i0}/W$ are the usual normalized "jet" energies, and $\mathcal{F}(\mathbf{p})$ is a generalized structure function for the struck parton. The structure function is generalized in the sense that it depends upon the transverse component of the momentum as well as the longitudinal.

Clearly, the essence of Equation A.54 is contained in the quantities T_X, where $X \in \{U, L, T, I\}$. These T_X are the projections of the hadronic tensor $T_{\mu\nu}$ for various virtual photon polarizations:

$$\begin{aligned} T_U &\equiv \frac{1}{2}(T_{++}+T_{--}) \\ T_L &\equiv T_{00} \\ T_T &\equiv -\frac{1}{2}(T_{+-}+T_{-+}) \\ T_I &\equiv \frac{1}{\sqrt{2}}(T_{-0}+T_{0-}-T_{+0}-T_{0+}) \end{aligned} \tag{A.56}$$

with

$$\begin{aligned} T_{ss'} &\equiv \epsilon^{\mu *}_{(s)} T_{\mu\nu} \epsilon^{\nu}_{(s')} & s &\in \{+,0,-\}. \\ \epsilon^{\mu}_{(0)} &= \tfrac{1}{Q}(|\mathbf{q}|;0,0,-q_0), & \epsilon^{\mu}_{(\pm)} &= \mp\tfrac{1}{\sqrt{2}}(0;1,\pm i,0). \end{aligned} \tag{A.57}$$

In order to present explicit answers, we will calculate the results in the form:

$$\begin{aligned} T_U &= \tfrac{1}{2}T_1(\ \alpha_{1U}+\alpha_{2U}\cos 2\hat{\varphi}_1+\alpha_{3U}\cos\hat{\varphi}_1) \\ T_L &= \ T_1(\ \alpha_{1L}+\alpha_{2L}\cos 2\hat{\varphi}_1+\alpha_{3L}\cos\hat{\varphi}_1) \\ T_T &= \tfrac{1}{2}T_1[\ \cos 2\varphi_3(\alpha_{1T}+\alpha_{2T}\cos 2\hat{\varphi}_1+\alpha_{3T}\cos\hat{\varphi}_1) \\ &\qquad +\sin 2\varphi_3(\beta_{2T}\sin 2\hat{\varphi}_1+\beta_{3T}\sin\hat{\varphi}_1)] \\ T_I &= -\tfrac{2}{Q}T_1[\ \cos\varphi_3(\alpha_{1I}+\alpha_{2I}\cos 2\hat{\varphi}_1+\alpha_{3I}\cos\hat{\varphi}_1) \\ &\qquad +\sin\varphi_3(\beta_{2I}\sin 2\hat{\varphi}_1+\beta_{3I}\sin\hat{\varphi}_1)], \end{aligned} \tag{A.58}$$

which is identical to Reference [21] Equation 2.22.

In addition to considering the various spin projections of the $T^{\mu\nu}$, we will also find it useful to decompose $T^{\mu\nu}$ in terms of the particle four-momenta as in Reference [21]

[1]The definition of Γ used by Joshipura and Kramer is different from the one used in this thesis (see Equation 2.7 on page 33). We will use Joshipura and Kramer's definition in this appendix section.

Equation 2.8:

$$\begin{aligned} T_{\mu\nu} &= T_1 A_\mu A_\nu + T_2 A^1_\mu A^1_\nu + T_3(A^1_\mu A_\nu + A_\mu A^1_\nu) \\ &\quad + T_4(A^1_\mu A_\nu - A_\mu A^1_\nu) + T_5(g_{\mu\nu} + q_\mu q_\nu/Q^2), \end{aligned} \tag{A.59}$$

with

$$A_\mu \equiv \left(p + \frac{p\cdot q}{Q^2} q\right)_\mu, \qquad A^1_\mu \equiv \left(p_1 + \frac{p_1\cdot q}{Q^2} q\right)_\mu. \tag{A.60}$$

Noting that $\epsilon \cdot q = 0$ and that all of our T_X's involve contractions with ϵ's, we can use $A^\mu \to p^\mu$ and $A^\mu_1 \to p^\mu_1$. We can also use the fact that the tensor is symmetric when calculated up to first order in α_S to drop the T_4 term. This yields the following expression for the hadronic tensor:

$$T^{\mu\nu} = T_1 p^\mu p^\nu + T_2 p^\mu_1 p^\nu_1 + T_3(p^\mu_1 p^\nu + p^\mu p^\nu_1) + T_5 g^{\mu\nu}. \tag{A.61}$$

Before calculating these hadronic tensor projections T_n explicitly, we will collect some useful general expressions from Ref. [21] for later use.

$$\begin{aligned} p_{1T}\cos\varphi_1 &= \hat{p}_{1T}(\cos\theta_3\cos\varphi_3\cos\hat{\varphi}_1 - \sin\varphi_3\sin\hat{\varphi}_1) + \hat{p}_{1L}\sin\theta_3\cos\varphi_3 \\ p_{1T}\sin\varphi_1 &= \hat{p}_{1T}(\cos\theta_3\sin\varphi_3\cos\hat{\varphi}_1 + \cos\varphi_3\sin\hat{\varphi}_1) + \hat{p}_{1L}\sin\theta_3\sin\varphi_3 \\ p_{1L} &= -\hat{p}_{1T}\sin\theta_3\cos\hat{\varphi}_1 + \hat{p}_{1L}\cos\theta_3 \end{aligned} \tag{A.62}$$

$$\begin{aligned} P = |\mathbf{q}| &= (W^2+Q^2)/2W \\ q_0 &= (W^2-Q^2)/2W \\ p_T &= |\mathbf{p_3}|\sin\theta_3 \\ p_L &= P - |\mathbf{p_3}|\cos\theta_3 \\ p_0 &= \sqrt{p_L^2 + p_T^2} \\ \hat{s} &= W^2(1-x_3) \\ \hat{t} &= t_0 + t_1\cos\hat{\varphi}_1 \\ \hat{u} &= u_0 - t_1\cos\hat{\varphi}_1 \\ t_0 &= -x_1 W q_0 - 2P\hat{p}_{1L}\cos\theta_3 - Q^2 \\ t_1 &= 2P\hat{p}_{1T}\sin\theta_3 \\ u_0 &= -\hat{s} - t_0 - Q^2 \end{aligned} \tag{A.63}$$

In contrast to Reference [21], we are denoting the partonic Mandelstam variables as $\hat{s}$, $\hat{t}$, and $\hat{u}$. They used the symbols s, t, and u instead, which we reserve for the muon-nucleon Mandelstam variables (see, for instance, Section A.2). More explicitly,

the definitions are:

$$\begin{aligned} \hat{s} &\equiv (p_1 + p_2)^2 = (p + q)^2 \\ \hat{t} &\equiv (q - p_1)^2 \\ \hat{u} &\equiv (q - p_2)^2. \end{aligned} \tag{A.64}$$

Now that we have established the general framework for attacking the problem, we are in a position to calculate explicit results. There is no disagreement with Reference [21] to this point.

A.3.2 Explicit Results for Gluon Bremsstrahlung

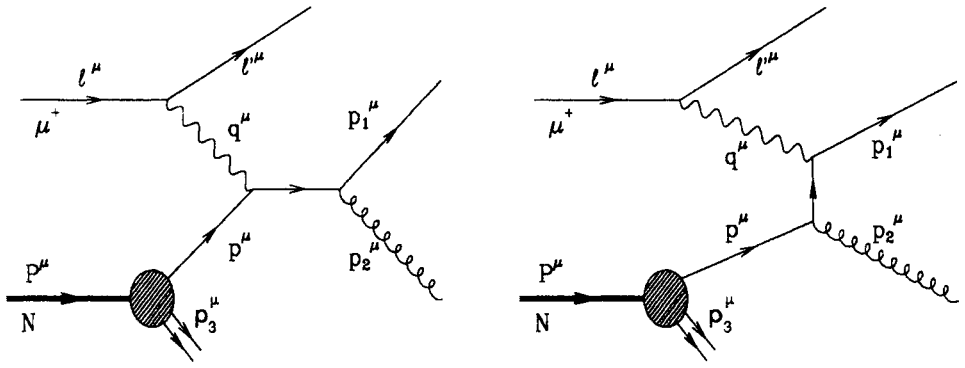

Figure A-2: Gluon Bremsstrahlung.
Feynman diagrams corresponding to gluon bremsstrahlung: a) s-channel and b) t-channel

We can calculate the explicit contribution to the cross-section from the Feynman diagrams in Figure A-2. We start from Ref. [21] Equation 2.9:

$$\begin{aligned} T_1 &= T_2 &&= -2e^2 c_2 g^2 Q_f^2 \frac{4Q^2}{\hat{s}\hat{t}} \\ T_3 &= T_4 &&= 0 \\ T_5 & &&= +2e^2 c_2 g^2 Q_f^2 \left(\frac{\hat{t}^2 + \hat{s}^2 - 2\hat{u}Q^2}{\hat{s}\hat{t}} \right) \end{aligned} \tag{A.65}$$

where Q_f is the struck parton charge and $c_2 = \frac{4}{3}$ is the QCD color factor appropriate to this class of diagrams. Using Equations A.56, A.57, A.61, and A.65 we can confirm

Ref. [21] Equation 2.11:

$$\begin{aligned}
T_U &= \frac{1}{2}T_1\left(p_T^2 + p_{1T}^2 + \frac{2(p\cdot q)^2}{Q^2} + \frac{2(p_1\cdot q)^2}{Q^2}\right)\\
T_L &= T_1\left(p_T^2 + p_{1T}^2\right)\\
T_T &= \frac{1}{2}T_1(p_T^2\cos 2\varphi + p_{1T}^2\cos 2\varphi_1)\\
T_I &= -\frac{2}{Q}T_1[p_T(|\mathbf{q}|p_0 + q_0p_L)\cos\varphi + p_{1T}(|\mathbf{q}|p_{10} + q_0p_{1L})\cos\varphi_1].
\end{aligned} \tag{A.66}$$

Substituting expressions from Equations A.62 and A.63 into Equation A.66, and writing the results in the form of Equation A.58 yields:

$$\begin{aligned}
\alpha_{1L} &= \hat{p}_{1T}^2 + (\hat{p}_{1L}^2 - \frac{1}{2}\hat{p}_{1T}^2 + |\mathbf{p_3}|^2)\sin^2\theta_3\\
\alpha_{2L} &= -\frac{1}{2}\hat{p}_{1T}^2\sin^2\theta_3\\
\alpha_{3L} &= \hat{p}_{1T}\hat{p}_{1L}\sin 2\theta_3
\end{aligned}$$

$$\begin{aligned}
\alpha_{1U} &= \alpha_{1L} + \frac{t_1^2}{4Q^2} + \frac{1}{2Q^2}[(\hat{s}+Q^2)^2 + (t_0+Q^2)^2]\\
\alpha_{2U} &= \alpha_{2L} + \frac{t_1^2}{4Q^2}\\
\alpha_{3U} &= \alpha_{3L} + \frac{t_1(t_0+Q^2)}{Q^2}
\end{aligned}$$

$$\begin{aligned}
\alpha_{1T} &= (|\mathbf{p_3}|^2 + \hat{p}_{1L}^2 - \frac{1}{2}\hat{p}_{1T}^2)\sin^2\theta_3 && (= \alpha_{1L} - \hat{p}_{1T}^2)\\
\alpha_{2T} &= \hat{p}_{1T}^2(1 - \frac{1}{2}\sin^2\theta_3) && (= \alpha_{2L} + \hat{p}_{1T}^2)\\
\alpha_{3T} &= \hat{p}_{1T}\hat{p}_{1L}\sin 2\theta_3 && (= \alpha_{3L})\\
\beta_{2T} &= -\hat{p}_{1T}^2\cos\theta_3\\
\beta_{3T} &= -2\hat{p}_{1T}\hat{p}_{1L}\sin\theta_3
\end{aligned} \tag{A.67}$$

$$\begin{aligned}
\alpha_{1I} &= \sin\theta_3[-|\mathbf{p_3}|(|\mathbf{q}|p_0 + q_0p_L) + |\mathbf{q}|p_{10}\hat{p}_{1L} + q_0(\hat{p}_{1L}^2 - \frac{1}{2}\hat{p}_{1T}^2)\cos\theta_3]\\
\alpha_{2I} &= -\frac{1}{4}q_0\hat{p}_{1T}^2\sin 2\theta_3\\
\alpha_{3I} &= |\mathbf{q}|p_{10}\hat{p}_{1T}\cos\theta_3 + q_0\hat{p}_{1L}\hat{p}_{1T}\cos 2\theta_3\\
\beta_{2I} &= \frac{1}{2}q_0\hat{p}_{1T}^2\sin\theta_3\\
\beta_{3I} &= -|\mathbf{q}|p_{10}\hat{p}_{1T} - q_0\hat{p}_{1L}\hat{p}_{1T}\cos\theta_3.
\end{aligned}$$

The step from Equation A.66 to Equation A.67 is straightforward, but involves a lot of algebraic manipulation. This step was checked using a computer algebraic manipulation package[2]. The results for the gluon bremsstrahlung case in the appendix of Ref [21] are all correct except for α_{2U}. Equation A.67 above contains the correct expression for α_{2U}.

A.3.3 Explicit Results for Photon-Gluon Fusion

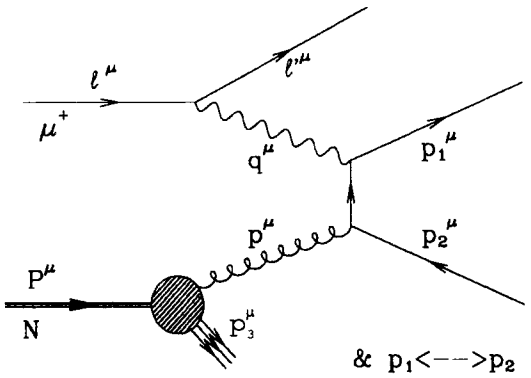

Figure A-3: Photon-Gluon Fusion.
Feynman diagram corresponding to photon-gluon fusion.

We can calculate the explicit contribution to the cross-section from the diagram in Figure A-3.

We start with the expression for $T_{\mu\nu}$ in the note at the bottom of page 216 in Ref. [21]:

$$T_{\mu\nu} = 2g^2e^2Q_f^2c_3 \left[\frac{1}{p\cdot p_2}(\{p,p_1\}_{\mu\nu} - \{p_1,p_2\}_{\mu\nu} + \{p_2,p_2\}_{\mu\nu}) \right.$$
$$+ \frac{1}{p\cdot p_1}(\{p,p_2\}_{\mu\nu} - \{p_1,p_2\}_{\mu\nu} + \{p_1,p_1\}_{\mu\nu}) \qquad \text{(A.68)}$$
$$\left. + \frac{p_1\cdot p_2}{p\cdot p_1 p\cdot p_2}(2\{p_1,p_2\}_{\mu\nu} - \{p,p_1\}_{\mu\nu} - \{p,p_2\}_{\mu\nu}) \right],$$

where:

$$\{p_A,p_B\}_{\mu\nu} \equiv p_{A\mu}p_{B\nu} + p_{B\mu}p_{A\nu} - g_{\mu\nu}p_A\cdot p_B, \qquad \text{(A.69)}$$

[2]Mathematica^{TM}

where Q_f is the outgoing quark charge and $c_3 = \frac{1}{2}$ is the color factor for the photon-gluon fusion diagram as defined in Ref. [53].

Expanding this result and comparing with Equation A.61 yields:

$$\begin{aligned} T_1^g = \frac{1}{2}T_2^g = -T_3^g &= 8e^2c_3g^2Q_f^2\frac{Q^2}{tu} \\ T_4^g &= 0 \end{aligned} \tag{A.70}$$

which agrees with Reference [21] Equation 2.33, and:

$$T_5^g = -T_1^g\left(\frac{\hat{s}^2+Q^4-2\hat{t}\hat{u}}{4Q^2}\right) \tag{A.71}$$

which does not. Reference [21] is in error.

Using Equations A.56, A.61, A.70, and A.71, we obtain the following expressions for the T_X^g's:

$$\begin{aligned} T_L^g &= T_1^g\left(p_{1T}^2+p_{2T}^2\right) = T_1^g\left(p_T^2+2p_{1T}^2+2p_{1T}p_T\cos(\varphi_3-\varphi_1)\right) \\ T_U^g &= \frac{1}{2}T_L^g+\frac{1}{2}T_1^g\left(\frac{\hat{s}^2+Q^4-2\hat{t}\hat{u}}{2Q^2}\right) \\ T_T^g &= \frac{1}{2}T_1^g\left(p_T^2\cos 2\varphi_3+2p_{1T}^2\cos 2\varphi_1+2p_{1T}p_T\cos(\varphi_3+\varphi_1)\right) \\ T_I^g &= -\frac{2}{Q}T_1^g[p_T(|\mathbf{q}|p_0+q_0p_L)\cos\varphi-p_T(|\mathbf{q}|p_{10}+q_0p_{1L})\cos\varphi \\ &\qquad +2p_{1T}(|\mathbf{q}|p_{10}+q_0p_{1L})\cos\varphi_1-p_{1T}(|\mathbf{q}|p_0+q_0p_L)\cos\varphi_1]. \end{aligned} \tag{A.72}$$

Substituting the values of the various momenta from Equations A.62 and A.63 into Equation A.72, and writing the results in the form of Equation A.58 yields:

$$\begin{aligned} \alpha_{1L}^g &= \hat{p}_{1T}^2(1+\cos^2\theta_3)+[(|\mathbf{p_3}|+\hat{p}_{1L})^2+\hat{p}_{1L}^2]\sin^2\theta_3 \\ \alpha_{2L}^g &= -\hat{p}_{1T}^2\sin^2\theta_3 \\ \alpha_{3L}^g &= \hat{p}_{1T}(2\hat{p}_{1L}+|\mathbf{p_3}|)\sin 2\theta_3 \end{aligned}$$

$$\begin{aligned} \alpha_{1U}^g &= \alpha_{1L}^g+\frac{1}{2Q^2}(t_1^2+\hat{s}^2+Q^4-2t_0u_0) \\ \alpha_{2U}^g &= \alpha_{2L}^g+\frac{t_1^2}{2Q^2} \\ \alpha_{3U}^g &= \alpha_{3L}^g+\frac{t_1(t_0-u_0)}{Q^2} \end{aligned}$$

$$\alpha_{1T}^g = [(\hat{p}_{1L}+|\mathbf{p_3}|)^2+\hat{p}_{1L}^2-\hat{p}_{1T}^2]\sin^2\theta_3 \qquad (=\alpha_{1L}^g-2\hat{p}_{1T}^2)$$

$$
\begin{aligned}
\alpha^g_{2T} &= \hat{p}^2_{1T}(1+\cos^2\theta_3) && (=\alpha^g_{2L}+2\hat{p}^2_{1T}) \\
\alpha^g_{3T} &= \hat{p}_{1T}(2\hat{p}_{1L}+|\mathbf{p_3}|)\sin 2\theta_3 && (=\alpha^g_{3L}) \\
\beta^g_{2T} &= -2\hat{p}^2_{1T}\cos\theta_3 \\
\beta^g_{3T} &= -2\hat{p}_{1T}(2\hat{p}_{1L}+|\mathbf{p_3}|)\sin\theta_3
\end{aligned}
\tag{A.73}
$$

$$
\begin{aligned}
\alpha^g_{1I} &= -\sin\theta_3[q_0\hat{p}^2_{1T}\cos\theta_3-(2\hat{p}_{1L}+|\mathbf{p_3}|)(|\mathbf{q}|p_{10}+q_0\hat{p}_{1L}\cos\theta_3)+(\hat{p}_{1L}+|\mathbf{p_3}|)(Pp_0+q_0p_L)] \\
\alpha^g_{2I} &= -\frac{1}{2}\hat{p}^2_{1T}q_0\sin 2\theta_3 \\
\alpha^g_{3I} &= \hat{p}_{1T}[-\cos\theta_3(Pp_0+q_0p_L-2Pp_{10})+2q_0\hat{p}_{1L}\cos 2\theta_3-q_0|\mathbf{p_3}|\sin^2\theta_3] \\
\beta^g_{2I} &= q_0\hat{p}^2_{1T}\sin\theta_3 \\
\beta^g_{3I} &= \hat{p}_{1T}(Pp_0+q_0p_L-2Pp_{10}-2\hat{p}_{1L}q_0\cos\theta_3).
\end{aligned}
$$

As was the case for the gluon-bremsstrahlung calculation, the last step in the derivation of the coefficients involved a lot of algebra and was checked using a computer program. The above results for the photon-gluon fusion case agree with those in the appendix of Ref [21] except for α^g_{1L}, α^g_{1U}, α^g_{2U}, β^g_{2T}, α^g_{3I}, and β^g_{3I}. Equation A.73 above is correct, while the corresponding results in Ref [21] are incorrect.

A.3.4 Summary

In this section I presented a calculation of the parton-level phi asymmetry to $\mathcal{O}(\alpha_s)$ in the presence of primordial $k_\perp$ for massless quarks. The results were formulated in terms of the coefficients α_{nX} and β_{nX} as defined in Reference [21]. Some of their explicit results were found to be in error, and the correct answers were derived.

Appendix B

Implementing the Phi Asymmetry in LEPTO

This Appendix, along with Appendix A, is intended to serve as documentation for the changes that have been made to the LEPTO 5.2 code (Matrix Element formulation) used in this thesis. The new code was designed to include the parton-level phi asymmetry due to the presence of primordial transverse momentum of the partons. The new code was designed to be modular and should be transportable to any future releases of LEPTO that use a matrix element formulation with a minimal amount of work. In fact, it was developed for LEPTO 4.3 and easily converted for use with LEPTO 5.2 (ME). Within the E665 software structure, this phi asymmetry code can be switched on and off using the PATCHY switch: PHIASYMM.

The first step in this process of modeling the phi asymmetry in the LUND was to improve the theory for the phi asymmetry at zeroth order so that it did not demand that $k_\perp^2 \ll Q^2$ and to correct mistakes that exist in the literature concerning the theory of phi asymmetry at first order. Such theoretical details can be found in Appendix A. The next step in the process was to express the theory in a form that fit nicely in the LUND structure. This is outlined in Sections B.3 and B.4.

This Appendix is divided into Sections as follows:

Section B.1 contains an overview of the normal logical flow of the LEPTO code as well as my modifications.

Section B.2 contains an explicit description of the LEPTO subroutines that have been modified or added, and E665-specific details concerning the use of the code.

Section B.3 contains a discussion of the internal LUND coordinate system and how

it relates to the coordinate system of Joshipura and Kramer which is used in Appendix A.

Section B.4 contains explicit expressions for the azimuthal angular distribution as used in my code.

Section B.5 contains an explicit description of the algorithm used to generate the azimuthal angular distribution.

B.1 Overview of the LEPTO Algorithm

In this section we discuss the logical flow of the LEPTO code before and after the phi asymmetry is implemented. The variables used here have been defined elsewhere, primarily in Chapter 2 and Appendix A. The definitions of the variables can also be found in the Glossary (Appendix E).

The normal way that the LEPTO code runs in the Matrix Element formulation is as follows:

1. Given $F_2(x, Q^2)$, calculate the cross-section as a function of x and Q^2. Roll a random x and Q^2 according to this distribution.
2. Again based on x and Q^2 cross-sections, decide which process (simple quark scattering, gluon bremsstrahlung, or photon-gluon fusion) has occurred.
3. If a QCD process is indicated, choose energy fractions x_1 and x_2, for the forward partons according to the cross-section for that particular QCD process.
4. Pick a $k_\perp$ according to an arbitrary distribution which is totally independent of the previous steps.
5. In the case of a QCD process, pick a $\hat{\varphi}_1$ according to the approximate $\mathcal{O}(\alpha_s)$ QCD cross-section with $k_\perp = 0$, given x, Q^2, x_1, and x_2.
6. Pick a φ_3 ($\vec{k}_\perp$ direction) according to a flat distribution.
7. Proceed to hadronize and perform detector modeling.

The main problem with the above method is that ignores the effect on the phi asymmetry due to $k_\perp$. For the zeroth order process, there should be a strong φ_3 dependence, at least for Q^2 less than about 8 GeV^2. For the QCD process, there should be a complicated dependence on both φ_3 and $\hat{\varphi}_1$.

The above method also ignores two other effects: 1) the total cross-section for a given $Q^2 \times x_{B_j}$ bin should depend on the $k_\perp$ of the struck partons; and 2) for QCD events, the cross-section as a function of x_1 and x_2 should also depend upon $k_\perp$. These last two effects are not very important, especially since we don't really know the exact $k_\perp$ distribution of the partons in the nucleon anyway.

A proper handling of the primordial $k_\perp$ at $\mathcal{O}(\alpha_s)$ would entail a complete rewrite of the LEPTO code. We should implement the full cross-section:

$$\frac{d^7\sigma}{dQ^2 dx_{B_j} dk_\perp^2 dx_1 dx_2 d\varphi_3 d\hat{\varphi}_1}$$

form the very beginning. Fortunately, the primary effect that we are interested in can be handled with only a slight modification of the existing code. We will assume that the $k_\perp$-dependence can be factored out and will only affect the phi distribution of the partons. We will continue to use the $k_\perp = 0$ approximations for $d^2\sigma/(dQ^2 dx_{B_j})$ and $d^2\sigma/(dx_1 dx_2)$. These approximations should be harmless.

Given a fixed Q^2, W^2, x_1, x_2, and $k_\perp$, we can find the remaining azimuthal dependence $\frac{d\sigma}{d\varphi_3 d\hat{\varphi}_1}$. An explicit expression for this quantity can be found in Section B.4. Armed with this distribution, we can then modify the LUND code, changing only steps 5 and 6 in the normal sequence described above. The new code behaves as follows, with the changes underlined.

1. Given $F_2(x, Q^2)$, calculate the cross-section as a function of x and Q^2. Roll a random x and Q^2 according to this distribution.

2. Again based on x and Q^2 cross-sections, decide which process (simple quark scattering, gluon bremsstrahlung, or photon-gluon fusion) has occurred.

3. If a QCD process is indicated, choose energy fractions x_1 and x_2, for the forward partons according to the cross-section for that particular QCD process.

4. Pick a $k_\perp$ according to an arbitrary distribution which is totally independent of the previous steps.

5. In the case of a QCD process, pick a $\hat{\varphi}_1$ and a φ_3 according to the full $\mathcal{O}(\alpha_s)$ QCD cross-section given x, Q^2, x_1, x_2, and $k_\perp$.

6. In the case of a zeroth order process (simple quark or antiquark scattering), pick a φ_3 ($\vec{k}_\perp$ direction) according to the cross-section given x, Q^2, and $k_\perp$.

7. Proceed to hadronize and perform detector modeling.

B.2 Code Organization

In order to understand the changes that have been made to the code, it's necessary to know the organization of the code in a bit more detail. Lund Subroutine `LEPTO` is the top-level subroutine of the LEPTO package. Subroutine `LEPTO` normally behaves as follows (in the ME formulation):

1. Choose x_{B_J}, Q^2, and decide which process has occurred.
2. Define the parton kinematics more precisely, ignoring $k_\perp$:
   - For a leading order event, `CALL LQEV`.
   - For a gluon bremsstrahlung event, `CALL LQGEV`, which chooses the x_1, x_2, and $\hat{\varphi}_1$.
   - For a photon-gluon fusion event, `CALL LQQBEV`, which chooses the x_1, x_2, and $\hat{\varphi}_1$.
3. For all events, `CALL LPRIKT`, which picks a $\vec{k}_\perp$ according to an exponential in $k_\perp^2$ and isotropically in φ_3. Note: This will tend to wash out any phi asymmetry generated in `LQGEV` or `LQQBEV`.
4. Proceed to hadronize and perform detector modeling.

My version of the phi asymmetry changes the subroutines `LEPTO`, `LQGEV`, and `LQQBEV`. It also includes two new subroutines: `PHIQCD` and `LPHIKT`. The new version of S/R `LEPTO` behaves as follows:

1. Choose x_{B_J}, Q^2, and decide which process has occurred.
2. Define the parton kinematics more precisely:
   - For a leading order event, `CALL LQEV`.
   - For a gluon bremsstrahlung event, `CALL LQGEV`.
     - ⋆ S/R `LQGEV` chooses x_1 and x_2 as usual.
     - ⋆ S/R `LQGEV` calls the new S/R `PHIQCD`
       - * S/R `PHIQCD` chooses a $k_\perp$ magnitude according to the usual LUND S/R `LPRIKT`.
       - * S/R `PHIQCD` chooses the φ_3 and $\hat{\varphi}_1$ according to the full $\mathcal{O}(\alpha_s)$ $d^2N/d\hat{\varphi}_1 d\varphi_3$ distribution.
   - For a photon-gluon fusion event, `CALL LQQBEV`.

- ⋆ S/R `LQQBEV` chooses x_1 and x_2 as usual.
- ⋆ S/R `LQQBEV` calls the new S/R `PHIQCD`
  - ∗ S/R `PHIQCD` chooses a $k_\perp$ magnitude according to the usual LUND S/R `LPRIKT`.
  - ∗ S/R `PHIQCD` chooses the φ_3 and $\hat{\varphi}_1$ according to the full $\mathcal{O}(\alpha_s)$ $d^2N/d\hat{\varphi}_1 d\varphi_3$ distribution.

3. For lowest order events only, `CALL LPHIKT` to generate $k_\perp$ and φ_3 according to the Cahn-like phi asymmetry as described in Section A.2 rather than the LUND default of a flat phi distribution. Note: For QCD events, the $k_\perp$ has already been chosen.

4. Proceed to hadronize and perform detector modeling.

The calling sequences to the new subroutines `PHIQCD` and `LPHIKT` are shown on the following pages:

```
      SUBROUTINE PHIQCD(PROC, RW2, RQ2, RY, RX1, RX2, RP1THT, RP1LHT,
     >                        RP2LHT,   RSIGPT, RPHI1H, RTHET3, RPHI3 )
+SELF,IF=DOCL1.
*********************************************************************
*                                                                   *
* S/R PHIQCD     Mark D. Baker                                      *
*                                                                   *
*   Given the parton kinematics, choose a primordial Kt and find the  *
* azimuthal angles according to the O(alpha-s) + O(alpha-s*Kt)      *
* cross-section.                                                    *
*                                                                   *
* References:  M. Baker - PhD Thesis (MIT) - (1992)                 *
*              Joshipura and Kramer - J. Phys. G 8 (1982) 209       *
*                                                                   *
*  N.B. There are typos in the equations in Joshipura and Kramer.   *
*       These are corrected in my thesis (MDB).                     *
*                                                                   *
* This subroutine assumes that RW2, RQ2, RX1, RX2, RP1THT, RP1LHT have *
* already been chosen by the Lund. It generates a Theta_3 (RTHET3) by  *
* using a standard Lund-type exponential dist. in primordial Pt**2:    *
* dN/dPt**2 ~ exp(-Pt**2/sigpt**2). It then generates the azimuthal    *
* angles RPHI1H and RPHI3 according to the cross section.           *
*                                                                   *
* This subroutine is meant to be used with LEPTO 4.3 or 5.2 (ME).   *
*                                                                   *
* Inputs:                                                           *
* PROC (C*4) = 'QQB' or 'QG' defines the process                    *
* RW2, RQ2, RY are the usual DIS kinematic variables (W2,Q2,Y).     *
* RX1, RX2 are the energy fractions of the forward jets (Xi = 2*Ei/W)  *
* RP1THT    is p-hat_1T, the Pt of jet 1 WRT the target jet.        *
* RP1LHT    is p-hat_1L, the Pl of jet 1 WRT the target jet (p_1L <0). *
* RP2LHT    is p-hat_2L, the Pl of jet 2 WRT the target jet (p_2L <0). *
* RSIGPT    is the RMS primordial Pt desired.                       *
*                                                                   *
* NOTE: The following angles are defined ala Joshipura and Kramer's    *
*       paper. They can be implemented in the LUND S/R's LQQBEV     *
*       or LQGEV by applying the following active rotations in the  *
*       Lorentz frames as defined by LUND.                          *
*                                                                   *
*       LQGEV:  R_z(-Phi3) * R_y(-Theta3) * R_z(-Phi1-hat)          *
*       LQQBEV: R_z(-Phi3) * R_y(-Theta3) * R_z(Pi-Phi1-hat)        *
*                                                                   *
* Outputs:                                                          *
*                                                                   *
* RPHI1H is the Phi of jet 1 with respect to the target jet defined in *
```

```
*        Joshipura and Kramer's (X,Y,Z) frame.                          *
*                                                                       *
* RTHET3 is the theta of jet 3 about the incoming proton axis.          *
*                                                                       *
* RPHI3  is the Phi of jet 3 about the incoming proton axis in the      *
*        hadronic cm with x defined so that Px(sc.) > 0, Py(sc.) = 0    *
*        i.e. Joshipura and Kramer's (x,y,z) frame.                     *
*                                                                       *
*************************************************************************
```

```
      SUBROUTINE LPHIKT(S,PT,PHI)
************************************************************************
*                                                                      *
*   S/R LPHIKT    Mark D. Baker                                        *
*                                                                      *
*   Generate size (PT) and azimuthal angle (Phi) of primordial Kt,     *
*   using a Cahn-type phi-dependence with an improved cutoff.          *
*   This asymmetry only makes sense for single quark-jet events.       *
*   This routine is meant to be used with LEPTO 4.3 or LEPTO 5.2 (ME). *
*                                                                      *
*   This is a modification of Lepto 4.3 S/R LPRIKT which was flat in   *
*   phi. S/R LPRIKT is still needed to generate other Pt dists.        *
*                                                                      *
*   The Lund doc. claims that this generation is gaussian in KT:       *
*   dN/dKt ~ exp (-Kt**2/K0**2).                                       *
*                                                                      *
*   Actually, the distribution is exponential in KT**2:                *
*   dN/dKt**2 ~ exp (-Kt**2/K0**2).                                    *
*   When Phi is flat, this corresponds to gaussian Kx and Ky...        *
*                                                                      *
*   Refs.: Baker, M. - PhD Thesis, MIT,(1992)                          *
*          Cahn, R.  - Phys. Rev. D 40 (1989) 3107                     *
*          Cahn, R.  - Phys. Lett. 78B (1978)  269                     *
*                                                                      *
*   The improved method is due to repeating Cahn's original analysis   *
*   without the assumption that Kt << Q. This provides a natural       *
*   kinematic cutoff in the cross section. The following approxima-    *
*   tions remain:                                                      *
*                                                                      *
*        1) The quark mass is neglected.                               *
*        2) The target remnant mass is neglected.                      *
*        3) The cross-section as a function of Q^2, x is assumed to be *
*           independent of Kt. Only the Phi distribution is affected.  *
*                                                                      *
************************************************************************
```

The new code was pre-released into the E665 MPAM version 36.05 and fully released in MPAM version 38 and later. One needs to use the correction PAM L1C0102 or later for Lepto 4.3 or L3C0102 for Lepto 5.2. Additionally, several lines must be included in your cradle:

Place the line

```
+USE,PHIASYMM.                          Enable Phi Asymmetry
```

somewhere near the top of the cradle.

On IBM Machines (including the Amdahl), you need the following lines:

```
+PAM,LUN=27, IF=IBM, IF=LUND52.          L3CPAM
+PAM,LUN=28, IF=IBM, IF=LUND52.          L3PAM01
+PAM,LUN=29, IF=IBM, IF=LUND43.          L1CPAM
+PAM,LUN=42, IF=IBM, IF=LUND43.          L1PAM01
```

placed just before the +PAM of the MPAM.

On the Vax, you need the following lines:

```
+PAM, LUN=11,T=ATTACH, IF= VAX, IF=LUND52. "L3CPAM"
+PAM, LUN=11,T=ATTACH, IF= VAX, IF=LUND52. "L3PAM"
+PAM, LUN=11,T=ATTACH, IF= VAX, IF=LUND43. "L1CPAM"
+PAM, LUN=11,T=ATTACH, IF= VAX, IF=LUND43. "L1PAM"
```

placed just before the +PAM of the MPAM.

Place the lines

```
+USE,P=L1COR,T=EXE,IF=LUND43........LEPTO 4.3 CORRECTION SET
+USE,P=L3COR,T=EXE,IF=LUND52........LEPTO 5.2 CORRECTION SET
```

somewhere before the +PAM of the L3CPAM and L1CPAM.

B.3 Coordinate Systems

The coordinate system used in Appendix Section A.3 differs from the coordinate system used to define the FORTRAN variables in the LUND Monte Carlo. Both coordinate systems are defined below as well as the transformation between them.

Probably the most confusing aspect of this whole business is how to apply the selected values for θ_3, φ_3 and $\hat{\varphi}_1$ to the LUND event.

B.3.1 LQGEV Coordinate System

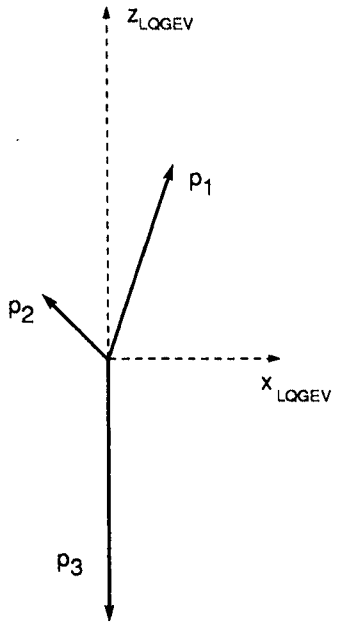

Figure B-1: Coordinate System for Lund Routine LQGEV.
This drawing shows the three jets as they are first generated by LQGEV. The jets later undergo an active rotation into the normal Lund CM frame depending on the value of φ_3, θ_3, and $\hat{\varphi}_1$. If $\varphi_3 = \theta_3 = \hat{\varphi}_1 = 0$, then the initial and final frames are equivalent and no rotation is necessary.

In subroutine `LQGEV`, which handles the gluon bremsstrahlung case, we generate 4-momenta for our jets in the initial `LQGEV` Lorentz frame:

$$\begin{aligned} p_1 &= \mathtt{P(J1,}\mu\mathtt{)}, \\ p_2 &= \mathtt{P(J2,}\mu\mathtt{)}, \\ p_3 &= \mathtt{P(J3,}\mu\mathtt{)} + \mathtt{P(J4,}\mu\mathtt{)}. \end{aligned}$$

It should be noted that in the LUND code μ ranges from 1-4, with their $\mu = 4$ corresponding to our usual $\mu = 0$. The initial `LQGEV` frame is defined so that $\vec{p}_3$ points along $-\hat{z}_{LQGEV}$ and so that $\vec{p}_1$ is in the $(+\hat{x}_{LQGEV}, +\hat{z}_{LQGEV})$ quadrant. This is shown in Figure B-1. It should be noted the target remnant jet in `LQGEV` is sometimes broken up into two pieces: Jet 3 and "Jet" 4. In such cases, p_3^μ will be the sum of the two backward jets. We want to rotate all of the jets into the `LEPTO` frame where the

virtual photon momentum points along the $+\hat{z}_{LEPTO}$ axis and the scattered muon is in the $(+\hat{x}_{LEPTO}, +\hat{z}_{LEPTO})$ quadrant. If $\varphi_3 = \theta_3 = \hat{\varphi}_1 = 0$ then the LEPTO and LQGEV frames are equivalent.

Subroutine LQGEV chooses values for θ_3, φ_3, and $\hat{\varphi}_1$ according to the $k_\perp$ distribution and the cross section. Once this is done, it must rotate the jet momentum vectors to their correct positions. This means that it uses an active rotation. The coordinate axes, which we will call $\hat{x}_L$, $\hat{y}_L$, and $\hat{z}_L$, remain fixed. Before the rotation $\hat{z}_L = \hat{z}_{LQGEV}$ and after the rotation $\hat{z}_L = \hat{z}_{LEPTO}$ (and similarly for $\hat{x}_L$ and $\hat{y}_L$).

Now, let us proceed with our rotations. First we want $\vec{p}_1$ to have $\varphi = \hat{\varphi}_1$ about the $\hat{p}_3$-axis. In order to accomplish this, we rotate the whole event by $-\hat{\varphi}_1$ about the $\hat{z}_L$-axis. The rotation of $-\hat{\varphi}_1$ is due to the fact that initially $\hat{p}_3 = -\hat{z}_L$. Next, we want to rotate $\vec{p}_3$ so that it makes angles: (θ_3, φ_3) with the $-\hat{z}_L$-axis. This is equivalent to a rotation which sends a vector pointing along the $\hat{z}_L$-axis to a new vector with polar coordinates: $(-\theta_3, -\varphi_3)$. This entire series can be written as the following active rotation:

$$\mathcal{R}_{\hat{z}_L}(-\varphi_3)\mathcal{R}_{\hat{y}_L}(-\theta_3)\mathcal{R}_{\hat{z}_L}(-\hat{\varphi}_1) \tag{B.1}$$

The code to accomplish these rotations in Lepto 4.3 is:

```
CALL LUROBO( 0., -PHI1HT, 0., 0., 0.)
CALL LUROBO( -THETA3, -PHI3, 0., 0., 0.).
```

The code to accomplish these rotations in Lepto 5.2 is:

```
CALL DUROBO( 0., -PHI1HT, 0., 0., 0.)
CALL DUROBO( -THETA3, -PHI3, 0., 0., 0.).
```

B.3.2 LQQBEV Coordinate System

Subroutine LQQBEV, which handles the photon-gluon fusion case, generates 4-momenta for the jets in the initial LQQBEV frame:

$$\begin{aligned} p_1 &= \mathrm{P(J1,}\mu\mathrm{)}, \\ p_2 &= \mathrm{P(J3,}\mu\mathrm{)}, \\ p_3 &= \mathrm{P(J2,}\mu\mathrm{)} + \mathrm{P(J4,}\mu\mathrm{)}. \end{aligned}$$

Note that the meaning of J2 and J3 are different here than they were in subroutine LQGEV. We define our initial LQQBEV frame so that $\vec{p}_3$ points along $-z_{LQQBEV}$ and $\vec{p}_2$ is in the $(+x_{LQQBEV}, +z_{LQQBEV})$ quadrant. This is shown in Figure B-2. This initial jet

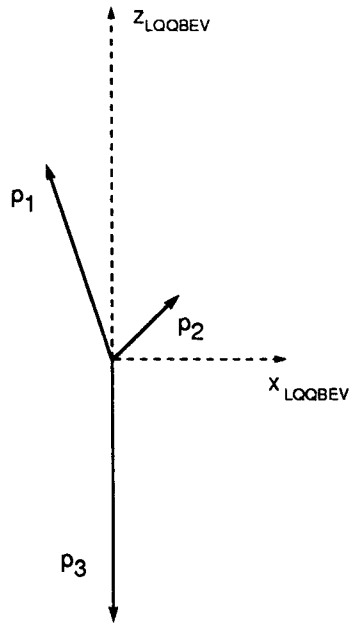

Figure B-2: Coordinate System for Lund Routine LQQBEV.
This drawing shows the three jets as they are first generated by LQQBEV. The jets later undergo an active rotation into the normal Lund CM frame depending on the value of φ_3, θ_3, and $\hat{\varphi}_1$. If $\varphi_3 = \theta_3 = 0$ and $\hat{\varphi}_1 = \pi$ then the initial and final frames are equivalent and no rotation is necessary.

configuration is different from the LQGEV case where it was $\vec{p}_1$ that pointed into the positive quadrant. As before, the target remnant jet in LQQBEV is sometimes broken up into two pieces. Also as before, $\mu = 4$ corresponds to the $\mu = 0$ in our usual convention.

We must again choose values for θ_3, φ_3, and $\hat{\varphi}_1$ from the $k_\perp$ distribution and from the cross-section. We must again perform an active rotation on the jet momentum vectors so that the jets are correctly described in the standard LEPTO reference frame. No rotation is necessary if $\varphi_3 = \theta_3 = 0$ and $\hat{\varphi}_1 = \pi$ because the LQQBEV and LEPTO frames are then equivalent.

We again want $\vec{p}_1$ to have an azimuthal angle of $\hat{\varphi}_1$ about the $\hat{p}_3$-axis. In order to accomplish this, we rotate the whole event by $\pi - \hat{\varphi}_1$ about the z_L-axis. The extra rotation of π is due to the fact that the $\vec{p}_1$ starts out pointing away from x_L ($\varphi = \pi$) instead of toward it. The rotation of $-\hat{\varphi}_1$ is again due to the fact that $\hat{p}_3 = -\hat{z}_L$ initially. Next, we again want to rotate $\vec{p}_3$ so that it makes angles: (θ_3, φ_3) with $-z_L$. This again corresponds to a rotation of $(-\theta_3, -\varphi_3)$ with respect to $+z_L$. This can be written:

$$\mathcal{R}_{\hat{z}_L}(-\varphi_3)\mathcal{R}_{\hat{y}_L}(-\theta_3)\mathcal{R}_{\hat{z}_L}(\pi - \hat{\varphi}_1) \tag{B.2}$$

The code to accomplish these rotations in Lepto 4.3 is:

```
CALL LUROBO( 0., 3.141529-PHI1HT, 0., 0., 0.)
CALL LUROBO( -THETA3, -PHI3, 0., 0., 0.).
```

The code to accomplish these rotations in Lepto 5.2 is:

```
CALL DUROBO( 0., 3.141529-PHI1HT, 0., 0., 0.)
CALL DUROBO( -THETA3, -PHI3, 0., 0., 0.).
```

B.4 Explicit Expressions for the Distributions

We need to express the theory of phi asymmetry in a form that fits nicely in the LUND structure. This is outlined below. We will start with the expression for the full QCD cross-section at fixed Q^2, W^2, x_1, x_2 and $k_\perp$, as given by equations A.54 and A.58 in Appendix A. Given fixed values for Q^2, W^2, x_1, x_2 and $k_\perp$, we know that the following variables are also fixed: x_3, η, y, Γ, $|p_3|$, θ_3, s, t_0, t_1, u_0, $P = |q|$, q_0. It should be noted that T_1 and T_1^g are functions of $\hat{t}$ and $\hat{u}$ which are in turn functions

of $\cos\hat{\varphi}_1$. Assembling, we have:

$$\begin{aligned}\frac{d^2\sigma}{d\varphi_3 d\hat{\varphi}_1} \propto T_1(\hat{\varphi}_1) \times \{ \quad & (A_1 + \quad A_2\cos 2\hat{\varphi}_1 + A_3\cos\hat{\varphi}_1) + \\ & (B_1 + \quad B_2\cos 2\hat{\varphi}_1 + B_3\cos\hat{\varphi}_1)\cos\varphi_3 + \\ & (C_1 + \quad C_2\cos 2\hat{\varphi}_1 + C_3\cos\hat{\varphi}_1)\cos 2\varphi_3 + \\ & (\qquad D_2\sin 2\hat{\varphi}_1 + D_3\sin\hat{\varphi}_1)\sin\varphi_3 + \\ & (\qquad E_2\sin 2\hat{\varphi}_1 + E_3\sin\hat{\varphi}_1)\sin 2\varphi_3 \quad \},\end{aligned} \tag{B.3}$$

with:

$$\begin{aligned} A_n &= \frac{1}{2}\alpha_{nU} + \frac{2(1-y)}{[1+(1-y)^2]}\alpha_{nL} \\ B_n &= -\frac{2}{Q}\frac{(2-y)\sqrt{1-y}}{[1+(1-y)^2]}\alpha_{nI} \\ C_n &= \frac{1}{2}\frac{2(1-y)}{1+(1-y)^2}\alpha_{nT} \\ D_n &= -\frac{2}{Q}\frac{(2-y)\sqrt{1-y}}{[1+(1-y)^2]}\beta_{nI} \\ E_n &= \frac{1}{2}\frac{2(1-y)}{[1+(1-y)^2]}\beta_{nT}, \end{aligned} \tag{B.4}$$

and with the coefficients α_{nX} and β_{nX} as given in equation A.67 or A.73 depending upon the process. For gluon bremsstrahlung, we should note that:

$$T_1(\hat{\varphi}_1) \propto \frac{1}{|\hat{t}|} \propto (|t_0| - t_1\cos\hat{\varphi}_1)^{-1}, \tag{B.5}$$

while for photon-gluon fusion, we have:

$$T_1^g(\hat{\varphi}_1) \propto \frac{1}{\hat{t}\hat{u}} \propto \left[(t_0u_0 - \frac{1}{2}t_1^2) + t_1(u_0 - t_0)\cos\hat{\varphi}_1 - \frac{1}{2}t_1^2\cos 2\hat{\varphi}_1\right]^{-1}. \tag{B.6}$$

The results contained in section A.3 assume that all masses are negligible. Actually, the mass of the nucleon M and of the target remnant (which we will denote as M_3) aren't negligible with respect to $\sqrt{Q^2}$. Additionally, the up and down quark masses aren't quite zero in the Lund. Because of these nonzero masses, it is important to be careful in choosing the exact definitions of various quantities in our calculations. Definitions that are equivalent for $m_q = M_3 = 0$ may differ for non-zero m_q and M_3. Therefore, some of the expressions that we use in the LEPTO code are not identical to the theoretical expressions from Section A.3 except in the limit $m_q \to 0$ and $M_3 \to 0$.

An additional concern is the fact that we are allowing the struck parton (whether it is a quark or a gluon) to go off mass shell. The reason for this is that we are following the conventional choice by LEPTO of choosing $k_\perp$ completely independently of M_3 and x_3. In order to keep the parton exactly on mass shell, M_3, x_3, and $k_\perp$ must be constrained. This constraint is due to the following equations:

$$\begin{aligned} p^\mu &= P^\mu - p_3^\mu, && \text{(B.7)} \\ p^2 &= m^2 = 0, && \text{(B.8)} \\ P^2 &= M^2, && \text{(B.9)} \\ p_3^2 &= M_3^2. && \text{(B.10)} \end{aligned}$$

These equations cannot be simultaneously satisfied unless x_3 is a specific function of M_3 and $k_\perp$. I have chosen to ignore this problem and to let p^μ go slightly off mass shell as the standard default version of LEPTO does.

The various parton quantities are defined below in terms of the partonic energies and momenta: $p_{10} \equiv E_1$, $\hat{p}_{1T}$, $\hat{p}_{1L}$, E_2, $\hat{p}_{2L}$, and p_T.

$$\begin{aligned} q_0 &= \frac{W^2 - Q^2 - M^2}{2W} \\ P &= \left(\left(\frac{W^2 + Q^2 + M^2}{2W} \right)^2 - M^2 \right)^{\frac{1}{2}} \approx \frac{W^2 + Q^2 - M^2}{2W} \\ |\mathbf{q}| &\equiv P \\ x_i &= \frac{2E_i}{W} \\ |\mathbf{p_3}| &= -\hat{p}_{1L} - \hat{p}_{2L} \\ \theta_3 &= \sin^{-1} \frac{p_T}{|\mathbf{p_3}|} \\ p_L &= P - |\mathbf{p_3}| \cos\theta_3 \\ p_0 &= \frac{W}{2}(x_1 + x_2 - 1) + \frac{Q^2 + M^2}{2W} \qquad (\neq \sqrt{p_L^2 + p_T^2}) \\ \hat{s} &= \frac{W^2}{4}(x_1 + x_2)^2 - (|\mathbf{p_3}|)^2 \\ t_0 &= -Q^2 - x_1 W q_0 - 2P\hat{p}_{1L}\cos\theta_3 \\ u_0 &= -Q^2 - x_2 W q_0 - 2P\hat{p}_{2L}\cos\theta_3 \\ t_1 &= 2\hat{p}_{1T} P \sin\theta_3 \end{aligned} \qquad \text{(B.11)}$$

The α_{nX} and β_{nX} coefficients are then defined in the code as they are in Appendix section A.3.

B.5 Methodology: Generating a Distribution

In order to implement the phi asymmetry in the LUND Monte Carlo, we must be able to generate random numbers according to a distribution (such as $dN/dk_\perp^2$ or $d^2N/d\varphi_3 d\hat{\varphi}_1$). The specific form for the distribution may be chosen by guessing, fitting a phenomenological distribution to data, or by taking the result of a theoretical calculation.

We start with a normalized distribution dN/dx in some variable x. From this we want to generate a sample of quantities $\{x_i\}$ randomly distributed according to dN/dx. Broadly speaking, there are two methods for accomplishing this task. In both cases, we assume that are are able to generate a random number r between 0.0 and 1.0 according to a flat distribution $dN/dr = 1$. The first method involves finding a one-to-one map from $r \rightarrow x$ such that x is distributed as desired. The second method relies on brute force. There are other less general tricks available for specific cases (such as a one-dimensional gaussian), but these will not be covered here.

B.5.1 Finding a One-to-One Map

The one-to-one map method is outlined below. This is the method used to generate the $k_\perp$ distribution in LEPTO.

Since we know that $dN/dr = 1$, we can easily find a function $r(x)$ which will cause x to be distributed as desired. First we note that

$$\frac{dr(x)}{dx} = \frac{dN}{dr}\frac{dr}{dx} = \frac{dN}{dx}. \tag{B.12}$$

Then we perform an integral to find $r(x)$ as follows:

$$r(x) = \int_{-\infty}^{x} dx' \frac{dN}{dx'}. \tag{B.13}$$

If this function is one-to-one and invertible, then we can find $x(r)$. Once one has this map $x(r)$, one simply generates a set of random numbers $\{r_i\}$ according to a flat distribution, and plugs them into the formula $x_i = x(r_i)$.

Unfortunately, not all distributions can be integrated and inverted this way even in principle, let alone in practice. This method tends to work well for simple one-dimensional functions such as polynomials and exponentials. Section 2.4.2 contains an explicit example of how $k_\perp$ is generated in the Lund using this method.

B.5.2 Brute Force Method

When a one-to-one map is not available, one must either rely on clever tricks or brute force. The brute force method works well when one has a distribution dN/dx which is nonzero over a limited range in x. Angular distributions, which are limited to the range $-\pi < \varphi \leq \pi$, can often be generated this way.

In order to generate a distribution according to $dN/dx \equiv f(x)$, where $x \in [a, b]$, perform the following steps:

1. Define $P(x) = f(x)/F$ where F is any constant such that $F \geq \max_{x\in[a,b]} f(x)$.
2. Roll a number $r_1 \in [0, 1]$ according to a flat distribution.
3. Set $x_i = r_1 \cdot (b - a) + a$.
4. Roll a number $r_2 \in [0, 1]$ according to a flat distribution.
5. IF $r_2 \leq P(x_i)$ THEN Keep x_i ELSE Goto Step 2.

This method will generate the desired distribution of x_i's, but it is not guaranteed to ever converge. If the area under the curve $P(x)$ is small compared to $b-a$, then this method can be quite inefficient. On the other hand, If the area under the curve $P(x)$ is large, than the method is quite well-behaved. For simple trigonometric functions such as $\cos x$ and $\cos 2x$, this method is adequate. In any case, we want to choose the smallest value for F that we can find which is consistent with $F \geq \max f(x)$.

B.5.3 Implementing the Phi Asymmetry Cross Section by Brute Force

Implementing the $\mathcal{O}(1)$ Term

In order to implement a phi dependence of the form:

$$\frac{dN}{d\varphi} \propto A + B\cos\varphi + C\cos 2\varphi, \tag{B.14}$$

we need only note that this expression will never exceed $|A| + |B| + |C|$. We can then use the brute force method. We roll a φ according to a flat distribution and then keep it with the following probability:

$$P(\varphi) = \frac{1}{|A| + |B| + |C|}(A + B\cos\varphi + C\cos 2\varphi). \tag{B.15}$$

This is the method used in subroutine `LPHIKT` to generate the phi asymmetry for leading order events.

Implementing the $\mathcal{O}(\alpha_s)$ Term

As stated in section B.4, we want to generate a two-dimensional distribution of the form:

$$\frac{d\sigma}{d\varphi_3 d\hat{\varphi}_1} \propto \times N(\hat{\varphi}_1, \varphi_3)/\Delta(\hat{\varphi}_1) \tag{B.16}$$

where

$$\begin{aligned} N(\hat{\varphi}_1, \varphi_3) = \; & (A_1 + A_2 \cos 2\hat{\varphi}_1 + A_3 \cos \hat{\varphi}_1) + \\ & (B_1 + B_2 \cos 2\hat{\varphi}_1 + B_3 \cos \hat{\varphi}_1) \cos \varphi_3 + \\ & (C_1 + C_2 \cos 2\hat{\varphi}_1 + C_3 \cos \hat{\varphi}_1) \cos 2\varphi_3 + \\ & (\quad D_2 \sin 2\hat{\varphi}_1 + D_3 \sin \hat{\varphi}_1) \sin \varphi_3 + \\ & (\quad E_2 \sin 2\hat{\varphi}_1 + E_3 \sin \hat{\varphi}_1) \sin 2\varphi_3 \quad \} \end{aligned} \tag{B.17}$$

and

$$\Delta(\hat{\varphi}_1) = \begin{cases} |t_0| - t_1 \cos \hat{\varphi}_1 & \text{for GB,} \\ (t_0 u_0 - \frac{1}{2} t_1^2) + t_1 (u_0 - t_0) \cos \hat{\varphi}_1 - \frac{1}{2} t_1^2 \cos 2\hat{\varphi}_1 & \text{for PGF.} \end{cases} \tag{B.18}$$

In order to do this, we will use a brute force probability distribution of the form:

$$P(\hat{\varphi}_1, \varphi_3) = \frac{\Delta_0}{N_m} \frac{N(\hat{\varphi}_1, \varphi_3)}{\Delta(\hat{\varphi}_1)}. \tag{B.19}$$

In order to complete this prescription, we must find values for Δ_0 and N_m such that:

$$0 < \Delta_0 \leq \min_{\hat{\varphi}_1} \Delta(\hat{\varphi}_1),$$

and

$$N_m \geq \max_{[\hat{\varphi}_1, \varphi_3]} N(\hat{\varphi}_1, \varphi_3) > 0.$$

In order to make this choice more evident, let us rewrite N in a useful form:

$$\begin{aligned} N(\hat{\varphi}_1, \varphi_3) = \Big\{ \quad & (A_1 + A_2 \cos 2\hat{\varphi}_1 + A_3 \cos \hat{\varphi}_1) + \\ & (B_1 \cos \varphi_3 + C_1 \cos 2\varphi_3) + \\ & \Big(\frac{B_3 + D_3}{2} \cos(\hat{\varphi}_1 - \varphi_3) + \frac{B_3 - D_3}{2} \cos(\hat{\varphi}_1 + \varphi_3)\Big) + \\ & \Big(\frac{C_2 + E_2}{2} \cos(2\hat{\varphi}_1 - 2\varphi_3) + \frac{C_2 - E_2}{2} \cos(2\hat{\varphi}_1 + 2\varphi_3)\Big) + \\ & \Big(\frac{B_2 + D_2}{2} \cos(2\hat{\varphi}_1 - \varphi_3) + \frac{B_2 - D_2}{2} \cos(2\hat{\varphi}_1 + \varphi_3)\Big) + \\ & \Big(\frac{C_3 + E_3}{2} \cos(\hat{\varphi}_1 - 2\varphi_3) + \frac{C_3 - E_3}{2} \cos(\hat{\varphi}_1 + 2\varphi_3)\Big) \Big\}. \end{aligned} \tag{B.20}$$

This quantity is difficult to formally maximize, but it can be maximized in a piecewise fashion, yielding a number N_m which is larger than the maximum:

$$\begin{aligned} N_m = \; & |A_1| + |A_2| + |A_3| + |B_1| + |C_1| + \\ & \frac{|B_3 + D_3|}{2} + \frac{|B_3 - D_3|}{2} + \\ & \frac{|C_2 + E_2|}{2} + \frac{|C_2 - E_2|}{2} + \\ & \frac{|B_2 + D_2|}{2} + \frac{|B_2 - D_2|}{2} + \\ & \frac{|C_3 + E_3|}{2} + \frac{|C_3 - E_3|}{2}. \end{aligned} \tag{B.21}$$

It should be noted that this choice of definition of N was made with the knowledge that many terms, such as C_2 and E_2, are very nearly equal and opposite. The function $\Delta(\hat{\varphi}_1)$ can be written in a more general form:

$$\Delta(\hat{\varphi}_1) = \delta_1 + \delta_2 \cos \hat{\varphi}_1 + \delta_3 \cos 2\hat{\varphi}_1, \tag{B.22}$$

with $\delta_1 > 0$ and $\delta_3 \leq 0$. It is possible to find the mathematical minimum of such a function rigorously. We can recast the problem in term of $x \equiv \cos \hat{\varphi}_1$:

$$\Delta_0 = \min_{x \in [-1,1]} \{\delta_1 - \delta_3 + \delta_2 x + 2\delta_3 x^2\}. \tag{B.23}$$

Since $\delta_3 \leq 0$, the curvature is everywhere non-positive and this function has no actual minimum over the real numbers. It is either a parabola that opens downward or a straight line. The minimum over our range of interest $x \in [-1, 1]$ must occur at one

of the end points: $x \in \{-1, 1\}$. Therefore:

$$\begin{aligned} \Delta_0 &= \min_{x\in\{-1,1\}} \{\delta_1 - \delta_3 + \delta_2 x + 2\delta_3 x^2\} \\ &= \min\{\delta_1 \pm \delta_2 + \delta_3\} \\ &= \delta_1 - |\delta_2| + \delta_3. \end{aligned} \tag{B.24}$$

This is the basic method that is used in subroutine `PHIQCD` to generate the appropriate distribution in φ_3 and $\hat{\varphi}_1$.

B.6 Summary

The existing Monte Carlo for Leptoproduction: Lepto version 5.2 (Matrix Element) neglects an important theoretical effect: the phi asymmetry due to the primordial transverse momentum ($k_\perp$) of the struck parton. A related theoretical effect, the phi asymmetry due to gluon radiation and photon-gluon fusion, is implemented in Lepto 5.2, but only under the approximation that $k_\perp = 0$.

This Appendix section described how the Lepto 5.2 (ME) Monte Carlo used by E665 was modified to incorporate the effect of $k_\perp$ on the phi asymmetry. The effect of $k_\perp$ was incorporated both at leading order and for hard QCD processes. The phi asymmetry calculations that were used were based on modifications of previous work by Cahn [19, 20] and by Joshipura and Kramer [21]. The theoretical details are contained in Appendix A.

Appendix C

Analysis Details

This Appendix contains a detailed description of two analysis procedures. Section C.1 describes the Rank Mixing Acceptance Correction which was applied in Section 5.3.1. Section C.2 describes the propagation of errors which allows us to estimate the error on p_T and φ_h. The error propagation was used in Section 5.5.3.

C.1 Rank Mixing Acceptance Correction

The *Overall Efficiency* for detecting and reconstructing a particle is the product of several factors. The first factor is the *Target Transmission Probability* which is the probability that a produced hadron makes it out of the target without undergoing a secondary interaction. The second factor is the *Chamber Acceptance*, which is the probability that a charged hadron makes it into the detector and generates enough hits in the chambers to allow the track to be found, at least in principle. The Chamber Acceptance includes both the geometric acceptance of the detector and the individual chamber efficiencies. The last factor in the Overall Efficiency is the *Reconstruction Efficiency*. This is the probability that a track is properly reconstructed given that it generated enough hits in the detector. We will also define the *Full Acceptance* as the product of the Chamber Acceptance and Reconstruction Efficiency, ignoring the Target Transmission.

In order to correct for rank mixing from measured charged particles to true particles (charged and uncharged), we must also make some assumptions about the neutral particles. We will assume that the neutral particles make up 1/3 of the total produced

hadrons and are distributed in z_h and φ_h as follows:

$$D_n(z,\varphi)_{h^0} = \frac{1}{2}\left[D_n(z,\varphi)_{h^+} + D_n(z,\varphi)_{h^-}\right] \tag{C.1}$$

This assumption is reasonable, but unproven.

Let us define a measured distribution for hadrons of a given rank:

$$D_n^m(z,\varphi) \equiv \left.\frac{1}{N_{\mu'}}\frac{d^2N_n}{dzd\varphi}\right|_{meas.} \tag{C.2}$$

where $n \in \{1,2,3,\ldots\}$ refers to the rank and m denotes that it is a measured distribution and not a true distribution. Similarly, let us define the true distributions:

$$D_n(z,\varphi) \equiv \left.\frac{1}{N_{\mu'}}\frac{d^2N_n}{dzd\varphi}\right|_{true}. \tag{C.3}$$

Let us also define:

$$D_n^m(z) \equiv \left.\frac{1}{N_{\mu'}}\frac{dN_n}{dz}\right|_{meas.} = \int_0^{2\pi} d\varphi D_n^m(z,\varphi), \tag{C.4}$$

$$D_n(z) \equiv \left.\frac{1}{N_{\mu'}}\frac{dN_n}{dz}\right|_{true} = \int_0^{2\pi} d\varphi D_n(z,\varphi). \tag{C.5}$$

Let us write the overall efficiency function as ϵ; in general, this is a detailed function $\epsilon(z, p_T, \varphi_h, Q^2, \nu)$. In practice, the functionality is dominated by the spectrometer acceptance which is primarily a function of the hadron momentum. We will assume that the efficiency doesn't depend upon φ_h and that it can be described as a function of z_h.[1] Thus we will use the description $\epsilon(z)$. For the purpose of our rank mixing correction, we can make an even simpler assumption. Let's assume that the efficiency is a constant, independent of z_h. This is a good assumption for $z_h > 0.2$ and will introduce a small systematic error for $0.1 < z_h < 0.2$.

The measured Rank 1 distribution can be written as a function of the true distributions:

$$D_1^m(z,\varphi)dzd\varphi = \epsilon D_1(z,\varphi)dzd\varphi + (1-\epsilon)\epsilon D_2(z,\varphi)dzd\varphi + (1-\epsilon)^2\epsilon D_3(z,\varphi)dzd\varphi + \ldots \tag{C.6}$$

The first term is the probability that we found the leading hadron, ϵ, times the probability that it was in a particular range of z and φ, $D_1(z,\varphi)dzd\varphi$. The second term

[1] References [25] and [50] both showed that a φ asymmetry was not generated by the apparatus, justifying the assumption that the efficiency is independent of φ_h.

is the probability that we missed the true first hadron, $(1-\epsilon)$, times the probability that we identified the true second hadron, ϵ, times the probability that the second hadron was in the right range of z and ϵ. The third term is the probability of missing both the first and second hadron, $(1-\epsilon)^2$, times the probability that we found the third hadron, ϵ, times the probability that it's in the right range of z and φ. We will truncate the series after three terms. The number of measured particles for $z > 0.1$ with Rank 4 is quite small compared to Rank 1 (see Figure 5-13e on page 157. We can write Equation C.6 as:

$$D_1^m(z,\varphi) = \epsilon D_1(z,\varphi) + (1-\epsilon)\epsilon D_2(z,\varphi) + (1-\epsilon)^2\epsilon D_3(z,\varphi) + \ldots \tag{C.7}$$

In a similar fashion, we can write an expression for the measured Rank 2 distributions:

$$D_2^m(z,\varphi) = \epsilon^2 D_2(z,\varphi) + 2(1-\epsilon)\epsilon^2 D_3(z,\varphi) + \ldots \tag{C.8}$$

The first term requires that the both the first and second particles are found properly, hence the ϵ^2. The second term is really the sum of two disjoint cases:

1. Rank 1 Found. Rank 2 Missing. Rank 3 found.

2. Rank 1 Missing. Rank 2 Found. Rank 3 found.

Each case has probability $\epsilon^2(1-\epsilon)$. Since the two cases are disjoint, their probabilities can simply be added.

Finally, we have:

$$D_3^m(z,\varphi) = \epsilon^3 D_3(z,\varphi) + \ldots \tag{C.9}$$

Now, we can truncate all of these series and then we have three equations in three unknowns (the three true distributions). We can solve them one by one:

$$D_3(z,\varphi) = \frac{1}{\epsilon^3} D_3^m(z,\varphi) \tag{C.10}$$

$$\begin{aligned} D_2(z,\varphi) &= \frac{1}{\epsilon^2}\left[D_2^m(z,\varphi) - 2(1-\epsilon)\epsilon^2 D_3(z,\varphi)\right] \\ &= \frac{1}{\epsilon^2}\left[D_2^m(z,\varphi) - 2\frac{(1-\epsilon)}{\epsilon} D_3^m(z,\varphi)\right] \end{aligned} \tag{C.11}$$

$$\begin{aligned} D_1(z,\varphi) &= \frac{1}{\epsilon}\left\{D_1^m(z,\varphi) - (1-\epsilon)\epsilon D_2(z,\varphi) - (1-\epsilon)^2\epsilon D_3(z,\varphi)\right\} \\ &= \frac{1}{\epsilon}\left\{D_1^m(z,\varphi) - \frac{(1-\epsilon)}{\epsilon}\left[D_2^m(z,\varphi) - 2\frac{(1-\epsilon)}{\epsilon}D_3^m(z,\varphi)\right]\right. \\ &\quad \left. - \left(\frac{1-\epsilon}{\epsilon}\right)^2 D_3^m(z,\varphi)\right\} \\ &= \frac{1}{\epsilon}\left\{D_1^m(z,\varphi) - \frac{(1-\epsilon)}{\epsilon}D_2^m(z,\varphi) + \left(\frac{1-\epsilon}{\epsilon}\right)^2 D_3^m(z,\varphi)\right\} \quad \text{(C.12)} \end{aligned}$$

We are interested in the quantity $2\langle\cos\varphi\rangle$ as a function of z_h for a given rank. Let us define the measured and true values as $b_n^m(z)$ and $b_n(z)$ respectively. We can express this as:

$$b_n(z) \equiv 2\frac{\int_0^{2\pi}\cos\varphi D_n(z,\varphi)d\varphi}{\int_0^{2\pi} D_n(z,\varphi)d\varphi}, \quad \text{(C.13)}$$

or more succinctly as:

$$b_n(z) = \frac{2}{D_n(z)}\int_0^{2\pi}\cos\varphi D_n(z,\varphi)d\varphi. \quad \text{(C.14)}$$

Similarly:

$$b_n^m(z) = \frac{2}{D_n^m(z)}\int_0^{2\pi}\cos\varphi D_n^m(z,\varphi)d\varphi. \quad \text{(C.15)}$$

We can combine the above equations into an expression for the TRUE Rank 1 phi asymmetry in terms of the MEASURED phi asymmetries for Ranks 1–3:

$$b_1(z) = \frac{\frac{1}{\epsilon}\left\{D_1^m(z)b_1^m(z) - \frac{(1-\epsilon)}{\epsilon}D_2^m(z)b_2^m(z) + \left(\frac{1-\epsilon}{\epsilon}\right)^2 D_3^m(z)b_3^m(z)\right\}}{\frac{1}{\epsilon}\left\{D_1^m(z) - \frac{(1-\epsilon)}{\epsilon}D_2^m(z) + \left(\frac{1-\epsilon}{\epsilon}\right)^2 D_3^m(z)\right\}} \quad \text{(C.16)}$$

This can be simplified:

$$b_1(z) = \frac{\left\{b_1^m(z) - \frac{(1-\epsilon)}{\epsilon}\frac{D_2^m(z)}{D_1^m(z)}b_2^m(z) + \left(\frac{1-\epsilon}{\epsilon}\right)^2\frac{D_3^m(z)}{D_1^m(z)}b_3^m(z)\right\}}{\left\{1 - \frac{(1-\epsilon)}{\epsilon}\frac{D_2^m(z)}{D_1^m(z)} + \left(\frac{1-\epsilon}{\epsilon}\right)^2\frac{D_3^m(z)}{D_1^m(z)}\right\}} \quad \text{(C.17)}$$

Similarly, we have:

$$b_2(z) = \frac{\left\{b_2^m(z) - 2\frac{(1-\epsilon)}{\epsilon}\frac{D_3^m(z)}{D_2^m(z)}b_3^m(z)\right\}}{\left\{1 - 2\frac{(1-\epsilon)}{\epsilon}\frac{D_3^m(z)}{D_2^m(z)}\right\}} \quad \text{(C.18)}$$

Note that the distributions $D_n^m(z)$ only appear in ratios. This means that we need only measure these ratios. This is good news since any errors in normalization ($\frac{1}{N_{\mu'}}$) will cancel. In fact, since only ratios are needed, we need not normalize the distributions at all. We can fill the Rank 1 z-distribution for all events and fill the Rank 2 z-distribution for the same events and just divide the two. The $\frac{1}{N_{\mu'}}$ factors will cancel.

In addition to the above formalism, we will need three things:

1. The overall efficiency for finding a charged particle.
2. The ratios of observed z-distributions for charged particles of ranks 1–3.
3. The measured distributions of B/A for each rank: 1–3.

The first item can be assembled from existing information. The full acceptance can be found in Reference [25] (see especially Figures 5.17, 5.21, and Table 5.5). This information applies to particles with $E > 6$ GeV and $\nu > 100$ GeV. We will take the following values for the full acceptance for charged particles: $\epsilon_{\pm}^{(FA)} = 0.80$ for $z > 0.2$ and $\epsilon_{\pm}^{(FA)} = 0.74$ for $0.1 < z < 0.2$. Corrections will not be attempted for $z < 0.1$ because the acceptance is both poor and strongly varying in this region. The small time-dependence of the efficiency will be ignored and treated as a systematic error along with the unmeasured time-dependence for the pre-December 1 data. We assume that the efficiency for detecting neutrals is exactly zero and that $\frac{1}{3}$ of the particles are neutral. This yields an effective full acceptance of $\epsilon^{(FA)} = 0.53$ for $z > 0.2$ and $\epsilon^{(FA)} = 0.49$ for $0.1 < z < 0.2$.

The effect of target rescattering can be estimated from the inelastic scattering cross-section for pions from deuterium. In Section 3.3, the number of nuclear interaction lengths in the D_2 target was found to be 0.342. One nuclear interaction length is the mean "distance" (in g/cm^2) that a pion will travel before undergoing an inelastic scatter from the deuterium. The target rescattering is roughly independent of the hadron energy and the particle type (among hadrons) and can be treated as an overall loss factor.

If a hadron passes through a distance of ζ interaction lengths, its transmission probability is:

$$T(\zeta) = e^{-\zeta}.$$

However, the DIS interaction vertices are uniformly distributed throughout the length of the target. The average transmission probability for a target of overall length ζ_0 is

$$\overline{T} = \frac{1}{\zeta_0}\int_0^{\zeta_0} T(\zeta)d\zeta = \frac{1}{\zeta_0}\int_0^{\zeta_0} e^{-\zeta}d\zeta = \frac{1-e^{-\zeta_0}}{\zeta_0} \qquad \text{(C.19)}$$

For $\zeta_0 = 0.342$, this corresponds to $\overline{T} = 0.847$. This means that our overall efficiency for all particles is $\epsilon = 0.45$ for $z > 0.2$ and $\epsilon = 0.42$ for $0.1 < z < 0.2$.

The second item in the above list, the ratios of observed z distributions by rank, we will get directly from the data. See Figure 5-13 on page 157. It should be noted that $D^m_{4+}(z) \ll D^m_1(z)$ for $z > 0.1$, justifying the truncation of the series in Equation C.6 and following.

The third item in the list, the measured dependence of B/A on z_h and rank, can be found in Figure 5-9 on page 151. Figure 5-14 on page 158 shows the result of performing the correction described in this section.

C.2 Propagation of Errors

In this section we will discuss the propagation of errors from the track and vertex parameters to the physics variables $p_T^{(h)}$ and φ_h. We will use the term *error matrix* and *covariance matrix* interchangeably. As described in Bevington [2], an error matrix quantifies the spread of a set of measured values from the true values due to measurement error. For example, if we have a set of measured quantities x_i and y_i with averages $\bar{x}$ and $\bar{y}$, we can construct a matrix

$$\begin{pmatrix} \sigma_x^2 & \sigma_{xy}^2 \\ \sigma_{yx}^2 & \sigma_y^2 \end{pmatrix},$$

with

$$\sigma_x^2 \equiv \left\langle (x-\bar{x})^2 \right\rangle, \qquad \sigma_y^2 \equiv \left\langle (y-\bar{y})^2 \right\rangle, \qquad \sigma_{xy}^2 = \sigma_{yx}^2 \equiv \langle (x-\bar{x})(y-\bar{y}) \rangle .$$

An error matrix is defined in a given basis, such as the basis $\{x, y\}$ used above. In other words, we must choose a set of independent variables to measure before the error matrix is well-defined.

The main purpose of this chapter is to show how to transform an error matrix from the PTMV-parameter-basis used by our reconstruction program into the basis where the physics variables such as p_T and φ are defined. Part of this task has already been accomplished [54]. The results will be derived from scratch in this section, but they are consistent with the previous treatment.

PTMV Parameters

The PTMV reconstruction program provides us with a vertex position for the primary vertex:

$$\vec{R} \equiv \{X_{vtx}, Y_{vtx}, Z_{vtx}\}\,, \tag{C.20}$$

as well as a 3×3 symmetric covariance matrix describing the errors:

$$\sigma^2_{\vec{R}} \equiv \begin{pmatrix} \sigma^2_X & \sigma^2_{XY} & \sigma^2_{XZ} \\ \sigma^2_{YX} & \sigma^2_Y & \sigma^2_{YZ} \\ \sigma^2_{ZX} & \sigma^2_{ZY} & \sigma^2_Z \end{pmatrix}. \tag{C.21}$$

The reconstruction program also provides us with the track parameters for the beam muon, the scattered muon, and the hadron:

$$\begin{aligned} \check{L} &= \{Y_{trk}, Z_{trk}, Y', Z', 1/p\}_{\mu}\,, \\ \check{L}' &= \{Y_{trk}, Z_{trk}, Y', Z', 1/p\}_{\mu'}\,, \\ \check{P} &= \{Y_{trk}, Z_{trk}, Y', Z', 1/p\}_{h}\,. \end{aligned} \tag{C.22}$$

These track parameters are reported at the point on the track which is closest to the vertex position. Any two of the three parameters X_{trk}, Y_{trk}, and Z_{trk} are independent. We have chosen to use Y and Z. We also have 5×5 covariance matrices for each track. We will treat the 19 parameters contained in $\vec{R}$, $\check{L}$, $\check{L}'$, and $\check{P}$ as independent and uncorrelated. This assumption is only approximately valid. The vertex position is determined from the track parameters of the muons and any hadrons that are fit to the primary vertex. This means that the vertex position and track parameters are not really independent.

Under our assumptions, our initial covariance matrix is given by:

$$S^2_0 \equiv \begin{pmatrix} \sigma^2_{\vec{R}} & 0 & 0 & 0 \\ 0 & \sigma^2_{\check{L}} & 0 & 0 \\ 0 & 0 & \sigma^2_{\check{L}'} & 0 \\ 0 & 0 & 0 & \sigma^2_{\check{P}} \end{pmatrix}. \tag{C.23}$$

We will propagate this error matrix in three steps:

1. $\vec{R}, \check{L}, \check{L}', \check{P} \rightarrow \vec{l}, \vec{l}', \vec{p}_h$
2. $\vec{l}, \vec{l}', \vec{p}_h \rightarrow \vec{q}, \vec{l}', \vec{p}_h$
3. $\vec{q}, \vec{l}', \vec{p}_h \rightarrow p_T, \varphi_h$

Transforming from $\{\vec{R}, \check{L}, \check{L}', \check{P}\} \rightarrow \{\vec{l}, \vec{l}', \vec{p}_h\}$

In order to transform our covariance matrix, we will need to use a Jacobian:

$$\frac{\partial(\vec{l}, \vec{l}', \vec{p}_h)}{\partial(\vec{R}, \check{L}, \check{L}', \check{P})}. \tag{C.24}$$

We will use the following conventions when referring to Jacobians such as $\frac{\partial \vec{u}}{\partial \vec{v}}$: $J_{ij} = \frac{\partial u_j}{\partial v_i}$. In other words:

$$\frac{\partial \vec{u}}{\partial \vec{v}} \equiv \begin{pmatrix} \frac{\partial u_1}{\partial v_1} & \frac{\partial u_2}{\partial v_1} & \frac{\partial u_3}{\partial v_1} \\ \frac{\partial u_1}{\partial v_2} & \frac{\partial u_2}{\partial v_2} & \frac{\partial u_3}{\partial v_2} \\ \frac{\partial u_1}{\partial v_3} & \frac{\partial u_2}{\partial v_3} & \frac{\partial u_3}{\partial v_3} \end{pmatrix}. \tag{C.25}$$

In this notation, our first transformation Jacobian is given by:

$$J_{(0\rightarrow 1)} \equiv \frac{\partial(\vec{l}, \vec{l}', \vec{p}_h)}{\partial(\vec{R}, \check{L}, \check{L}', \check{P})} = \begin{pmatrix} \frac{\partial \vec{l}}{\partial \vec{R}} & \frac{\partial \vec{l}'}{\partial \vec{R}} & \frac{\partial \vec{p}_h}{\partial \vec{R}} \\ \frac{\partial \vec{l}}{\partial \check{L}} & 0 & 0 \\ 0 & \frac{\partial \vec{l}'}{\partial \check{L}'} & 0 \\ 0 & 0 & \frac{\partial \vec{p}_h}{\partial \check{P}} \end{pmatrix} \tag{C.26}$$

and the transformation is given by:

$$S_1^2 = J_{0\rightarrow 1}^T S_0^2 J_{0\rightarrow 1} \tag{C.27}$$

with S_1^2 being the 9×9 covariance matrix on $\vec{l}$, $\vec{l}'$, and $\vec{p}_h$. In discussing such large matrices, we will use a convenient notation for some of the sub-matrices. For instance, the matrix S_1^2 is composed of 9 distinct 3×3 submatrices including

$$\sigma^2_{\vec{l}\vec{l}'} = \begin{pmatrix} \sigma^2_{l_x l'_x} & \sigma^2_{l_x l'_y} & \sigma^2_{l_x l'_z} \\ \sigma^2_{l_y l'_x} & \sigma^2_{l_y l'_y} & \sigma^2_{l_y l'_z} \\ \sigma^2_{l_z l'_x} & \sigma^2_{l_z l'_y} & \sigma^2_{l_z l'_z} \end{pmatrix}.$$

Due to the symmetry of the overall covariance matrix, we know that $\sigma^2_{\vec{u}\vec{v}} = (\sigma^2_{\vec{v}\vec{u}})^T$.

Using this notation, we can write the transformation of the error matrix more

explicitly:

$$\begin{pmatrix} \sigma^2_{\vec{l}\vec{l}} & \sigma^2_{\vec{l}\vec{l}'} & \sigma^2_{\vec{l}\vec{p}_h} \\ \sigma^2_{\vec{l}'\vec{l}} & \sigma^2_{\vec{l}'\vec{l}'} & \sigma^2_{\vec{l}'\vec{p}_h} \\ \sigma^2_{\vec{p}_h\vec{l}} & \sigma^2_{\vec{p}_h\vec{l}'} & \sigma^2_{\vec{p}_h\vec{p}_h} \end{pmatrix} = \begin{pmatrix} \left(\frac{\partial\vec{l}}{\partial\vec{R}}\right)^T & \left(\frac{\partial\vec{l}}{\partial\vec{L}}\right)^T & 0 & 0 \\ \left(\frac{\partial\vec{l}'}{\partial\vec{R}}\right)^T & 0 & \left(\frac{\partial\vec{l}'}{\partial\vec{L}'}\right)^T & 0 \\ \left(\frac{\partial\vec{p}_h}{\partial\vec{R}}\right)^T & 0 & 0 & \left(\frac{\partial\vec{p}_h}{\partial\vec{P}}\right)^T \end{pmatrix} \times$$
$$\begin{pmatrix} \sigma^2_{\vec{R}} & 0 & 0 & 0 \\ 0 & \sigma^2_{\vec{L}} & 0 & 0 \\ 0 & 0 & \sigma^2_{\vec{L}'} & 0 \\ 0 & 0 & 0 & \sigma^2_{\vec{P}} \end{pmatrix} \begin{pmatrix} \frac{\partial\vec{l}}{\partial\vec{R}} & \frac{\partial\vec{l}'}{\partial\vec{R}} & \frac{\partial\vec{p}_h}{\partial\vec{R}} \\ \frac{\partial\vec{l}}{\partial\vec{L}} & 0 & 0 \\ 0 & \frac{\partial\vec{l}'}{\partial\vec{L}'} & 0 \\ 0 & 0 & \frac{\partial\vec{p}_h}{\partial\vec{P}} \end{pmatrix} . \tag{C.28}$$

Even more explicitly, we have:

$$\sigma^2_{\vec{l}\vec{l}} = \left(\frac{\partial\vec{l}}{\partial\vec{L}}\right)^T \sigma^2_{\vec{L}} \left(\frac{\partial\vec{l}}{\partial\vec{L}}\right) + \left(\frac{\partial\vec{l}}{\partial\vec{R}}\right)^T \sigma^2_{\vec{R}} \left(\frac{\partial\vec{l}}{\partial\vec{R}}\right), \tag{C.29}$$

$$\sigma^2_{\vec{l}'\vec{l}'} = \left(\frac{\partial\vec{l}'}{\partial\vec{L}'}\right)^T \sigma^2_{\vec{L}'} \left(\frac{\partial\vec{l}'}{\partial\vec{L}'}\right) + \left(\frac{\partial\vec{l}'}{\partial\vec{R}}\right)^T \sigma^2_{\vec{R}} \left(\frac{\partial\vec{l}'}{\partial\vec{R}}\right), \tag{C.30}$$

$$\sigma^2_{\vec{p}_h\vec{p}_h} = \left(\frac{\partial\vec{p}_h}{\partial\vec{P}}\right)^T \sigma^2_{\vec{P}} \left(\frac{\partial\vec{p}_h}{\partial\vec{P}}\right) + \left(\frac{\partial\vec{p}_h}{\partial\vec{R}}\right)^T \sigma^2_{\vec{R}} \left(\frac{\partial\vec{p}_h}{\partial\vec{R}}\right), \tag{C.31}$$

$$\sigma^2_{\vec{l}\vec{l}'} = \left(\frac{\partial\vec{l}}{\partial\vec{R}}\right)^T \sigma^2_{\vec{R}} \left(\frac{\partial\vec{l}'}{\partial\vec{R}}\right), \tag{C.32}$$

$$\sigma^2_{\vec{l}\vec{p}_h} = \left(\frac{\partial\vec{l}}{\partial\vec{R}}\right)^T \sigma^2_{\vec{R}} \left(\frac{\partial\vec{p}_h}{\partial\vec{R}}\right), \tag{C.33}$$

$$\sigma^2_{\vec{l}'\vec{p}_h} = \left(\frac{\partial\vec{l}'}{\partial\vec{R}}\right)^T \sigma^2_{\vec{R}} \left(\frac{\partial\vec{p}_h}{\partial\vec{R}}\right). \tag{C.34}$$

The various derivatives in the Jacobian can be found as follows. Consider the behavior of a particle of momentum $\vec{p}$ and charge $q_p = \pm 1$ in the CVM field. We can treat this as a uniform magnetic field along the negative z-axis. Let's define $\eta = \pm 1$ to be the sign of p_x. If we define $\vec{e} \equiv \hat{p}$, then we can write:

$$e_x = \frac{\eta}{\sqrt{1 + Y'^2 + Z'^2}}, \qquad e_y = Y' e_x, \qquad e_z = Z' e_x, \tag{C.35}$$

and

$$\vec{p} = p\vec{e}. \tag{C.36}$$

Let's also define

$$e_\perp \equiv \sqrt{e_x^2 + e_y^2} = \sqrt{1 - e_z^2}. \tag{C.37}$$

The following derivatives are then straightforward:

$$\begin{array}{lll} \frac{\partial p_x}{\partial Y'} = -pe_x^3 Y', & \frac{\partial p_y}{\partial Y'} = pe_x^3(1 + Z'^2), & \frac{\partial p_z}{\partial Y'} = -pe_x^3 Y'Z', \\ \frac{\partial p_x}{\partial Z'} = -pe_x^3 Z', & \frac{\partial p_y}{\partial Z'} = -pe_x^3 Y'Z', & \frac{\partial p_z}{\partial Z'} = pe_x^3(1 + Y'^2), \end{array} \tag{C.38}$$

and

$$\frac{\partial p_i}{\partial 1/p} = -pp_i. \tag{C.39}$$

We must also find the derivative of the measured 3-momentum of the particle with respect to a shift in the vertex position. Even if we measure the track parameters perfectly, we depend on the vertex position to tell us the point of closest approach and therefore the momentum direction vector $\vec{e}$. An error in the vertex position translates into an error in the point of closest approach and therefore into an error on the measured momentum vector. In considering these effects we will make use of the fact that the distance between the track and the vertex is much less than the radius of curvature for the track. This means that we can treat the vertex position as if it were initially on the track.

A charged particle in a uniform magnetic field travels in a helix. According to Jackson [55] (Equation 12.42), the radius of curvature of a helical track is given by:

$$\begin{aligned} \rho &= \frac{10^4}{3}\frac{p_\perp}{B}\frac{\text{gauss cm}}{\text{MeV/c}} \\ &= \frac{10}{3}\frac{p_\perp}{B}\frac{\text{Tm}}{\text{GeV/c}}, \end{aligned} \tag{C.40}$$

where 3 is actually a shorthand for 2.99997925. We can write this as

$$\rho = \frac{p_\perp}{\kappa}, \tag{C.41}$$

where $\kappa = \frac{3}{10}B\frac{\text{GeV/c}}{\text{Tm}}$. For the CVM field: $\vec{B} = -1.5131266\ \text{T}\ \hat{z}_{E665}$. Therefore

$$\begin{aligned} \kappa &= (1.5131266)(0.299997925)\frac{\text{GeV/c}}{\text{m}} \\ &= 0.4539065\frac{\text{GeV/c}}{\text{m}} \end{aligned} \tag{C.42}$$

Now if the vertex position is moved, but the track parameters are held constant, we must move along the track to a new point-of-closest-approach. For instance, if $R_i^{vtx} \rightarrow R_i^{vtx} + \delta R_i$, we must travel a distance

$$\delta s = e_i \delta R_i \tag{C.43}$$

along the helix. Let's parameterize the helical track using the azimuthal angle ψ about the $\hat{z}_{E665}$ axis. It is a property of a helix that:

$$\rho \delta \psi = e_\perp \delta s. \tag{C.44}$$

Combining Equations C.43 and C.44 yields:

$$\frac{\partial \psi}{\partial R_i^{vtx}} = \frac{\delta \psi}{\delta s} \frac{\delta s}{\delta R_i^{vtx}} = \frac{e_\perp}{\rho} e_i = \frac{\kappa}{p} e_i \tag{C.45}$$

Since the $\vec{B}$ field in the CVM points along $-\hat{z}_{E665}$ and $\dot{\vec{e}} \propto q_p \vec{e} \times \vec{B}$, we know that a positively charged particle will travel in a counterclockwise path about the z_{E665} axis. This means that:

$$\frac{\partial e_x}{\partial \psi} = -q_p e_y, \qquad \frac{\partial e_y}{\partial \psi} = +q_p e_x, \qquad \frac{\partial e_z}{\partial \psi} = 0. \tag{C.46}$$

Combining Equations C.36, C.45, and C.46 yields:

$$\frac{\partial p_x}{\partial R_i^{vtx}} = -\kappa q_p e_i e_y, \qquad \frac{\partial p_y}{\partial R_i^{vtx}} = +\kappa q_p e_i e_x, \qquad \frac{\partial p_z}{\partial R_i^{vtx}} = 0. \tag{C.47}$$

Finally, it is clear that holding the vertex position constant and moving the track by an amount $\vec{r}$ is equivalent to holding the track constant and moving the vertex position by an amount $-\vec{r}$. Therefore:

$$\frac{\partial \vec{p}}{\partial Y_{trk}} = -\frac{\partial \vec{p}}{\partial Y_{vtx}}, \qquad \frac{\partial \vec{p}}{\partial Z_{trk}} = -\frac{\partial \vec{p}}{\partial Z_{vtx}} \tag{C.48}$$

Equations C.47 and C.48 hold for the momentum of any charged particle in a magnetic field. In particular it holds for $\vec{p} \in \{\vec{l}, \vec{l}', \vec{p}_h\}$. Equation C.28 along with the other formulae in this section allow us to transform both the particle momenta and the covariance matrix from the basis of measured track and vertex parameters in an event to the basis of particle three-momentum vectors.

Transforming from $\{\vec{l},\vec{l}',\vec{p}_h\} \rightarrow \{\vec{q},\vec{l}',\vec{p}_h\}$

The transformation $\vec{l},\vec{l}',\vec{p}_h \rightarrow \vec{q},\vec{l}',\vec{p}_h$ is much simpler than the previous one. The Jacobian is given by:

$$\frac{\partial(\vec{q},\vec{l}',\vec{p}_h)}{\partial(\vec{l},\vec{l}',\vec{p}_h)} \equiv \begin{pmatrix} \frac{\partial\vec{q}}{\partial\vec{l}} & \frac{\partial\vec{l}'}{\partial\vec{l}} & \frac{\partial\vec{p}_h}{\partial\vec{l}} \\ \frac{\partial\vec{q}}{\partial\vec{l}'} & \frac{\partial\vec{l}'}{\partial\vec{l}'} & \frac{\partial\vec{p}_h}{\partial\vec{l}'} \\ \frac{\partial\vec{q}}{\partial\vec{p}_h} & \frac{\partial\vec{l}'}{\partial\vec{p}_h} & \frac{\partial\vec{p}_h}{\partial\vec{p}_h} \end{pmatrix} = \begin{pmatrix} \bar{1} & 0 & 0 \\ -\bar{1} & \bar{1} & 0 \\ 0 & 0 & \bar{1} \end{pmatrix} \tag{C.49}$$

where $\bar{1}$ denotes a 3×3 unit matrix. Therefore the transformation is:

$$\begin{pmatrix} \sigma^2_{\vec{q}\vec{q}} & \sigma^2_{\vec{q}\vec{l}'} & \sigma^2_{\vec{q}\vec{p}_h} \\ \sigma^2_{\vec{l}'\vec{q}} & \sigma^2_{\vec{l}'\vec{l}'} & \sigma^2_{\vec{l}'\vec{p}_h} \\ \sigma^2_{\vec{p}_h\vec{q}} & \sigma^2_{\vec{p}_h\vec{l}'} & \sigma^2_{\vec{p}_h\vec{p}_h} \end{pmatrix} = \begin{pmatrix} \bar{1} & -\bar{1} & 0 \\ 0 & \bar{1} & 0 \\ 0 & 0 & \bar{1} \end{pmatrix} \begin{pmatrix} \sigma^2_{\vec{l}\vec{l}} & \sigma^2_{\vec{l}\vec{l}'} & \sigma^2_{\vec{l}\vec{p}_h} \\ \sigma^2_{\vec{l}'\vec{l}} & \sigma^2_{\vec{l}'\vec{l}'} & \sigma^2_{\vec{l}'\vec{p}_h} \\ \sigma^2_{\vec{p}_h\vec{l}} & \sigma^2_{\vec{p}_h\vec{l}'} & \sigma^2_{\vec{p}_h\vec{p}_h} \end{pmatrix} \begin{pmatrix} \bar{1} & 0 & 0 \\ -\bar{1} & \bar{1} & 0 \\ 0 & 0 & \bar{1} \end{pmatrix} \tag{C.50}$$

This transformation leaves the 2×2 subarray in the lower right hand corner invariant:

$$\begin{pmatrix} \sigma^2_{\vec{l}'\vec{l}'} & \sigma^2_{\vec{l}'\vec{p}_h} \\ \sigma^2_{\vec{p}_h\vec{l}'} & \sigma^2_{\vec{p}_h\vec{p}_h} \end{pmatrix} \Longrightarrow \begin{pmatrix} \sigma^2_{\vec{l}'\vec{l}'} & \sigma^2_{\vec{l}'\vec{p}_h} \\ \sigma^2_{\vec{p}_h\vec{l}'} & \sigma^2_{\vec{p}_h\vec{p}_h} \end{pmatrix} \tag{C.51}$$

while the following new elements arise:

$$\sigma^2_{\vec{q}\vec{q}} = \sigma^2_{\vec{l}\vec{l}} - \sigma^2_{\vec{l}\vec{l}'} - \sigma^2_{\vec{l}'\vec{l}} + \sigma^2_{\vec{l}'\vec{l}'} \tag{C.52}$$

$$\sigma^2_{\vec{q}\vec{l}'} = \sigma^2_{\vec{l}\vec{l}'} - \sigma^2_{\vec{l}'\vec{l}'} \tag{C.53}$$

$$\sigma^2_{\vec{q}\vec{p}_h} = \sigma^2_{\vec{l}\vec{p}_h} - \sigma^2_{\vec{l}'\vec{p}_h}. \tag{C.54}$$

Transforming from $\{\vec{q},\vec{l}',\vec{p}_h\} \rightarrow p_T$

In order to convert from $\{\vec{p}_h,\vec{q},\vec{l}'\}$ to p_T we must first set up some definitions and identities:

$$\begin{aligned} &\vec{p}_T \equiv \vec{p}_h - \hat{q}\ \vec{p}_h \cdot \hat{q}, \quad && p_L \equiv \vec{p}_h \cdot \hat{q}, \quad && p_T^2 = p_h^2 - (\vec{p}_h \cdot \hat{q})^2, \\ &\hat{p}_T \equiv \vec{p}_T / p_T, && && \hat{q} \equiv \vec{q}/|\vec{q}\ |. \end{aligned} \tag{C.55}$$

Then we must perform some simple derivatives:

$$\frac{\partial|\vec{q}\,|}{\partial\vec{q}} = \hat{q}, \tag{C.56}$$

$$\frac{\partial\hat{q}_j}{\partial q_i} = \frac{|\vec{q}\,|\delta_{ij} - q_j\hat{q}_i}{|\vec{q}\,|^2} = \frac{1}{|\vec{q}\,|}(\delta_{ij} - \hat{q}_i\hat{q}_j), \tag{C.57}$$

$$\frac{\partial(\vec{p}_T)_j}{\partial p_i} = (\delta_{ij} - \hat{q}_i\hat{q}_j). \tag{C.58}$$

Now we can start assembling derivatives for the final Jacobian in the case of p_T. First we note that p_T is a function of $\vec{q}$ and $\vec{p}_h$ alone and is independent of $\vec{l}'$.

$$\frac{\partial p_T^2}{\partial\vec{l}'} = \frac{\partial p_T}{\partial\vec{l}'} = 0 \tag{C.59}$$

Next, we can find the dependence on $\vec{p}_h$ by differentiating the expression for p_T^2 in Equation C.55:

$$\frac{\partial p_T^2}{\partial\vec{p}_h} = 2\vec{p}_h - 2\hat{q}p_L = 2\vec{p}_T, \tag{C.60}$$

$$\frac{\partial p_T}{\partial\vec{p}_h} = \hat{p}_T. \tag{C.61}$$

Similarly, we can find the dependence on $\vec{q}$:

$$\frac{\partial p_T^2}{\partial q_i} = -2p_L p_j\frac{\partial\hat{q}_j}{\partial q_i} = -2p_L p_j\frac{1}{|\vec{q}\,|}(\delta_{ij} - \hat{q}_i\hat{q}_j) = -2\frac{p_L}{|\vec{q}\,|}(\vec{p}_T)_i\ . \tag{C.62}$$

So,

$$\frac{\partial p_T^2}{\partial\vec{q}} = -2\frac{p_L}{|\vec{q}\,|}\vec{p}_T, \tag{C.63}$$

$$\frac{\partial p_T}{\partial\vec{q}} = -\frac{p_L}{|\vec{q}\,|}\hat{p}_T \tag{C.64}$$

Finally, we can assemble the answer:

$$\boxed{\sigma^2_{p_T} = \frac{\partial p_T}{\partial q_i}\sigma^2_{q_iq_j}\frac{\partial p_T}{\partial q_j} + 2\frac{\partial p_T}{\partial q_i}\sigma^2_{q_ip_j}\frac{\partial p_T}{\partial p_j} + \frac{\partial p_T}{\partial p_i}\sigma^2_{p_ip_j}\frac{\partial p_T}{\partial p_j}}\ . \tag{C.65}$$

where the derivatives are given by Equations C.61 and C.64 above. We also know that

$$\sigma_{p_T^2} = 2p_T\sigma_{p_T}. \tag{C.66}$$

Transforming from $\{\vec{q}, \vec{l}', \vec{p}_h\} \rightarrow \varphi_h$

The variable φ_h is a bit more complicated than p_T since it involves all three vectors: $\vec{q}$, $\vec{l}'$, and $\vec{p}_h$. In addition to Equation C.55 above, we need to define the transverse component of $\vec{l}'$ as well as the unit vector corresponding to $\vec{l}'_T$:

$$\vec{l}'_T \equiv \vec{l}' - \hat{q}\ \vec{l}' \cdot \hat{q}, \qquad l'_L \equiv \vec{l}' \cdot \hat{q}, \qquad \hat{x}' \equiv \vec{l}'_T / l'_T. \tag{C.67}$$

Now, $\hat{x}'$ and $\hat{z}' \equiv \hat{q}$ form a cartesian coordinate system along with $\hat{y}' \equiv \hat{z}' \times \hat{x}'$. We can express the vector $\vec{p}_h$ in this coordinate system as $\{p'_x, p'_y, p'_z\}$. In this same frame, but expressed in cylindrical coordinates, $\vec{p}_h$ is $\{p_L, p_T, \varphi_h\}$. This means that

$$\cos\varphi_h = \hat{x}' \cdot \hat{p}_T. \tag{C.68}$$

We can also write:

$$\begin{aligned} \hat{p}_T &= \hat{x}' \cos\varphi_h + \hat{y}' \sin\varphi_h, \\ \hat{\varphi} &= -\hat{x}' \sin\varphi_h + \hat{y}' \cos\varphi_h. \end{aligned} \tag{C.69}$$

From Equation C.69, we can derive the following identities which will be useful later:

$$\begin{aligned} \hat{x}' - \hat{p}_T \cos\varphi_h &= -\hat{\varphi} \sin\varphi_h, \\ \hat{p}_T - \hat{x}' \cos\varphi_h &= \hat{y}' \sin\varphi_h, \end{aligned} \tag{C.70}$$

and

$$\hat{x}' \cdot \hat{q} = \hat{p}_T \cdot \hat{q} = 0. \tag{C.71}$$

Now, we will collect some useful derivatives. First we have:

$$\begin{aligned} \frac{\partial(\vec{p}_T)_j}{\partial q_i} &= -\hat{q}_j p_k \frac{\partial \hat{q}_k}{\partial q_i} - \frac{\partial \hat{q}_j}{\partial q_i} p_L \\ &= -\frac{1}{|\vec{q}\,|}\left[\hat{q}_j(p_i - p_L \hat{q}_i) + p_L(\delta_{ij} - \hat{q}_i \hat{q}_j)\right] \\ &= -\frac{1}{|\vec{q}\,|}\left[(\vec{p}_T)_i \hat{q}_j + p_L(\delta_{ij} - \hat{q}_i \hat{q}_j)\right]. \end{aligned} \tag{C.72}$$

Next, we have:

$$\begin{aligned} \frac{\partial(\hat{p}_T)_j}{\partial p_i} &= \frac{1}{p_T^2}\left(p_T \frac{\partial(\vec{p}_T)_j}{\partial p_i} - \frac{\partial p_T}{\partial p_i}(\vec{p}_T)_j\right) \\ &= \frac{1}{p_T}\left(\delta_{ij} - \hat{q}_i \hat{q}_j - (\hat{p}_T)_i (\hat{p}_T)_j\right), \end{aligned} \tag{C.73}$$

and by analogy ($\vec{p}_h \leftrightarrow \vec{l}'$):

$$\frac{\partial \hat{x}'_j}{\partial l'_i} = \frac{1}{l'_T}\left(\delta_{ij} - \hat{q}_i\hat{q}_j - \hat{x}'_i\hat{x}'_j\right). \tag{C.74}$$

Next, we have:

$$\begin{aligned}
\frac{\partial(\hat{p}_T)_j}{\partial q_i} &= \frac{1}{p_T}\left(\frac{\partial(\vec{p}_T)_j}{\partial q_i} - \frac{\partial p_T}{\partial q_i}(\hat{p}_T)_j\right) \\
&= \frac{1}{p_T}\left\{-\frac{1}{|\vec{q}\,|}\left[(\vec{p}_T)_i\hat{q}_j - p_L(\delta_{ij} - \hat{q}_i\hat{q}_j)\right] - (\hat{p}_T)_j\left(\frac{p_L}{|\vec{q}\,|}(\hat{p}_T)_i\right)\right\} \\
&= -\frac{p_L}{p_T|\vec{q}\,|}(\delta_{ij} - \hat{q}_i\hat{q}_j - (\hat{p}_T)_i(\hat{p}_T)_j) - (\hat{p}_T)_i\frac{\hat{q}_j}{|\vec{q}\,|},
\end{aligned} \tag{C.75}$$

and again by analogy ($\vec{p}_h \leftrightarrow \vec{l}'$):

$$\frac{\partial \hat{x}'_j}{\partial q_i} = -\frac{l'_L}{l'_T|\vec{q}\,|}\left(\delta_{ij} - \hat{q}_i\hat{q}_j - \hat{x}'_i\hat{x}'_j\right) - \hat{x}'_i\frac{\hat{q}_j}{|\vec{q}\,|}. \tag{C.76}$$

With this collection of derivatives in hand, we are ready to assemble the derivatives of $\cos\varphi_h$ with respect to $\vec{q}$, $\vec{l}'$, and $\vec{p}_h$.

$$\frac{\partial \cos\varphi_h}{\partial p_i} = \hat{x}'_j\frac{\partial(\hat{p}_T)_j}{\partial p_i} = \hat{x}'_j\frac{1}{p_T}(\delta_{ij} - \hat{q}_i\hat{q}_j - (\hat{p}_T)_i(\hat{p}_T)_j), \tag{C.77}$$

or

$$\frac{\partial \cos\varphi_h}{\partial \vec{p}_h} = \frac{1}{p_T}(\hat{x}' - \hat{p}_T\cos\varphi_h) = -\frac{\sin\varphi_h}{p_T}\hat{\varphi}, \tag{C.78}$$

which means that

$$\frac{\partial \varphi_h}{\partial \vec{p}_h} = \frac{1}{p_T}\hat{\varphi}. \tag{C.79}$$

Similarly

$$\frac{\partial \cos\varphi_h}{\partial \vec{l}'} = \frac{1}{l'_T}(\hat{p}_T - \hat{x}'\cos\varphi_h) = +\frac{\sin\varphi_h}{l'_T}\hat{y}', \tag{C.80}$$

or

$$\frac{\partial \varphi_h}{\partial \vec{l}'} = -\frac{1}{l'_T}\hat{y}'. \tag{C.81}$$

Finally, we come to the dependence on $\vec{q}$:

$$\begin{aligned}\frac{\partial \cos\varphi_h}{\partial q_i} &= \frac{\partial \hat{x}'_j}{\partial q_i}(\hat{p}_T)_j + \hat{x}'_j\frac{\partial(\hat{p}_T)_j}{\partial q_i} \\ &= -\frac{l'_L}{l'_T|\vec{q}\,|}((\hat{p}_T)_i - \hat{x}'_i\cos\varphi_h) - \frac{p_L}{p_T|\vec{q}\,|}(\hat{x}'_i - (\hat{p}_T)_i\cos\varphi_h), \qquad \text{(C.82)}\end{aligned}$$

or

$$\begin{aligned}\frac{\partial \cos\varphi_h}{\partial \vec{q}} &= -\frac{l'_L}{l'_T|\vec{q}\,|}\sin\varphi_h\hat{y}' + \frac{p_L}{p_T|\vec{q}\,|}\sin\varphi_h\hat{\varphi} \\ &= \frac{\sin\varphi_h}{|\vec{q}\,|}\left(-\frac{l'_L}{l'_T}\hat{y}' + \frac{p_L}{p_T}\hat{\varphi}\right). \qquad \text{(C.83)}\end{aligned}$$

This means that:

$$\frac{\partial\varphi_h}{\partial\vec{q}} = \frac{1}{|\vec{q}\,|}\left(\frac{l'_L}{l'_T}\hat{y}' - \frac{p_L}{p_T}\hat{\varphi}\right). \qquad \text{(C.84)}$$

Now all that remains is to assemble the final expression for σ^2_φ:

$$\boxed{\begin{aligned}\sigma^2_\varphi = {} & \frac{\partial\varphi}{\partial q_i}\sigma^2_{q_iq_j}\frac{\partial\varphi}{\partial q_j} + \frac{\partial\varphi}{\partial l'_i}\sigma^2_{l'_il'_j}\frac{\partial\varphi}{\partial l'_j} + \frac{\partial\varphi}{\partial p_i}\sigma^2_{p_ip_j}\frac{\partial\varphi}{\partial p_j} \\ & + 2\frac{\partial\varphi}{\partial q_i}\sigma^2_{q_il'_j}\frac{\partial\varphi}{\partial l'_j} + 2\frac{\partial\varphi}{\partial q_i}\sigma^2_{q_ip_j}\frac{\partial\varphi}{\partial p_j} + 2\frac{\partial\varphi}{\partial l'_i}\sigma^2_{l'_ip_j}\frac{\partial\varphi}{\partial p_j}\end{aligned}} \qquad \text{(C.85)}$$

Note that

$$\sigma_{\cos\varphi_h} = \sin\varphi\sigma_\varphi. \qquad \text{(C.86)}$$

Appendix D

The Fermilab E665 Collaboration

M. R. Adams[6], S. Aïd[9,x], P. L. Anthony[10,a], M. D. Baker[10], J. Bartlett[4], A. A. Bhatti[13,b], H. M. Braun[14], W. Busza[10], J. M. Conrad[5], G. Coutrakon[4,c], R. Davisson[13], I. Derado[11], S. K. Dhawan[15], W. Dougherty[13], T. Dreyer[1,x], K. Dziunikowska[8], V. Eckardt[11], U. Ecker[14,x], M. Erdmann[1,e], A. Eskreys[7], J. Figiel[7], H. J. Gebauer[11], D. F. Geesaman[2], R. Gilman[2,d], M. C. Green[2,f], J. Haas[1], C. Halliwell[6], J. Hanlon[4], D. Hantke[11], V. W. Hughes[15], H. E. Jackson[2], D. E. Jaffe[6,o], G. Jancso[11], D. M. Jansen[13,l], S. Kaufman[2], R. D. Kennedy[3], T. Kirk[4,g], H. G. E. Kobrak[3], S. Krzywdzinski[4], S. Kunori[9], J. J. Lord[13], H. J. Lubatti[13], D. McLeod[6], S. Magill[6,g], P. Malecki[7], A. Manz[11], H. Melanson[4], D. G. Michael[5,h], W. Mohr[1], H. E. Montgomery[4], J. G. Morfin[4], R. B. Nickerson[5,i], S. O'Day[9,j], K.Olkiewicz[7], L. Osborne[10], V.Papavassiliou[15,g], B. Pawlik[7], F. M. Pipkin[5,q], E. J. Ramberg[9,j], A. Röser[14,r], J. J. Ryan[10], A. Salvarani[3,k], H.Schellman[12], M. Schmitt[5,m], N. Schmitz[11], K. P. Schüler[15], H. J. Seyerlein[11], A. Skuja[9], G. A. Snow[9], S. Söldner-Rembold[11], P. H. Steinberg[9,q], H. E. Stier[1,q], P. Stopa[7], R. A. Swanson[3], R. Talaga[9,g], S. Tentindo-Repond[2,n], H.-J. Trost[2], M. Vidal[11] M. Wilhelm[1], J. Wilkes[13], H. Venkataramania[15], Richard Wilson[5], W. Wittek[11], S. A. Wolbers[4], T. Zhao[13]

[1] Albert-Ludwigs-Universität Freiburg i. Br., Germany
[2] Argonne National Laboratory, Argonne IL USA
[3] University of California, San Diego, CA USA
[4] Fermi National Accelerator Laboratory, Batavia, IL USA
[5] Harvard University, Cambridge, MA USA
[6] University of Illinois, Chicago, IL USA
[7] Institute for Nuclear Physics, Krakow, Poland
[8] Institute for Nuclear Physics, Academy of Mining and Metallurgy, Krakow, Poland
[9] University of Maryland, College Park, MD USA
[10] Massachusetts Institute of Technology, Cambridge, MA USA
[11] Max-Planck-Institute, Munich, Germany
[12] Northwestern University, Evanston, IL USA
[13] University of Washington, Seattle, WA USA
[14] University of Wuppertal, Wuppertal, Germany
[15] Yale University, New Haven, CT USA

[a] Current address: Lawrence Livermore National Laboratory, Livermore, CA 94550, USA.
[b] Current address: The Rockefeller University, New York NY 10021, USA.
[c] Current address: Loma Linda University Medical Center, Loma Linda CA 92350 USA.
[d] Current address: Rutgers University, Piscataway, NJ 08855, USA.
[e] Current address: DESY, Notkestr.85,2000 Hamburg, Germany.
[f] Current address: LeCroy Research Systems, Spring Valley, NY 10977, USA.
[g] Current address: Argonne National Laboratory, Argonne, IL 60439, USA.
[h] Current address: California Institute of Technology, Pasadena, CA 91125, USA.
[i] Current address: Oxford University, Oxford, UK.
[j] Current address: Fermi National Accelerator Laboratory, Batavia, IL 60510, USA.
[k] Current Address A. T. & T, Bell Labs. 2000 North Naperville Road, Naperville, IL, USA.
[l] Current address: Los Alamos National Laboratory, Los Alamos, NM, USA
[m] Current address: University of Wisconsin, Madison, Wisconsin, USA
[n] Current address: Northern Illinios University, Dekalb, IL 60115, USA.
[o] Current address: Laboratoire de l'Accelerateur Lineaire, Orsay, FRANCE.
[p] Current address: Buero Schellmann, Rabenhorst 29, Hamburg 65, Germany
[q] Deceased.
[r] Current address: Ruhrnuniversität Bochum, D-4630 Bochum 1, Germany
[x] Current address: Unknown.

Appendix E

Glossary

This Appendix contains a glossary of terms and a list of symbols. The glossary of terms consists primarily of acronyms or terms that are specific to high-energy physics or to the E665 experiment at Fermilab. The list of symbols refers to the various physics variables that are used in this thesis. Some symbols that are used only very locally are not included.

E.1 Glossary of Terms

Bay: A space between the absorbers in the Muon Identification system. This is where the PTM, SPM, and SMS chambers resided.

Beam Spectrometer: The portion of the E665 Detector which measured the momenta of the incoming muons in the beam. See Section 3.2.

Beam-hole module: A special PTM module through which the muon beam passed. These modules were deadened in the middle to prevent beam-loading of the PTMs and to allow the PTMs to be used as one of the inputs to the WAM2 trigger.

BS: **B**eam **S**pectrometer.

Bucket: An accelerator RF **bucket**. Muons arrived in the Muon lab at intervals of roughly 19 ns. A bucket refers to the roughly 1 ns wide time period during which a muon may be expected to arrive.

CAL: The Electromagnetic **Cal**orimeter used in E665. See Section 3.6.

CERN: A $p\bar{p}$ collider in Geneva, Switzerland.

CCM: The **C**hicago **C**yclotron **M**agnet. This magnet, originally from the Cyclotron at the University of Chicago, provided the bending which allowed us to measure particle momenta in the E665 apparatus.

CVM: The **C**ERN **V**ertex **M**agnet. This magnet, borrowed from CERN, served two purposes. It bent the trajectories of particles so that their momentum could be measured in the Streamer Chamber and also compensated for the bending in the CCM, yielding a focusing condition which simplified triggering.

C0: Čerenkov Detector number 0. An E665 Detector Element. See Section 3.7.

C1: Čerenkov Detector number 1. An E665 Detector Element. See Section 3.7.

DC: The **D**rift **C**hambers. This E665 detector element, which was split into two pieces, the DCA and DCB chambers, tracked particle trajectories downstream of the CCM magnet, improving the momentum resolution. See Section 3.4.

DCA: **D**rift **C**hamber group **A**. The upstream group of DCs.

DCB: **D**rift **C**hamber group **B**. The downstream group of DCs.

DESY: An accelerator facility in Hamburg, Germany.

DIS: **D**eep **I**nelastic **S**cattering. This refers to inelastic lepton-nucleon scattering where, in general, the nucleon is broken up. Technically, *Deep* Inelastic Scattering refers to scattering where the 4-momentum and energy transfers are large: $Q^2 \gg M^2$ and $\nu \gg M$.

DR: **D**ata **R**eduction program. A standard E665 computer program which ran on a sample of events that had already been reconstructed by the PTMV program. The DR program implemented a set of cuts in order to trim down the sample to one that contained events of particular physics interest. See Section 4.4.

EMC: The **E**uropean **M**uon **C**ollaboration. This group performed a series of muon scattering experiments in the North Area of the CERN Accelerator Facility.

E665: Fermilab **E**xperiment # **665**. The muon scattering experiment at Fermi National Accelerator Laboratory which is described in this thesis.

FCAL: **F**ast **CAL**orimeter-based Physics Trigger.

Fermilab: **Fermi** National Accelerator **Lab**oratory. The U.S. Department of Energy accelerator facility in Batavia, Illinois. The experiment described in this thesis was performed there.

Filter: The **Filter** program. A standard E665 computer program which attempted to remove junk events from the raw data sample. The specific cuts imposed depended upon the trigger type, but the basic idea was to only keep events which resulted from some sort of scattering in the target. See Section 4.2.

FNAL: **F**ermi **N**ational **A**ccelerator **L**aboratory. See **Fermilab.**

Forward Spectrometer: This portion of the E665 Detector measured the momenta of outgoing particles. See Section 3.4.

FS: **F**orward **S**pectrometer.

GeV: **G**iga **e**lectron **V**olt. 10^9 electron Volts. The GeV is the fundamental unit of energy in particle physics. It is equal to the energy gained by an electron traversing a voltage differential of 10^9 volts. In this thesis, the speed of light c is set to unity, which means that the GeV is also a unit of momentum and mass, which would normally be given by GeV/c and GeV/c^2 respectively.

HALO: An E665 trigger which selected events with **halo** muons in them. A *halo* muon was a muon from the beam which was outside the main beam profile.

HERA: An electron-proton collider at DESY.

Interspill: The 35 s period during which the muon beam was inactive between spills.

JETSET: The Lund Monte Carlo for **Jet** Fragmentation and e^+ e^-collisions. This package is used in this thesis to fragment the partons which are generated by the Lund package LEPTO. See Section 2.4.

LAT: **L**arge **A**ngle Physics **T**rigger. This was the physics trigger which selected the event sample used in this thesis. See Section 3.8.

LEPTO: The Lund Monte Carlo for Deep Inelastic **Lepto**n-nucleon scattering. This package generates partons which are then fragmented by the Lund package JETSET. A modified version of LEPTO which includes azimuthal asymmetry at the parton level (due to $k_\perp$) was used in this thesis. See Section 2.4 and Appendix B.

Lund: A Monte Carlo package which has been written and maintained by physicists at the Department of Theoretical Physics of the University of **Lund**. It includes several subpackages, such as LEPTO and JETSET.

MeV: **M**ega **e**lectron **V**olt. 10^6 eV. 10^{-3} GeV. See GeV.

Module: In the PTM and PTA detector systems this term refers to a unit of construction consisting of a group of 15 wires. See Section 3.5.3.

Monte Carlo: A type of program which models a physical process on a statistical basis using random numbers. Event parameters are generated according to a phenomenological or theoretical distribution of possible outcomes.

PBT: **B**eam **T**agging **P**roportional Tubes. These chambers measured the incoming beam trajectory through the Beam Spectrometer, allowing the incoming muon energy to be determined. See Section 3.2.

PC: **P**roportional **C**hambers. Three packages of multiwire proportional chambers between the CVM and CCM. These packages were known as PC1, PC2, and PC3. See Section 3.4.

PCF: **P**roportional **C**hambers, **F**orward Spectrometer. Five triplets of multiwire proportional chambers. Four of the triplets were inside the CCM, allowing us to follow the curved particle trajectories in the magnetic field. See Section 3.4.

PCLAT: An E665 trigger formed by requiring an **LAT** along with a **PC** hit multiplicity requirement See Section 3.8.

PCSAT: An E665 trigger formed by requiring an **SAT** along with a **PC** hit multiplicity requirement See Section 3.8.

PCN: **P**roportional **C**hamber **N**. Another name for the PC detector packages. It refers to the fact that the individual chambers were known as PC1, PC2, and PC3. See Section 3.4.

PCV: **P**roportional **C**hamber **V**ertex. This set of multiwire proportional chambers resided just downstream of the CVM and tracked both wide angle and normal particles. Having the PCV on a track improved the momentum resolution. See Section 3.4.

PSA: **S**mall **P**roportional Chamber group **A**. This E665 detector element was responsible for tracking charged particles which remained in the beam profile downstream of the CCM. See Section 3.4.

PSC: **S**mall **P**roportional Chamber group **C**. A new E665 detector element that was added for the 1990-1991 data-taking run. See Section 3.9.

PSLAT: An E665 trigger: **LAT** **P**re**S**caled by a factor of 16. See Section 3.8.

PSSAT: An E665 trigger: **SAT** **P**re**S**caled by a factor of 64. See Section 3.8.

PTA: **P**roportional **T**ube **A**rray. This E665 detector element was built by the MIT group and instrumented jointly by the MIT and UCSD groups. Its main purpose was to detect wide angle particles. See Section 3.7.

PTM: **P**roportional **T**ubes for **M**uon identification. This E665 detector element was built by the MIT group and instrumented jointly by the MIT and UCSD groups. Its main purpose was to detect muon tracks downstream of the absorber so that muon tracks in the forward spectrometer could be identified. See Section 3.5.3.

PTMV: **P**attern Recognition, **T**rack Fitting, **M**uon Matching, and **V**ertex Finding program. This program was the E665 Offline Event Reconstruction program. See Section 4.3.

QCD: **Q**uantum **C**hromo**D**ynamics is a field theory which describes the behavior of strongly interacting particles such as quarks and gluons.

QED: **Q**uantum **E**lectro**D**ynamics is a field theory which describes the behavior of photons and leptons quite well. This theory is a unification of Quantum Mechanics and Electrodynamics (which includes Special Relativity).

QPM: The **Q**uark **P**arton **M**odel is a model for the structure of hadrons. It describes hadrons as collections of quarks, gluons, and antiquarks which are point particles (partons). These partons can interact directly with external probes such as a muon. The QPM is discussed in this thesis in several forms: Naive, QCD-improved, and $k_\perp$-improved. See Section 2.3.

Rank: An ordering in the energy of a particle within an event. The most energetic particle is Rank 1, the second most energetic particle is Rank 2, etc.

Rank mixing: An effect due to imperfect reconstruction whereby the Rank of a particle is mismeasured. For instance, if we fail to find the Rank 1 particle we will incorrectly assume that the Rank 2 particle is Rank 1.

RBEAM: An E665 trigger: **R**andom Sampling of the **BEAM** used by the LAT.

RBSAT: An E665 trigger: **R**andom Sampling of the **B**eam used by the **SAT**.

RF: **R**adio **F**requency. The Fermilab accelerator uses RF cavities with a frequency of 53.1 MHz.

RICH: **R**ing-**I**maging Čerenkov detector. An E665 detector element. See Section 3.7.

SAT: **S**mall **A**ngle Physics **T**rigger. See Section 3.8.

SBT: **B**eam **T**agging **S**cintillators. An E665 detector element used in the triggers and in rejecting out-of-time beam particles. See Section 3.2.

SC: **S**treamer **C**hamber. An E665 detector element. See Section 3.7.

Simple acceptance correction: This refers to the procedure of correcting plots for the fact that some particles are missing due to **acceptance**. The term "acceptance" is defined as the probability of detecting and reconstructing a particle. A **simple** correction ignores the effects of Rank Mixing and simply weights each particle found by the inverse of its acceptance.

SM: **S**tandard **M**odel. The standard model of particle physics which describes our current understanding of the fundamental particles of nature and their mutual interaction. See Section 2.1.

SMS: **S**mall **M**uon **S**cintillators. An E665 Detector element residing in the beam region downstream of the Steel Absorber which detected muons remaining in the beam profile. They were used in triggering the experiment and in identifying muon tracks in the Forward Spectrometer. See Section 3.5.

SPM: Large **M**uon **S**cintillators. An E665 Detector element residing downstream of the Steel Absorber which detected muons which scattering out of the beam profile. They were used in some of the triggers. See Section 3.5.

Spill: The 22 s spill period when muons were available during the 57 s accelerator spill cycle.

Split: The **Split** program. A standard E665 computer program which split the data from the raw tapes into machine-independent tapes containing only one particular trigger or class of triggers. See Section 4.2.

SUM: **S**cintillator, **U**pstream **M**uon. A new E665 detector element that was added for the 1990-1991 data-taking run. See Section 3.9.

SVJ: **S**cintillator **V**eto **J**aws. An E665 Detector element which was used in the triggers to limit the useable beam phase space. See Section 3.2.

SVS: **S**mall **V**eto **S**cintillator. A new E665 detector element that was added for the 1990-1991 data-taking run. See Section 3.9.

SVW: **S**cintillator **V**eto **W**all. An E665 Detector element which was used in the physics triggers to eliminate wide halo muons and in the HALO trigger to select them. See Section 3.2.

S_∞: The **infinite** momentum frame. A Lorentz Frame in which the target nucleon is moving with an arbitrarily large momentum. See Section 2.3.

T: **T**esla.

Tesla: A unit of magnetic field strength. It is equivalent to 10^4 Gauss.

Tm: **T**esla **m**eters.

TOF: **T**ime-**O**f-**F**light chambers. An E665 detector element. See Section 3.7.

VDC: **V**ertex **D**rift **C**hambers. A new E665 detector element that was added for the 1990-1991 data-taking run. This chamber replaced the Streamer Chamber. See Section 3.9.

WAM2: **W**ide **A**ngle **M**uon Level **2** Trigger. A trigger component implemented for the 1990–1991 data taking runs that used signals from the PTMs as inputs.

E.2 Glossary of Symbols

This glossary is organized in alphabetical order from a–z and then α–ω. These entries are intended as reminders and not as complete stand-alone definitions. All of the quantities are precisely defined in the text of the thesis.

$b_n(z)$: The true distribution of $2\langle\cos\varphi\rangle$ as a function of z_h for the Rank n hadron.

$b_n^m(z)$: The measured distribution of $2\langle\cos\varphi\rangle$ as a function of z_h for the Rank n charged hadron.

B/A: A ratio of fit parameters obtained by fitting the form: $dN/d\varphi = A + B\cos\varphi + C\cos 2\varphi$. $B/A \approx 2\langle\cos\varphi\rangle$.

B/F: The **B**ack over **F**ront energy ratio in the calorimeter.

C/A: A ratio of fit parameters obtained by fitting the form: $dN/d\varphi = A + B\cos\varphi + C\cos 2\varphi$. $C/A \approx 2\langle\cos 2\varphi\rangle$.

$D_n(z)$: The true distribution of $\frac{1}{N_{\mu'}} dN/dz_h$ for the Rank n hadron.

$D_n(z,\varphi)$: The true distribution of $\frac{1}{N_{\mu'}} d^2N/dz_h d\varphi$ for the Rank n hadron.

$D_n^m(z)$: The measured distribution of $\frac{1}{N_{\mu'}} dN/dz_h$ for the Rank n charged hadron.

$D_n^m(z,\varphi)$: The measured distribution of $\frac{1}{N_{\mu'}} d^2N/dz_h d\varphi$ for the Rank n charged hadron.

e_i: The charge of particle i in units of the positron charge.

E: The beam muon energy (in the lab frame).

E': The scattered muon energy (in the lab frame).

$f_1(y)$: $(2-y)\sqrt{1-y}/[1+(1-y)^2]$. See Equation 2.53 on page 51 and the surrounding text.

$f_2(y)$: $(1-y)/[1+(1-y)^2]$. See Equation 2.53 on page 51 and the surrounding text.

$F_1(x_{Bj}, Q^2)$: A structure function which parameterizes the structure of the nucleon as seen by an electromagnetic probe.

$F_2(x_{Bj}, Q^2)$: A structure function which parameterizes the structure of the nucleon as seen by an electromagnetic probe.

$g^{\mu\nu}$: The metric tensor of special relativity.

$k_\perp$: The initial primordial transverse momentum of the struck parton with respect to the virtual photon direction.

K: The flux of virtual photons generated by a muon which scatters with a given set of kinematic variables Q^2 and ν.

l^μ: The four-momentum of the beam muon.

l'^μ: The four-momentum of the scattered muon.

m_l: The muon mass.

m_q: The quark mass (for a given flavor of quark).

$m_\perp$: $= \sqrt{m_q^2 + k_\perp^2}$ for the incoming quark.

M: The nucleon mass (usually taken as the proton mass).

$N_{\mu'}$: The **N**umber of scattered **mu**ons. This quantity is often used to normalize distributions.

$N_{0.05}$: The Calorimeter Plane **N**umber by which **5%** of the energy of a shower has been deposited.

p^μ: The four-momentum of the incoming parton that is struck by the virtual photon in the Quark Parton Model.

p'^μ: The four-momentum of the outgoing parton after it is struck by the virtual photon in the Naïve Quark Parton Model.

p_1^μ: In a gluon bremsstrahlung diagram, the four-momentum of the outgoing quark or anti-quark. In a photon-gluon fusion diagram, the four-momentum of the outgoing quark.

$\hat{p}_{1T}$: The transverse momentum of forward parton 1 with respect to the common forward axis $\hat{Z}^*$ in a gluon bremsstrahlung or photon-gluon fusion event.

p_h^μ: The four-momentum of a hadron.

p_T: Transverse momentum. This is sometimes used in a generic sense and sometimes refers to a specific hadron. In Appendix A and Equation 2.55, p_T refers to the primordial $k_\perp$.

$p_T^{(h)}$: The transverse momentum of a specific hadron.

P^μ: The initial four-momentum of the target nucleon.

P_{χ^2}: A statistical quantity which is the likelihood of a particular χ^2 value (or larger) arising by chance given a normal distribution with the appropriate number of degrees of freedom.

$q_i(\xi, Q^2)$: The distribution of quarks of type i inside the nucleon.

q^μ: The four-momentum of the virtual photon.

Q: $= \sqrt{Q^2}$.

Q^2: The negative invariant mass-squared of the virtual photon.

$\hat{q}$: The direction unit vector of the virtual photon 3-momentum in the lab frame.

R: The ratio of longitudinal to transverse cross-sections for virtual photon interacting with a nucleon. See Section 2.3.

s: $s \equiv (l + p)^2$. Muon-parton invariant mass-squared.

$\hat{s}$: $\hat{s} \equiv (p + q)^2$. Virtual photon-parton invariant mass-squared.

$\hat{t}$: $\hat{t} \equiv (q - p_1)^2$.

u: $u \equiv (l' - p)^2$.

$\hat{u}$: $\hat{u} \equiv (q - p_2)^2$.

$W_1(Q^2, \nu)$: A model-independent parameterization of the nucleon structure as seen by an electromagnetic probe.

$W_2(Q^2, \nu)$: A model-independent parameterization of the nucleon structure as seen by an electromagnetic probe.

W^2: The invariant mass-squared of the hadronic final state.

x, x_{Bj}: $= Q^2/(2P \cdot q)$. This is the Bjorken scaling variable.

x_F: $= p_{||}/p_{||}^{(max)}$ in the hadronic center of mass frame.

x_i: For $i \in \{1,2,3\}$. The energy fraction of parton (or jet) i: $x_i = 2E_i/W$.

y, y_{B_j}: $P \cdot q / P \cdot l$. This is ν/E if the target nucleon is at rest in the lab frame.

z, z_h: $P \cdot p_h / P \cdot q$. This is E_h/ν if the target nucleon is at rest in the lab frame.

z_{h1}: z_h for a Rank 1 hadron.

$\hat{z}$: In Chapter 2 and Appendix A, this is the direction unit vector of the nucleon in the hadronic cm frame (S). By definition $\hat{z} = -\hat{q}$.

$\hat{Z}^*$: In the hadronic cm frame, this is an axis pointing in the direction of the $\sum \vec{p}$ of the forward partons. It should be directly opposite the target remnant momentum direction $\hat{p}_3$. It defines the z-axis for the $\hat{S}$ frame.

α: (1) The fine-structure constant describing the electromagnetic interaction; (2) the orientation angle of a wire with respect to the horizontal; (3) the angle between the beam muon and the virtual photon in the lab frame.

α^*: The orientation angle of a wire with respect to the vertical.

α': The angle between the scattered muon and the virtual photon in the lab frame.

α_s: The QCD coupling constant describing the strength of the strong interaction. In general, it can be considered a function of Q^2 or some other variable.

Γ: This is a factor relating $\sigma_{\gamma^* p}$ to $\sigma_{\mu p}$. The definition of this factor in Chapter 2 is different from that in Appendix A.

$\delta()$: This refers to the Dirac delta function. Its properties are described in Section 1.2.

ϵ: The efficiency for detecting a particle in the E665 Spectrometer. This takes into account both the acceptance and the reconstruction efficiency.

ε: A parameter describing the polarization of a virtual photon with a given Q^2 and ν.

ε^μ: A polarization 4-vector. Usually used to describe the polarization of a virtual photon.

η: (1) The longitudinal momentum fraction of the quark with respect to the nucleon in the hadronic cm frame: p_L/P; (2) The mean energy per pad in the Calorimeter; (3) In Appendix C, the direction that a track is propagating from the primary vertex. It is equal to the sign of p_x in the E665 coordinate system.

θ: The muon scattering angle in the lab frame.

λ: Helicity.

Λ: The longitudinal center-of-gravity of a shower in the Calorimeter.

ν: The virtual photon energy in the lab frame (technically, in the target nucleon rest frame).

ξ: In the Quark Parton Model: the longitudinal momentum fraction of the initial parton with respect to the target nucleon in the infinite momentum frame (S_∞). In the Naïve QPM, this is equal to x_{B_j}.

ξ': The ratio x_{B_j}/ξ.

σ: A generic symbol for a cross-section or the rms-width of a distribution.

σ_L: The cross-section for a nucleon to interact with a longitudinally polarized virtual photon. In general it is a function of Q^2 and ν.

σ_q: A LUND Monte Carlo Parameter. The rms-width of the distribution of hadronization p_T.

σ_T: The cross-section for a nucleon to interact with a transversely polarized virtual photon. In general it is a function of Q^2 and ν.

$\varphi, \varphi_1, \varphi_3$: In Appendix A, these are the azimuthal angle of p, p_1, p_3 around the nucleon axis in the cm frame. Sometimes, φ is used in a generic sense to describe an azimuthal angle.

φ': The azimuthal angle of the outgoing quark around the virtual photon axis in the case of a simple quark or antiquark scattering event.

φ_h: The measured azimuthal angle of a hadron about the virtual photon axis with respect to the scattered muon.

φ_{h1}: φ_h for a Rank 1 hadron.

$\hat{\varphi}_1$: The azimuthal angle of p_1 about the target remnant axis in the $\hat{S}$ frame.

$\phi_\mu^{(lab)}$: The azimuthal angle of the scattered muon about the beam direction with respect to the E665 Y-axis. This angle is defined in the lab frame.

χ^2: A statistical quantity which is the sum of squared normalized residuals. It is used to evaluate the validity of a fit.

Bibliography

[1] E665. Muon scattering with hadron detection at the Tevatron: A proposal to Fermilab, 1980.

[2] Philip R. Bevington. *Data Reduction and Error Analysis for the Physical Sciences.* McGraw-Hill, 1969.

[3] F. Dyson. Divergence of perturbation theory in quantum electrodynamics. Phys. Rev. **85**(4) (1952) 631.

[4] Francis Halzen and Alan D. Martin. *Quarks & Leptons: An Introductory Course in Modern Particle Physics.* John Wiley & Sons, 1984. Deep inelastic scattering is covered in Chapters 8-9. Helicity and chirality are covered in Chapters 5-6.

[5] L. Mo and Y. Tsai. Radiative corrections to elastic and inelastic ep and νp scattering. Rev. Mod. Phys. **41** (1969) 205.

[6] J. I. Friedman and H.W. Kendall. Ann. Rev. Nucl. Sci. **22** (1972) 203.

[7] R.K. Ellis et al. Perturbation theory and the parton model in QCD. Nucl. Phys. B **152** (1979) 285.

[8] C. F. von Weizsäcker. Z. Phys. C **88** (1934) 612.

[9] E. J. Williams. Phys. Rev. **45** (1934) 729.

[10] G. Altarelli and G. Parisi. Asymptotic freedom in parton language. Nucl. Phys. **B126** (1977) 298.

[11] Richard P. Feynman. *Photon-Hadron Interactions.* W. A. Bejamin Inc., 1972.

[12] M. Bengtsson, G. Ingelman, and T. Sjöstrand. Nucl. Phys. **B301** (1988) 554.

[13] J. Chay, S. Ellis, and J.W. Stirling. Azimuthal asymmetry in lepton-proton scattering at high energies. Phys. Lett. B **269** (1991) 175.

[14] J.B. Kogut. Massive μ-pair production in hadron-hadron collisions and the asymptotically free parton model. Phys. Lett. **65B** (1976) 377.

[15] P.V. Landshoff. The transverse momentum of partons. Phys. Lett. **66B** (1977) 452.

[16] F.E. Close, F. Halzen, and D.M. Scott. What is the transverse momentum of partons? Phys. Lett. **68B** (1977) 447.

[17] A. König and P. Kroll. A realistic calculation of the azimuthal asymmetry in semi-inclusive deep inelastic scattering. Z. Phys. C **16** (1982) 89.

[18] H. Georgi and H.D. Politzer. Clean test of quantum chromodynamics in μp scattering. PRL **40**(1) (1978) 3.

[19] Robert N. Cahn. Azimuthal dependence in leptoproduction: A simple parton model calculation. Phys. Lett. **78B** (1978) 269.

[20] Robert N. Cahn. Critique of simple parton-model calculations of azimuthal dependence in leptoproduction. Phys. Rev. D **40** (1989) 3107.

[21] A. S. Joshipura and G. Kramer. Parton transverse momentum corrections in leptoproduction cross sections. J. Phys. G: Nucl. Phys. **8** (1982) 209.

[22] R.D. Peccei and R. Rückl. Energy flow and energy correlations in deep inelastic scattering. Nucl. Phys. B **162** (1980) 125.

[23] A. Mendez. QCD predictions for semi-inclusive and inclusive leptoproduction. Nucl. Phys. **B145** (1978) 199.

[24] J.G. Morfin and W.K. Tung. Parton distributions from a global analysis of deep inelastic scattering and lepton-pair production. Z. Phys. C **52** (1991) 13.

[25] John James Ryan. *Particle Production in Deep Inelastic Muon Scattering.* PhD thesis, Massachusetts Institute of Technology, February 1991.

[26] Mark D. Baker. Modelling the PC support garlands in the E665 Monte Carlo (MC2). Monte Carlo Note MC046, FNAL E665, January 1992.

[27] E665: M.R. Adams et al. A spectrometer for muon scattering at the Tevatron. NIM **A291** (1990) 533.

[28] Jorge G. Morfin. The polarized mode of the Tevatron muon beam. Beam/Trigger Note BT063, FNAL E665, 1988.

[29] H. Fenker. A standard beam PWC for Fermilab. Technical Report TM-1179, FNAL, 1983.

[30] Particle Data Group. Review of particle properties. Phys. Lett. **B204** (1988) 1.

[31] Douglas Grant Michael. *A Study of Transverse Momentum and Jets Using Forward Hadrons and Photons in Deep Inelastic Muon Scattering at 490 GeV/c.* PhD thesis, Harvard University, April 1990.

[32] Michael Henry Schmitt. *Deep Inelastic Exclusive ρ^0 Production using 485 GeV Muons.* PhD thesis, Harvard University, October 1991.

[33] EMC: J.P. Albanese et al. NIM **212** (1983) 111.

[34] Silhacène Aïd. *Measurement of the Ratio of Neutron Cross-Section to Proton Cross-Section in Muon Deep Inelastic Scattering at 490 GeV/c.* PhD thesis, University of Maryland, 1991.

[35] Don Geesaman et al. Data acquisition for FNAL E665. IEEE Trans. on Nucl. Sci. **36** (1989) 1528.

[36] J. Conrad, H. Kobrak, and R. Nickerson. The E665 Level-II trigger logic. Beam/Trigger Note BT053, FNAL E665, February 1988.

[37] P. Madden. Private Conversation, 1991.

[38] J. Conrad. Is the "dead region" dead enough? A preliminary study. Beam/Trigger Note BT080, FNAL E665, March 1989.

[39] Anwar Ahmad Bhatti. *The Ratio of the Proton and Neutron Structure Functions in 490 GeV/c Deep Inelastic Muon Scattering.* PhD thesis, University of Washington, June 1991.

[40] Alexandro F. Salvarani. *Forward Hadron Production in Muon Deep Inelastic Scattering at 490 GeV from Deuterium and Xenon.* PhD thesis, University of California, San Diego, 1991.

[41] W. Wittek. Internal Report EMCSW/81/14, EMC, 1981.

[42] Erik J. Ramberg. *Neutral Pion and Eta Production in Deep Inelastic Muon Scattering at 480 GeV.* PhD thesis, University of Maryland, 1991.

[43] J.J. Aubert et al. Transverse momentum of charged hadrons observed in deep inelastic muon scattering. Phys. Lett. **95B** (1980) 306.

[44] B. Andersson, G. Gustafson, and T. Sjöstrand. Z. Phys. **C12** (1982) 49.

[45] M. Arneodo et al. Transverse momentum and its compensation in current and target jets in deep inelastic muon-proton scattering. Phys. Lett. **149B** (1984) 415.

[46] M. Arneodo et al. Jet production and fragmentation properties in deep inelastic muon scattering. Z. Phys. **C36** (1987) 527.

[47] C. Tao et al. Transverse momentum and angular distributions of hadrons in muon-proton scattering and tests of quantum chromodynamics. PRL **44** (1980) 1726.

[48] J. J. Aubert et al. Measurement of hadronic azimuthal distributions in deep inelastic muon proton scattering. Phys. Lett. **130B** (1983) 118.

[49] M. Arneodo et al. Measurement of hadron azimuthal distributions in deep inelastic muon proton scattering. Z. Phys. C **34** (1987) 277.

[50] Douglas M. Jansen. *Transverse Momentum and the Energy Flow of Charged Hadrons Produced in 490 GeV/c Deep Inelastic Muon Scattering.* PhD thesis, University of Washington, 1991.

[51] W.A. Loomis et al. Hadron production in muon–proton and muon–deuterium collisions. Phys. Rev. D **19** (1979) 2543.

[52] Elliot Leader and Enrico Predazzi. *An Introduction to Gauge Theories and the New Physics.* Cambridge University Press, 1982.

[53] Ch. Rumpf, G. Kramer, and J. Willrodt. Jet cross sections in leptoproduction from QCD. Z. Phys. C **7** (1981) 337.

[54] Wolfgang Wittek. Calculation of kinematic quantities (+ errors) from the 4-momenta of the incoming and outgoing muon in the routine KINQU. Software Note SW127, FNAL E665, September 1990.

[55] J.D. Jackson. *Classical Electrodynamics.* John Wiley & Sons, second edition, 1975.

Art is long, and Time is fleeting,
And our hearts, though stout and brave,
Still, like muffled drums, are beating
Funeral marches to the grave.

Henry Wadsworth Longfellow